# ABSTRACT

Title of dissertation: OBSERVABILITY-BASED SAMPLING AND ESTIMATION OF FLOWFIELDS USING MULTI-SENSOR SYSTEMS

Levi D. DeVries, Doctor of Philosophy, 2014

Dissertation directed by: Professor Derek A. Paley
Department of Aerospace Engineering

The long-term goal of this research is to optimize estimation of an unknown flowfield using an autonomous multi-vehicle or multi-sensor system. The specific research objective is to provide theoretically justified, nonlinear control, estimation, and optimization techniques enabling a group of sensors to coordinate their motion to target measurements that improve observability of the surrounding environment, even when the environment is unknown. Measures of observability provide an optimization metric for multi-agent control algorithms that avoid spatial regions of the domain prone to degraded or ill-conditioned estimation performance, thereby improving closed-loop control performance when estimated quantities are used in feedback control. The control, estimation, and optimization framework is applied to three applications of multi-agent flowfield sensing including (1) environmental sampling of strong flowfields using multiple autonomous unmanned vehicles, (2) wake sensing and observability-based optimal control for two-aircraft formation flight, and (3) bio-inspired flow sensing and control of an autonomous unmanned underwater vehicle.

For environmental sampling, this dissertation presents an adaptive sampling algorithm steering a multi-vehicle system to sampling formations that improve flowfield ob-

servability while simultaneously estimating the flow for use in feedback control, even in strong flows where vehicle motion is hindered. The resulting closed-loop trajectories provide more informative measurements, improving estimation performance. For formation flight, this dissertation uses lifting-line theory to represent a two-aircraft formation and derives optimal control strategies steering the follower aircraft to a desired position relative to the leader while simultaneously optimizing the observability of the leader's relative position. The control algorithms guide the follower aircraft to a desired final position along trajectories that maintain adequate observability and avoid areas prone to estimator divergence. Toward bio-inspired flow sensing, this dissertation presents an observability-based sensor placement strategy optimizing measures of flowfield observability and derives dynamic output-feedback control algorithms autonomously steering an underwater vehicle to bio-inspired behavior using a multi-modal artificial lateral line. Beyond these applications, the broader impact of this research is a general framework for using observability to assess and optimize experimental design and nonlinear control and estimation performance.

# OBSERVABILITY-BASED SAMPLING AND ESTIMATION OF FLOWFIELDS USING MULTI-SENSOR SYSTEMS

by

Levi D. DeVries

Dissertation submitted to the Faculty of the Graduate School of the
University of Maryland, College Park in partial fulfillment
of the requirements for the degree of
Doctor of Philosophy
2014

Advisory Committee:
Dr. Derek A. Paley, Chair/Advisor
Dr. Robert M. Sanner
Dr. David L. Akin
Dr. J. Sean Humbert
Dr. Kayo Ide, Dean's Representative

# Dedication

To my family

## Acknowledgments

First and foremost, I sincerely thank my advisor, Dr. Derek Paley, for his guidance and support during my graduate study. Reflecting on my experiences under Dr. Paley's mentorship, I am reminded of a quote from Bill Bradley, "Leadership is unlocking people's potential to become better." Coming from a background in physics and mathematics, I sometimes wonder how Dr. Paley had the patience for a student who had no idea what a PID controller was, let alone how to use one in a real application. I thank him for seeing potential in me, for providing patient guidance, careful review of my progress and manuscripts, and for his friendship. His commitment to academic scholarship, leadership, and service, while always retaining the importance of family, are values to which I will always aspire.

I also gratefully acknowledge the colleagues and collaborators whose advice and interactions have provided solutions to puzzling research problems. Dr. Sharan Majumdar, Doug Koch, and Dr. Kayo Ide were instrumental in the development of the adaptive algorithm for environmental sampling. Dr. Xiaobo Tan, Dr. Sean Humbert, Dr. Sheryl Coombs, Frank Lagor, Badri Ranganathan, and Hong Lei provided invaluable feedback that greatly improved the end result of the bio-inspired sensing and control work. I also thank the acquaintances, colleagues, and friends whose interactions have generated new research ideas and enriched my perspectives; specifically Blaine Rhoads and Maziar Hemati for providing insight for the formation flight work.

For their time, feedback, and suggestions, I sincerely thank my dissertation committee members, Professors Rob Sanner, Dave Akin, Sean Humbert, and Kayo Ide. Their advice, encouragement, and suggestions throughout my studies have strengthened my research and broadened my understanding of academia, research practices, and the aerospace

profession in general.

I cherish the friendships made with my colleagues in the Collective Dynamics and Control Laboratory, which has become a second home that I will truly miss. Dr. Sachit Butail, Dr. Cammy Peterson, Dr. Nina Mahmoudian, CDR. Tracie Severson, Seth Napora, Nitin Sydney, Amanda Chicoli, Frank Lagor, Daigo Shishika, Dr. Derrick Yeo, and Chin Gian have provided countless happy memories. To the undergraduate researchers who are too many to mention, I thank you for providing new perspectives on problems and bringing enthusiasm and passion to the lab.

Throughout my studies I was fortunate to have access to many facilities at the University of Maryland as well as the expertise of other graduate students, without which I wouldn't have accomplished my research goals. I acknowledge the Space Systems Lab for allowing me use of the Neutral Buoyancy Research Facility and including me in the SCUBA diving rotation, specifically Dr. Max Di Capua, Nick Limparis, and Kate McBryan. I also thank the many graduate students in the department of aerospace engineering whose expertise in complementary subjects have brought new perspectives to this research. I especially thank Andrew Lind who has been patient with my modest understanding of fluid dynamics and has been a sounding board for new ideas, however infeasible they may be. I also greatly appreciate the administrative staff in the Department of Aerospace Engineering, especially Lavita Williams, Debora Chandler, Laura Thoreson, and Thomas Hurst, for placing countless equipment orders.

Outside of academic work, I thank my friends for reminding me that there is more to life than the next paper deadline. To my second family, Ali, Oliver, and Zack Landow, I can not express enough gratitude for the all the laughs, adventures, and encouragement you have provided over these past few years. Your kindness and generosity have helped

me make the east coast my home away from home. I am grateful to Tom Flynn, Cory Johnson, Nikolett Varsa, Robert Hellauer III, Liz Beck, Dustin Alinger, Zach Cummins, Steve Sherman, and all my Minnesota friends for all of the fun times and for providing much needed respite from the difficulties of research. I also thank Futoshi and Sumika Shishika for their incredible kindness during my time in Tokyo.

Finally, I want to extend my utmost gratitude to my family for their unwavering support. My parents, Jim and Adelle, are the inspiration that drives me to chase my dreams, no matter what obstacles might lie along the path. For as long as I can remember, my dad has instilled a work ethic where if something is worth doing, it's worth doing right. My mom has been a model of caring and compassion to which I will always strive, but never hope to achieve. To my siblings, Nathan and Pam, Shannon and Adam, you are role models that I will always look up to. Thank you for your sincere interest in my research and for enduring my circuitous answers to the recurring question, "what is it that you do, exactly?" Finally, to my niece and nephew, Lauren and Tucker, your laughter and antics never fail to brighten my day. To all my family, this dissertation is dedicated to you.

I acknowledge financial support from the National Science Foundation under Grant No. CMMI0928416, the Office of Naval Research under Grant No. N00014-12-1-0149, the Air Force Office of Scientific Research under Grant No. FA95501310162, and the 2013-2014 Link Foundation Ocean Engineering and Instrumentation Fellowship Program.

It is impossible to remember all those who have helped me along this journey, and I apologize to those I've inadvertently left out.

Table of Contents

List of Figures

# Chapter 1: Introduction

As human beings, our insatiable curiosity compels a desire to understand the world around us. To do so, we take careful observations of dynamic processes in our environment and seek to understand the underlying principles governing our observations. For example, early weather forecasters observed the motion and formation of clouds to predict the onset of ominous weather within coming hours. Unsatisfied with lead times on the order of hours, we developed sophisticated measurement tools to provide observations from multiple sensing modalities, allowing us to predict long term weather patterns and the onset of storms days before they occur [1].

More recently, scientists and engineers have developed sophisticated autonomous systems to collect the vital observations needed to expand our understanding of the world. In *environmental sampling* applications, autonomous vehicles are tasked with collecting observations that can lead to better understanding of spatiotemporal dynamic processes in nature. In other applications, sensors are developed using inspiration from nature to allow autonomous systems to better characterize their environment, thereby improving their capability for autonomy. Indeed, by incorporating *bio-inspired* design, we have advanced engineered robotic systems from simple mechanical apparatuses to extremely sophisticated machines that emulate sensorimotor properties perfected over billions of years of evolution.

A common thread to both environmental sampling and bio-inspired sensing and

control is that multiple sensing agents (agents are defined as vehicles or sensors mounted on a vehicle) are used to produce an estimate of the environment in which the vehicles operate. Often, the goal is to produce an estimate of the fluid dynamics in the domain of the system. For example, unmanned aircraft have been used to estimate wind speeds in a tropical cyclone [2], formation flying birds use distributed sensing modalities to estimate the wake produced by their neighbors [3], and a sensor array emulating the fish lateral line has been used to estimate the local fluid motion near an underwater robotic vehicle [4]. By collecting observations that encapsulate the most informative data about the flowfield, the resulting estimation performance can be improved. This is accomplished using coordinated control and optimization to steer the vehicles (or place the sensors) to (in) locations that best observe the most influential domains of the fluid model. By improving the observability of the flow domain, the multi-vehicle (multi-sensor) system is better able to estimate the flowfield.

This dissertation presents a mathematical framework for improving autonomous control and estimation performance in a flowfield by optimizing the control to best observe the flow, even in an unknown flowfield. The framework is applied to three applications of autonomous control: (1) environmental sampling and estimation of strong, spatially-varying flowfields using multiple unmanned vehicles, (2) wake sensing and control for aircraft in close formation flight, and (3) bio-inspired hydrodynamic sensing and control of an underwater vehicle. For environmental sampling with multiple autonomous vehicles in a strong flowfield, decentralized control algorithms steer the vehicles to coordinated sampling formations that maximize observability of the flow domain. We optimize the control parameters using measures of flowfield observability as a cost metric. In wake sensing for close formation flight of autonomous aircraft, this dissertation incorporates measures

of flowfield observability to guide the design of autonomous controllers that regulate the relative position of vehicles while simultaneously improving estimation of the flowfield created by lead vehicle's wake. For bio-inspired flow sensing and control, this dissertation derives a sensor placement strategy that optimizes observability of the hydrodynamic environment and derives estimation and control strategies to enable autonomous operation of an underwater vehicle outfitted with an artificial lateral line. We also describe the experimental implementation of bio-inspired flow sensing and autonomous control on a robotic prototype outfitted with an artificial lateral line. The results of this dissertation enable greater autonomy of unmanned multi-vehicle systems, allowing the vehicles to gather new observations that may help scientists further understand dynamic processes in our environment.

## 1.1 Statement of Problem

This research seeks to understand the interconnectedness of control and estimation for the purpose of optimizing an autonomous multi-vehicle or multi-sensor systems ability to estimate its environment. Specifically, this dissertation combines tools from nonlinear control, nonlinear estimation, and observability optimization to improve autonomy of multi-vehicle or multi-sensor systems that estimate flowfields, as illustrated in Figure 1.1. To understand Figure 1.1, note that control dictates the spatiotemporal observations gathered by each sensor, which significantly affects the resulting estimate of the flowfield, as illustrated by the arrow from the control to estimation blocks in Figure 1.1. Similarly, if estimates of the flow are used in feedback control, the accuracy of the estimate significantly affects the performance of the control. Therefore, there is an inherent need for an optimization procedure that produces control signals whose resulting trajectories generate

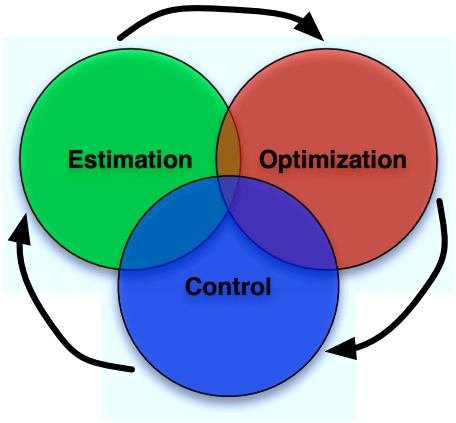


Figure 1.1: This research seeks to understand the interconnectedness of nonlinear control, estimation, and optimization for sensing flowfields using autonomous, multi-agent systems.

observations that improve estimation, thereby improving the ensuing control performance. Throughout this dissertation, measures of flowfield observability serve as an optimization metric.

When applied to environmental sampling, wake sensing for formation flight, and bio-inspired hydrodynamic sensing and control, the main challenges addressed in this dissertation are as follows.

**Environmental Sampling**:

1. *Derive decentralized control algorithms steering vehicles to coordinated sampling formations subject to strong flowfields*[1] *that can hinder vehicle motion.*

2. *Generate multi-vehicle sampling formations that target measurements providing optimal observability of the flowfield, even when the flowfield is unknown.*

**Wake Sensing for Formation Flight**:

[1] A strong flowfield is defined as a flow where the flowspeed can exceed the speed of the vehicle relative to the flow. In a strong flow, the vehicle's direction of travel is limited and forward progress may be impossible.

1. *Design a strategy to estimate the position of a lead aircraft by assimilating noisy aerodynamic measurements distributed along the follower aircraft's wing.*

2. *Characterize spatial coordinates where the follower aircraft's estimation strategy is prone to degraded estimation performance.*

3. *Derive a feedback control algorithm that steers the follower aircraft to a desired position relative to the leader, uses estimates of the leader aircraft position, and avoids areas with poor flowfield observability.*

**Bio-inspired Flow Sensing and Control**:

1. *Design a strategy to configure the placement of sensors within an artificial lateral line array such that they are best able to observe fluid motion.*

2. *Derive an estimation strategy to assimilate noisy measurements from a multi-modal artificial lateral line and estimate flow characteristics needed for feedback control. Use the estimated flow properties to derive feedback control strategies emulating bio-inspired behavior.*

3. *Use dynamic output feedback control to demonstrate rheotaxis and station-holding behaviors on a robotic fish prototype outfitted with an artificial lateral line.*

## 1.2 Background and Related Work

This section provides an overview of related work in the areas of environmental sampling and multi-vehicle control, close formation flight, and bio-inspired sensing and control for underwater vehicles. Due to the depth and cross-disciplinary nature of these three relatively unrelated applications, it is impossible to provide a complete survey of

all research pertinent to these topics; however, this section provides reference to the most relevant works of which the results of this dissertation are related. In addition, Section 1.2.4 provides a brief history and overview of observability with regard to dynamical systems. References to the works presented in this section are also provided throughout the dissertation.

### 1.2.1 Environmental Sampling

Unmanned aerial vehicles (UAVs) have shown great value in their ability to explore harsh physical environments that are too dangerous for manned platforms. For example, autonomous underwater vehicles have shed light on some of the deepest trenches of the sea [5] and robotic rovers have explored expanses of the desolate martian landscape [6]. Recently, autonomous vehicles have been proposed as a safe and effective way to penetrate extreme weather systems such as hurricanes and tornados [7], shedding light on physical processes that may be inaccessible to manned vehicles or remote sensing techniques [8], [9]. Unmanned aircraft can fly in hurricanes at altitudes lower than it is safe for manned aircraft to operate [9] and can target observations at regions of interest within the storm [10]. In 2006, an Aerosonde unmanned aircraft flying at low altitude successfully penetrated a typhoon eyewall while streaming temperature, pressure, and windspeed data to a remote command center [9]. In 2010, the Global Hawk UAV passed over Hurricane Earl at high altitude while collecting temperature, convection, and precipitation measurements [11], [12]. In addition, smaller unmanned aircraft have been utilized to sample within pre-tornadic supercell thunderstorms [13].

The ability to target observations in the environment is achieved by coordinating the motion of a group of vehicles, motivating the field of *coordinated control*. It is often

desirable for vehicles to collect in-situ observations at regular intervals along a repeated pattern, thereby measuring data with a suitable spatiotemporal sampling density. Multiple long-endurance vehicles deployed in a coordinated manner can collect data over vast spatial and temporal domains while simultaneously regulating the sampling densities of their measurements according to the variability of the environment.

Recently, many authors have contributed coordinated control algorithms for two-dimensional vehicle motion in a flowfield [14], [15], [16], [17], [18]. A few notable works are described as follows, presented in order from the flow-free to strong flow settings. Sepulchre et al. [14] provided decentralized algorithms to stabilize planar parallel and circular formations in a flow-free setting, as well as symmetric circular formations in which vehicle separation is regulated around the circular formation. Zhang et al. used orbit functions [19], [20] to coordinate multi-vehicle motion around closed curves. Arranz, Seuret, and Canudas de Wit [21], [17] provided decentralized control algorithms steering vehicles to circular formations with time-varying radius and position. Paley and Peterson [15] extended the parallel and circular formation results to motion in a time-invariant, moderate flowfield, including time-splay circular formations (formations in which a vehicle revisits a point on the formation at regular time intervals) in a uniform flowfield, whereas Techy, Paley, and Woolsey [16] extended the moderate-flow results to motion around convex loops. Similar work includes that of Frew et al. [22] who used Lyapunov analysis to generate guidance vector fields in a known flowfield. The extension to time-varying flows was made by Peterson and Paley [23]. Bakolas and Tsiotras [24] provided control algorithms providing coverage of a desired region subject to strong flows, however, they assumed a kinematic model of vehicle motion rather than a dynamic vehicle model of the previously noted works.

A flurry of literature has been produced extending planar coordination results to three dimensions, ranging from simple three-dimensional self-propelled particle models to high fidelity models of aircraft motion. A few notable works include Justh and Krishnaprasad [25] who utilized a three-dimensional self-propelled particle model to derive multi-vehicle steering control algorithms that stabilize rectilinear, circular, and helical formations in a flow-free setting. Using a similar model, Scardovi et al. [26] provided formation control algorithms assuming varying communication topologies between vehicles. Hernandez and Paley [27] extended the results to three-dimensional motion coordination in a time-invariant, moderate flowfield. Using a simplified model of aircraft motion with low-level autopilots, Ren and Beard [28] derive trajectory tracking control algorithms for a single vehicle that can be applied to a multi-vehicle application. For a complete review of three-dimensional aircraft models, autopilot design, and guidance algorithms, see [29].

Control strategies developed for motion in a flowfield often assume the flow is known. In order to achieve the desired results in an unknown or partially known flowfield, each vehicle must estimate the local flow. For general vehicle models, prior works have generated flowfield estimates from noisy local flow measurements using a nonlinear observer [23], a distributed consensus filter [30], and a particle filter [31]. Notable research includes Lynch, Schwartz, Yang, and Freeman [32] who utilized decentralized proportional-integral average consensus estimators coupled with Kalman filters to estimate environmental fields using sensor platforms with time-varying communication topologies and Peterson and Paley [33] who implemented a distributed information-consensus filter to estimate the coefficients of a flowfield defined by a finite number of basis functions.

Many techniques have been utilized to estimate the wind fields specific to aircraft flight. Chao and Chen [34] employed multiple UAVs to estimate parameters associated

with a partial differential equation approximating a wind field, whereas Mulgund and Stengel [35] implemented an extended Kalman filter to provide wind shear estimates for use in feedback control of an aircraft. Lawrance and Sukkarieh [36] used Gaussian process regression to estimate a wind field for exploration and exploitation of gliding UAVs and Langelaan, Alley, and Neidhoefer [37] provide a general method for estimating wind fields for small unmanned aerial vehicles outfitted with basic position and rate sensing hardware. In related work with underwater vehicles, Thompson et al. [38] derive path planning procedures using flowfield predictions of ocean currents generated using a forecast model.

Experimental demonstration of coordinated control algorithms has been pursued by many researchers using ground [39] [40], [41], air [42], [43], [44], [45], and underwater [8], [38], [46], [47] vehicles. Notable works include Peterson [42] who demonstrated closed-loop control of two unmanned aircraft to circular formations in an estimated wind field. Techy, Woolsey, and Schmale III synchronized dual aircraft formations for aerobiological sampling [43]. In the underwater environment, Napora and Paley [46], [48] demonstrated parallel and circular formations using a fleet of autonomous underwater vehicles using closed-loop feedback control with motion capture. Leonard et al. [8] coordinated multiple underwater gliders to target observations for measuring dynamical processes in the ocean.

Although coordinated control and flowfield estimation techniques enable operation in unknown flowfields, there exists a need to adaptively optimize multi-vehicle sampling trajectories such that they provide the most informative data in a spatiotemporal environment. For example, large-scale severe weather systems such as hurricanes span tens to hundreds of thousands of square kilometers [49], which is more than a typical unmanned aerial vehicle can cover alone. Similarly, resolving three-dimensional circulation processes in the ocean requires high resolution and synoptic sampling by multiple coordinated sam-

pling platforms [50].

A body of literature has been produced addressing the adaptive sampling and optimization problem, of which a few notable works are mentioned here. Graham and Cortes [51] optimize sampling trajectories of a robotic sensor network in a random spatiotemporal field, minimizing the maximum predictive variance of an estimator over the space of network trajectories. Leonard et al. [8] adaptively optimized glider trajectories to minimize a measure of the mean square error of the estimate of a spatiotemporal field. Cortes, Hernandez, Karatas, and Bullo [51] derive an adaptive coordination algorithm providing optimal coverage of a spatial domain. Choi and How [52] present and path planning model for informative forecasting using measures of mutual information to reduce uncertainty in a forecast model. Sydney and Paley [53] provide multi vehicle controls to sample nonstationary spatiotemporal fields characterized by spatial and temporal decorrelation scales.

### 1.2.2 Formation Flight

An extensive body of literature has been produced regarding the modeling of close formation flight [54], from the aerodynamics of birds in formation [55] to power savings produced by specific aircraft formations [56]. A large portion of the close-formation modeling, [57], [58], [59] control, [60], [61] and experimental [62] studies have focused on formations that produce significant reductions in the induced drag on an aircraft flying within the wake of another aircraft. Blake and Multhopp [57] model a two aircraft formation using potential flow theory and derive relative positions providing optimal aerodynamic efficiency savings. Pachter, D'Azzo and Proud [60] derive a feedback control algorithm stabilizing a linearized model of two aircraft formation flight. Chichka, Wolfe, and Speyer [58]

extend the results to a model a three aircraft in a tight formation. Most of these works utilize lifting-line or vortex-lattice methods [63], [64] to model the aerodynamics of aircraft interactions. In closely related work, Dogan and Sato [65], and Dogan, Lewis, and Blake [66] address the modeling and experimental study of aerodynamic and dynamical effects related to aerial refueling and present a feedback controller to stabilize a two-aircraft refueling maneuver.

Success of close-formation flight is predicated on knowledge of the lead aircraft's relative position and the characteristics of its associated wake. There are significantly less publications regarding estimation of the relative aircraft positions for close formation flight. In experimental work conducted by the National Aeronautics and Space Administration (NASA), high precision GPS measurements blended with integrated inertial measurement systems were incorporated used to experimentally validate autonomous formation flight [67]. Envisioning operation in GPS denied environments, Hemati, Eldredge, and Speyer [68], [69] used lifting-line theory to model a two-aircraft formation and utilized extended Kalman filtering (EKF) and particle filtering techniques to estimate parameters of the lead aircraft's wake using distributed aerodynamic measurements taken along the follower aircraft's wing. In that work, the authors noted that both estimation strategies had difficulty reliably estimating the lead aircraft position and found that filter divergence was dependent on the initial relative aircraft positions.

### 1.2.3 Biologically Inspired Sensing and Control

Stream-dwelling fish have a remarkable ability to navigate tumultuous, unknown environments riddled with obstacles [70]. In fact, many species exhibit a behavior known as station-holding, in which individuals are able to sense the relative position of an obstacle

in a current and hold position in its wake [71]. Similarly, fish are known to orient upstream in a flowfield, a behavior known as (positive) rheotaxis [70]. These behaviors are mediated by sensing modalities such as vision and the lateral line. In fact, fish are able to navigate in the absence of light or without vision [70]. The lateral line is also believed to play an important role in schooling [72] and sensing predators [73], prey [74], and other features within their environment [75], [76]. A bio-inspired artificial lateral line can significantly improve an underwater robot's ability to characterize its surroundings, thereby improving its ability to operate in environments where traditional sensing modalities are hindered.

The lateral line system is composed of hundreds to thousands of receptors, known as neuromasts, distributed along the body of the fish [71]. Neuromasts are divided into two categories: superficial neuromasts, located on the external surface of the fish, consist of hair cells encased in a gelatinous dome called a cupula [77] and sense local flow velocity [78]; canal neuromasts are located under the skin in fluid filled canals and sense pressure differences between adjacent pores of the canal [79], [80].

Several recent works describe an artificial lateral line for underwater vehicle sensing [81], [82]. For example, Yang et al. [81] created an artificial lateral line using an array of micro-fabricated hot-wire anemometry sensors. Many similar works have emulated the function of the canal lateral line system by using pressure [79], [83], [84], optical [85], and capacitive [86] sensor arrays. Artificial superficial neuromast sensors have been developed using various materials including ionic polymer metal composites (IPMC) [87], multi-layered silicon beams [88], and encapsulated metal-oxide semiconductors [89]. For a comprehensive review of biomimetic hair sensors similar to the superficial neuromast system, see Tao and Yu [82].

Previous works have incorporated single-modality sensor arrays for bio-inspired

closed-loop control. Gao and Triantafyllou [90] used a pressure sensor array to control the angle of attack of an underwater vehicle with respect to a free stream flow. Salumae and Kruusma used pressure difference measurements to demonstrate rheotaxis [91]. In other work, the same authors used empirical methods to demonstrate station-holding [92].

Similar works have focused on flow-sensing using an artificial lateral line, rather than feedback control. Fernandez used particle filtering techniques to track vortices near a pressure sensor array [4], whereas Venturelli et al. [79] showed that the position of a Karman vortex street can be discriminated using a pressure sensor array. Ren and Mohseni [76] investigated how an array of canal lateral line sensors are affected by the presence of a Karman vortex street, which is a hydrodynamic structure characterized by vortices of opposite circulation strength shed from an upstream obstacle.

### 1.2.4 Observability

Throughout this dissertation, measures of observability are used to optimize the multi-agent sensing system. Observability in control theory is a measure of how well the state variables of a system can be determined by measurements of its outputs. Here, the general goal is to place a finite number of sensors in a (moving or static) configuration that maximizes (minimizes) observability (unobservability) of states characterizing a flowfield model. For a thorough discussion of observability in linear systems, see [93], whereas as review of nonlinear observability is in [94]. Notions of nonlinear observability were first introduced by Hermann and Krener [95] using techniques from differential geometry. By calculating the rank of the dynamic and output vector field's Lie algebra gradient, a binary assessment of local observability, known as the observability rank condition [95], or Kalman condition [94], is achieved.

Analytical calculation of observability can be difficult to assess for even simple nonlinear systems, motivating recent empirical techniques. Lall, Marsden, and Glavaski [96] introduced the *empirical observability Gramian* for balanced model reduction of nonlinear control systems, which is advantageous for high dimensional and highly nonlinear systems since it only requires the ability to simulate the system [97]. Subsequently, it was shown that the empirical observability Gramian is proportional to the Fisher information matrix [98], differing by only the measurement noise covariance. This implies empirical observability analysis can be used as a metric that predicts estimation performance, but is independent of measurement noise characteristics.

Since its inception, empirical observability techniques have been used in a wide range of applications including model reduction of high-dimensional nonlinear systems [96], optimization of a sensor placement in monitoring chemical reactions [99], and more recently, evaluating the effectiveness of candidate sampling trajectories (or sensor placements) for flowfield estimation [97], [100], [101]. Krener and Ide [97] used the nonlinear observability rank condition [95] to evaluate the effectiveness of Eulerian and Lagrangian drifter sensors with no control authority; the authors in [102], [103] assimilated Lagrangian drifter measurements in an extended Kalman filter to estimate ocean flows. Hinson and Morgansen [100], [101] used observability to derive control algorithms and sensor placement strategies improving for wind direction identification in aircraft and for wake estimation on a pitching and heaving airfoil. Observability techniques have also been in satellite tracking applications [104] and for placing sensors to monitor power systems [105].

## 1.3 Contributions of Dissertation

This dissertation makes contributions to the general fields of multi-vehicle control theory, environmental sampling, autonomous close-formation flight, and bio-inspired sensing and control. Some results from this dissertation have been published or are submitted for publication [106], [107], [108], [78]. Early versions of the published work include the conference papers [109], [110], [111], [112], [113], [114]. Some results, including much of the bio-inspired flow sensing analysis and experimental work, along with the wake sensing and formation flight results, have not appeared elsewhere. The contributions are organized into three general categories in which they lie, notably environmental sampling, wake sensing for formation flight, and bio-inspired sensing and control. They are as follows.

**Environmental Sampling**

This dissertation:

1. Derives theoretically-justified, decentralized multi-vehicle control algorithms steering vehicles to desired sampling formations subject to known, strong flowfields that can hinder vehicle motion. Due to the presence of strong flowfields that can make forward progress impossible, notions of trajectory feasibility are defined to enable derivation of kinematic conditions ensuring feasibility of a desired sampling trajectory. Feasibility analysis facilitates derivation of multi-vehicle control algorithms steering vehicles to desired sampling formations in a strong flowfield. This dissertation derives control algorithms autonomously steering vehicles to parallel, circular, folium, and spirograph motion primitives; the motion primitives enable derivation of multi-vehicle control algorithms steering the collection of vehicles to formations with

- Specified position of the formation center
- Specified radial position of the formation center and arbitrary azimuth
- Regulated spacing between vehicles along the formation; specifically, equal spacing between vehicles is known as the splay formation
- Regulated speed along the formation.

This work considers two- and three-dimensional vehicle motion models. For three-dimensional motion, this dissertation derives autonomous multi-vehicle control algorithms allowing the vehicles to cooperate with the flow to coordinate multi-vehicle motion without changing the flow-relative speed of the vehicle. Previous results required vehicles to change their flow-relative speed, which can decrease vehicle endurance [115].

2. Presents a recursive Bayesian filtering formulation for estimating the flowfield by assimilating noisy measurements of the flow collected from multiple sampling vehicles in space and time.

3. Proposes an adaptive sampling algorithm that optimizes multi-vehicle sampling formations to maximize flowfield observability while simultaneously estimating the flowfield. Measures of flowfield observability provide a metric for iteratively optimizing the parameters defining a family of desired sampling formations. Estimates of the flowfield are utilized in the feedback control and optimization procedures.

**Wake Sensing for Formation Flight**

1. Analyzes observability of lead aircraft position using distributed aerodynamic measurements on followers wing.

2. Presents a recursive Bayesian filtering framework incorporating noisy measurements from multiple sensing modalities to estimate the leader aircraft position relative to the follower.

3. Provides optimal control algorithms for two-aircraft formation flight using measures of observability to avoid spatial domains prone to degraded estimation performance. The observability-based optimization routine improves closed-loop performance when estimates of the the leader position are used in feedback control.

**Bio-inspired Control and Hydrodynamic Sensing**

1. Derives a sensor placement strategy optimizing measures of flowfield observability. Using a Monte-Carlo simulation analysis, the optimized sensor array is shown to outperform 99.9% of random configurations when estimating properties of a uniform flowfield.

2. Presents recursive Bayesian and particle filtering frameworks for estimating flow properties using noisy, distributed measurements from a multi-modal artificial lateral line.

3. Provides theoretically justified vehicle control algorithms enabling autonomous execution of bio-inspired behaviors. Using estimated flowfield properties for feedback control, we derive control algorithms steering vehicles to rheotactic behavior, the tendency of fish to orient upstream, and station-holding, the tendency of fish to hold position behind an upstream obstacle.

4. Experimentally demonstrates rheotaxis and station-holding on a robotic prototype outfitted with a multi-modal artificial lateral line composed of flow and pressure sensors.

## 1.4 Outline of Dissertation

Chapter 2 presents the fundamental mathematical and analytical tools used to address the control, estimation, and optimization problems addressed throughout this dissertation. It introduces the general form of the nonlinear systems considered in this work, providing basic notation to clarify and streamline presentation throughout the dissertation. The chapter is organized according to the mathematical concepts used for each of the components in the technical approach, shown in Figure 1.1. Sections 2.1 and 2.2 describe the mathematical tools used to derive control algorithms for the multi-vehicle or multi-sensor sampling and estimation problem in Chapters 3, 5, and 6. Section 2.1.1 provides an overview of Lyapunov-based control techniques used to steer a group of vehicles to a desired sampling formation, whereas Section 2.1.2 describes tools from optimal control utilized in deriving observability-based control algorithms for close formation flight in Chapter 6. When deriving multi-vehicle control algorithms in Chapter 3, we assume an underlying communication topology between vehicles; Section 2.2 reviews tools from graph theory that mathematically specify these communication topologies. Section 2.3 provides a review of nonlinear and empirical observability measures that serve as optimization metrics allowing a multi-sensor system to maximize the observability of a physical process. Section 2.4 summarizes two nonlinear flowfield estimation techniques including the grid-based recursive Bayesian filter and the particle filter. The grid-based recursive Bayesian filter is implemented in the environmental sampling, formation flight, and bio-inspired sensing applications; the particle filter is implemented for nonlinear, high-dimensional state-space models of vortex flows in Chapter 7.

Chapter 3 derives decentralized multi-vehicle control algorithms steering a collection

of vehicles to a desired sampling formation, even in the presence of strong flows that can disrupt vehicle motion. Section 3.1 models a collection of vehicles in a flowfield as self-propelled particles and derives particle motion models with respect to both inertial and rotating reference frames. Section 3.1 also provides two-dimensional flowfield models used in the control and sampling examples of Chapters 3 and 5. In a strong flow the flowspeed can exceed the flow-relative speed of an individual vehicle, implying that forward progress is not possible in all regions of the flow. This issue motivates the study of trajectory and formation feasibility in a strong flowfield, presented in Section 3.2.

Feasibility analysis provides insight for choosing sampling formations that are feasible and provide the best spatiotemporal sampling density for the goals of the multi-vehicle sampling mission. Section 3.3 uses the feasibility analysis of Section 3.2 and derives control algorithms steering a vehicle to feasible sampling formations. The chapter considers four basic formation primitives including a straight line, circle, folium, and a spirograph. Section 3.4 uses the results of Section 3.3 to derive decentralized *multi-vehicle* control algorithms steering vehicles to a formation of the desired motion primitive.

Chapter 4 extends the two-dimensional results to motion in three dimensions and unknown flowfields by considering a three-dimensional self-propelled vehicle model and a flowfield with a vertical gradient. A recursive Bayesian filter assimilates noisy measurements of the local flow from multiple vehicles, producing an estimate of the global three-dimensional flowfield. By utilizing the variation of flowspeed with altitude, the vehicles are able to coordinate motion without changing their flow-relative speed, which can significantly extend their range and time of operation.

Chapter 5 provides a multi-vehicle, adaptive sampling algorithm that uses measures of flowfield observability to optimize parametric inputs to a coordinated sampling

formation. We consider the application of sampling in an idealized hurricane using a fleet of unmanned aircraft. Section 5.1 presents the sampling problem and defines the control objective. Section 5.2 applies nonlinear observability measures to evaluate candidate sampling trajectories in a Rankine vortex. Section 5.3 builds upon the observability analysis and presents an observability-based adaptive sampling algorithm that maximizes flowfield observability over the space of parameterized candidate sampling formations using estimates of the flowfield. The vehicles collect noisy measurements of the flow and implement a recursive Bayesian filter to estimate the flowfield parameters. Using the estimated flowfield, we calculate the smallest singular value of the empirical observability Gramian to optimize sampling trajectories over a given time interval. The optimized sampling formation parameters and the estimated flowfield are implemented in a decentralized multi-vehicle control from Chapter 3 to steer vehicles to the optimal sampling formation. Section 5.4 illustrates results of simulating the adaptive sampling algorithm in moderate and strong flowfields, and analyzes characteristics of the algorithm's performance.

Chapter 6 applies the control, estimation, and observability optimization tools to close formation flight of two aircraft. Section 6.1 uses lifting-line theory to develop a model of two aircraft in formation flight. Section 6.2 provides quantitative analysis of the observability of a lead aircraft's wake parameters given distributed measurements of differential pressure collected along the follower's wing. Section 6.3 reviews details of the recursive Bayesian filter when used to estimate parameters defining the lead aircraft's wake. Section 6.4 formulates two observability-based optimal control strategies steering the follower aircraft to a desired position relative to the leader while maximizing observability of the lead aircraft parameters along its trajectories. Section 6.5 combines the analysis and control design of previous sections, providing numerical examples of forma-

tion flight and aerial refueling maneuvers in which estimates generated by the recursive Bayesian filter are incorporated in the optimal control strategies.

Chapter 7 applies nonlinear control, estimation, and observability optimization to the design and operation of a bio-inspired robotic fish prototype. Section 7.1 uses potential flow theory to model the flow around a streamlined underwater vehicle in a uniform flowfield and in the wake of an obstacle. Building upon the flow models of Section 7.1, Section 7.2 presents a state-space motion and measurement model for an underwater vehicle outfitted with a multi-modal artificial lateral line. Section 7.3 uses measures of flowfield observability to derive a sensor placement strategy optimizing measures of flowfield observability in a uniform flow. A recursive Bayesian formulation is implemented to estimate properties of the free stream flow. Analysis of Monte Carlo simulations shows the optimized sensor configuration outperforms 99.9% of all sensor configurations. Section 7.4 derives and simulates theoretically-justified control algorithms steering the vehicle to bio-inspired behaviors including rheotaxis and station-holding. Section 7.5 presents the design, fabrication, and implementation of a bio-inspired lateral line incorporating ionic polymer metal composite (IPMC) and pressure sensors in a distributed array. It also presents a novel bootstrapping calibration method enabling use of the multi-modal artificial lateral line without external position or orientation references. Finally, Section 7.6 provides experimental results demonstrating rheotaxis and station-holding behaviors using the multi-modal artificial lateral line control system.

Chapter 8 concludes by summarizing the contributions of the dissertation in Section 8.1 and describing ongoing and future work in Section 8.2. In each section, the contributions and ongoing work recommendations are categorized starting with general comments and then according to the application under which they apply. To efficiently find defini-

tions, terminology, and important concepts, the end of the dissertation contains an index of key terms with corresponding page numbers.

# Chapter 2: Mathematical Background

Throughout this chapter, consider an $N$-dimensional (possibly) nonlinear system with $P$ outputs. Let $\mathbf{x}(t) \in \mathbb{R}^N$ represent the $N$-dimensional state-vector of a dynamical system at time $t$ and $\boldsymbol{\beta}(t) \in \mathbb{R}^P$ denote a $P$-dimensional vector of measurements[1]. For example, $\mathbf{x}(t)$ could represent $N = 6$ scalar quantities describing the position and velocity of a vehicle in three-dimensional space such that

$$\mathbf{x}(t) = [x(t), y(t), z(t), \dot{x}(t), \dot{y}(t), \dot{z}(t)]^T \in \mathbb{R}^6,$$

and $\boldsymbol{\beta}(t) \in \mathbb{R}$ may represent a measurement of the vehicle's speed, i.e. $P = 1$, $\boldsymbol{\beta}(t) = \sqrt{\dot{x}(t)^2 + \dot{y}(t)^2 + \dot{z}(t)^2}$. Assume the state vector $\mathbf{x}(t)$ evolves in time according to

$$\dot{\mathbf{x}}(t) = \boldsymbol{h}(\mathbf{x}(t)) + \sum_{k=1}^{M} \boldsymbol{g}_k(\mathbf{x}(t), u_k(t)), \tag{2.1}$$

where $\boldsymbol{h}(\cdot) : \mathbb{R}^N \to \mathbb{R}^N$ and $\boldsymbol{g}_k(\cdot)$, $k = 1, \ldots, M$ are time-invariant functions of $\mathbf{x}(t)$ and $\mathbf{u}(t) = [u_1, \ldots, u_M] \in \mathbb{R}^M$ is an $M$-dimensional control vector. Combining (2.1) with the output $\boldsymbol{\beta}(t)$ gives the autonomous, nonlinear state-space form

$$\begin{aligned} \dot{\mathbf{x}}(t) &= \boldsymbol{h}(\mathbf{x}(t)) + \sum_{k=1}^{M} \boldsymbol{g}_k(\mathbf{x}(t), u_k(t)) \\ \boldsymbol{\beta}(t) &= \boldsymbol{q}(\mathbf{x}(t)), \end{aligned} \tag{2.2}$$

where $\boldsymbol{q}(\cdot) : \mathbb{R}^N \to \mathbb{R}^P$ is a (possibly) nonlinear output function of $\mathbf{x}(t)$.

[1]Bold fonts represent a matrix such as an $N \times 1$ matrix, $\boldsymbol{x} = [x_1\ x_2\ ...\ x_N]^T$, or an $N \times N$ matrix, $\boldsymbol{L} \in \mathbb{R}^{N \times N}$.

## 2.1 Nonlinear and Optimal Control

This section provides an overview of the control methods used throughout this dissertation. The coordinated multi-vehicle sampling and bio-inspired control problems addressed in Chapters 3, 4, 5, and 7 utilize Laypunov-based control and analysis techniques to drive each system to a desired equilibrium or steady-state. Section 2.1.1 provides a review of Lyapunov-based stability and control analysis in the context of a general dynamical system and provides discussion of an additional tool, the invariance principle, that allows one to prove stability of the resulting control algorithms even after relaxing the constraining assumptions in Lyapunov's method. Sections 2.1.2 and 2.1.3 present optimal control and path planning frameworks that are utilized in the design of optimal trajectories for formation flight, discussed in Chapter 6.

### 2.1.1 Lyapunov-based control

Given the equations of motion (2.1), the goal of Lyapunov-based control is to derive a control vector $\mathbf{u}(t)$ driving the state to a desired equilibrium point or steady-state behavior. To begin, Lyapunov's stability theorem is as follows [116].

Lyapunov's Stability Theorem: [116, pp. 114] Let $\mathbf{x}^*$ denote a zero-input equilibrium point of (2.1) such that $\boldsymbol{h}(\mathbf{x}^*) = \mathbf{0}$. (Without loss of generality assume $\mathbf{x}^* = 0$ [116]). Consider a domain $D \subset \mathbb{R}^N$ containing $\mathbf{x}^*$ and a continuously differentiable function[2] $S(\mathbf{x})$ with the properties $S(\mathbf{x}^*) = 0$ and $S(\mathbf{x}) > 0$ in $D - \{\mathbf{x}^*\}$. If $\dot{S}(\mathbf{x}) \leq 0$ in $D$ then $\mathbf{x}^*$ is stable in the sense of Lyapunov and if $\dot{S}(x) < 0$ in $D - \{\mathbf{x}^*\}$ then $\mathbf{x}^*$ is asymptotically stable [116, pp. 114].

[2]The variable $t$ is omitted for brevity. Note that all state and control variables are functions of time.

For proof see [116, pp. 114–116].

The primary goal in Lyapunov-based control is to find a Lyapunov function whose derivative can be manipulated by a suitable control to enforce negative definiteness. Given the equations of motion (2.1), the time derivative of $S(\mathbf{x})$ is

$$\begin{aligned} \dot{S}(\mathbf{x}) &= \tfrac{\partial S}{\partial \mathbf{x}}\dot{\mathbf{x}} = \tfrac{\partial S}{\partial \mathbf{x}}(\boldsymbol{h}(\mathbf{x}) + \boldsymbol{g}(\mathbf{x},\mathbf{u})) \\ &= \tfrac{\partial S}{\partial \mathbf{x}}\boldsymbol{h}(\mathbf{x}) + \tfrac{\partial S}{\partial \mathbf{x}}\boldsymbol{g}(\mathbf{x},\mathbf{u}). \end{aligned} \tag{2.3}$$

To ensure asymptotic stability of $\mathbf{x}^*$, one must design a feedback control $\mathbf{u}(t) = \mathbf{u}(\mathbf{x}(t))$ such that

$$\tfrac{\partial S}{\partial \mathbf{x}}h(\mathbf{x}) + \tfrac{\partial S}{\partial \mathbf{x}}\boldsymbol{g}(\mathbf{x},\mathbf{u}) < 0, \tag{2.4}$$

for all $\mathbf{x} \in D$. The control vector $\mathbf{u}$ can often be chosen to ensure that $\dot{S}$ is at least negative semi-definite, proving stability in the sense of Lyapunov but not asymptotic stability. The following provides an overview of the LaSalle's invariance principle [116], which can be used to prove asymptotic stability even when $\dot{S}$ is negative semi-definite and relaxes the requirement that $S$ be positive definite in the domain $D$.

The invariance principle relies on mathematical definitions from set theory, namely the concepts of compact and positively invariant sets . For brevity, the definitions are simply stated here; however, a complete review can be found in [116, pp. 127]. A set $U \subset \mathbb{R}^N$ is compact if it is closed and bounded. A closed set is one in which every convergent sequence with elements in $U$ converges to a point in $U$. Moreover, a bounded set is one in which all points within the set lie within a fixed distance of one another. A set $U$ is positively invariant if a solution $\mathbf{x}(t)$ to (2.1) with $\mathbf{x}(0) \in U$ remains in $U$ for all $t \geq 0$, i.e.

$$\mathbf{x}(0) \in U \implies \mathbf{x}(t) \in U, \quad \forall t \geq 0. \tag{2.5}$$

With the definitions of compact and positively invariants sets, LaSalle's invariance principle is stated as follows [116, pp. 128].

LaSalle's Invariance Principle: [116, pp. 126–129] Let $U \subset D$ be a compact set that is positively invariant with respect to (2.1) (with control $\mathbf{u}(\mathbf{x})$). Consider a continuously differentiable function $S$ such that $\dot{S} \leq 0$ in $U$ and let $Q$ be the set of points in $U$ for which $\dot{S} = 0$. Let $W$ be the largest invariant set in $Q$. Every solution starting in $U$ approaches $W$ as $t \to \infty$.

For proof see [116, pp. 128].

Important advantages provided by the invariance principle are that (1) the potential function $S$ need not be positive definite (but can be), and (2) asymptotic stability is established even when $\dot{S} \leq 0$ if the only solution $\mathbf{x}(t)$ that can stay in the set $Q = \{\mathbf{x} \in D | \dot{S}(\mathbf{x}) = 0\}$ is the solution $\mathbf{x}^*$. The goal of the feedback control design is to derive $\mathbf{u} = \mathbf{u}(\mathbf{x})$ such that the closed-loop dynamics satisfy the requirements of the invariance principle, thereby establishing asymptotic stability of a desired equilibrium point or equilibrium set.

### 2.1.2 Optimal Control

This section presents an overview of the classical optimal control formulation as follows. The goal of the optimal control problem is to derive a control $\mathbf{u}_{opt}(t)$ driving the state from an initial condition $\mathbf{x}(t_0) = \mathbf{x}_0$ at time $t_0$ to the desired final state $\mathbf{x}_{des} = \mathbf{x}(t_f)$ at time $t_f$ that minimizes the metric

$$J_C(\mathbf{x}(t_0), \mathbf{u}(t); R) = \int_{t_0}^{t_0+t_f} l(\mathbf{x}(t)) + \mathbf{u}(t)^T \mathbf{R}\mathbf{u}(t) \, \mathrm{d}t, \tag{2.6}$$

where $l(\cdot)$ is a cost function dependent on $\mathbf{x}$ and $\mathbf{R} \in \mathbb{R}^{P \times P}$ is a constant, positive definite matrix weighting the control inputs $\mathbf{u}(t)$. Imposing an additional constraint on the control such that $||\mathbf{u}(t)|| \leq u_{max}$, bounds the control effort. Minimizing (2.6) is a constrained nonlinear optimization problem whose solution provides the control sequence $\mathbf{u}_{opt}(t)$ that produces the optimal trajectory with respect to the cost function while minimizing control effort.

Calculating the solution to (2.6) is computationally expensive and can be intractable for complicated dynamics (2.1) and cost functions $l(\mathbf{x})$. For linear systems with a quadratic cost function $l(\mathbf{x}) = \mathbf{x}^T Q \mathbf{x}$, where $Q \in \mathbb{R}^{N \times N}$, the analytical solution provides the familiar linear quadratic regulator (LQR) control result. In Chapter 6, we assume the cost function is dependent on observability measures and use the numerical optimization software package GPOPS [117], [118] in MATLAB to calculate the control $\mathbf{u}(t)$, $t \in [t_0, t_f]$ that minimizes (2.6). The optimal control $\mathbf{u}_{opt}(t)$ drives the state to $\mathbf{x}_{des}$ while maximizing observability and minimizing control authority.

### 2.1.3 Level Set Methods for Optimal Path Planning and Control

When state estimates are used in feedback control, the formulation presented above requires iterative calculation of the optimal control values, which can be computationally expensive and therefore difficult to implement in real-time. It also requires specification of a feasible horizon time that may be unknown *a priori* given any control actuation limits. An alternative approach incorporates a weighted wavefront expansion, known as the fast marching method [119], to generate an optimal "cost-to-go" potential relative to the desired final state $\mathbf{x}_{des}$. By construction, the gradient of this potential function provides the optimal control with respect to a given cost function. This method does not

require iterative calculation of the control since the potential is calculated over the entire state-space, making the control computationally inexpensive compared to the previous formulation control and easier to implement in real-time.

The optimal path planning problem is formulated as follows [119, pg. 284–291]. Given a desired final state $\mathbf{x}_{des}$, the goal is to find the trajectory $\mathcal{L}(\upsilon) : [0, \infty) \to \mathbb{R}^N$ from $\mathbf{x}_{des}$ to any point $\mathbf{x}_0$ that minimizes the cost metric [119]

$$\int_{\mathbf{x}_{des}}^{\mathbf{x}_0} l(\mathcal{L}(\upsilon))\mathrm{d}\upsilon,$$

where $\upsilon$ is the arc-length parameterization of the path $\mathcal{L}$ and $l(\cdot)$ is the cost function evaluated along $\mathcal{L}$. Let the minimum cost required to travel *from* $\mathbf{x}_{des}$ to a point $\mathbf{x}$ be [119]

$$J_W(\mathbf{x}) \triangleq \min_{\mathcal{L}} \int_{\mathbf{x}_{des}}^{\mathbf{x}} l(\mathcal{L}(\upsilon))\mathrm{d}\upsilon, \tag{2.7}$$

such that the level set $J_W(\mathbf{x}) = C$ is the set of points that can be reached with minimal cost $C$. By construction, level sets are orthogonal to the minimal cost paths [119] implying that the optimal path descends the gradient of $J_W(\mathbf{x})$.

The fast marching method [119] is a wavefront propagation technique that is used to efficiently compute $J_W(\mathbf{x})$ for the domain around $\mathbf{x}_{des}$ [119, pg. 86–99]. Since the optimal path descends the gradient of $J_W(\mathbf{x})$, the optimal feedback control is

$$\mathbf{u}_{opt} = -K_W \nabla J_W(\mathbf{x}), \tag{2.8}$$

where the gain $K_W > 0$. Assuming the desired final location is fixed, the cost potential $J_W(\mathbf{x})$ need be calculated only once to produce all possible optimal paths.

Section 2.3 presents measures of observability of a nonlinear system. By using a measure of observability as the cost function in (2.6) and (2.7), the resulting control algorithms drive the system to a desired state while maximizing the observability over

the trajectory. The next section provides an overview of tools from graph theory that mathematically represent communication topologies between vehicles in a multi-vehicle system.

## 2.2 Graph Theory

Chapters 3 and 5 present decentralized multi-vehicle control algorithms steering vehicles to coordinated sampling formations. To allow individual vehicles to calculate their control in a distributed manner, assume there is a communication topology allowing vehicles to share information with one another, such as position and velocity. This section presents tools from graph theory that model the communication topologies as matrices.

A graph is a mathematical representation of points where pairs of points are connected or share information along links [120]. For example, the points could represent computers in a network and the links could represent a pathway by which a message can be shared between two computers. Each point in the graph is called a vertex, and each connection is called an edge [120]. Edges can be directed, meaning information can be passed in only one direction between the vertices, or undirected, implying information passes both directions between vertices [120].

Following [121], assume the communication topology between a group of vehicles is defined by an undirected graph $\mathcal{G}(\mathcal{V}, \mathcal{E})$ consisting of $n$ vertices $\mathcal{V} = \{v_1, \ldots, v_n\}$ representing each vehicle and edges $(i, j) \in \mathcal{E}$ representing a communication link between vertices $v_i$ and $v_j$ [122]. Let $\mathcal{N}(k) = \{j | (j, k) \in \mathcal{E}\}$ be the set of vertices connected to $k$, called the set of neighbors.

The matrices associated with the graph $\mathcal{G}$ are as follows. The adjacency matrix $\boldsymbol{Z}$ of $\mathcal{G}$ has dimension $n \times n$ with elements $Z_{ij} = 1$ if $(v_j, v_i) \in \mathcal{E}$ and zero otherwise [123]. $\boldsymbol{Z}$

represents all the vehicle connections in $\mathcal{E}$ in matrix form. Let $\boldsymbol{H} \in \mathbb{R}^{n\times n}$ be the degree matrix whose $i$th diagonal entry corresponds to the number of edges associated with the $i$th vertex. The Laplacian matrix $\boldsymbol{L} = \boldsymbol{H} - \boldsymbol{Z}$ has the important property that for a complex vector $\boldsymbol{r} \in \mathbb{C}^n$ the inner product[3] $\langle \boldsymbol{r}, \boldsymbol{L}\boldsymbol{r}\rangle$ vanishes only when $\boldsymbol{r} = \mathbf{1}r_0$, where $\mathbf{1} \in \mathbb{R}^n$ is a vector of ones and $r_0$ is a scaler [121]. The complex quadratic form $\langle \boldsymbol{r}, \boldsymbol{L}\boldsymbol{r}\rangle$ is the total length of the polygonal line connecting communicating vertices [121] which, when minimized, corresponds to coordinated motion. This work considers an all-to-all communication topology , which corresponds to the Laplacian matrix

$$\boldsymbol{L} = \boldsymbol{I}_n - \tfrac{1}{n}\mathbf{1}\mathbf{1}^T, \tag{2.9}$$

where $\boldsymbol{I}_n$ is the $n \times n$ identity matrix. Extensions to limited communication topologies are possible [17], [124], but outside the scope of this work.

## 2.3 Nonlinear and Empirical Observability

As defined in Section 1.2.4, observability in control theory is a measure of how well the state variables of a system can be determined from its outputs. In linear systems, observability is characterized by the observability rank condition [93], which is a special case of the observability rank condition of a nonlinear system [95]. A nonlinear system is called observable if two states are indistinguishable only if the states are identical [95] and is determined using tools from differential geometry. This section provides an overview of mathematical notions of observability as well as measures of observability in linear and nonlinear systems.

[3] $\langle x, y\rangle \triangleq \mathrm{Re}\,(x^*y)$, where $x^*$ is the complex conjugate of $x$, denotes the inner product of complex numbers $x$ and $y$.

### 2.3.1 Observability of a Dynamical System

By definition, a system is observable at time $t_0$ if there exists a finite $t_1 > t_0$ such that knowledge of the input $\mathbf{u}(t)$, $t \in [t_0, t_1]$ and measurements from the output $\boldsymbol{\beta}(t)$, $t \in [t_0, t_1]$ are sufficient to uniquely determine the initial state $\mathbf{x}(t_0) = \mathbf{x}_0$ [93]. For a nonlinear system of the form (2.2), local observability can be established using tools from differential geometry namely, the Lie derivative. A brief review of nonlinear observability analysis follows. For detailed discussion of nonlinear observability techniques, the interested reader is referred to [94]. We begin by presenting the observability rank condition, which provides a binary analysis of local observability for a nonlinear system.

The first order Lie derivative $L^1_{\boldsymbol{h}}\boldsymbol{q}$ specifies the rate of change of the function $\boldsymbol{q}(\cdot)$ in the direction of the function $\boldsymbol{h}(\cdot)$ defined by [94], [100]

$$L^1_{\boldsymbol{h}}\boldsymbol{q} = \frac{\partial \boldsymbol{q}}{\partial \mathbf{x}}\boldsymbol{h}(\mathbf{x}). \tag{2.10}$$

Higher order derivatives can be calculated such that the $k$th Lie derivative is given by

$$L^k_{\boldsymbol{h}}\boldsymbol{q} = \frac{\partial}{\partial \mathbf{x}}\left[L^{k-1}_{\boldsymbol{h}}\boldsymbol{q}\right]\boldsymbol{h}. \tag{2.11}$$

Note that (2.10) and (2.11) are the Lie derivatives with respect to the drift vector field $\boldsymbol{h}(\mathbf{x})$. One can also calculate Lie derivatives with respect to the control vector fields $\boldsymbol{g}_k(\mathbf{x})$ and mixed higher order derivatives can be obtained via combinations of the drift and control vector fields. Let $\mathcal{G}$ denote the observability Lie algebra spanning the Lie derivatives of the output function $\boldsymbol{q}(\mathbf{x})$ with respect to the drift vector field $\boldsymbol{h}(\mathbf{x})$ and the control vector fields $\boldsymbol{g}_j(\mathbf{x}, \mathbf{u})$ $(j = 1, \ldots, M)$ [94], [95], [100],

$$\mathcal{O} = \text{span}\{L_{\mathbf{F}_1} L_{\mathbf{F}_2} \ldots L_{\mathbf{F}_k} q_j\}, \quad j \in P,\ k = 1, 2, \ldots \tag{2.12}$$

where $\mathbf{F}_i \in \{h, g_1, \ldots, g_M\}$ for $i \in \{1, \ldots, k\}$ [94]. The gradient $d\mathcal{O}$ represents the observation space of (2.2) [125]. The observability rank condition states that the system (2.2) is locally observable at $\mathbf{x}_0$ if $d\mathcal{O}$ evaluated at $\mathbf{x}_0$ has dimension $N$ [94], [95]. Note that since the observability space $\mathcal{O}$ contains high order mixed Lie derivatives, the gradient $d\mathcal{O}$ can be difficult to calculate analytically even for simple nonlinear systems.

Note that the observability rank condition provides only a binary analysis of local observability rather than a continuous measure. For this reason, Gramian-based approaches are commonly used to calculate an $N \times N$ observability Gramian whose singular values correspond to the observability of the system's modes [126]. To calculate the classical observability Gramian, the system must be linearized. By assuming linearization about a nominal equilibrium condition, the linear (time-invariant) state-space representation of 2.2 is

$$\begin{aligned} \dot{\mathbf{x}}(t) &= A\mathbf{x}(t) + B\mathbf{u}(t) \\ \boldsymbol{\beta}(t) &= C\mathbf{x}(t). \end{aligned} \tag{2.13}$$

The linear observability Gramian over the interval $[t_0, t_f]$ is defined [126]

$$\boldsymbol{W}_O = \int_{t_0}^{t_f} e^{A^T\tau} C^T C e^{A\tau} \mathrm{d}\tau. \tag{2.14}$$

If $\boldsymbol{W}_O$ has rank $N$, then the linear system (2.13) is observable [93].

For a nonlinear system, a linear realization about an equilibrium is one option, but it fails to adequately model the input/output relationship of the nonlinear system over a wide range of operating conditions [97]. One alternative for determining the observability of a nonlinear system is to use the empirical observability Gramian [97], also known as the observability covariance matrix, [96], [127] which does not require linearization but merely the ability to simulate the nonlinear system. The empirical observability Gramian is useful because it approximates the input-output behavior of a nonlinear system more

accurately than the observability Gramian found by linearization [127] and is equal to (2.14) for a linear system.

This work focuses primarily on assessing the observability of the states or parameters needed for feedback control, which may represent a subset of the states contained in the total state vector $\mathbf{x}(t)$. Let $\mathbf{\Omega} \subseteq \mathbf{x}$ be the set of states or parameters upon which one calculates the empirical observability Gramian. The empirical observability Gramian is a Hermitian matrix defined as follows. Let $\epsilon_i \mathbf{e}_i$ be a small displacement of the initial state (parameter) along the $i^{\text{th}}$ unit vector $\mathbf{e}_i \in \mathbb{R}^G$ and let $\mathbf{\Omega} \in \mathbb{R}^G$ be the nominal parameter values. The $(i,j)^{\text{th}}$ component of the $G \times G$ empirical observability Gramian $W_O$ is [97]

$$\begin{aligned} \boldsymbol{W}_O(i,j) &= \tfrac{1}{4\epsilon_i \epsilon_j} \int_0^T \left[\boldsymbol{\beta}^{+i}(\tau) - \boldsymbol{\beta}^{-i}(\tau)\right]^T \left[\boldsymbol{\beta}^{+j}(\tau) - \boldsymbol{\beta}^{-j}(\tau)\right] \mathrm{d}\tau, \\ & \qquad i = 1, \ldots, G, \ j = 1, \ldots, G, \end{aligned} \tag{2.15}$$

where $\mathbf{\Omega}^{\pm i} = \mathbf{\Omega} \pm \epsilon_i \mathbf{e}_i$ produces the output $\boldsymbol{\beta}^{\pm i} = q(\mathbf{x}; \mathbf{\Omega}^{\pm i})$. The empirical and linear observability Gramians are matrices measuring the local sensitivity of the outputs to changes in the initial state $\mathbf{x}_0$. In either case, if the Gramian has rank $N$ the system is locally observable. Though the rank test provides an assessment of whether the system is locally observable, the following section describes measures of the observability Gramian that assess how close the system is to being unobservable and how observability differs between modes of the system.

For systems in which the output $\boldsymbol{\beta}(\mathbf{x}; \mathbf{\Omega})$ is a continuous function of time-invariant parameters $\mathbf{\Omega}$, the observability Gramian and the Fisher information matrix are closely related [98]. The Fisher information matrix $\boldsymbol{F}$ provides a measure of the information content within a set of noisy measurements and is associated with the inverse of the measurement covariance matrix [128]. In the limit that $\epsilon_i \to 0$, (2.15) becomes

$$\lim_{\epsilon_i \to 0} \frac{\boldsymbol{\beta}^{+i} - \boldsymbol{\beta}^{-i}}{2\epsilon_i} = \frac{\partial \boldsymbol{\beta}}{\partial \Omega_i}. \tag{2.16}$$

For infinitesimally small perturbations, the empirical observability Gramian (2.15) is approximated by

$$\boldsymbol{W}_O \approx \begin{bmatrix} \langle \frac{\partial \boldsymbol{\beta}}{\partial \Omega_1}, \frac{\partial \boldsymbol{\beta}}{\partial \Omega_1} \rangle & \cdots & \langle \frac{\partial \boldsymbol{\beta}}{\partial \Omega_1}, \frac{\partial \boldsymbol{\beta}}{\partial \Omega_G} \rangle \\ \vdots & \ddots & \vdots \\ \langle \frac{\partial \boldsymbol{\beta}}{\partial \Omega_G}, \frac{\partial \boldsymbol{\beta}}{\partial \Omega_1} \rangle & \cdots & \langle \frac{\partial \boldsymbol{\beta}}{\partial \Omega_G}, \frac{\partial \boldsymbol{\beta}}{\partial \Omega_G} \rangle \end{bmatrix} \in \mathbb{R}^{G \times G}. \tag{2.17}$$

Let

$$\mathbf{B} \triangleq \left[ \frac{\partial \boldsymbol{\beta}}{\partial \Omega_1}, \ldots, \frac{\partial \boldsymbol{\beta}}{\partial \Omega_G} \right]^T \in \mathbb{C}^{G \times P}. \tag{2.18}$$

If one assumes each measurement is independent with equal noise variance, the statistics of any noise corrupting the measurements can be modeled by the diagonal sensor noise covariance matrix $\mathbf{R}$ given by $\mathbf{R} = R_0 \mathbf{I}_{G \times G}$ where $R_0$ is the sensor noise variance. Under this assumption, the approximate empirical observability Gramian (2.17) becomes

$$\boldsymbol{W}_O \approx \tfrac{1}{R_0} \mathbf{B}\mathbf{B}^* = \tfrac{1}{R_0} \boldsymbol{F}, \tag{2.19}$$

which is proportional to the Fisher information matrix $\boldsymbol{F} = \mathbf{B}\mathbf{B}^*$ [98].

### 2.3.2 Measures of Observability

In linear systems theory, the singular values $\sigma_j$ of the observability Gramian determine the relative ease in determining the initial states of a linear system from the outputs generated over a time interval [93, p. 125-126]. Large singular values imply that it is easy to invert the mapping from outputs to initial states [97]. The reciprocal of the smallest singular value $\sigma_{min}$ of the observability Gramian, called the unobservability index, is a measure of the relative ease in which an estimation scheme can determine the initial state of a system [97]; large values imply that the system is difficult to observe, whereas small values indicate the opposite. The unobservability index is [97]

$$\xi \triangleq 1/\sigma_{min}. \tag{2.20}$$

In stochastic estimation, a large value of $\xi$ implies that noise in the measurements will significantly impact the estimate error. Conversely, a small value of $\xi$ implies that the estimation error may not be sensitive to measurement noise [97].

The unobservability index is just one of several metrics providing a measure of observability. For instance, the estimation condition number [99], [97]

$$\lambda = \frac{\sigma_{max}}{\sigma_{min}} = \sigma_{max}\xi, \tag{2.21}$$

reflects the degree of variability in the observability of the system. A large value of $\lambda$ implies that a small perturbation in one direction may have a more pronounced effect on the output than a large perturbation in another direction, which implies that the observability of the system is sensitive to the perturbation direction and the estimation problem may be ill-conditioned [97].

Several other metrics of the observability gramian have been proposed to analyze the sensor placement problem [99], [98] including the trace, maximum singular value, determinant, and trace of the inverse [99], [98] of the observability Gramian. Maximizing the trace corresponds to maximizing the $\mathcal{L}_2$ norm of the outputs [98], whereas maximizing the determinant corresponds to a maximization of independence between outputs [98]. Minimizing the trace of the inverse is comparable to minimizing the error covariance [98]. One can also optimize individual elements along the diagonal of the observability Gramian, which correspond to the observability of individual states. Assuming a system is observable, this dissertation primarily focuses on the unobservability index (2.20) and the estimation condition (2.21) in Chapters 5, 6, and 7, since they measure the least observable mode and the anticipated estimation performance, respectively. For deeper analysis of the observability of an individual state or for observability metrics applicable to unobservable systems, 7 also focuses on individual elements of the observability Gramian.

## 2.4 Bayesian Estimation

This section presents nonlinear filtering schemes to estimate unknown states (or parameters) of the model (2.2). Throughout this dissertation we focus on estimating the states (parameters) $\mathbf{\Omega} \subseteq \mathbf{x}$ that characterize a flowfield model and are important for feedback control. For a linear system with Gaussian noise, the optimal Bayesian filter is the Kalman filter, whereas for a nonlinear system with nonlinear noise, a common Bayesian filter is a particle filter [129].

This section presents two versions of the Bayesian filter namely, the grid-based recursive Bayesian filter and the particle filter. In the grid-based method a $G$-dimensional grid represents a subset of all possible values of the true state vector $\mathbf{\Omega}$. Each element within the grid represents an estimate of the state and has a corresponding probability density quantifying the likelihood that it represents the true state. The probability density of each estimate is recursively updated as measurements are assimilated in space and time. In the particle filter each particle represents an estimate of the state and has a weight corresponding to the likelihood that the particle represents the true state. The state of each particle evolves in time using the dynamics of the system and its weight evolves recursively as measurements are assimilated. Section 2.4.1 presents the grid-based recursive Bayesian filter and Section 2.4.2 presents the particle filter.

### 2.4.1 Grid-based Recursive Bayesian Filter

The discrete-time Bayesian formalism proceeds as follows [129]. Let $\hat{\mathbf{\Omega}}(t)$ denote the state estimate at time $t$, $\tilde{\boldsymbol{\beta}}_k(t)$ denote the $k^{\text{th}}$ sensors's noisy observation at time $t$, and $\mathbf{A}_k(t) = \{\tilde{\boldsymbol{\beta}}_k(1), \ldots, \tilde{\boldsymbol{\beta}}_k(t)\}$ denote the set of observations from sensor $k$ up to time $t$.

The posterior probability of the state $\hat{\mathbf{\Omega}}(t)$ given $\mathbf{A}_k(t)$ is [129]

$$p(\mathbf{\Omega}(t)|\mathbf{A}(t)) = \kappa p(\tilde{\boldsymbol{\beta}}(t)|\mathbf{\Omega}(t)) \int p(\mathbf{\Omega}(t)|\mathbf{\Omega}(t-\Delta t)) p(\mathbf{\Omega}(t-\Delta t)|\mathbf{A}(t-\Delta t)) \mathrm{d}\mathbf{\Omega}(t-\Delta t), \quad (2.22)$$

where the coefficient $\kappa$ is chosen so that $p(\hat{\mathbf{\Omega}}(t)|\mathbf{A}_k(t))$ has unit integral over the state space. The conditional probability $p(\tilde{\boldsymbol{\beta}}(t)|\mathbf{\Omega}(t))$ is a likelihood function, which represents the probability that the state $\mathbf{\Omega}(t)$ generated the observation $\tilde{\boldsymbol{\beta}}(t)$. The motion model $p(\mathbf{\Omega}(t)|\mathbf{\Omega}(t-\Delta t))$ represents a nonlinear operator that updates the probability density function from $t-\Delta t$ to $t$, [130, p. 372-375] assuming known control inputs $\mathbf{u}$. For linear motion, define the motion matrix $\Psi$ and let $p(\mathbf{\Omega}(t)|\mathbf{\Omega}(t-\Delta t)) = \mathcal{N}(\Psi\mathbf{\Omega}(t-\Delta t); \Sigma_p)$, where $\mathcal{N}(\Psi\mathbf{\Omega}(t-\Delta t); \Sigma_p)$ is normally distributed white noise with mean $\Psi\mathbf{\Omega}(t-\Delta t)$ and covariance matrix $\Sigma_p$. The quantity $p(\mathbf{\Omega}(t-\Delta t)|\mathbf{A}(t-\Delta t))$ is the prior probability density resulting from measurements taken up to $t-\Delta t$. At $t = 0$ the prior probability is assumed to be uniformly distributed in the absence of information other than the parameter lower and upper bounds. The maximum likelihood estimate $\hat{\mathbf{\Omega}}$ of the lead aircraft parameters is associated with the point in parameter space corresponding to the maximum of the posterior probability density, i.e.,

$$\hat{\mathbf{\Omega}} = \text{mode } p(\mathbf{\Omega}(t)|\mathbf{A}(t)). \quad (2.23)$$

Suppose the $k^{\text{th}}$ sensor obtains the following noisy measurement at time $t$:

$$\tilde{\boldsymbol{\beta}}_k(t) = \boldsymbol{\beta}_k(t) + \boldsymbol{\eta}_k(t), \in \mathbb{R}^P,$$

where the noise $\eta_k(t) \sim \mathcal{N}(0, \sigma_k^2)$ is normally distributed with zero mean and variance $\sigma_k^2$. For each point $\mathbf{\Omega}(t)$ in the $G$-dimensional state space, let the likelihood function be a multi-variate Gaussian, i.e.,

$$p(\tilde{\boldsymbol{\beta}}_k(t)|\mathbf{\Omega}(t)) = \frac{1}{\sqrt{2\pi|\Sigma|}} \exp[-\tfrac{1}{2}[\boldsymbol{\beta}_k(\mathbf{\Omega}(t)) - \tilde{\boldsymbol{\beta}}_k(t)]^T \Sigma^{-1} [\boldsymbol{\beta}_k(\mathbf{\Omega}(t)) - \tilde{\boldsymbol{\beta}}_k(t)]], \quad (2.24)$$

where $\Sigma = \text{diag}(\sigma_1^2, \ldots, \sigma_G^2)$. Assuming measurements are taken from $k = 1, \ldots, n$ sensors, the total likelihood function is the product of the likelihood functions produced by all $n$ sensor measurements

$$p(\tilde{\boldsymbol{\beta}}(t)|\boldsymbol{\Omega}(t)) = \prod_{k=1}^{n} p(\tilde{\boldsymbol{\beta}}_k(t)|\boldsymbol{\Omega}(t)), \tag{2.25}$$

where $p(\tilde{\boldsymbol{\beta}}_k(t)|\boldsymbol{\Omega}(t))$ is given by (2.24). (Note, (2.25) assumes that the $k$th sensor communicates its measurement to either a central hub or to every other sensor such that all agents have knowledge of $p(\boldsymbol{\Omega}(t)|\mathbf{A}(t))$ in (2.22). Distributed versions of (2.22) are possible [32], [42] but beyond the scope of this work.)

### 2.4.2 Particle Filter

Particle filtering is a Bayesian estimation technique in which each particle represents an estimate of the state $\boldsymbol{\Omega}$ given the measurements $\boldsymbol{A}(t)$ [131]. This estimation scheme is well suited for systems of high-dimension with nonlinear dynamics and nonlinear measurement noise models. For a detailed discussion of the particle filter estimation algorithm, see Arulampalam et al. [131]. Assuming $L_p$ particles, each particle $\boldsymbol{l}_i = \hat{\boldsymbol{\Omega}}_i$ has an associated weight $w_i$, such that the weighted sum of particles approximate the posterior probability density function

$$p(\boldsymbol{\Omega}(t)|\boldsymbol{A}(t)) \approx \sum_{k=1}^{L_p} w_k(t)\delta(\boldsymbol{\Omega}(t) - \boldsymbol{l}_k(t)), \tag{2.26}$$

where $\delta(\cdot)$ is the Dirac delta function [131]. Particles with a larger weight have higher probability of representing the true state $\boldsymbol{\Omega}$ than particles with a lower weight. In the limit that $L_p \to \infty$ the particle distribution and associated weights approach the continuous probability density function $p(\boldsymbol{\Omega}(t)|\boldsymbol{A}(t))$ [131]. The $i$th particle evolves in time via (2.1) assuming that the kinematics of each element in $\boldsymbol{l}_i(t)$ is subject to independent, zero-mean, Gaussian process noise $\boldsymbol{\eta} = \mathcal{N}(0, \boldsymbol{\sigma})$ with variance $\boldsymbol{\sigma}^2 = (\sigma_1^2, \ldots, \sigma_G^2)$. The corresponding

particle weights are updated recursively in time such that

$$w_k(t) = \kappa p(\boldsymbol{\beta}(t)|\boldsymbol{l}_k(t))w_k(t - \Delta t), \tag{2.27}$$

where $p(\boldsymbol{\beta}(t)|\boldsymbol{l}_k(t))$ is the likelihood function (2.25) and $\kappa$ is a normalizing constant such that $\sum_{k=1}^{L_p} w_k(t) = 1$.

# Chapter 3: Motion Coordination in a Flowfield

The goal of this chapter is to provide distributed control algorithms steering a group of vehicles to families of sampling formations that regulate spatiotemporal sampling density and provide basic motion primitives upon which a sampling mission may be built. This chapter considers coordinated formations including straight lines, circles, folium patterns, and the spirograph.

## 3.1 Two-Dimensional Self-propelled Particle Model in a Time-invariant Flow

This section models two-dimensional motion of an unmanned vehicle using a self-propelled particle model in the presence of a time-invariant flowfield. Section 3.1.1 presents a model of multi-particle motion with respect to an inertial reference frame, whereas Section 3.1.2 represents the particle kinematics with respect to a rotating reference frame. The vehicle motion models are used to derive multi-vehicle control algorithms in Section 3.4. Section 3.1.3 provides models of two-dimensional flow used throughout Chapters 3, 4, and 5.

### 3.1.1 Particle Motion With Respect to an Inertial Reference Frame

This section extends an existing dynamic model common to many works on collective motion [15], [16], [17], [18], [132]. The model consists of a collection of $n$ self-propelled Newtonian particles. Each particle is subject to a control force normal to its velocity and

travels at a constant speed relative to an external flowfield. It is assumed without loss of generality that the flow-relative speed is unity. Given a ground-fixed inertial reference frame $\mathcal{I}$ with origin $O$ (identified with the complex plane), the $k$th particle's position is represented by the vector $\mathbf{r}_{k/O}$, or in complex coordinates $[\mathbf{r}_{k/O}]_{\mathcal{I}} \triangleq r_k = x_k + iy_k \in \mathbb{C}$. Given the unit-speed assumption, the $k$th particle's velocity can be represented by $e^{i\theta_k}$, a point on the unit circle. Using complex coordinates, the $k$th particle's flow-relative velocity is $e^{i\theta_k} = \cos\theta_k + i\sin\theta_k$.

The state-feedback control $u_k$ determines the $k$th particle's rate of change of velocity orientation (steering control). The equations of motion for the $k$th particle in the absence of a flowfield are[1]

$$\begin{aligned} \dot{r}_k &= e^{i\theta_k} \\ \dot{\theta}_k &= u_k(\mathbf{r}, \boldsymbol{\theta}), \quad k = 1, \ldots, n. \end{aligned} \tag{3.1}$$

State-feedback control algorithms $u_k(\mathbf{r}, \boldsymbol{\theta})$ utilizing $\mathbf{r}$ and $\boldsymbol{\theta}$ drive each particle to the desired collective motion and have been extensively studied in recent years [21], [17], [14], [132], [18], [124].

In the presence of a time-invariant flowfield $f_k = f(r_k) \in \mathbb{C}$ each particle's velocity is represented by the vector sum of its velocity relative to the flow and the flow velocity relative to the inertial frame $\mathcal{I}$, as illustrated in Figure 3.1. In this case, the $k$th particle's motion is governed by

$$\begin{aligned} \dot{r}_k &= e^{i\theta_k} + f_k \\ \dot{\theta}_k &= u_k(\mathbf{r}, \boldsymbol{\theta}), \quad k = 1, \ldots, n. \end{aligned} \tag{3.2}$$

Here the flow magnitude is allowed to exceed the speed of the particle relative to the flow. Let $\gamma_k$ represent the orientation of the $k$th particle's inertial velocity and $s_k$ its

[1]We drop the subscript and use bold fonts to represent an $n \times 1$ matrix, e.g., $\boldsymbol{r} = [r_1\ r_2\ \ldots\ r_n]^T$ and $\boldsymbol{\theta} = [\theta_1\ \theta_2\ \ldots\ \theta_n]^T$.

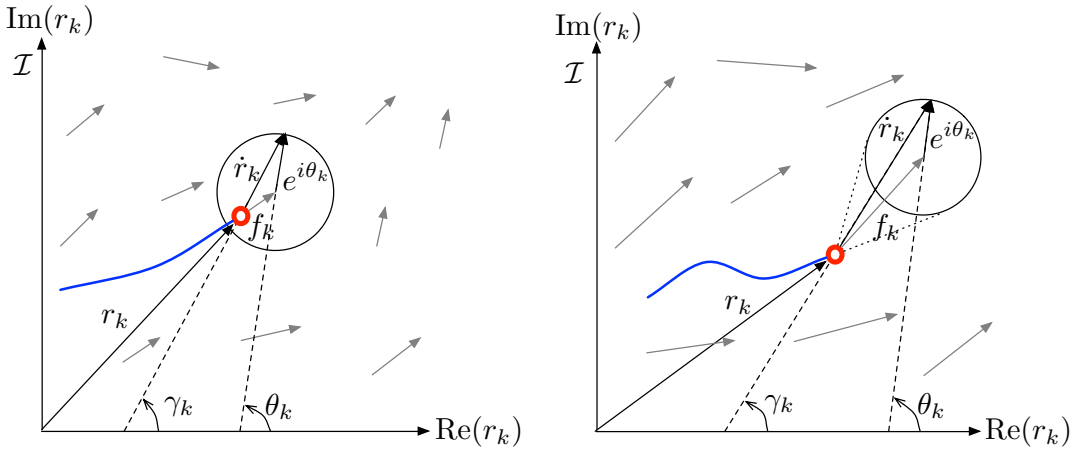


(a) (b)

Figure 3.1: The inertial velocity of a particle is the sum of the flow velocity relative to the ground and the velocity of the particle relative to the flow. Illustration of particle velocity in a (a) moderate flowfield and (b) strong flowfield. In a strong flowfield the direction of travel is limited.

magnitude. Previous work on motion coordination in a moderate flow [15], i.e., where $|f_k| < 1$, utilized the following coordinate transformation:

$$\gamma_k \triangleq \arg(e^{i\theta_k} + f_k) \tag{3.3}$$

$$s_k \triangleq |e^{i\theta_k} + f_k|. \tag{3.4}$$

Under this transformation, the equations of motion (3.2) become

$$\begin{aligned} \dot{r}_k &= s_k e^{i\gamma_k} \\ \dot{\gamma}_k &= \nu_k, \end{aligned} \tag{3.5}$$

where $\nu_k$ is the control relative to the fixed inertial frame $\mathcal{I}$. Controls $u_k$ and $\nu_k$ are related by[2]

$$u_k = \frac{\nu_k - \langle f_k', i\rangle}{1 - s_k^{-1}\langle e^{i\gamma_k}, f_k\rangle} = \frac{s_k\nu_k - s_k\langle f_k', i\rangle}{s_k - \langle e^{i\gamma_k}, f_k\rangle}, \tag{3.6}$$

[2] $\langle x, y\rangle \triangleq \mathrm{Re}\,(x^* y)$, where $x^*$ is the complex conjugate of $x$, denotes the inner product of complex numbers $x$ and $y$.

where $f_k' = \frac{\partial f_k}{\partial r_k}$. Figure 3.1 illustrates the particle model in both the moderate (Fig. 3.1(a)) and strong flow (Fig. 3.1(b)) regimes. Note that a unit circle centered at the tip of $f_k$ represents the possible values of $\dot{r}_k = e^{i\theta_k} + f_k$.

Paley and Peterson [15] showed that in a moderate flow the transformation (3.6) defines a one-to-one mapping between $u_k$ (control of the flow-relative velocity orientation) and $\nu_k$ (control of the velocity relative to $\mathcal{I}$), since the denominator of (3.6) is never zero. This result allowed development of control laws for (3.2), extending those developed for the flow-free model (3.1). However, for flow speeds greater than or equal to the vehicle speed, the transformation (3.6) is no longer one-to-one. To see this, consider a particle at position $r_k$ subject to a strong flow as shown in Figure 3.1(b). A unit circle drawn about the tip of $f_k$ defines the possible orientations of the total velocity $\dot{r}_k = e^{i\theta_k} + f_k$. In a strong flow, the unit circle is not guaranteed to enclose $r_k$, which implies that the set of possible inertial velocity orientations is a subset of the circle (called the cone of admissable directions by Bakolas and Tsiotras [24]). In a moderate flow as illustrated in Figure 3.1(a) the unit circle encloses $r_k$, implying that any given $\theta_k$ corresponds to a single $\gamma_k$. Thus, in any moderate flow a given $\theta_k$ maps to a single $\gamma_k$, but in a strong flow a given $\gamma_k$ maps to one of two possible $\theta_k$'s. The speed $s_k$ is required to determine $\theta_k$ as shown in Figure 3.1(b). Lemma 1 identifies two singularities in the transformation (3.6).

**Lemma 1.** *For $|f_k| \geq 1$, the transformation (3.6) is singular when $\theta_k = \arg(f_k) \pm \cos^{-1}(|f_k|^{-1})$.*

*Proof.* Substituting $e^{i\gamma_k} = |e^{i\theta_k} + f_k|^{-1}(e^{i\theta_k} + f_k)$ and (3.4) into the denominator of (3.6) implies that $u_k$ is singular when

$$s_k = \langle e^{i\gamma_k}, f_k \rangle = |e^{i\theta_k} + f_k|^{-1} \langle e^{i\theta_k} + f_k, f_k \rangle = {s_k}^{-1} \left( \langle e^{i\theta_k}, f_k \rangle + |f_k|^2 \right). \tag{3.7}$$

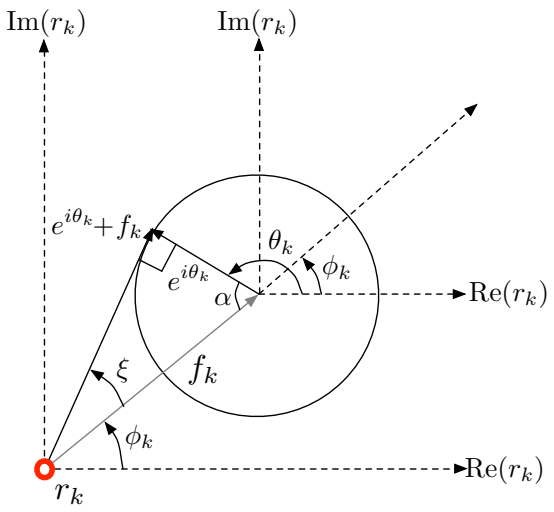


Figure 3.2: Orientation relations corresponding to the singularities of (3.6).

If one considers the flow $f_k$ in its polar form $f_k = |f_k|e^{i\psi_k}$, where $\psi_k = \arg(f_k)$, substitution into (3.7) and solving for $\langle e^{i\theta_k}, e^{i\psi_k}\rangle$ gives

$$\langle e^{i\theta_k}, e^{i\psi_k}\rangle = \cos(\psi_k - \theta_k) = |f_k|^{-1}\left(s_k^2 - |f_k|^2\right) = |f_k|^{-1}\left(|e^{i\theta_k} + f_k|^2 - |f_k|^2\right). \quad (3.8)$$

Figure 3.2 shows that when $e^{i\theta_k}$ is drawn such that $\left|e^{i\theta_k} + f_k\right|$ is tangent to a unit circle drawn about $f_k$, a right triangle is formed with hypotenuse $|f_k|$ and sides $\left|e^{i\theta_k} + f_k\right|$ and $\left|e^{i\theta_k}\right|$. Since the vector triad forms a right triangle [133] let $\xi \triangleq \sin^{-1}(|f_k|^{-1})$, and since the sum of the interior angles of a triangle are supplementary,

$$\xi + \lambda + \frac{\pi}{2} = \pi. \quad (3.9)$$

By projecting $f_k$, note that

$$\theta_k - \psi_k + \lambda = \pi. \quad (3.10)$$

Equating (3.10) and (3.9) and taking the cosine of the result implies

$$\cos(\theta_k - \psi_k) = -|f_k|^{-1}, \quad (3.11)$$

which when substituted into (3.8) gives the Pythagorean Theorem, $|e^{i\theta_k} + f_k|^2 + 1 = |f_k|^2$. Thus, when $s_k = \langle e^{i\gamma_k}, f_k \rangle$, $\theta_k$ is such that $e^{i\theta_k}$, $f_k$, and $e^{i\theta_k} + f_k$ form a right triangle. Solving (3.11) for $\theta_k$ while noting $\cos(\theta_k - \psi_k) = \cos(\psi_k - \theta_k)$ completes the proof. □

Lemma 1 shows that strong flows introduce singularities in the coordinate transform (3.6), resulting in an unbounded turn rate. However, the design of the vehicle and the medium in which it travels dictate the maximum controlled rate of turn a priori. The turn-rate constraint can be modeled as saturation of $u_k$, in which case (3.2) becomes

$$\begin{aligned} \dot{r}_k &= e^{i\theta_k} + f_k \\ \dot{\theta}_k &= \text{sat}\left(u_k\left(\mathbf{r}, \boldsymbol{\theta}\right); u_{max}\right), \end{aligned} \tag{3.12}$$

where

$$\text{sat}\left(u; u_{max}\right) = \begin{cases} u_{max}, & u > u_{max} \\ u, & -u_{max} \leq u \leq u_{max} \\ -u_{max}, & u < -u_{max}. \end{cases} \tag{3.13}$$

In the notation of Chapter 2 the state vector is $\mathbf{x} = [\boldsymbol{r}, \boldsymbol{\theta}]^T$. The drift vector field is $\boldsymbol{h}(\mathbf{x}) = [e^{i\theta_1} + f_1, \ldots, e^{i\theta_n} + f_n, \mathbf{0}_{n\times 1}]^T$ and $g_k = 0$ for $k = 1, \ldots, n$ and $g_k = \text{sat}(u_k; u_{max})$ otherwise.

The saturation model (3.12) allows use of model (3.5) to design $\nu_k$ and (3.6) to map $\nu_k$ to $u_k$. Unless restricted by the vehicle dynamics, $u_{max}$ must be chosen large enough so that $\nu_{max} = \nu_{max}(u_{max}) > |\kappa_{max} s_{max}|$, where $\kappa_{max}$ is the maximum desired curvature of the particle trajectory and $s_{max}$ is the maximum particle speed along the trajectory. (The relation between $u_{max}$ and $\nu_{max}$ is discussed by Peterson and Paley. [23]) The upper bound on $\nu_k$ is represented using $\dot{\gamma}_k = \text{sat}\left(\nu\left(\mathbf{r}, \theta\right); \nu_{max}\right)$. As $\theta_k$ approaches either singularity provided in Lemma 1, $\dot{\theta}_k$ remains bounded, passing through the singular point at a constant rate $\pm u_{max}$.

### 3.1.2 Particle Motion with Respect to a Rotating Reference Frame

This section derives a dynamic model of self-propelled particle motion in a rotating reference frame. By steering a group of vehicles to a formation with respect to a rotating reference frame, the resulting inertial frame formation revisits regions of the environment at specified intervals in time, thereby regulating the azimuthal and radial sampling density in the inertial reference frame. A proposed sampling formation is that of a spirograph which, when viewed with respect to a frame rotating at constant angular rate, a spirograph becomes a circular trajectory. Control algorithms producing circular trajectories are discussed in Section 3.3.2.

Let $\mathcal{I} = (O, \mathbf{e}_1, \mathbf{e}_2, \mathbf{e}_3)$ represent an inertial reference frame with origin $O$ and $\mathcal{B} = (O, \mathbf{b}_1, \mathbf{b}_2, \mathbf{b}_3)$, where $\mathbf{b}_3 = \mathbf{e}_3$, represent a rotating reference frame with angular velocity ${}^{\mathcal{I}}\boldsymbol{\omega}^{\mathcal{B}} = \Omega \mathbf{e}_3$. (Complex notation is used to represent Cartesian coordinates in $\mathcal{I}$ and $\mathcal{B}$.) The orientation $\alpha = \Omega t + \alpha(0)$ of frame $\mathcal{B}$ with respect to $\mathcal{I}$ satisfies $\mathbf{e}_1 \cdot \mathbf{b}_1 = \cos\alpha$, as shown in Figure 3.3(a). The inertial kinematics of the $k$th particle with respect to $O$ are described by $r_k \triangleq [\mathbf{r}_{k/O}]_{\mathcal{I}}$ and ${}^{\mathcal{I}}\mathbf{v}_{k/O} \triangleq \frac{{}^{\mathcal{I}}d}{dt}(\mathbf{r}_{k/O})$. Assume for now there is no flow. Let the path frame $\mathcal{C}_k = (k, \mathbf{c}_1, \mathbf{c}_2, \mathbf{c}_3)$ be a frame with origin at the $k$th particle's position, where $\mathbf{c}_3 = \mathbf{e}_3$, $\mathbf{c}_1 = {}^{\mathcal{I}}\mathbf{v}_{k/O}/h_k$, and $h_k \triangleq \|{}^{\mathcal{I}}\mathbf{v}_{k/O}\| = 1$ is the speed of the particle. Variable $\theta_k$ is the orientation of the velocity, so $\mathbf{e}_1 \cdot \mathbf{c}_1 = \cos\theta_k$.

Since frame $\mathcal{B}$ shares its origin with frame $\mathcal{I}$, the kinematics of the $k$th particle in frame $\mathcal{B}$ are given by $\tilde{r}_k \triangleq [\mathbf{r}_{k/O}]_{\mathcal{B}}$ and ${}^{\mathcal{B}}\mathbf{v}_{k/O} \triangleq \frac{{}^{\mathcal{B}}d}{dt}(\mathbf{r}_{k/O})$. As in frame $\mathcal{I}$, this gives rise to the path frame $\mathcal{D}_k = (k, \mathbf{d}_1, \mathbf{d}_2, \mathbf{d}_3)$, with origin at $\tilde{r}_k$, where $\mathbf{d}_3 = \mathbf{e}_3$, $\mathbf{d}_1 = {}^{\mathcal{B}}\mathbf{v}_{k/O}/\tilde{h}_k$, and $\tilde{h}_k \triangleq \|{}^{\mathcal{B}}\mathbf{v}_{k/O}\|$ represents the speed of the $k$th particle relative to frame $\mathcal{B}$. In $\mathcal{B}$-frame coordinates, $(\tilde{x}_k, \tilde{y}_k)_{\mathcal{B}}$, the position and velocity are given by $\mathbf{r}_{k/O} = \tilde{x}_k \mathbf{b}_1 + \tilde{y}_k \mathbf{b}_2$

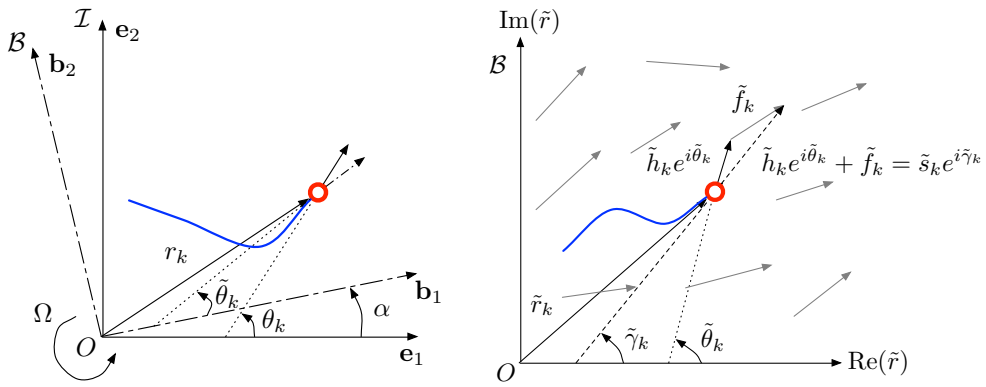


(a) (b)

Figure 3.3: The orientation of the $k$th particle's velocity (a) in no flow and (b) in flow $\tilde{f}$.

and ${}^{\mathcal{B}}\mathbf{v}_{k/O} = \dot{\tilde{x}}_k\mathbf{b}_1 + \dot{\tilde{y}}_k\mathbf{b}_2$, respectively, which implies $\tilde{h}_k = \sqrt{\dot{\tilde{x}}_k^2 + \dot{\tilde{y}}_k^2}$. Let $\tilde{\theta}_k$ be the orientation of ${}^{\mathcal{B}}\mathbf{v}_{k/O}$ relative to $\mathbf{b}_1$, so that $\mathbf{b}_1 \cdot \mathbf{d}_1 = \cos\tilde{\theta}_k$.

The transport equation [134, p. 433–435], ${}^{\mathcal{I}}\mathbf{v}_{k/O} = {}^{\mathcal{B}}\mathbf{v}_{k/O} + {}^{\mathcal{I}}\boldsymbol{\omega}^{\mathcal{B}} \times \mathbf{r}_{k/O}$, gives the kinematic relationship

$$h_k\mathbf{c}_1 = \tilde{h}_k\mathbf{d}_1 + \Omega\mathbf{b}_3 \times (\tilde{x}_k\mathbf{b}_1 + \tilde{y}_k\mathbf{b}_2) = \tilde{h}_k\mathbf{d}_1 + \Omega(\tilde{x}_k\mathbf{b}_2 - \tilde{y}_k\mathbf{b}_1). \tag{3.14}$$

Noting that $\mathbf{c}_1 = \cos\theta_k\mathbf{e}_1 + \sin\theta_k\mathbf{e}_2$, (3.14) can be written

$$h_k\cos(\theta_k - \alpha)\,\mathbf{b}_1 + h_k\sin(\theta_k - \alpha)\,\mathbf{b}_2 = \left(\tilde{h}_k\cos\tilde{\theta}_k - \Omega\tilde{y}_k\right)\mathbf{b}_1 + \left(\tilde{h}_k\sin\tilde{\theta}_k + \Omega\tilde{x}_k\right)\mathbf{b}_2. \tag{3.15}$$

The inertial derivative of (3.14), assuming $h_k$ is constant, gives

$$h_k\dot{\theta}_k\mathbf{c}_2 = \dot{\tilde{h}}_k\mathbf{d}_1 + \tilde{h}_k\left(\dot{\tilde{\theta}}_k + \Omega\right)\mathbf{d}_2 - \left(\Omega\dot{\tilde{y}}_k + \Omega^2\tilde{x}_k\right)\mathbf{b}_1 + \left(\Omega\dot{\tilde{x}}_k - \Omega^2\tilde{y}_k\right)\mathbf{b}_2. \tag{3.16}$$

By utilizing $\mathbf{c}_2 = -\sin(\theta_k - \alpha)\,\mathbf{b}_1 + \cos(\theta_k - \alpha)\,\mathbf{b}_2$, (3.16) results in the following scalar equations of motion relative to reference frame $\mathcal{B}$:

$$\begin{aligned} -h_k u_k\sin(\theta - \alpha) &= \dot{\tilde{h}}_k\cos\tilde{\theta}_k - \tilde{h}_k(\dot{\tilde{\theta}}_k + \Omega)\sin\tilde{\theta}_k - \tilde{x}_k\Omega^2 - \dot{\tilde{y}}_k\Omega \\ h_k u_k\cos(\theta_k - \alpha) &= \dot{\tilde{h}}_k\sin\tilde{\theta}_k + \tilde{h}_k(\dot{\tilde{\theta}}_k + \Omega)\cos\tilde{\theta}_k - \tilde{y}_k\Omega^2 + \dot{\tilde{x}}_k\Omega. \end{aligned} \tag{3.17}$$

Note that substituting $\dot{\tilde{x}}_k = \tilde{h}_k \cos\tilde{\theta}_k$ and $\dot{\tilde{y}}_k = \tilde{h}_k \sin\tilde{\theta}_k$ into (3.17) and using (3.15) to eliminate $\theta_k - \alpha$ and $h_k$ gives

$$\begin{aligned} -u_k\tilde{h}_k \sin\tilde{\theta}_k - u_k\Omega\tilde{x}_k &= \dot{\tilde{h}}_k \cos\tilde{\theta}_k - \tilde{h}_k(\dot{\tilde{\theta}}_k + \Omega)\sin\tilde{\theta}_k - \tilde{x}_k\Omega^2 - \tilde{h}_k \sin\tilde{\theta}_k\Omega \\ u_k\tilde{h}_k \cos\tilde{\theta}_k - u_k\Omega\tilde{y}_k &= \dot{\tilde{h}}_k \sin\tilde{\theta}_k + \tilde{h}_k(\dot{\tilde{\theta}}_k + \Omega)\cos\tilde{\theta}_k - \tilde{y}_k\Omega^2 + \tilde{h}_k \cos\tilde{\theta}_k\Omega. \end{aligned} \tag{3.18}$$

Solving (3.18) for $\dot{\tilde{h}}_k$ and $\dot{\tilde{\theta}}_k$, respectively, with complex notation $\tilde{r}_k = \tilde{x}_k + i\tilde{y}_k$, results in the equations of motion of the $k$th particle relative to frame $\mathcal{B}$:

$$\begin{aligned} \dot{\tilde{r}}_k &= \tilde{h}_k e^{i\tilde{\theta}_k} \\ \dot{\tilde{h}}_k &= (\Omega^2 - u_k\Omega)\langle \tilde{r}_k, e^{i\tilde{\theta}_k}\rangle \\ \dot{\tilde{\theta}}_k &= u_k - 2\Omega + \tilde{h}_k^{-1}(\Omega^2 - u\Omega)\langle \tilde{r}_k, ie^{i\tilde{\theta}_k}\rangle \triangleq \tilde{u}_k. \end{aligned} \tag{3.19}$$

Let $\tilde{u}_k$ be defined as the steering control with respect to rotating frame $\mathcal{B}$. The mapping from $\tilde{u}_k$ to $u_k$ is

$$u_k = \frac{\tilde{u}_k\tilde{h}_k + 2\Omega\tilde{h}_k - \Omega^2\langle \tilde{r}_k, ie^{i\tilde{\theta}_k}\rangle}{\tilde{h}_k - \Omega\langle \tilde{r}_k, ie^{i\tilde{\theta}_k}\rangle}. \tag{3.20}$$

Equations (3.19) and (3.20) are the equations of motion of a self-propelled particle represented in coordinates relative to a frame rotating with constant angular rate $\Omega$. Note that the mapping from $\tilde{u}_k$ to $u_k$ is singular when $\tilde{h}_k = \Omega\langle \tilde{r}_k, ie^{i\tilde{\theta}_k}\rangle$. Lemma 2 establishes the singular conditions with respect to the inertial speed $h_k$.

**Lemma 2.** *The control transform (3.20) is singular when* $h_k = \Omega\langle \tilde{r}_k, e^{i\tilde{\theta}_k}\rangle$.

*Proof.* The absolute value of (3.14) squared gives

$$h_k^2 = \tilde{h}_k^2 + \Omega^2\langle \tilde{r}, \tilde{r}\rangle - 2\Omega\langle \tilde{r}, ie^{i\tilde{\theta}_k}\rangle. \tag{3.21}$$

Substituting the singular condition $\tilde{h}_k = \Omega\langle \tilde{r}_k, ie^{i\tilde{\theta}_k}\rangle$ into (3.21) yields

$$\begin{aligned} h_k^2 &= \Omega^2\langle \tilde{r}_k, ie_k^{i\tilde{\theta}}\rangle^2 + \Omega^2\langle \tilde{r}_k, \tilde{r}_k\rangle - 2\Omega^2\langle \tilde{r}_k, ie^{i\tilde{\theta}_k}\rangle^2 \\ &= \Omega^2\langle \tilde{r}_k, e^{i\tilde{\theta}_k}\rangle^2, \end{aligned}$$

revealing a relation between the speed of a particle and its position. The mapping can become singular when

$$h_k = \Omega \langle \tilde{r}_k, e^{i\tilde{\theta}_k} \rangle. \tag{3.22}$$

Specifically, if the vehicle is assumed to travel at unit speed in the inertial frame the mapping is singular if $\Omega^{-1} = \langle \tilde{r}_k, e^{i\tilde{\theta}_k} \rangle$. □

The singularity identified in Lemma 2 occurs when the speed of the vehicle is zero with respect to frame $\mathcal{B}$. For example, when $e^{i\tilde{\theta}_k}$ is normal to $\tilde{r}_k$ and $\Omega > 0$, the singular condition simplifies to $\Omega^{-1} = |\tilde{r}_k|$.

Next, augment the dynamics presented in (3.19) to include flow terms represented by $\tilde{f}_k$. Note $\tilde{f}_k = \tilde{f}(\tilde{r}_k) \in \mathbb{C}$, is assumed to be time invariant with respect to frame $\mathcal{B}$, which implies that the corresponding flowfield with respect to frame $\mathcal{I}$ is azimuthally symmetric about $O$. Again, adapting the kinematic model of the effect of the flow that is used to derive (3.2), the flowfield with respect to the rotating reference frame is incorporated into (3.19) so that

$$\begin{aligned} \dot{\tilde{r}}_k &= \tilde{h}_k e^{i\tilde{\theta}_k} + \tilde{f}_k \\ \dot{\tilde{h}}_k &= (\Omega^2 - u_k \Omega) \langle \tilde{r}_k, e^{i\tilde{\theta}_k} \rangle \\ \dot{\tilde{\theta}}_k &= \tilde{u}_k. \end{aligned} \tag{3.23}$$

Note $u_k$ is still calculated from $\tilde{u}_k$ using (3.20).

Path-planning applications desire control of the total velocity of the particle rather than the flow-relative velocity. For this reason let

$$\tilde{s}_k \triangleq |\tilde{h}_k e^{i\tilde{\theta}_k} + \tilde{f}_k| \tag{3.24}$$

$$\tilde{\gamma}_k \triangleq \arg(\tilde{h}_k e^{i\tilde{\theta}_k} + \tilde{f}_k), \tag{3.25}$$

such that $\dot{\tilde{r}}_k = \tilde{s}_k e^{i\tilde{\gamma}_k}$. Figure 3.3(b) illustrates the following relations

$$\begin{aligned} \tilde{s}_k \cos\tilde{\gamma}_k &= \tilde{h}_k \cos\tilde{\theta}_k + \langle \tilde{f}_k, 1\rangle \\ \tilde{s}_k \sin\tilde{\gamma}_k &= \tilde{h}_k \sin\tilde{\theta}_k + \langle \tilde{f}_k, i\rangle, \end{aligned} \tag{3.26}$$

which after division yield

$$\tan\tilde{\gamma}_k = \frac{\tilde{h}_k \sin\tilde{\theta}_k + \langle \tilde{f}_k, i\rangle}{\tilde{h}_k \cos\tilde{\theta}_k + \langle \tilde{f}_k, 1\rangle}. \tag{3.27}$$

Taking the time derivative of (3.27) and using (3.26) gives

$$\begin{aligned} \dot{\tilde{\gamma}}_k &= \tilde{s}_k^{-1}\langle \dot{\tilde{f}}_k, ie^{i\tilde{\gamma}_k}\rangle - \tilde{s}_k^{-1}\left(\Omega^2 - u_k\Omega\right)\left[\langle \tilde{r}_k, \tilde{s}_k e^{i\tilde{\gamma}_k}\rangle - \langle \tilde{r}_k, \tilde{f}_k\rangle\right]\langle \tilde{f}_k, ie^{i\tilde{\gamma}_k}\rangle \tilde{h}_k^{-2} \\ &\quad + \tilde{s}_k^{-1}\left(\tilde{s}_k - \langle \tilde{f}_k, e^{i\tilde{\gamma}_k}\rangle\right)\tilde{u}_k \\ &\triangleq \tilde{\nu}_k, \end{aligned} \tag{3.28}$$

where $\tilde{\nu}_k$ represents control of the total velocity orientation with respect to the rotating frame and $\dot{\tilde{f}}_k = \frac{\partial \tilde{f}_k}{\partial \tilde{r}_k}\dot{\tilde{r}}_k$. Using (3.28) with (3.20) yields the following mapping between $u_k$ and $\tilde{\nu}_k$ necessary for implementing a control designed in the rotating frame for use in the inertial frame:

$$u_k = \tfrac{m_1 + m_2 - m_3}{w_1 + w_2 - w_3}, \tag{3.29}$$

where

$$\begin{aligned} m_1 &= \tilde{s}_k\tilde{\nu}_k - \langle \dot{\tilde{f}}_k, ie^{i\gamma_k}\rangle + 2\Omega\left(\tilde{s}_k - \langle \tilde{f}_k, e^{i\gamma_k}\rangle\right) \\ m_2 &= \Omega^2\langle \tilde{r}_k, \tilde{s}_k e^{i\gamma_k} - \tilde{f}_k\rangle\langle \tilde{f}_k, ie^{i\tilde{\gamma}_k}\rangle\tilde{h}_k^{-2} \\ m_3 &= \Omega^2\left(\tilde{s}_k - \langle \tilde{f}_k, e^{i\tilde{\gamma}_k}\rangle\right)\langle \tilde{r}_k, i\tilde{s}_k e^{i\tilde{\gamma}_k} - i\tilde{f}_k\rangle\tilde{h}_k^{-2} \\ w_1 &= \tilde{s}_k - \langle \tilde{f}_k, e^{i\tilde{\gamma}_k}\rangle - \Omega\left|\tilde{f}_k\right|^2\tilde{h}_k^{-2}\langle \tilde{r}_k, ie^{i\tilde{\gamma}_k}\rangle \\ w_2 &= \Omega\tilde{s}_k\tilde{h}_k^{-2}\left(\langle \tilde{r}_k, i\tilde{f}_k\rangle + \langle \tilde{r}_k, e^{i\tilde{\gamma}_k}\rangle\langle \tilde{f}_k, ie^{i\tilde{\gamma}_k}\rangle + \langle \tilde{f}_k, e^{i\tilde{\gamma}_k}\rangle\langle \tilde{r}_k, ie^{i\tilde{\gamma}_k}\rangle\right) \\ w_3 &= \Omega\tilde{s}_k\tilde{h}_k^{-2}\langle \tilde{r}_k, ie^{i\tilde{\gamma}_k}\rangle. \end{aligned}$$

The equations of motion of the $k$th particle with respect to a rotating frame subject

to a flowfield are:

$$\begin{aligned}\dot{\tilde{r}}_k &= \tilde{s}_k e^{i\tilde{\gamma}_k} \\ \dot{\tilde{h}}_k &= \left(\Omega^2 - u_k\Omega\right)\langle \tilde{r}_k, \tilde{s}_k e^{i\tilde{\gamma}_k} - \tilde{f}_k\rangle \tilde{h}_k^{-1} \\ \dot{\tilde{\gamma}}_k &= \tilde{\nu}_k,\end{aligned} \tag{3.30}$$

where $u_k$ is given by (3.29). Similar to the inertial-frame dynamics, saturation of $u_k$ is used to avoid singularities in the transformations (3.20) and (3.29).

For a known, spatially varying flowfield, $\tilde{s}_k$ can be calculated as follows [15]. Let $\tilde{f}_k = \tilde{f}_{x,k} + i\tilde{f}_{y,k}$ be the flowfield at $\tilde{r}_k$, where $\tilde{f}_{x,k} = \langle \tilde{f}_k, 1\rangle$ and $\tilde{f}_{y,k} = \langle \tilde{f}_k, i\rangle$ represent the real and imaginary parts of the flow respectively. By definition (3.24) gives

$$\tilde{s}_k = \sqrt{\tilde{h}_k^2 - \tilde{f}_{x,k}^2 - \tilde{f}_{y,k}^2 + 2\tilde{s}_k\left(\tilde{f}_{x,k}\cos\tilde{\gamma}_k + \tilde{f}_{y,k}\sin\tilde{\gamma}_k\right)}. \tag{3.31}$$

Squaring this result and utilizing the quadratic formula to solve for $\tilde{s}_k$ gives

$$\tilde{s}_k = \langle e^{i\tilde{\gamma}_k}, \tilde{f}_k\rangle + \sqrt{\tilde{h}_k^2 - \langle ie^{i\tilde{\gamma}_k}, \tilde{f}_k\rangle^2}, \tag{3.32}$$

where the positive root is taken since $\tilde{s}_k > 0$.

### 3.1.3 Flowfield Models

This section presents time-invariant, two-dimensional flowfields used to simulate the multi-vehicle control algorithms derived in this chapter. (Extensions to three-dimensional flows with a vertical flowspeed gradient are discussed in Chapter 4.) Specifically, three flowfield models are considered including a random, spatially correlated flow, a uniform flow, and an idealized hurricane model known as a Rankine vortex. Each model serves as an example of an environmental flow upon which simulations of the multi-vehicle control algorithms derived in Section 3.3 are examined. The Rankine vortex model is used in Chapter 5 to analyze the observability-based adaptive sampling algorithm in an idealized

hurricane environment. Figure 3.4 shows each flowfield model plotted in the complex plane.

This work characterizes a random velocity field by assuming exponential spatial correlation in the two-dimensional plane. The random flowfield is homogenous, implying that the correlation scales are constant in space. For this work, assume the correlation constant is 0.5% of the spatial domain and the flow speeds are scaled such that the maximum flowspeed is 1.4. The interested reader is referred to [115] and its associated references for further discussion of random fields. The random flowfield used in this chapter is illustrated in Figure 3.4(a) and is evaluated at discrete locations. Interpolating between grid locations provides a continuous flowfield for simulating particle motion. The shaded regions denote areas of the flowfield where the flowspeed is greater than the flow-relative speed of the each vehicle, i.e. $|f_k| \geq 1$.

A uniform flow is characterized by its direction which, without loss of generality is aligned with the positive real axis. The uniform flowfield is

$$f(r_k) = \psi \in \mathbb{R}, \tag{3.33}$$

where $0 < |\psi| < 1$, as illustrated in Figure 3.4(b). We restrict the uniform flow to moderate flow speeds since, in a strong uniform flowfield, the particles have no control authority to maintain a position and will therefore be pushed downstream indefinitely.

In a Rankine vortex [97] the tangential windspeed increases linearly with radius to its maximum flowspeed $v_{max}$ at the radius of maximum wind $r_{max}$ and exponentially decreases for radii greater than $r_{max}$ with exponential decay constant $\mu$. The Rankine vortex model is $\arg(f_k) = \arg(ir_k)$ with

$$|f(r_k)| = \begin{cases} v_{max}\left(|r_k|/r_{max}\right), & 0 < |r_k| \leq r_{max} \\ v_{max}\left(|r_k|/r_{max}\right)^{-\mu}, & |r_k| > r_{max}, \end{cases} \tag{3.34}$$

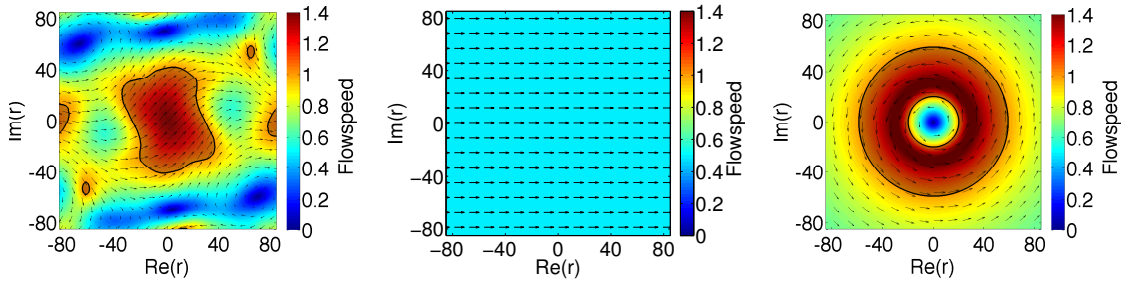


(a) (b) (c)

Figure 3.4: (a) Random flowfield with constant spatial decorrelation scales; (b) uniform flowfield; and (c) Rankine vortex.

where radius $r = r_{max}$ represents the eyewall of an idealized hurricane. Figure 3.4(c) shows an illustration of the Rankine vortex model with $r_{max} = 30$, $v_{max} = 1.5$, and $\mu = 0.6$; the shaded region depicts where $|f_k| \geq 1$.

## 3.2 Trajectory Feasibility in a Strong Flow

Strong flows present the possibility that a desired trajectory or formation is not feasible. This section derives the kinematic conditions a flowfield must satisfy to ensure trajectory feasibility. Conditions are derived for trajectories relative to both inertial and rotating reference frames. These results have similarities to that of Bakolas and Tsiotras in assessing the reachability of two points within a flowfield for a kinematic model of an aircraft [24]; however, this work considers flowfields that can vary continuously through space rather than flowfields that are assumed to be regionally uniform.

### 3.2.1 Feasibility With Respect to an Inertial Reference Frame

A strong flowfield presents a challenge to coordinated motion if an individual vehicle is unable to reach the desired trajectory. Moreover, the desired trajectory itself may not

be achievable if even a portion of the trajectory opposes the flow. The following analysis describes a set of constraints the flow must satisfy such that a given desired trajectory is feasible. (Equivalently, one can view the constraints as limiting the possible trajectories in a given flowfield.)

For a vehicle to travel along curve $\mathcal{L}$, the flow at every point on the path must be such that the vehicle can maintain a velocity tangent to $\mathcal{L}$. That is, for every point on the desired trajectory, the component of the flow normal to $\mathcal{L}$ must be less than the vehicle speed relative to the flow. For a unit speed particle and tangent vector $e^{i\gamma_k}$, this implies that the absolute value of the inner product between the normal vector $ie^{i\gamma_k}$ and the flow $f_k$ must satisfy $|\langle ie^{i\gamma_k}, f_k\rangle| \leq 1$. If $\langle e^{i\gamma_k}, f_k\rangle \leq 0$, then the flow opposes (or is normal to) the direction of the trajectory and must therefore have magnitude less than one. If $\langle e^{i\gamma_k}, f_k\rangle > 0$, then the flow must only satisfy the normal constraint. This result is summarized as follows:

**Theorem 1.** *Trajectory $\mathcal{L}$ is feasible in flowfield $f$ if, for all $r_k \in \mathcal{L}$, $f_k = f(r_k)$ satisfies*

$$\begin{aligned} \langle e^{i\gamma_k}, f_k\rangle &\leq 0 \text{ and } |f_k| < 1, \text{or} \\ \langle e^{i\gamma_k}, f_k\rangle &> 0 \text{ and } |\langle ie^{i\gamma_k}, f_k\rangle| \leq 1, \end{aligned} \tag{3.35}$$

*where $e^{i\gamma_k}$ is tangent to $\mathcal{L}$ at $r_k$.*

Theorem 1 implies that the flow vector at a given point on the trajectory must lie within a U-shaped envelope oriented along the trajectory tangent, shown by the shaded region in Figure 3.5(a). Trajectories that do not satisfy (3.35) are not feasible. Theorem 1 allows one to quantify regions of a known, time-invariant flowfield in which parametric families of feasible trajectories are found. Analysis over the entire space of candidate trajectory centers produces a map of regions in which feasible trajectories can be achieved.

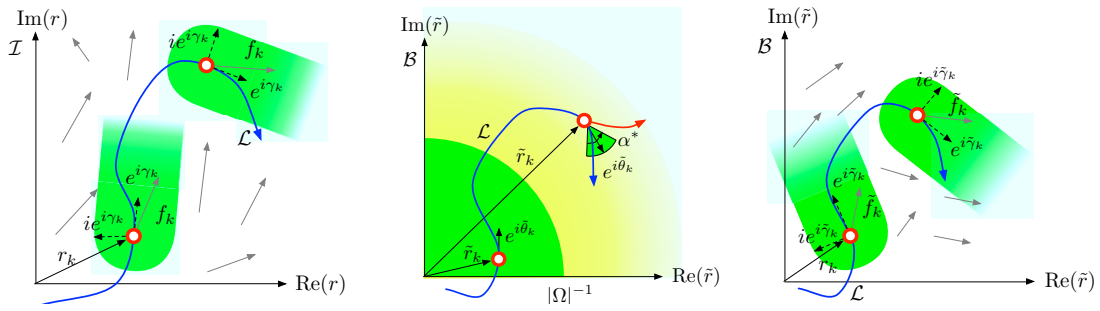


(a) (b) (c)

Figure 3.5: Feasibility constraint for a) inertial frame, b) rotating flow-free frame, and c) rotating with-flow reference frame.

Figures 3.6(a) and 3.6(b) illustrate the feasible regions for fixed-size circular and folium trajectories of radius (lobe length) 20 in a randomly generated strong flowfield, whereas Figures 3.6(c) and 3.6(d) illustrate feasibility in a strong Rankine vortex ($v_{max} = 1.2$). A trajectory whose center lies in the shaded region is not feasible; unshaded regions are feasible. Three example trajectories are plotted in each figure. Portions of a trajectory plotted with a thin red line indicate where the flow fails to satisfy Theorem 1, whereas portions shown in green satisfy the constraint. Note feasibility analysis reveals that feasible circles and folia are centered close to the origin in the Rankine vortex. Moreover, quadrifolia centered about the origin with lobe length 20 are in a moderate flow regime for the majority of the trajectory. This analysis implies that quadrifolium formations may be a poor candidate sampling trajectory in strong flows due to their infeasibility over large areas and lack of feasible sampling at $r_{max}$.

### 3.2.2 Feasibility with Respect to a Rotating Reference Frame

Section 3.1.2 derives the dynamics of a self-propelled particle with respect to a rotating reference frame. The equations of motion in Equations (3.19) and (3.30) reveal

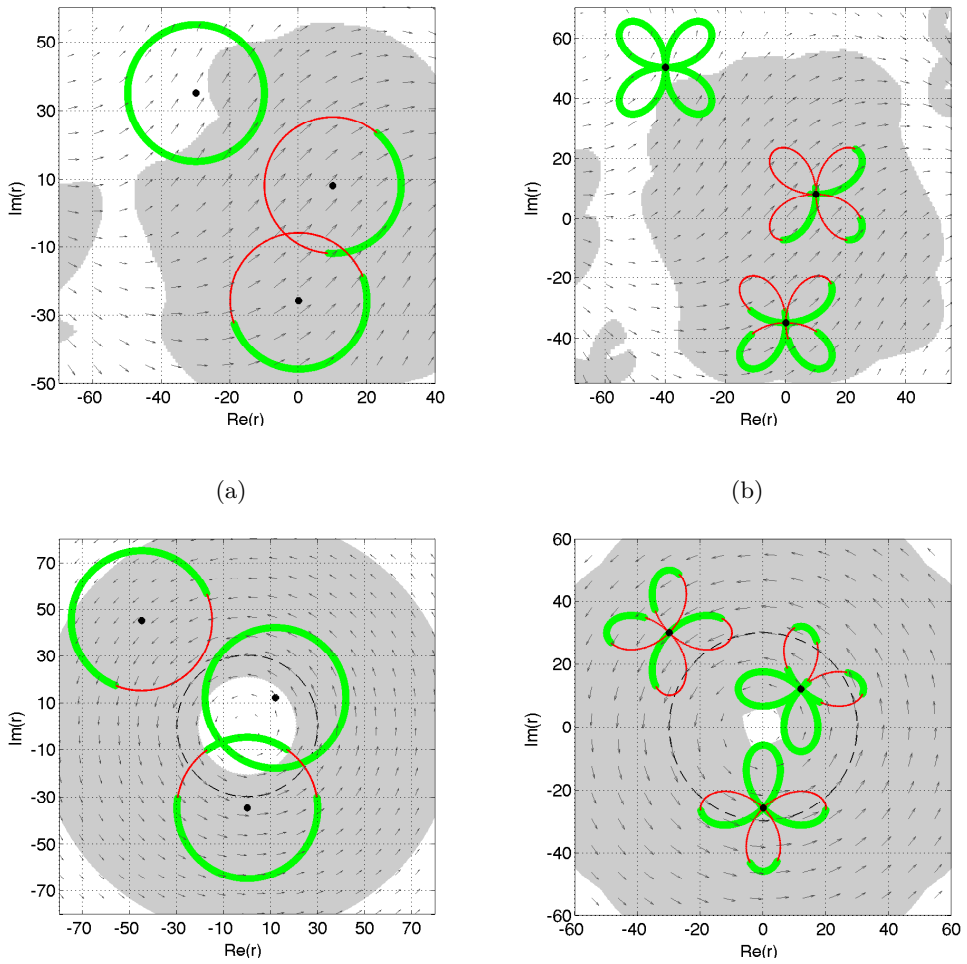


Figure 3.6: Feasible regions of circular (a,c) and quadrifolium (b,d) formations with radius (lobe length) 20 in random and Rankine vortex flowfields.

that the speed of the particle in the rotating frame is a dynamic variable whose time derivative depends on the position and velocity of the particle. This subsection defines kinematic constraints on motion with respect to a rotating reference frame.

In the absence of an external flow, the kinematic terms arising from the rotating reference frame $\mathcal{B}$ affect the speed $\tilde{h}_k$ of the vehicle with respect to $\mathcal{B}$. For a constant-speed particle traveling in the direction of rotation, the speed of the particle with respect to $\mathcal{B}$ is a decreasing function of the rotation rate and the distance to the center of rotation.

For a given trajectory to be feasible with respect to the rotating frame, a particle must maintain forward progress over the entire trajectory, which implies the following result. It is assumed that a fixed point in the rotating frame is not a feasible trajectory.

**Lemma 3.** *Trajectory $\mathcal{L}$ in frame $\mathcal{B}$ rotating at rate $\Omega$ is a feasible solution to (3.19) if, for all $\tilde{r}_k \in \mathcal{L}$, $|\tilde{r}_k| < |\Omega|^{-1}$, or if $|\tilde{r}_k| \geq |\Omega|^{-1}$ and*

$$\Omega\langle \tilde{r}_k, ie^{i\tilde{\theta}_k}\rangle > 0 \text{ and } |\Omega\langle \tilde{r}_k, e^{i\tilde{\theta}_k}\rangle| \leq 1, \tag{3.36}$$

*where $e^{i\tilde{\theta}_k}$ is tangent to $\mathcal{L}$ at $\tilde{r}_k$.*

*Proof.* Summing the squared components of (3.15) and using $h_k = 1$ yields

$$1 = \tilde{h}_k^2 + \Omega^2\left(\tilde{x}_k^2 + \tilde{y}_k^2\right) + 2\Omega\tilde{h}_k(\tilde{x}_k \sin\tilde{\theta}_k - \tilde{y}_k \cos\tilde{\theta}_k).$$

Completing the square to solve for $\tilde{h}_k$ and simplifying with $\tilde{r}_k = \tilde{x}_k + i\tilde{y}_k$ gives

$$\tilde{h}_k = \Omega\langle \tilde{r}_k, ie^{i\tilde{\theta}_k}\rangle + \sqrt{1 - \Omega^2\langle \tilde{r}_k, e^{i\tilde{\theta}_k}\rangle^2}, \tag{3.37}$$

where the positive root is taken since $\tilde{h}_k > 0$ is required to maintain forward progress. Note that the inner products $\langle \tilde{r}_k, ie^{i\tilde{\theta}_k}\rangle$ and $\langle \tilde{r}_k, e^{i\tilde{\theta}_k}\rangle$ differ in phase by $\pi/2$ which implies that for $|\tilde{r}_k| < |\Omega|^{-1}$, (3.37) is real and positive. A trajectory is infeasible if (3.37) is negative or complex, implying that for $|\tilde{r}_k| \geq |\Omega|^{-1}$, a feasible trajectory must satisfy (3.36). □

Lemma 3 is illustrated for $\Omega > 0$ in Figure 3.5(b). Feasible trajectories in the rotating frame with $|\tilde{r}_k| \geq |\Omega|^{-1}$ must travel in a direction opposing the rate of rotation. The range of feasible directions of travel is determined by the position of the vehicle and rate of rotation of the rotating frame. Notice that in complex notation, (3.15) can be written $e^{i(\theta_k - \alpha)} = \tilde{h}_k e^{i\tilde{\theta}_k} + i\Omega\tilde{r}_k$. Therefore, one can represent the velocity with respect to

the rotating frame as $\tilde{h}_k e^{i\tilde{\theta}_k} = e^{i(\theta_k - \alpha)} - i\Omega\tilde{r}_k$. The range of feasible velocities with respect to the rotating frame is thus defined by a unit circle drawn about the tip of $-i\Omega\tilde{r}_k$. In a similar manner to a vehicle's range of travel in a strong flowfield, it can be shown that for $|\tilde{r}_k| \geq |\Omega|^{-1}$, the angular range $\alpha^*$ of feasible directions of travel about $\arg(-i\Omega\tilde{r}_k)$ is given by $\alpha^* = 2\sin^{-1}\left(|\Omega\tilde{r}_k|^{-1}\right)$. $\alpha^*$ can be calculated by replacing the vector $f_k$ with $-i\Omega\tilde{r}_k$ in Figure 3.1(b) (also see Figure 3.2 in Appendix A) and noting that $\alpha^*$ is the angle formed between the two lines tangent to the unit circle.

When an external flowfield is present as in (3.23), the feasibility constraint on the flowfield in a rotating frame is similar to Theorem 1. The transport equation [134, p. 433-435] represented in complex coordinates with respect to frame $\mathcal{B}$ gives

$$e^{i(\theta_k - \alpha)} + f_k e^{-i\alpha} = \tilde{s}_k e^{i\tilde{\gamma}_k} + i\Omega\tilde{r}_k. \tag{3.38}$$

An external flowfield is represented with respect to the rotating frame via the transport equation such that in complex coordinates

$$f_k = \tilde{f}_k e^{i\alpha} + i\Omega\tilde{r}_k e^{i\alpha}, \tag{3.39}$$

where $\tilde{f}_k$ represents the flowfield relative to the rotating frame. Rearranging (3.39) reveals

$$f_k e^{-i\alpha} = \tilde{f}_k + i\Omega\tilde{r}_k, \tag{3.40}$$

which when substituted into (3.38) gives

$$\tilde{s}_k e^{i\tilde{\gamma}_k} = e^{i(\theta_k - \alpha)} + \tilde{f}_k. \tag{3.41}$$

Equation (3.41) shows that the total velocity of the $k$th particle with respect to frame $\mathcal{B}$ can be represented as a unit circle drawn about the tip of $\tilde{f}_k$. Similar to Theorem 1, for a particle to travel along curve $\mathcal{L}$ in rotating frame $\mathcal{B}$, the component of the flow

normal to the trajectory must be less than the vehicle speed with respect to the flow in the inertial frame. For a unit-speed particle with tangent vector $e^{i\tilde{\gamma}_k}$ in the rotating frame, this implies that the absolute value of the inner product between the normal vector $ie^{i\tilde{\gamma}_k}$ and the flow must satisfy $|\langle ie^{i\tilde{\gamma}_k}, \tilde{f}_k\rangle| \leq 1$. If $\langle e^{i\tilde{\gamma}_k}, \tilde{f}_k\rangle \leq 0$ then the flow is normal to or opposes the direction of travel and must therefore have magnitude less than one. If $\langle e^{i\tilde{\gamma}_k}, \tilde{f}_k\rangle > 0$ only the normal constraint must be satisfied. This implies the following result.

**Theorem 2.** *Trajectory $\mathcal{L}$ in rotating reference frame $\mathcal{B}$ is a feasible solution to (3.30) with flowfield $\tilde{f}$ if for all $\tilde{r}_k \in \mathcal{L}$, $\tilde{f}_k = \tilde{f}(\tilde{r}_k)$ is such that*

$$\begin{aligned} \langle e^{i\tilde{\gamma}_k}, \tilde{f}_k\rangle &\leq 0 \text{ and } |\tilde{f}_k| < 1 \text{ or} \\ \langle e^{i\tilde{\gamma}_k}, \tilde{f}_k\rangle &> 0 \text{ and } |\langle ie^{i\tilde{\gamma}_k}, \tilde{f}_k\rangle| \leq 1, \end{aligned} \tag{3.42}$$

*where $e^{i\tilde{\gamma}_k}$ is tangent to $\mathcal{L}$ at $\tilde{r}_k$.*

Similar to Theorem 1 but with respect to rotating reference frame $\mathcal{B}$, Theorem 2 implies that the flow vector $\tilde{f}_k$ must lie within a U-shaped envelope oriented along the trajectory tangent, shown by the shaded region in Figure 3.5(c). Note that Theorem 2 has no apparent dependence on $\tilde{r}_k$ and $\Omega$ as in Lemma 3. The dependence is implicit in $\tilde{f}_k$, which is a function of both the external flow $f_k$ and the kinematic term $i\Omega\tilde{r}_k$ as shown in (3.40). Figure 3.7 shows the feasibility of various spirograph parameter sets in the presence of a Rankine vortex. A spirograph is formed by traversing a circle centered at $c_0$ with radius $\omega_0^{-1}$ in the rotating reference frame. In each figure, the results are generalized by using non-dimensional parameters defining a spirograph $(\hat{\Omega}, \hat{\omega}_0, |\hat{c_0}|)$, where $\hat{\Omega} \triangleq (2\pi\Omega r_{max})/v_{max}$ (the period of revolution of a passive particle at $r_{max}$), $|\hat{c_0}| \triangleq |c_0|/r_{max}$ (non-dimensional distance of circle center from origin), and $\hat{\omega}_0 \triangleq \omega_0 r_{max}$ (non-dimensional radius of a circle in the rotating reference frame). The Rankine vortex parameters are $r_{max}$ and $v_{max}$. In

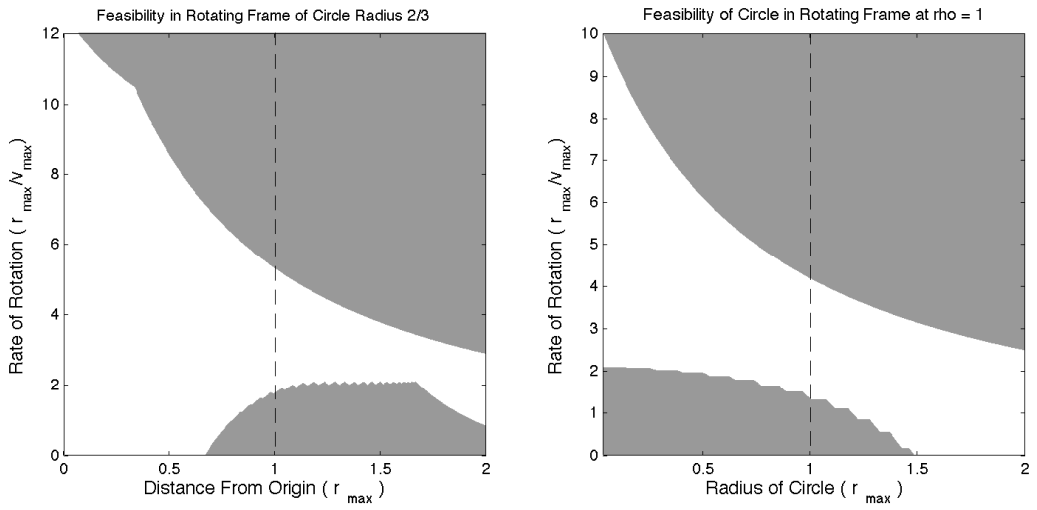


(a) (b)

Figure 3.7: Feasibility analysis of a) spirograph formations for varying non-dimensional $\hat{\Omega}$ and $|\hat{c_0}|$ values with fixed radius $\hat{\omega}_0^{-1} = 2/3$ and b) spirograph feasibility for varying $\hat{\Omega}$ and $\hat{\omega}_0^{-1}$ with $|\hat{c_0}| = 1$.

Figure 3.7(a), the feasibility of rate of rotation $\hat{\Omega}$ is plotted versus the distance of circle center from the origin for a counterclockwise circle of constant radius, $|\hat{\omega}_0|^{-1} = 2/3$. In 3.7(b), the feasibility of $\hat{\Omega}$ is plotted versus the radius of the circle for a fixed distance, $|\hat{c_0}| = 1$. Dark areas indicate where the parameter set $(\hat{\Omega}, \hat{\omega}_0, |\hat{c_0}|)$ is infeasible.

## 3.3 Control in (Strong) Flowfields: Motion Primitives for Flowfield Sampling

This section presents the derivation of control algorithms steering a vehicle to a desired trajectory. We derive control algorithms steering a vehicle to straight [15], circular [121], folium, and spirograph trajectories, which serve as motion primitives upon which a multi-vehicle sampling mission may be built. As illustrated in Figure 3.8, in a straight trajectory the vehicle steers to maintain a constant total velocity orientation. In circular, folium, and spirograph trajectories the control algorithm steers the $k$th vehicle about a

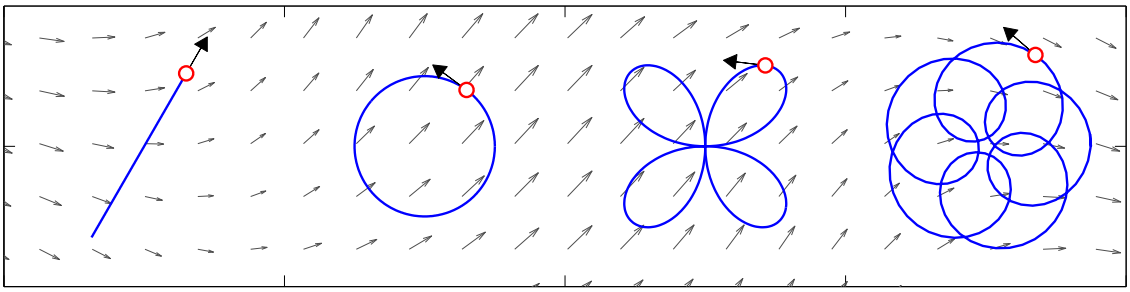

Figure 3.8: Straight, circular, quadrifolium, and spirograph motion primitives used for multi-vehicle sampling formations.

specified center of curvature $c_k$. When each vehicle's center of rotation is coincident, a multi-vehicle sampling formation is achieved. Section 3.4 provides multi-vehicle control algorithms steering each vehicle to a common center of rotation.

This section describes particle curvature control in a flow, following the work of Paley et al. [132], who produced decentralized algorithms to stabilize the family of convex loops called super-ellipses in a flow-free environment and Techy et al. [16], where the convex-loop results were extended to the vehicle model with (uniform) flow.

### 3.3.1 Control to Straight Trajectories

To travel in a straight line the $k$th vehicle must maintain a constant total velocity orientation $\gamma_k(t) = \gamma_0$, which necessitates steering when a spatially-varying flowfield is present. Following Paley and Peterson [15], using the coordinate transformations (3.3) and (3.4) and the control mapping (3.6), one maintains direct control of the rate of change of the total velocity, $\dot{\gamma}_k = \nu_k$. Therefore, if a feasible path exists, the $k$th vehicle travels in a straight line by implementing the control (3.6) with $\nu_k = 0$. Section 3.4 provides a decentralized multi-vehicle control steering vehicles to a parallel formation with desired heading $\gamma_{des}$, i.e. $\gamma_k(t) = \gamma_j(t) = \gamma_{des}$ for all $j, k = 1, \ldots, n$.

### 3.3.2 Control to Non-zero Curvature Trajectories

Our next goal is to drive the $k$th particle about a smooth, closed curve $\mathcal{L}$ with definite, bounded curvature, $\kappa_k$. To do so, $\mathcal{L}$ is parameterized by its center $c_k$. In a $c_k$-centered coordinate system the particle position $\rho_k$ is parameterized by the polar angle $\phi_k$. For a closed, convex curve $\mathcal{L}$, completion of one rotation about $\mathcal{L}$ sweeps through $2\pi$ radians. Thus, $\rho_k(\phi) \in \mathbb{R}$ where $\phi_k \in [0, 2\pi)$. The orientation of the particle's inertial velocity relative to the $c_k$ centered coordinate system is $\gamma_k$ and it is assumed that a smooth mapping $\gamma_k \mapsto \phi(\gamma_k)$ exists. The derivative $\frac{d\rho_k}{\mathrm{d}\phi_k}$ is tangent to $\mathcal{L}$, implying the constraint $e^{i\gamma_k} = \left|\frac{d\rho_k}{d\phi_k}\right|^{-1} \frac{d\rho_k}{d\phi_k}$.

The local curvature is [132]

$$\kappa_k(\phi_k) = \pm \frac{d\gamma_k}{d\sigma}, \tag{3.43}$$

where

$$\sigma(\phi_k) = \int_0^{\phi_k} \left|\frac{d\rho}{d\overline{\phi}}\right| d\overline{\phi} \tag{3.44}$$

is the arc length along the curve. Note that the sign of $\kappa_k$ determines the direction of rotation about the curve, which is either clockwise or counterclockwise. Equations (3.43) and (3.44) imply [132]

$$\kappa_k^{-1} = \pm \frac{d\sigma_k}{d\phi_k}\frac{d\phi_k}{d\gamma_k} = \pm \left|\frac{d\rho_k}{d\phi_k}\right| \frac{d\phi_k}{d\gamma_k}. \tag{3.45}$$

Under the tangent constraint, (3.45) can be written [132]

$$e^{i\gamma_k}\kappa_k^{-1} = \pm \frac{d\rho_k}{d\phi_k}\frac{d\phi_k}{d\gamma_k} = \frac{d\rho_k}{d\gamma_k}.$$

In a reference frame not centered at $c_k$, $\mathcal{L}$ has center of rotation

$$c_k \triangleq r_k \mp \rho_k(\gamma_k). \tag{3.46}$$

The time derivative along solutions of (3.5) gives the velocity of the center [15], [132]

$$\dot{c}_k = s_k e^{i\gamma_k} \mp \frac{d\rho_k}{d\gamma_k}\frac{d\gamma_k}{dt} = e^{i\gamma_k}\left[s_k \mp \kappa_k^{-1}\nu_k\right]. \tag{3.47}$$

From (3.47) note that the curvature control algorithm [15]

$$\nu_k = \pm\kappa_k(\gamma_k)s_k \tag{3.48}$$

forces $\dot{c}_k = 0$, implying that the $k$th particle drives about a stationary $\mathcal{L}$.

A simple example of this control strategy is that of a circular formation. A circle has constant curvature, $\kappa_k = \omega_0$ for all $k$, which for a unit speed particle defines a radius of $|\omega_0|^{-1}$, as illustrated in Figure 3.8. A particle traversing a circular trajectory has total velocity tangent to the radius of the circle. Thus, the center of the $k$th particle's trajectory is [15]

$$c_k = r_k + i\omega_0^{-1}\frac{\dot{r_k}}{|\dot{r_k}|} = r_k + i\omega_0^{-1}e^{i\gamma_k}. \tag{3.49}$$

An existing strategy for data collection in a hurricane is to fly a figure-four pattern through the center of the hurricane.[3] A continuously differentiable flight path covering similar spatial densities is that of the $b$-petalled folium, or polar rose, where $b \geq 3$ [135]. Specifically, the quadrifolium ($b = 4$) is a pattern similar to a figure-four with continuous curvature. In polar coordinates, the equation of the $b$-folium is $\rho_k = a\sin\left(g_k(b)\phi_k\right)$, where $\rho_k$ is the distance of the $k$th particle from the $c_k$, $b$ is the number of lobes[4], $\phi \in [0, 2\pi]$ is the central or polar angle, $a$ is the maximum radius of each lobe, and

$$g_k(b) = \begin{cases} b, & b \text{ odd} \\ b/2, & b \text{ even.} \end{cases}$$

Previous work required the curvature to be nonzero and the figure to be convex [16], [20], [132]. Here this convexity assumption is relaxed. The $b$-folium is not convex; however,

[3] Willoughby, H. and Majumdar, S., Personal Communication, July 14, 2011

[4] $b$ must be odd or divisible by four to be considered a folium.

its curvature is strictly positive (or negative). In traversing one rotation about the figure the particle velocity rotates through $2\pi(g(b)-1)$ radians for $b$ odd and $2\pi(g(b)+1)$ radians for $b$ even. Using curvature control (3.48) requires $\gamma_k$ to be defined over $2\pi(g(b)\pm 1)$ radians. To accomplish this, one can augment the state-space equations with an integer lobe-counter, $l_k \in \mathbb{N}$, which represents the number of lobes a particle has traversed. When a particle's inertial velocity orientation $\gamma_k$ reaches $2\pi$ rad, $l_k$ increases by one and the orientation angle $\gamma_k$ is reset to zero. Utilizing the curvature control as a function of $\gamma_k(\theta_k)$ and $l_k$ gives

$$\nu_k = \kappa_k(\gamma_k(\theta_k) + 2\pi l_k)s_k. \tag{3.50}$$

Equation (3.50) drives the $k$th particle about a non-convex figure with strictly positive (negative) curvature.

In the case of the folium, the curvature is the following function of the polar angle $\phi_k$:

$$\kappa_k\left(\phi_k; b\right) = \frac{\left|\rho_k^2 + 2\rho_k'^2 - \rho_k\rho_k''\right|}{\left(\rho_k^2 + \rho_k'^2\right)^{3/2}} = \frac{b^2 + b^2\sin^2\left(b\phi_k\right) + \cos^2\left(b\phi_k\right)}{a\left[\cos^2\left(b\phi_k\right) + b^2\sin^2\left(b\phi_k\right)\right]^{3/2}}. \tag{3.51}$$

In order to provide state feedback, one must specify $\phi_k$ as a function of the tangent angle $\gamma_k$ such that the curvature control law is valid. For the quadrifolium ($b = 4$) this relation is

$$\gamma_k\left(\phi_k\right) = \frac{1}{2}\pi + \phi_k - \tan^{-1}\left(\cot\phi_k - \tan\phi_k\right) + \pi\lfloor 2\phi_k/\pi\rfloor. \tag{3.52}$$

Note the tangent angle is a function of the polar angle, not vice versa. A look-up table is used to numerically implement (3.52). From (3.51) and (3.52) one can calculate the curvature as a function of the inertial orientation, such that the control (3.50) drives the particle around the quadrifolium trajectory.

### 3.3.3 Control to Spirograph Trajectories

An alternative to circular and folium trajectories is a spirograph trajectory. For a given rate of rotation $\Omega$ of frame $\mathcal{B}$, circle radius $|\omega_0|^{-1}$, and radius of circle center $|c_0|$, the feasibility of the resulting formation can be analyzed using Theorem 2. By applying the control (3.48) to the equations of motion (3.30), a particle will converge to a circle in frame $\mathcal{B}$, assuming the formation center is feasible in the rotating frame. A circular formation with nonzero center position produces a spirograph formation with respect to the inertial frame $\mathcal{I}$, as shown in Figure 3.8. The spirograph is an attractive sampling formation because it remains feasible in vortex flowfields while providing superior radial and azimuthal sampling density.

## 3.4 Control in (Strong) Flowfields: Decentralized Multi-vehicle Control

This section extends the results of the previous section by deriving multi-vehicle control algorithms steering vehicles to a prescribed formation dictated by the curvature control. In a parallel formation vehicles are steered to a desired inertial velocity orientation. For circular, $b$-folium, and spirograph formations, Lyapunov-based control techniques are used to steer each vehicle such that their centers of rotation are coincident.

### 3.4.1 Stabilization of a Parallel Formation

Synchronization of the total horizontal velocity orientation occurs when $\gamma_j = \gamma_k$ for all $j, k \in \{1, \ldots, n\}$ and corresponds to the maximum of the quantity [14], [15]

$$|p_\gamma| = \frac{1}{n} \left| \sum_{k=1}^{n} e^{i\gamma_k} \right|. \tag{3.53}$$

Furthermore, synchronization of all vehicle orientations to a desired feasible $\gamma_0$ corresponds to the minimum of the potential function formed using (3.53) and a cosine function such that

$$U(\boldsymbol{\gamma}, \boldsymbol{s}) = 1 - |p_\gamma|^2 + \sum_{k=1}^{n} a_{k0}(1 - \cos(\gamma_0 - \gamma_k)) \geq 0, \tag{3.54}$$

where $a_{k0} = 1$ if the $k$th vehicle has knowledge of $\gamma_0$ and zero otherwise. As long as $a_{k0} = 1$ for at least one vehicle, (3.54) is positive semi-definite in the space of relative orientations $\gamma_j - \gamma_k$, with equality to zero occurring only when $\gamma_k = \gamma_0$ for all $k \in \{1, \ldots, n\}$ [15]. The time derivative of (3.54) is

$$\dot{U} = -\sum_{k=1}^{n} \left[ \frac{2}{n} \langle p_\gamma, ie^{i\gamma_k} \rangle + a_{k0} \sin(\gamma_0 - \gamma_k) \right] \nu_k,$$

implying that the steering control

$$\nu_k = K_\gamma \left( \frac{2}{n} \langle p_\gamma, ie^{i\gamma_k} \rangle + a_{k0} \sin(\gamma_0 - \gamma_k) \right), \quad K_\gamma > 0, \tag{3.55}$$

guarantees $\dot{U} = -\sum_{k=1}^{n} K_\gamma \left[ \frac{2}{n} \langle p_\gamma, ie^{i\gamma_k} \rangle + a_{k0} \sin(\gamma_0 - \gamma_k) \right]^2 \leq 0$, which implies vehicles are steered to a critical point satisfying $\dot{U} = 0$. In a strong flow, the control (3.55) will steer the vehicle to $\gamma_{des}$ only if $\gamma_{des}$ is a feasible direction of travel. Parallel formations are addressed in Chapter 4.

### 3.4.2 Stabilization of a Single Vehicle to a Non-zero Curvature Formation with Specified Position

The results of Section 3.3.2 steer a vehicle to a closed curve, but do not specify the position of the formation in inertial space. Building upon Section 3.3.2, this section describes the design of a control law that steers a particle to a feasible formation with specified center of rotation in a strong flowfield. Lyapunov analysis is used to establish the stability of the formation in a strong flow when the initial formation center lies within

a feasible disk centered at a feasible steady-state reference center $c_0$. The notation $B(c, a)$ is used to represent a disk of radius $a$ centered at $c \in \mathbb{C}$.

**Theorem 3.** *Consider a strong flow $f_k$. Let $\mathcal{F}$ be a feasible region and $c_0 \in \mathbb{C}$. Let*

$$\nu_{max} > \max_{k,t} |\kappa(\gamma_k(t))s_k(t)| \tag{3.56}$$

*and $B(c_0, |c_k(0) - c_0|) \subset \mathcal{F}$. The model (3.12) with the mapping (3.6) and*

$$\nu_k = \text{sat}\left(\kappa_k\left(s_k + K\langle e^{i\gamma_k}, c_k - c_0\rangle\right); \nu_{max}\right) \tag{3.57}$$

*forces convergence of the kth particle to a formation centered at $c_0$.*

*Proof.* Consider the candidate potential function

$$S_{pres} = \frac{1}{2}|c_k - c_0|^2, \tag{3.58}$$

where $c_k$ is given by (3.46). The time derivative of (3.58) is

$$\dot{S}_{pres} = \langle c_k - c_0, \dot{c}_k\rangle = \langle c_k - c_0, e^{i\gamma_k}\rangle\left(s_k - \kappa_k^{-1}\nu_k\right). \tag{3.59}$$

Note from (3.57) that for $|\nu_k| < \nu_{max}$

$$\langle c_k - c_0, e^{i\gamma_k}\rangle = \frac{\nu_k - \kappa_k s_k}{K\kappa_k}. \tag{3.60}$$

Substituting this result into (3.59) gives

$$\dot{S}_{pres} = \left(\frac{\nu_k - \kappa_k s_k}{K\kappa_k}\right)\left(s_k - \kappa_k^{-1}\nu_k\right) = -\frac{(\nu_k - \kappa_k s_k)^2}{K\kappa_k^2} \leq 0. \tag{3.61}$$

When $|\nu_k| = \nu_{max}$, $\dot{V} < 0$ since $\nu_{max} > \max_{k,t}|\kappa_k s_k(t)|$. Consequently, $c_k$ is contained by $B(c_0, |c_k(0) - c_0|) \subset \mathcal{F}$. Moreover, solutions converge to the largest invariant set in which $\dot{V} = 0$. From (3.57) and (3.59) this set contains solutions for which $\nu_k = \kappa_k s_k$, which implies $c_k = c_0$. □

In flows with radial symmetry a prescribed center overdetermines the formation position with respect to the flowfield; one need only prescribe the radial position of the formation center to accomplish an equivalent spatiotemporal sampling density with respect to the flowfield. The following control algorithm steers the $k$th particle to a trajectory in which the steady-state value $|c_k| = |c_0| \in \mathbb{R}$ is specified. (The previous result and similar works [15], [23], [136] require the specification of $c_k$ or allow the center to be arbitrary.)

**Theorem 4.** *Consider a strong flowfield $f_k$. Let $\mathcal{F}$ be a feasible region and $|c_0| \in \mathbb{R}$ be a distance at which a feasible formation center exists. Let $\nu_{max}$ satisfy (3.56) and $B\left(|c_0|, ||c_k\left(0\right)| - |c_0||\right) \subset \mathcal{F}$. The model (3.12) with the mapping (3.6) and*

$$\nu_k = \text{sat}(\kappa_k(s_k + K\langle r_k, e^{i\gamma_k}\rangle(1 - |c_0||c_k|^{-1})); \nu_{max}), \quad K > 0, \tag{3.62}$$

*forces convergence of the $k$th particle to a formation with curvature $\kappa$ at distance $|c_0|$ from the origin of reference frame $\mathcal{I}$ with arbitrary azimuth.*

*Proof.* Consider the potential function

$$S_{arb} = \frac{1}{2}(|c_k| - |c_0|)^2, \tag{3.63}$$

where $|c_k|$ is the distance of circle center $k$ from origin $O$. The time derivative of (3.63) along solutions to the equations of motion (3.12) is

$$\begin{aligned} \dot{S}_{arb} &= (|c_k| - |c_0|)\tfrac{\mathrm{d}}{\mathrm{dt}}|c_k| \\ &= (|c_k| - |c_0|)|c_k|^{-1}\langle r_k, e^{i\gamma_k}\rangle(s_k - \kappa_k^{-1}\nu_k). \end{aligned} \tag{3.64}$$

Note from (3.62) that for $|\nu_k| < \nu_{max}$, the control (3.62) into (3.64) gives

$$\dot{S}_{arb} = -\sum_{k=1}^{n} K\langle r_k, e^{i\gamma_k}\rangle^2(1 - |c_0||c_k|^{-1})^2 \leq 0. \tag{3.65}$$

Moreover, when $\nu_k = \nu_{max}$, $\dot{S}_{arb} < 0$ since $\nu_{max} > \max_{k,t}|\kappa(\gamma_k(t))s_k(t)|$. Equation (3.65) implies that $\dot{S}_{arb}$ is negative semi-definite with $\dot{S}_{arb} = 0$ occurring when $|c_k| = |c_0|$ or

$\langle r_k, e^{i\gamma_k} \rangle = 0$. The invariant set $\Lambda$ for which $\dot{S}_{arb} = 0$ contains trajectories with $|c_k| = |c_0|$ or $\langle r_k, e^{i\gamma_k} \rangle = 0$. The invariance principle [116] stipulates that particle $k$ converges to $\Lambda$. Variation of (3.63) about the critical point $\langle r_k, e^{i\gamma_k} \rangle = 0$ shows that motion about $\langle r_k, e^{i\gamma_k} \rangle = 0$ is unstable since $\dot{S}_{arb} \leq 0$. □

Theorems 3 and 4 show that an individual particle will converge to a reference center provided that the reference center and a disk containing the initial particle centers lie within a feasible region. The reference center is called a prescribed center and any particle with information of the prescribed center is called an informed particle. The following analysis provides decentralized, multi-vehicle control algorithms that incorporate vehicle communication topologies in order to steer vehicles to a common formation center. We use the results of Theorems 3 and 4 to augment the multi-vehicle Lyapunov function and prescribe a desired formation position.

### 3.4.3 Stabilization of Non-zero Curvature, Multi-vehicle Formations

This section applies the results of the previous section and use Lyapunov analysis to design decentralized multi-vehicle controls that collectively steer the particles such that they achieve coincident centers, i.e., $c_k = c_j$ for all pairs $j, k = 1, \ldots, n$. Let $\boldsymbol{c} = [c_1 \; c_2 \; ... \; c_n]^T$ be an $n \times 1$ matrix of instantaneous centers of rotation where $c_k$ is given by (3.46). Consider the potential function [16]

$$S_m(\boldsymbol{r}, \boldsymbol{\gamma}) = \frac{1}{2} \langle \boldsymbol{c}, \boldsymbol{L}\boldsymbol{c} \rangle, \tag{3.66}$$

where $\boldsymbol{L}$ is the $n \times n$ Laplacian matrix defining the communication topology. This work assumes an all-to-all network corresponding to a Laplacian given by (2.9) [137]. (Extensions of the flow-free model to limited communication topologies is discussed in [124].)

Equation (3.66) is positive semi-definite in the space of particle positions and positive definite in the reduced space of relative circle centers. Equality to zero occurs when $\boldsymbol{c} = c_0\mathbf{1}$, $c_0 \in \mathbb{C}$. Using (3.47), the time derivative of (3.66) is [15], [16], [132]

$$\dot{S}_m(\mathbf{r}, \boldsymbol{\gamma}) = \sum_{k=1}^{n} \langle \dot{c}_k, \boldsymbol{L}_k \mathbf{c} \rangle = \sum_{k=1}^{n} \langle e^{i\gamma_k}, \boldsymbol{L}_k \mathbf{c} \rangle \left( s_k \mp \kappa_k^{-1} \nu_k \right), \tag{3.67}$$

where $\boldsymbol{L}_k$ is the $k$th row of $\boldsymbol{L}$. The control [16], [132]

$$\nu_k = \pm \kappa_k \left( s_k + K \langle e^{i\gamma_k}, \boldsymbol{L}_k \mathbf{c} \rangle \right) \tag{3.68}$$

substituted into (3.67) gives [16], [132]

$$\dot{S}_m(\mathbf{r}, \boldsymbol{\gamma}) = -K \sum_{k=1}^{n} \langle e^{i\gamma_k}, \boldsymbol{L}_k \mathbf{c} \rangle^2 \leq 0. \tag{3.69}$$

The invariance principle stipulates that solutions of (3.5) with control (3.68) converge to the largest invariant set $\Lambda$ where [132]

$$\langle e^{i\gamma_k}, \boldsymbol{L}_k \mathbf{c} \rangle \equiv 0. \tag{3.70}$$

Since $e^{i\gamma_k} \neq 0$, then $\boldsymbol{L}_k \mathbf{c} = 0$ in $\Lambda$, which is satisfied when the centers are coincident. Moreover, when (3.70) is satisfied the control in (3.68) simplifies to (3.48) which implies $\dot{\boldsymbol{c}} = 0$. (Note that this framework does not incorporate collision avoidance between particles.)

The following result shows that a multi-vehicle system having initial centers in a feasible region and at least one informed particle will converge to a prescribed center in the same feasible region.

**Corollary 1.** *Consider a strong flowfield $f_k$. Let $\mathcal{F}$ be a feasible region and $c_0 \in \mathbb{C}$. Let*

$$\nu_{max} > \max_{k,t} \left| \kappa(\gamma_k(t)) s_k(t) \right|,$$

*and*

$$B(c_0, \max_k \left| c_k(0) - c_0 \right|) \subset \mathcal{F}.$$

*The model (3.12) with the mapping (3.6) and*

$$\nu_k = \text{sat}\left(\kappa\left[s_k + K\left(\langle e^{i\gamma_k}, \boldsymbol{L}_k\mathbf{c}\rangle + a_{k0}\langle e^{i\gamma_k}, c_k - c_0\rangle\right)\right]; \nu_{max}\right), \quad K > 0, \tag{3.71}$$

*where* $a_{k0} = 1$ *for at least one particle and zero otherwise, forces convergence to the formation specified by the curvature function* $\kappa$ *centered at* $c_0$*.*

*Proof.* Consider the composite potential function formed by the sum of (3.66) and (3.57) [14]

$$S = \tfrac{1}{2}\langle \mathbf{c}, \boldsymbol{L}\mathbf{c}\rangle + \tfrac{1}{2}\textstyle\sum_{k=1}^{n} a_{k0}\left|c_k - c_0\right|^2. \tag{3.72}$$

The time derivative of (3.72) along solutions of (3.12) is

$$\dot{S} = \sum_{k=1}^{n}\left(\langle e^{i\gamma_k}, \boldsymbol{L}_k\mathbf{c}\rangle + a_{k0}\langle e^{i\gamma_k}, c_k - c_0\rangle\right)\left(s_k - \kappa^{-1}\nu_k\right). \tag{3.73}$$

For $\nu_k < \nu_{max}$ notice from (3.71)

$$\frac{\nu_k - \kappa s_k}{K\kappa} = \langle e^{i\gamma_k}, \boldsymbol{L}_k\mathbf{c}\rangle + a_{k0}\langle e^{i\gamma_k}, c_k - c_0\rangle$$

giving

$$\dot{S} = -\sum_{k=1}^{n}\frac{\left(\nu_k - \kappa s_k\right)^2}{K\kappa^2} \leq 0. \tag{3.74}$$

When $\nu_k = \nu_{max}$, $\dot{S} < 0$ since $\nu_{max} > \max_{k,t}\left|\kappa s_k(t)\right|$. Therefore the collection of particle centers is bounded within the ball $B\left(c_0, \left|c_k\left(0\right) - c_0\right|\right) \subset \mathcal{F}$. Solutions converge to the largest invariant set for which $\dot{S} = 0$, which occurs when $\nu_k = \kappa s_k$ for all $k$, implying from (3.71)

$$\langle e^{i\gamma_k}, \boldsymbol{L}_k\mathbf{c}\rangle + a_{k0}\langle e^{i\gamma_k}, c_k - c_0\rangle = 0 \tag{3.75}$$

for all $k$.

If $a_{k0} = 0$ for at most $n-1$ particles, then (3.75) is satisfied only if $\boldsymbol{L}_k\mathbf{c} = 0$, which occurs when $c_k = c_j$ for all $k$ and $j$. For $k$ with $a_{k0} = 1$, (3.75) is satisfied only if $c_k = c_0$. Therefore, $\mathbf{c}$ must satisfy $\mathbf{c} = c_0\mathbf{1}$ [15]. □

Note that the control is calculated based on the inertial variable $\gamma_k$, which corresponds to one of two values of $\theta_k$. This implies that the control does not differentiate between aligning or opposing the flowfield. In circulating flowfields with a circular formation, simulation results show that particles with random initial conditions converge to a circular formation in which particles aligned with the flow travelled faster than those anti-aligned. Simulations also show that increasing the gain $K$ in (3.71) tends to align particles with the flow.

Figures 3.9(a) and 3.9(b) show simulation results illustrating multi-vehicle control to circular and quadrifolium formations in the random strong flowfield shown previously in Figure 3.6. Particle trajectories are shown in blue. The circular formation parameters were $|\omega_0|^{-1} = 20$, $K = 0.1$, and $c_0 = -40+30i$ and the quadrifolium formation parameters were $a = 20$, $c_0 = -50 + 50i$. Note $c_0$ was chosen to be consistent with the feasibility analysis shown in Figure 3.6(a). The value of $\nu_{max}$ was calculated from $u_{max} = \pi/2$ rad/s. Note from Figures 3.6(a) and 3.9(a) that $B(\max_k |c_k(0) - c_0|)$ does not lie entirely in a feasible region as required by Corollary 1, yet the particle centers still converge to $c_0$. Figures 3.9(c) and 3.9(d) illustrate simulation results in a strong Rankine vortex. In Figure 3.9(c) the reference center is $c_0 = 0$ with circle radius $|\omega_0|^{-1} = r_{max}$, whereas Figure 3.9(d) has quadrifolium lobe length $a = 20$ and prescribes center $c_0 = 0$. The Rankine vortex is parameterized by $r_{max} = 30$, $v_{max} = 1.2$, and $\mu = 0.8$.

To guarantee particle convergence to a formation with coincident centers at a desired distance from the origin, augment the potential function (3.63) with the multi-vehicle formation center term $\frac{1}{2}\langle \boldsymbol{c}, \boldsymbol{L}\boldsymbol{c}\rangle$. Consider the potential

$$S = \frac{1}{2}\langle \boldsymbol{c}, \boldsymbol{L}\boldsymbol{c}\rangle + \sum_{k=1}^{n} \frac{1}{2} a_{k0}(|c_k| - |c_0|)^2, \tag{3.76}$$

where $a_{k0} = 1$ if the $k$th particle is informed of $|c_0|$ and zero otherwise. We have the

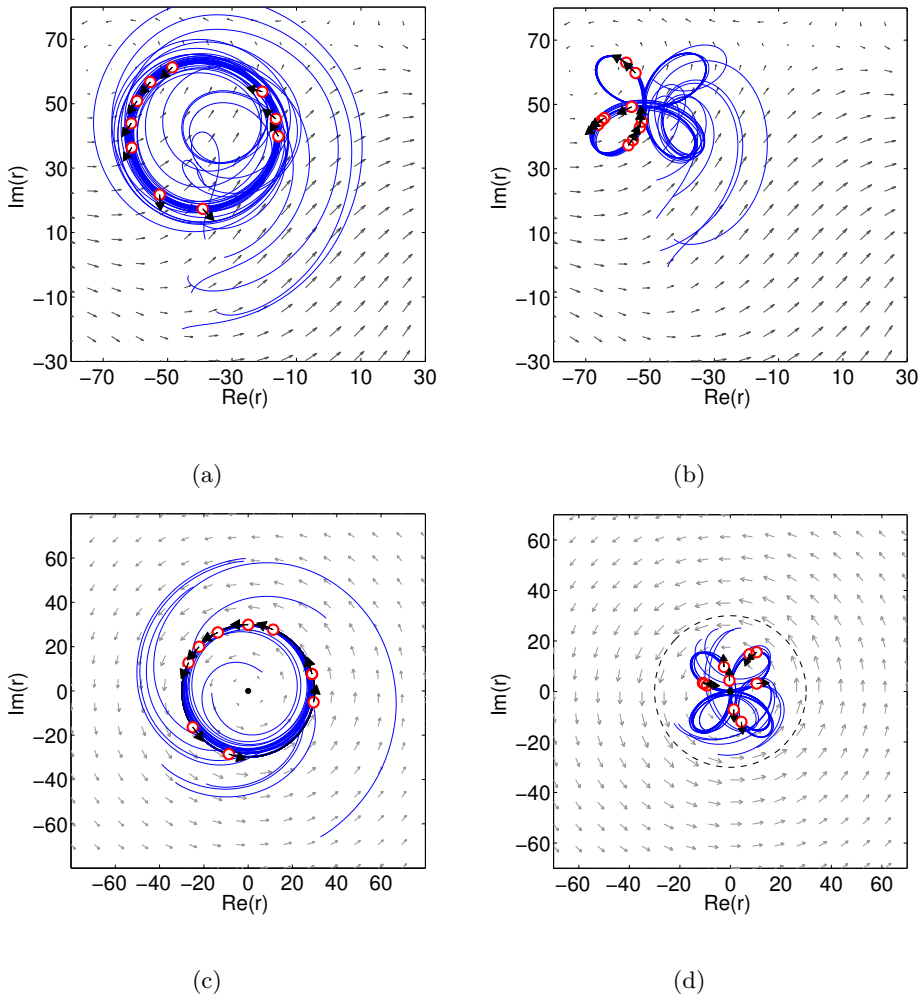


Figure 3.9: Simulation of $n = 10$ particles with (a,c) circular and (b,d) quadrifolium steering control in a random flowfield and Rankine vortex.

following result.

**Corollary 2.** *The particle model (3.12) with (3.6) and control*

$$\nu_k = \text{sat}(\kappa(s_k + K(\langle e^{i\gamma_k}, \boldsymbol{L}_k \boldsymbol{c}\rangle + \langle r_k, e^{i\gamma_k}\rangle(1 - |c_0||c_k|^{-1})); \nu_{max}), \quad K > 0 \tag{3.77}$$

*stabilizes the set of feasible formations with with curvature function $\kappa$ whose center has distance $|c_0|$ from the origin.*

*Proof.* The time derivative of (3.76) along solutions of (3.12) is

$$\dot{V} = \sum_{k=1}^{n} \left[ \langle e^{i\gamma_k}, \boldsymbol{L}_k \boldsymbol{c} \rangle + a_{k0}(1 - |c_k|^{-1}|c_0|) \langle r_k, e^{i\gamma_k} \rangle \right] (s_k - \kappa^{-1}\nu_k). \tag{3.78}$$

For $\nu_k < \nu_{max}$, substituting (3.77) into (3.78) gives

$$\dot{V} = -\sum_{k=1}^{n} K \left[ \langle e^{i\gamma_k}, \boldsymbol{L}_k \boldsymbol{c} \rangle + (1 - |c_k|^{-1}|c_0|) \langle r_k, e^{i\gamma_k} \rangle \right]^2 \leq 0. \tag{3.79}$$

Equation (3.79) implies that the vehicles converge to the largest invariant set $\Lambda$ for which

$$\left[ \langle e^{i\gamma_k}, \boldsymbol{L}_k \boldsymbol{c} \rangle + a_{k0}(1 - |c_0||c_k|^{-1}) \langle r_k, e^{i\gamma_k} \rangle \right] = 0 \tag{3.80}$$

For particles in which $a_{k0} = 0$ the quantity $\boldsymbol{L}_k \boldsymbol{c} = 0$ only when $c_k = c_j$ for all pairs $j, k$ [14]. For particles in which $a_{k0} = 1$ the largest invariant set satisfying (3.80) occurs when $\boldsymbol{c} = \mathbf{1}c_0$ with $|c_0|$ specified. Following the proof of Corollary 1, when $\nu_k = \nu_{max}$, $\dot{S} < 0$ since $\nu_{max} > \max_{k,t} |\kappa(\gamma_k(t)) s_k(t)|$. Variation of (3.76) about the critical points not satisfying $\boldsymbol{c} = \mathbf{1}c_0$ shows that motion about these points is unstable since $\dot{S} \leq 0$. By the invariance principle [116] solutions converge to $\Lambda$, which contains the desired set of feasible formations $\boldsymbol{c} = \mathbf{1}c_0$ where $|c_0|$ is specified. □

Figure 3.10(a) illustrates simulation of the control algorithm (3.77) with $n = 10$ particles in the random flowfield with $|\omega_0|^{-1} = 20$, $K = 0.1$, $a_{1,0} = a_{2,0} = a_{3,0} = 1$, and $a_{4,0} = a_{5,0} = a_{6,0} = 0$. Similar to Figure 3.9(a), the particles converge to a circular formation. The circle center lies a distance $|c_0| = 50$ from the origin with circle center azimuth dictated by the initial conditions of the vehicles. The possible circular formation center positions are denoted by the dashed line.

An alternative to circular and folium trajectories that achieves good sampling density and is feasible in a strong Rankine vortex is a spirograph trajectory. The spirograph family of formations combines the advantages of circular and folia formations in that they

generally align with the vortex while criss-crossing the radius of maximum wind. For a given rate of rotation $\Omega$, circle radius $|\omega_0|^{-1}$, and radius of circle center $|c_0|$, the feasibility of the resulting formation can be analyzed using Theorem 2. We extend Corollaries 1 and 2 to motion with respect to the rotating reference frame $\mathcal{B}$ using the particle dynamics (3.30) and feasibility analysis of Theorem 2. By applying the control (3.71) to the equations of motion (3.30), the particles will converge to a formation with a desired center, assuming the formation center is feasible in the rotating frame.

Figures 3.10(b) and 3.10(c) illustrate a simulation of the steering control (3.71) used in the equations of motion (3.30) for $n = 10$ particles. The formation parameters are $\Omega = 0.0125$ rad/s, $|\omega_0|^{-1} = 40$, and $|c_0| = 30$ ($\hat{\Omega} = 1.57$, $|\hat{\omega}_0|^{-1} = 4/3$ and $|\hat{c_0}| = 1$). Note from Figure 3.7(b) that this parameter set corresponds to a feasible formation as required. Figure 3.10(c) illustrates that a circular formation with respect to a rotating reference frame produces a spirograph formation in an inertial reference frame, shown in Figure 3.10(b). By manipulating $\hat{\Omega}$, $\hat{\omega}_0$, and $|\hat{c_0}|$, spirograph trajectories can be made to concentrate radial and azimuthal sampling densities to areas of interest within the vortex. This technique potentially provides superior sampling coverage as compared to the circular and quadrifolium formations of Figures 3.9(c) and 3.9(d).

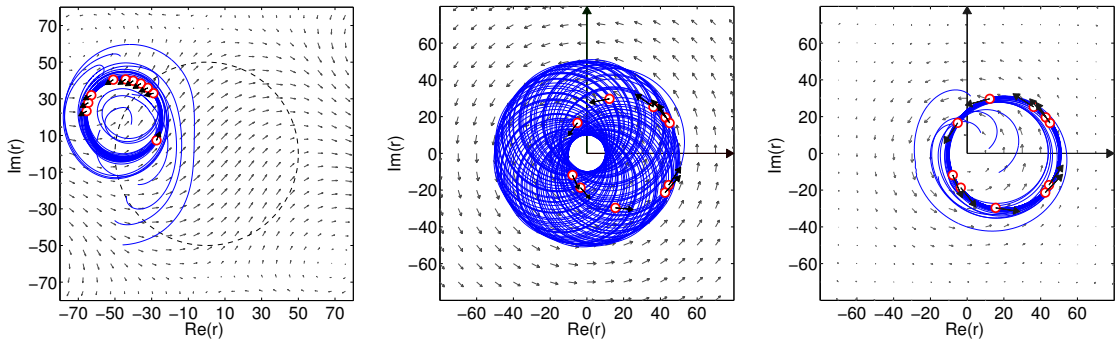


(a) (b) (c)

Figure 3.10: (a) Circular formation with specified circle center distance $|c_0| = 50$. Spirograph formation produced by utilizing circular control with respect to rotating frame with flow; viewed in (b) an inertial reference frame and (c) a rotating reference frame.

# Chapter 4: Extension to Three-Dimensional Particle Motion in an Unknown Time-invariant Shear Flow

This chapter extends the planar control algorithms to three dimensions and addresses how a multi-vehicle system may utilize vertical variation of wind as a means of maintaining coordination via altitude control. Previous works have utilized steering and flow-relative speed control to design decentralized multi-vehicle control algorithms that guide vehicles to sampling formations with a desired inter-vehicle spacing in a spatially-varying flowfield [15], [115]. However, to maximize endurance in many applications the vehicle speed relative to the flow is often assumed to be fixed. This chapter shows how total horizontal speed can be controlled indirectly by utilizing knowledge of the flowfield's vertical windspeed profile while maintaining a fixed flow-relative speed. Changing altitude to achieve the desired total horizontal speed enables inter-vehicle spacing to be regulated while simultaneously maximizing vehicle endurance. We finish this chapter by demonstrating the control coupled with recursive Bayesian estimation, where the Bayesian filter provides estimates of the flow for use in the control algorithm.

This chapter builds upon the two-dimensional results of the previous sections and provides (1) conditions for feasibility of a speed-regulated, three-dimensional trajectory with respect to the vehicle model in a shear flow; (2) decentralized control algorithms that steer vehicles to feasible equal-speed parallel formations and equal-speed circular formations in which vehicles are equally spaced in a spatially varying shear flow; and (3)

an implementation of the decentralized control laws using the estimated wind field based on a recursive Bayesian filter that assimilates noisy flow measurements. The control strategies are simulated on a realistic aircraft model to verify performance even when the simplifying assumptions of the aircraft model do not hold.

## 4.1 Three-Dimensional Vehicle Motion in a Shear Flow

This section extends the two-dimensional vehicle model to three dimensions, following Beard and McLain [29]. The two dimensional flow models are augmented to three dimensions by assuming the flowspeed changes with altitude. Simplifying assumptions are made to facilitate the design of theoretically justified steering and climb-rate controls that guide a set of vehicles to desired formations. Consider $n$ unmanned aircraft in which the $k$th vehicle's position with respect to a ground-fixed inertial reference frame is represented by the vector $\vec{r}_k = [x_k \ y_k \ z_{1,k}]^T$, where $x_k, y_k \in \mathbb{R}$ and $z_{1,k} \in \mathbb{R}^+$ for all $k = 1, \ldots, n$, and the velocity by $\dot{\vec{r}}_k = [\dot{x}_k \ \dot{y}_k \ \dot{z}_{1,k}]^T$. (The dual subscript $z_{1,k}$ represents the altitude of the $k$th vehicle and is used to clarify presentation of the second-order altitude dynamics that follow.) The position of the $k$th vehicle in the horizontal plane is $r_k = x_k + iy_k \in \mathbb{C}$ and the altitude $z_{1,k} \in \mathbb{R}^+$, as shown in Figure 4.1(a). In the absence of flow, the $k$th vehicle's horizontal velocity has magnitude $v_k$ and orientation $\theta_k = \tan^{-1}(\dot{y}_k/\dot{x}_k)$, such that $\dot{r}_k = v_k e^{i\theta_k}$. Assume each vehicle is equipped with a heading-angle autopilot [29] that controls the rate of change $\dot{\theta}_k$ of its horizontal flow-relative velocity orientation via the control $u_{1,k}$, which is bounded by a turn-rate constraint $|u_{1,k}| \leq u_{1,max}$, where $u_{1,max} > 0$.

The rate of change of the vehicle's flow-relative airspeed is $\dot{v}_k = (T_k/m_k - D_k/m_k - g\sin(\tan^{-1}(\dot{z}_{1,k}/v_k)))\cos(\tan^{-1}(\dot{z}_{1,k}/v_k))$, where $T_k$, $m_k$, $D_k$, and $\tan^{-1}(\dot{z}_{1,k}/v_k)$ are the vehicle's thrust, mass, drag, and flight path angle, and $g$ represents the acceleration due

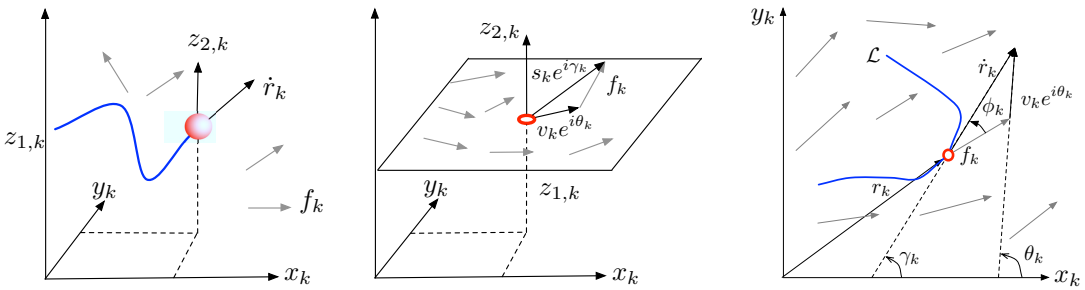


(a) (b) (c)

Figure 4.1: (a) Vehicle position in three dimensions; (b) flow-relative and total horizontal velocity orientation; and (c) total horizontal velocity of the $k$th vehicle.

to gravity [29]. The effects of flow velocity on flow-relative vehicle airspeed are assumed negligible, [138] because the horizontal spatial gradients are small. (Note that the scale of the horizontal and vertical motions typical of an environmental-sampling application differ by several orders of magnitude.) If the $k$th aircraft's horizontal velocity is much larger than its rate of climb so that $v_k \approx (v_k^2 + \dot{z}_{1,k}^2)^{1/2}$ and the vertical motion is regulated by an altitude-hold autopilot, [28], [29] then the altitude obeys $\ddot{z}_{1,k} = -\alpha_z \dot{z}_{1,k} + \alpha_h (z_k^c - z_{1,k})$, where $z_k^c$ is the commanded altitude, $\alpha_z > 0$, and $\alpha_h > 0$. Setting $\dot{z}_{1,k} = z_{2,k}$ and $z_k^c = (u_{2,k} + \alpha_z z_{2,k} + \alpha_h z_{1,k})/\alpha_h$, where $u_{2,k}$ is the vertical acceleration control, yields the (flow-free) equations of motion

$$\begin{aligned} \dot{r}_k &= v_k e^{i\theta_k} \\ \dot{\theta}_k &= u_{1,k} \\ \dot{z}_{1,k} &= z_{2,k} \\ \dot{z}_{2,k} &= u_{2,k} \\ \dot{v}_k &= \left(\tfrac{T}{m} - \tfrac{D}{m} - g \sin\left(\tan^{-1}(\tfrac{z_{2,k}}{v_k})\right)\right) \cos(\tan^{-1}(\tfrac{z_{2,k}}{v_k})). \end{aligned} \tag{4.1}$$

The climb rate of the $k$th aircraft satisfies $|z_{2,k}| \leq z_{2,max}$ with $z_{2,max} > 0$, which

implies

$$u_{2,k} = \begin{cases} 0, & z_{2,k} > z_{2,max} \\ u_{2,k} & -z_{2,max} \leq z_{2,k} \leq z_{2,max} \\ 0, & z_{2,k} < -z_{2,max}. \end{cases} \tag{4.2}$$

Assume the required rate of climb/descent is small compared to the horizontal speed maintained by the aircraft, which implies the flight path angle $\tan^{-1}(z_{2,k}/v_k)$ is negligible. Moreover, balancing the thrust and drag forces at equilibrium speed $v_{0,k}$ implies $\dot{v}_k = 0$ in (4.1) and $v_k = v_{0,k}$ is constant [28], [139].

The constant flow-relative speed model is augmented by including a time-invariant (moderate strength) flow $f_k$ whose magnitude varies with altitude. A wind model such as this can adequately represent many environmental systems of interest. For example, a hurricane exhibits vertical variation of wind at low altitudes [140]. The flow model assumes the flow is separable into horizontal and vertical terms, i.e.,

$$f_k = f(r_k, z_{1,k}) = f_{vert}(z_{1,k}) f_{hor}(r_k) \in \mathbb{C}, \tag{4.3}$$

where $f_{hor}(r_k) \in \mathbb{C}$ characterizes the dependence of horizontal flow direction on position $r_k$, given by the flow models in Section 3.1.3. The function $f_{vert}(z_{1,k}) \in \mathbb{R}^+$ describes the (smooth) dependence of the flow magnitude on altitude and is assumed to have the form [141]

$$f_{vert,k} = V_{ref} \frac{\ln(z_{1,k}/h_0)}{\ln(h_{ref}/h_0)}, \tag{4.4}$$

where $V_{ref}$ is the reference windspeed at reference altitude $h_{ref}$ and $h_0$ is a shaping parameter of the vertical gradient. Figure 4.1 shows the wind speed given by (4.4) plotted versus altitude, normalized by the $V_{ref}$, where $h_{ref} = 1$ km. Assuming the flow-relative speed of the $k$th vehicle is greater than the maximum flowspeed, i.e., $v_{0,k} > |f_k|$ for all $r_k$

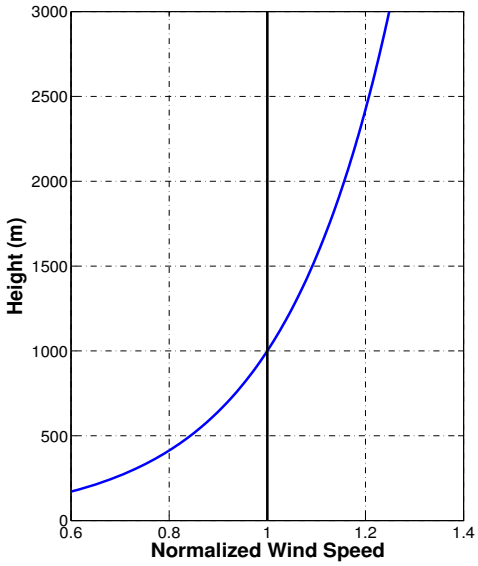


Figure 4.2: The wind shear model (4.4) is shown normalized by $W_{ref}$.

and $z_{1,k}$, implies each vehicle can maintain forward progress over ground at any altitude. At low altitudes, the model (4.4) is comparable with experimental hurricane data taken from 357 eyewall profiles from 17 hurricanes [140]. Note that in (4.4) the windspeed is monotonically increasing; for shear flows that have a local maximum, the model (4.4) is only valid for altitudes up to the altitude corresponding to the maximum wind speed.

In the presence of flowfield $f_k$, each vehicle's horizontal velocity is represented by the vector sum of its horizontal velocity relative to the flow and the flow velocity relative to the ground [15], [29]. The equations of motion of the $k$th vehicle become [15]

$$\begin{aligned} \dot{r}_k &= v_k e^{i\theta_k} + f_k \\ \dot{\theta}_k &= u_{1,k} \\ \dot{z}_{1,k} &= z_{2,k} \\ \dot{z}_{2,k} &= u_{2,k}, \end{aligned} \tag{4.5}$$

where $\dot{v}_k = 0$ because the vehicle's flow-relative speed is assumed to be constant.

Control design motivates derivation of the time rate of change of the total hor-

izontal velocity with respect to the control variables $u_{1,k}$ and $u_{2,k}$ in order to develop mappings between the control of the total and flow-relative velocities, respectively. Using the magnitude and direction of the total horizontal velocity [15] $s_k \triangleq |v_k e^{i\theta_k} + f_k|$ and $\gamma_k \triangleq \arg(v_k e^{i\theta_k} + f_k)$, respectively, the $k$th vehicle state as $\mathbf{x}_k \triangleq [r_k, z_{1,k}, z_{2,k}, \gamma_k, s_k]^T$. Note from Figure 4.1(b) and 4.1(c) that

$$s_k \cos\gamma_k = v_k \cos\theta_k + \langle f_k, 1\rangle \tag{4.6}$$

$$s_k \sin\gamma_k = v_k \sin\theta_k + \langle f_k, i\rangle. \tag{4.7}$$

Taking the time derivative of (4.6) and (4.7) assuming $\dot{v}_k = 0$ gives

$$\dot{s}_k \cos\gamma_k - s_k\dot{\gamma}_k \sin\gamma_k = -\dot{\theta}_k v_k \sin\theta_k + \langle \dot{f}_k, 1\rangle \tag{4.8}$$

$$\dot{s}_k \sin\gamma_k + s_k\dot{\gamma}_k \cos\gamma_k = \dot{\theta}_k v_k \cos\theta_k + \langle \dot{f}_k, i\rangle, \tag{4.9}$$

where $\dot{f}_k = \frac{\partial f_k}{\partial r_k}\dot{r}_k + \frac{\partial f_k}{\partial z_{1,k}} z_{2,k}$. Solving for $\dot{s}_k$ in (4.8) and substituting the result into (4.9) to solve for $\dot{\gamma}_k$ yields [15]

$$\dot{\gamma}_k = (1 - s_k^{-1}\langle f_k, e^{i\gamma_k}\rangle)u_{1,k} + \langle \tfrac{\partial f_k}{\partial r_k} e^{i\gamma_k}, ie^{i\gamma_k}\rangle + s_k^{-1}\langle \tfrac{\partial f_k}{\partial z_{1,k}}, ie^{i\gamma_k}\rangle z_{2,k} \triangleq \nu_k, \tag{4.10}$$

where $\nu_k$ is the effective steering control of the total horizontal velocity orientation including a vertical velocity term. Solving (4.10) for $u_{1,k}$ with respect to $\nu_k$ yields the transformation from absolute steering control $\nu_k$ to flow-relative steering control

$$u_{1,k} = \frac{\nu_k - \langle \frac{\partial f_k}{\partial r_k} e^{i\gamma_k}, ie^{i\gamma_k}\rangle - s_k^{-1}\langle \frac{\partial f_k}{\partial z_{1,k}}, ie^{i\gamma_k}\rangle z_{2,k}}{(1 - s_k^{-1}\langle f_k, e^{i\gamma_k}\rangle)}. \tag{4.11}$$

Note, the transformation (4.11) is well defined in moderate flowfields [15]. Similarly,

solving (4.9) for $\dot{\gamma}_k$, substituting the result into (4.8), and using (4.11) to solve for $\dot{s}_k$ gives

$$\begin{aligned}\dot{s}_k &= \underbrace{s_k\langle\frac{\partial f_k}{\partial r_k}e^{i\gamma_k},e^{i\gamma_k}\rangle+\frac{\langle f_k,ie^{i\gamma_k}\rangle(\nu_k-\langle\frac{\partial f_k}{\partial r_k}e^{i\gamma_k},ie^{i\gamma_k}\rangle)}{(1-s_k^{-1}\langle f_k,e^{i\gamma_k}\rangle)}}_{\triangleq A(\mathbf{x}_k)} \\ &\quad + \underbrace{\left(\langle\frac{\partial f_k}{\partial z_{1,k}},e^{i\gamma_k}\rangle-\frac{\langle f_k,ie^{i\gamma_k}\rangle\langle\frac{\partial f_k}{\partial z_{1,k}},ie^{i\gamma_k}\rangle}{s_k-\langle f_k,e^{i\gamma_k}\rangle}\right)}_{\triangleq B(\mathbf{x}_k)} z_{2,k},\end{aligned} \tag{4.12}$$

where $A(\mathbf{x}_k)$ and $B(\mathbf{x}_k)$ are nonlinear functions of $\mathbf{x}_k$. Let $\xi_k \triangleq A(\mathbf{x}_k)+B(\mathbf{x}_k)z_{2,k}$. The equations of motion for a vehicle subject to steering and altitude control become

$$\begin{aligned}\dot{r}_k &= s_k e^{i\gamma_k} \\ \dot{\gamma}_k &= \nu_k \\ \dot{z}_{1,k} &= z_{2,k} \\ \dot{z}_{2,k} &= u_{2,k} \\ \dot{s}_k &= \xi_k.\end{aligned} \tag{4.13}$$

Note that if $B(\mathbf{x}_k)\neq 0$ along a desired horizontal trajectory, the desired climb rate is

$$z_{2,k}^d = B^{-1}(\mathbf{x}_k)(\xi_k - A(\mathbf{x}_k)). \tag{4.14}$$

The equations of motion that facilitate the design of the total horizontal steering $\nu_k$ and speed $\xi_k$ controls are thus

$$\begin{aligned}\dot{r}_k &= s_k e^{i\gamma_k} \\ \dot{\gamma}_k &= \nu_k \\ \dot{s}_k &= \xi_k.\end{aligned} \tag{4.15}$$

Equation (4.15) represents the motion equations for which feedback controls $\nu_k$ and $\xi_k$ will be derived. To implement the horizontal steering and speed controls $\nu_k$ and $\xi_k$, one calculates $u_{1,k}$ using (4.10) and $z_{2,k}^d$ using (4.14). The next step is to design $u_{2,k}$ to ensure convergence of $z_{2,k}$ to $z_{2,k}^d$, provided $B(\mathbf{x}_k)\neq 0$.

## 4.2 Trajectory Feasibility Under Altitude Control

Even though altitude control is utilized as a means of maintaining a desired horizontal speed along a trajectory, not all speed-regulated trajectories are feasible. The following result defines conditions for feasible constant-speed trajectories using altitude control; it does not account for a vehicle's turn-rate constraints in the horizontal plane, which has been addressed previously [23].

**Theorem 5.** *Trajectory $\mathcal{L}$ traversed with desired speed $s_0$ is feasible under the vehicle model (4.5) in a moderate flowfield of the form (4.3) if, for all $r_k \in \mathcal{L}$, $B(\mathbf{x}_k) \neq 0$ and there exists an altitude $z_{1,k}$ such that the quantity*

$$s_0 \cos\phi_k \pm \sqrt{v_{0,k}^2 - s_0^2 \sin^2\phi_k}, \tag{4.16}$$

*is real, positive, and less than $v_{0,k}$, where $\phi_k = \gamma_k - \arg(f_k)$.*

*Proof.* For a vehicle to travel along horizontal trajectory $\mathcal{L}$ with desired speed $s_0$, the flow at every point along the curve must be such that the vehicle can maintain total horizontal velocity $s_0 e^{i\gamma_k}$ tangent to $\mathcal{L}$. With the flowfield $f_k$ given by (4.3), the angle $\phi_k \triangleq \gamma_k - \arg(f_k)$ between $s_0 e^{i\gamma_k}$ and $f_k$, shown in Figure 4.1(c) depends only on the horizontal position $r_k$ and not on the altitude $z_{1,k}$. The flow-relative horizontal velocity $v_k e^{i\theta_k}$ must satisfy the triangle equality such that $s_0 e^{i\gamma_k} = v_{0,k} e^{i\theta_k} + f_k$. The law of cosines implies $v_{0,k}^2 = s_0^2 + |f_k|^2 - 2s_0|f_k|\cos\phi_k$, which, when solved for $|f_k|$, gives $|f_k| = s_0\cos\phi_k \pm (v_{0,k}^2 - s_0^2\sin^2\phi_k)^{1/2}$. If, for all $r_k \in \mathcal{L}$, there exists a $z_{1,k}$ such that $|f_k|$ is real and positive, the trajectory $\mathcal{L}$ can be traversed with horizontal speed $s_0$ and is therefore feasible. Since $f_k$ is continuous in space, the desired $z_{1,k}$ is continuous along $\mathcal{L}$ (assuming sufficiently large climb-rate saturation $z_{2,max}$) and can be achieved if $B(\mathbf{x}_k) \neq 0$. □

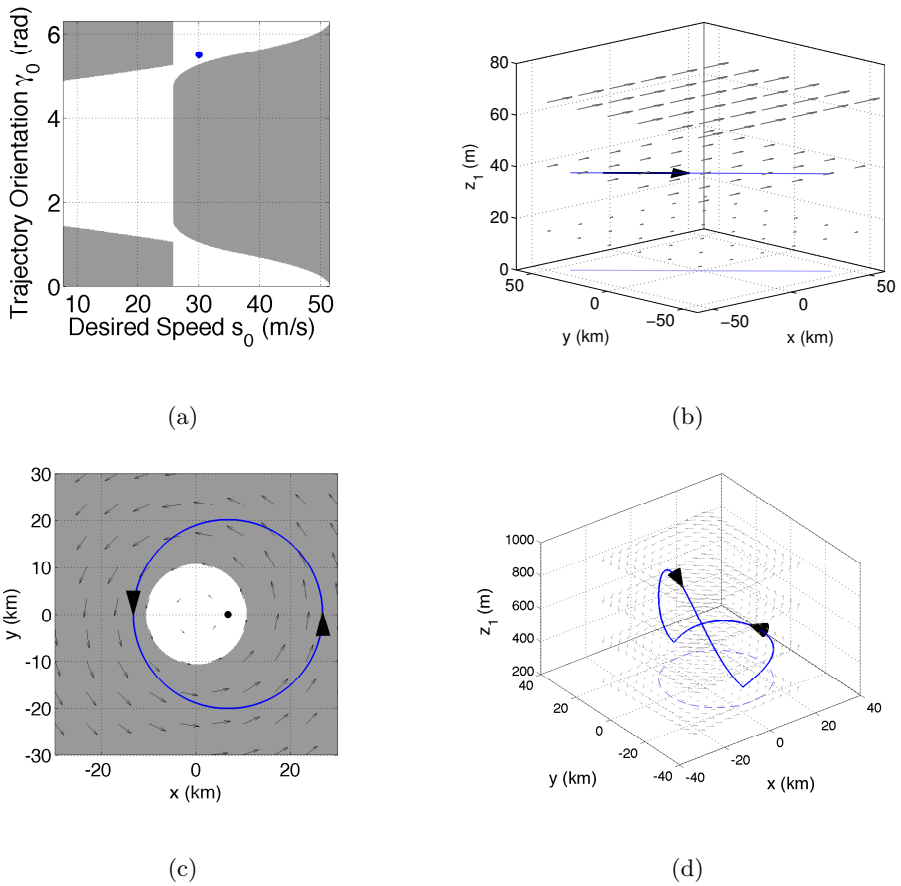


Figure 4.3: Feasibility regions for (a) straight trajectories in a uniform shear flow and (c) circular trajectories in a Rankine vortex with vertical wind shear. (b),(d) Three-dimensional trajectories corresponding to black dots in (a),(c), respectively. White regions in (a,c) are feasible formations and gray are not.

Theorem 5 is illustrated in Figure 4.3 for straight and circular trajectories at constant speed. To understand Figure 4.3(a), consider a straight trajectory in a uniform flowfield (3.33) with vertical wind shear given by (4.4). The trajectory is characterized by its (constant) velocity orientation $\gamma_k = \gamma_0$ and magnitude $s_k = s_0$. Figure 4.3(a) shows the results of a feasibility analysis over the space of trajectory orientations and speeds in a flowfield parameterized by $W_{ref} = 25.7$ m/s, $h_0 = 12$, and $h_{ref} = 1$ km, where $v_{0,k} = 25.7$ m/s is consistent with the cruise speed of the Aerosonde platform [142]. White

areas indicate that the trajectory characterized by the point in parameter space $(s_0, \gamma_0)$ is feasible, whereas gray areas indicate it is infeasible. The blue dot corresponds to the orientation and velocity of the trajectory in Figure 4.3(b), which maintains a constant speed $s_0 = 30$ m/s with orientation $\gamma_0 = 7\pi/4$. The flow is plotted at three altitudes to illustrate how flow speed changes with vertical position. The black cone represents the velocity orientation of a vehicle on the trajectory.

Figures 4.3(c) and (d) depict a constant-speed, counter-clockwise circular trajectory in a Rankine vortex (3.34) with vertical wind shear. The vertical shear is given by (4.4) with shear parameters $W_{ref} = 25.7$ m/s, $h_0 = 12$, and $h_{ref} = 1$ km. Figure 4.3(c) illustrates a planar representation of the feasibility of circular trajectories with radius $|\omega_0|^{-1} = 20.1$ km and constant speed $s_d = 1.66 v_{0,k}$ m/s, where $v_{0,k} = 25.7$ m/s is consistent with the cruise speed of the Aerosonde platform [142]. A representative feasible trajectory is shown by the blue circle, centered at $c = (1/3)r_{max} + 0i$ km (the center is represented by the black dot). A constant-speed circular formation whose center lies in the white area is feasible, whereas one centered in a gray area is infeasible. The Rankine vortex is parameterized by $r_{max} = 20.1$ km and $\mu = 0.6$, consistent with a small tropical storm [49] and is plotted over the feasibility map in Figure 4.3(c). The corresponding three-dimensional trajectory that maintains $s_d = 1.66 v_{0,k}$ m/s (shown in Figure 4.3(d)) is found by solving (4.4) for $z_{1,k}$ such that $|f_k|$ satisfies (4.16). The three dimensional trajectory is plotted over horizontal slices of the flow at equal interval altitudes; a horizontal projection of the trajectory is also shown. Note that maintaining constant total horizontal speed requires altitude variation, which is emphasized by exaggerating the scale difference between the vertical and horizontal axes of the figure.

## 4.3 Altitude-Induced Speed Control for Motion Coordination

Here we extend the two-dimensional control algorithms to stabilize feasible parallel, circular, and symmetric circular formations in a flowfield with wind shear. In a parallel formation, the orientation of each vehicle's total horizontal velocity is the same. In a circular formation, each vehicle rotates about the same fixed point; a symmetric circular formation is a circular formation with equal inter-vehicle spacing around the circle. Such formations are key motion primitives for environmental sampling networks [143].

### 4.3.1 Parallel-Formation Control with Speed Regulation

This section derives a decentralized control algorithm that stabilizes the feasible set of equal-speed parallel formations, even for vehicles traveling at different flow-relative speeds. Vehicles achieve equal horizontal velocity by converging to a desired altitude-rate control, rather than changing their flow-relative speed, which can reduce vehicle endurance. If the vehicles have the same flow-relative speed, then the steady-state altitudes are identical; otherwise the steady-state altitudes may differ.

The steering control for parallel motion is provided by 3.55, whereas the horizontal speed of the $k$th vehicle is controlled using the vertical acceleration $u_{2,k}$. However, $u_{2,k}$ does not appear explicitly in the time derivative of $s_k$. This motivates derivation of a speed control $\xi_k$, which gives a desired climb rate profile $z^d_{2,k}$ given by (4.14), and the design of $u_{2,k}$ such that $z_{2,k}$ converges to $z^d_{2,k}$. To design $\xi_k$, consider the positive semi-definite potential function

$$V_s = \frac{1}{2}\sum_{k=1}^{n}(s_0 - s_k)^2 \geq 0, \tag{4.17}$$

with equality occurring only when $s_k = s_0$ for all $k \in \{1, \ldots, n\}$ and feasible constant

reference speed $s_0 > 0$. The time derivative of (4.17) along solutions of (4.13) is

$$\dot{V}_s = -\sum_{k=1}^{n}(s_0 - s_k)\xi_k, \tag{4.18}$$

implying that the speed control

$$\xi_k = K_{sp}(s_0 - s_k), \quad K_{sp} > 0, \tag{4.19}$$

gives $\dot{V}_s \leq 0$ with equality occurring only when $s_k = s_0$ for all $k \in \{1, \ldots, n\}$. The steering and speed control analysis implies the following result.

**Theorem 6.** *Consider a uniform flowfield of the form (4.3) with wind shear (4.4). The model (4.15) with speed control (4.19) and turn-rate control (3.55) where $a_{k0} = 1$ for at least one vehicle, asymptotically stabilizes the set of feasible parallel formations in which $s_k = s_0$ and $\gamma_k = \gamma_0$ for all $k \in \{1, \ldots, n\}$.*

*Proof.* Consider the potential function formed by the sum of (3.54) and (4.17) that is positive definite and proper in the space of relative orientations $\gamma_j - \gamma_k$ and speeds $s_0 - s_k$, whose time derivative under controls (3.55) and (4.19) is

$$\dot{U}_s = \dot{U} + \dot{V}_s = -\sum_{k=1}^{n}\left(\left[\tfrac{1}{n}\langle p_\gamma, ie^{i\gamma_k}\rangle + a_{k0}\sin(\gamma_0 - \gamma_k)\right]^2 + K_{sp}(s_0 - s_k)^2\right) \leq 0. \tag{4.20}$$

By the invariance principle [116, p. 126-128], (4.20) ensures solutions converge to the largest invariant set $\Lambda$ for which $\dot{U}_s = 0$. From (4.20), the set $\Lambda$ contains solutions of (4.15) for which

$$\begin{aligned} 0 &= \left[\tfrac{1}{n}\langle p_\gamma, ie^{i\gamma_k}\rangle + a_{k0}\sin(\gamma_0 - \gamma_k)\right] \\ s_0 &= s_k, \end{aligned} \tag{4.21}$$

for all $k \in \{1, \ldots, n\}$. For $a_{k0} = 0$ the first equality in (4.21) is satisfied only when $\gamma_k = \gamma_j$ for all $\{k, j\} \in \{1, \ldots, n\}$ [15]. For $a_{k0} = 1$, the first equality is satisfied only if

$\gamma_k = \gamma_j = \gamma_0$, implying that all vehicles converge to the set $\gamma_0 = \gamma_k$ for all $k \in \{1, \ldots, n\}$. The second equality in (4.21) is satisfied only when $s_k = s_0$ for all $k \in \{1, \ldots, n\}$. □

Theorem 6 stabilizes vehicle speeds to a feasible reference value $s_0$, assuming each vehicle has knowledge of this value. This assumption is relaxed in the following result, in which a subset of vehicles obtain knowledge of $s_0$ by implementing a consensus algorithm [144].

**Corollary 3.** *Consider a uniform flowfield of the form (4.3) with shear model (4.4). The model (4.15) with turn-rate control (3.55) and speed control*

$$\xi_k = K_{sp} \left( a_{k0}(s_0 - s_k) + \frac{1}{n} \sum_{j=1}^{n} (s_j - s_k) \right), \quad K_{sp} > 0, \tag{4.22}$$

*where $a_{k0}$ is non-zero for at least one vehicle, steers vehicles to the set of feasible parallel formations in which $s_k = s_0$ and $\gamma_k = \gamma_0$ for all $k \in \{1, \ldots, n\}$.*

*Proof.* Following the proof of Theorem 6, use of the potential function (3.54) shows that the turn-rate control (3.55) steers horizontal vehicle velocity orientations to an invariant set $\Lambda$ that includes $\gamma_k = \gamma_0$ for all $k \in \{1, \ldots, n\}$. The speed of the $k$th vehicle with control (4.22) obeys

$$\dot{s}_k = K_{sp} \left[ a_{k0}(s_0 - s_k) + \sum_{j=1}^{n} (s_j - s_k) \right]. \tag{4.23}$$

Equation (4.23) represents a constant-reference consensus algorithm on a directed spanning tree with reference $s_0$. It follows from [145, Thm 3.1] that $s_k$ converges to $s_0$ for all $k \in \{1, \ldots, n\}$. □

The model (4.15) assumes kinematic control of $s_k$ through use of the desired climb rate (4.14). Since the dynamic model (4.13) is a second-order chain of integrators, define

the error variable $\lambda_k \triangleq z^d_{2,k} - z_{2,k}$ and consider

$$V_\lambda = \frac{1}{2}\sum_{k=1}^{n} \lambda_k^2, \tag{4.24}$$

whose derivative is $\dot{V}_\lambda = \sum_{k=1}^{n}(\dot{z}^d_{2,k} - u_{2,k})\lambda_k$. Note that the quantity $\dot{z}^d_{2,k}$ may contain second-order spatial derivatives of the flow that are difficult to approximate in a realistic application. This potential difficulty motivates use of the proportional control

$$u_{2,k} = K_\lambda \lambda_k, \quad K_\lambda > 0, \tag{4.25}$$

giving

$$\dot{V}_\lambda = \sum_{k=1}^{n}(\dot{z}^d_{2,k} - K_\lambda\lambda_k)\lambda_k, \tag{4.26}$$

and the following result.

**Proposition 1.** *Consider a uniform flowfield of the form (4.3) with wind shear (4.4). The model (4.5) with steering control (4.11) with (3.55), where $a_{k0} = 1$ for at least one vehicle, and vertical acceleration control (4.25) where $\lambda_k = z^d_{2,k} - z_{2,k}$ and $z^d_{2,k}$ is given by (4.14) and (4.22), has climb rate error $\lambda_k$ bounded by $|\lambda_k| \leq z_{2,max}/K_\lambda$.*

*Proof.* Equation (4.26) gives the time derivative of (4.24) under control (4.25). Since the vertical acceleration is bounded, feasible $z^d_{2,k}$ satisfy $|\dot{z}^d_{2,k}| \leq z_{2,max}$, implying $\dot{V}_\lambda \leq 0$ for all $|\lambda_k| \geq z_{2,max}/K_\lambda$, which can be made arbitrarily small by increasing $K_\lambda$. Therefore, solutions of (4.5) have vertical acceleration errors satisfying $|\lambda_k| \leq z_{2,max}/K_\lambda$. □

Figure 4.4 illustrates simulations of the equations of motion (4.5) with control provided by Corollary 3 and Proposition 1, $n = 6$ vehicles, and $K_{sp} = K_\gamma = K_\lambda = 0.1$ in a uniform flowfield. The flowfield with vertical shear is given by (4.3) with $f_{hor}(r_k) = \psi = 1$ yielding the flowfield parameterization $\mathbf{\Omega} = (\psi, W_{ref}, h_0)$, where $W_{ref} = 25.7$ m/s and $h_0 = 12$. The reference values $\gamma_0 = \pi/4$ radians and $s_0 = 1.4v_{0,k}$ m/s, where $v_{0,k} = 25.7$

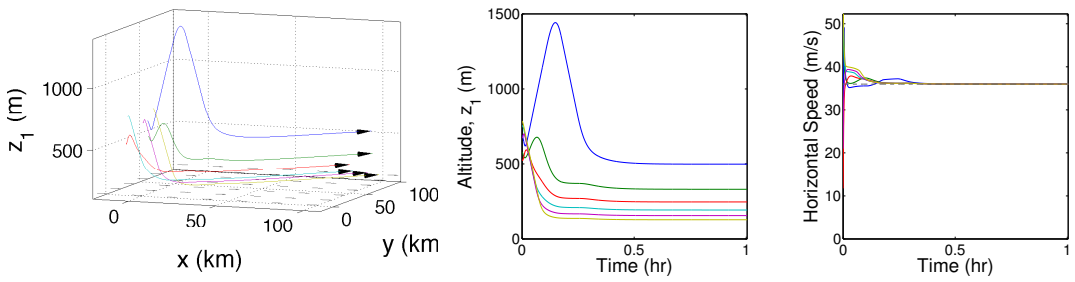


(a) (b) (c)

Figure 4.4: Illustration of vehicle (a) trajectories, (b) altitudes, and (c) total horizontal speeds when flow-relative speeds are not equal.

m/s, are chosen to be consistent with the feasibility analysis of Section 4.2. Flow-relative vehicle speeds are randomly chosen from the interval $v_{0,k} \in [25, 28]$ m/s. Note that non-identical vehicles reach consensus on total horizontal speed by autonomously converging to different altitudes.

### 4.3.2 Circular-Formation Control with Speed Regulation

A symmetric circular formation is a circular formation in which vehicles are spaced evenly about the circle. This section describes the design of distributed steering and altitude controls to stabilize the set of symmetric circular formations in a non-uniform flowfield with vertical shear, which was previously not possible in even uniform flows. In order to maintain uniform spacing around the horizontal projection of the formation, the vehicles regulate their total horizontal speed using altitude control rather than adjusting their flow-relative speed, which is fixed. This control technique is illustrated on an idealized hurricane model.

Vehicles are steered to a common reference center $c_0$ by adopting the steering control (3.71). The control algorithm (3.71) is extended to stabilize symmetric circular formations

in a non-uniform flowfield by regulating vehicle speed using altitude control. The progress of the $k$th vehicle around the circular formation is represented by a phase variable $\psi_k$ [15], [16]. When $s_k$ is constant, the phase of the $k$th vehicle satisfies $\psi_k = \gamma_k$, in which case the period of rotation is $T = 2\pi/(\omega_0 s_k)$.

This paper seeks to coordinate vehicle phases using an $(m, n)$-pattern potential, where $n$ is divisible by $m$, which is minimized by any arrangement of $m$ uniformly spaced clusters of $n/m$ vehicles [14]. The so-called splay formation corresponds to $m = n$ in which each cluster contains one vehicle. Let $U(\boldsymbol{\psi})$ be a rotationally symmetric phase potential that, by construction, is positive definite in the reduced space of relative vehicle phases [15], [16], [14]. (For an overview of rotationally symmetric phase potentials see Sepulchre et al. [14]) By definition, stable critical points of the potential function satisfy $\dot{U}(\psi) = 0$ and $\sum_{k=1}^{n} \partial U(\boldsymbol{\psi})/\partial \psi_k = 0$ and occur only in the desired $(m, n)$-pattern; all other critical points are unstable [15]. Addition of the phase potential forms the composite potential [15]

$$S_c(\mathbf{r}, \boldsymbol{\gamma}) = S_m(\boldsymbol{r}, \boldsymbol{\gamma}) + \tfrac{T}{2\pi} U(\boldsymbol{\psi}), \tag{4.27}$$

where $S_m$ is given by (3.72). Note $S_c(\boldsymbol{r}, \boldsymbol{\gamma})$ is positive definite in the reduced space of relative circle centers and relative phases. Using (3.73), the time derivative of (4.27) is [15]

$$\dot{S}_c = \sum_{k=1}^{n} \left( s_k \langle e^{i\gamma_k}, P_k \mathbf{c} \rangle + a_{k0} s_k \langle e^{i\gamma_k}, c_k - c_0 \rangle - \frac{\partial U}{\partial \psi_k} \right) \left( 1 - (\omega_0 s_k)^{-1} \nu_k \right). \tag{4.28}$$

Choosing the steering control

$$\nu_k = \omega_0 s_k \left[ 1 + K_\gamma \left( s_k \langle e^{i\gamma_k}, P_k \mathbf{c} \rangle + a_{k0} s_k \langle e^{i\gamma_k}, c_k - c_0 \rangle - \tfrac{\partial U}{\partial \psi_k} \right) \right], \tag{4.29}$$

yields $\dot{S}_c \leq 0$. Combining the circular phase potential function (4.27) with the horizontal speed potential function (4.17) yields the following result.

**Theorem 7.** *Let $s_0 > 0$ be a feasible constant reference speed. Consider the vehicle model (4.15) with flowfield (4.3) and shear model (4.4). The speed control*

$$\xi_k = K_{sp}(s_0 - s_k), \quad K_{sp} > 0, \tag{4.30}$$

*and steering control $\nu_k$ given by (4.29) stabilize the set of feasible symmetric circular formations centered at $c_0$ with radius $|\omega_0|_,^{-1}$ in which vehicle separation is determined by the critical points of $U(\boldsymbol{\psi})$ and $s_k = s_0$ for all $k \in \{1, \ldots, n\}$.*

*Proof.* Consider the potential function $V = S_c + V_s \geq 0$ formed by (4.27) and (4.17), which is positive definite and proper in the co-dimension two space of relative circle centers, relative phases, and (absolute) speeds. The time derivative of $V$ along solutions of (4.15) is given by the sum of (4.28) and (4.18), respectively, which are negative semi-definite under control [15] (4.29) and (4.19). According to the invariance principle [116, p. 126-128], vehicles converge to the largest invariant set $\Lambda$ for which $\dot{V} = 0$. From (4.28) and (4.18), the invariant set $\Lambda$ contains solutions of (4.13) for which

$$s_k \langle e^{i\gamma_k}, P_k \boldsymbol{c} \rangle + a_{k0} s_k \langle e^{i\gamma_k}, c_k - c_0 \rangle - \tfrac{\partial U}{\partial \psi_k} = 0, \tag{4.31}$$

and $s_k = s_0$ for all $k \in \{1, \ldots, n\}$. The set of circular formations centered at $c_0$ with radius $|\omega_0|^{-1}$ and vehicle spacing dictated by the minima of $U(\boldsymbol{\psi})$ is the only stable set of isolated equilibrium points in (4.31); all other isolated equilibria are unstable [14, Theorem 6]. Therefore, the only stable equilibrium points for which $\dot{V} \equiv 0$ is the set of circular formations centered at $c_0$ with radius $|\omega_0|^{-1}$, vehicle spacing dictated by the stable critical points of $U(\boldsymbol{\psi})$, and vehicle speed $s_k = s_0$ for all $k \in \{1, \ldots, n\}$. □

Relaxing the assumption that all vehicles have knowledge of the reference speed $s_0$ in Theorem 7 and instead using a consensus algorithm to reach agreement on a common reference speed gives the following result.

**Corollary 4.** *Let $s_0 > 0$ be a feasible constant reference speed. Consider the vehicle model (4.15) in flowfield (4.3) with wind shear (4.4). The speed control (4.22) and steering control $\nu_k$ given by (4.29), where $a_{k0}$ is nonzero for at least one vehicle, stabilize vehicle motion to the set of feasible circular formations centered at $c_0$ with radius $|\omega_0|^{-1}$ in which vehicle separation is determined by the critical points of $U(\boldsymbol{\psi})$ and $s_k = s_0$ for all $k \in \{1, \ldots, n\}$.*

*Proof.* With control (4.22) the dynamics of the $k$th vehicle's speed represent a constant-reference consensus algorithm on a directed spanning tree where the reference signal is $s_0$. It follows from [145, Thm 3.1] that $s_k$ converges to $s_0$, for all $k \in \{1, \ldots, n\}$. With $s_k = s_0$ for all $k = 1, \ldots, n$, equation (4.28) is negative semi-definite under steering control (4.11) with $\nu_k$ given by (4.29). By the invariance principle [116, p.126-128], it follows that vehicles are steered to the set of symmetric circular formations centered at $c_0$ with radius $|\omega_0|^{-1}$ and vehicle spacing dictated by the minima of $U(\boldsymbol{\psi})$ [14, Theorem 6]. □

The steering and speed controls of Theorem 7 and Corollary 4 are extended to the dynamic vehicle model (4.5) using the transformations (4.11) and (4.14) to calculate $u_{1,k}$ and $z^d_{2,k}$. The following result guarantees a bounded climb-rate error for the equal-speed symmetric circular steering controls of Theorem 7 and Corollary 4.

**Proposition 2.** *Consider a flowfield of the form (4.3) with wind shear (4.4). The model (4.5) with steering control (4.11) with (4.29), where $a_{k0} = 1$ for at least one vehicle, and vertical acceleration control (4.25) where $\lambda_k = z^d_{2,k} - z_{2,k}$, $z^d_{2,k}$ is given by (4.14), and $\xi_k$ by (4.22) has climb rate error $\lambda_k$ bounded by $|\lambda_k| \leq z_{2,max}/K_\lambda$.*

*Proof.* Equation (4.26) gives the time derivative of (4.24) under control (4.25). Since the climb rate is bounded, feasible $z^d_{2,k}$ satisfy $|\dot{z}^d_{2,k}| \leq z_{2,max}$, implying $\dot{V}_\lambda \leq 0$ for all $|\lambda_k| \geq z_{2,max}/K_\lambda$, which can be made arbitrarily small by increasing $K_\lambda$. Therefore,

solutions of (4.5) have climb rate errors satisfying $|\lambda_k| \leq z_{2,max}/K_\lambda$. □

To achieve a formation with equal inter-vehicle separation, consider an $(m,n)$-phase potential of the form [15]

$$U^{m,n}(\boldsymbol{\gamma}) = \sum_{j=1}^{m} K_j U_j,$$

where $K_j > 0$ for $j = (1,\ldots,m-1)$, $K_m < 0$, and [15]

$$U_j(\boldsymbol{\psi}) = \frac{n}{2}|p_{j\gamma}|^2, \quad \text{where} \quad p_{j\gamma} \triangleq \frac{1}{jn}\sum_{l=1}^{n} e^{ij\psi_l}.$$

Choosing $m = n$ stabilizes the splay formation of $n$ evenly spaced vehicles [14], [15].

Figure 4.5(a) depicts the feasibility of a constant-speed, counter-clockwise circular trajectory in an idealized hurricane model with vertical wind shear. The flowfield is given by (4.3), where $f_{hor}(r_k)$ is a Rankine vortex characterized by (3.34). The vertical shear is given by (4.4) with shear parameters $V_{ref} = 25.7$ m/s, $h_0 = 12$, and $h_{ref} = 1$ km. Figure 4.5(b) relaxes the zero flight-path angle and constant flow-relative velocity assumptions and illustrates simulation of the aircraft model (4.1) in a Rankine vortex. The drag, thrust, and mass of the vehicle are modeled after the Aerosonde unmanned aircraft, assuming nominal cruise speed $v_{0,k} = 25.7$ m/s at zero flight-path angle [29], [142]. The control is calculated using the results of Corollary 4 and Proposition 2 with $n = 6$ vehicles, centered at $c_0 = 6.7$ km, with control gains $K_\gamma = 10^{-4}$, $K_{sp} = 1$, $K_\lambda = 1.5$, and $a_{k0} = 1$ for three vehicles. Figure 4.5(a) overlays the converged vehicle formation over the two-dimensional feasibility map of Figure 4.3(c). Note that $c_0$ lies in the feasible region and that the vehicles are equally spaced along the formation. The Rankine vortex is parameterized by $r_{max} = 20.1$ km and $\mu = 0.6$, consistent with a small[1] tropical storm [49] and is plotted

[1] A small storm is chosen since it represents a situation in which the largest vertical variation is required compared to the horizontal distance covered, implying that larger flight path angles will occur compared to those encountered in vortices spanning greater horizontal distances.

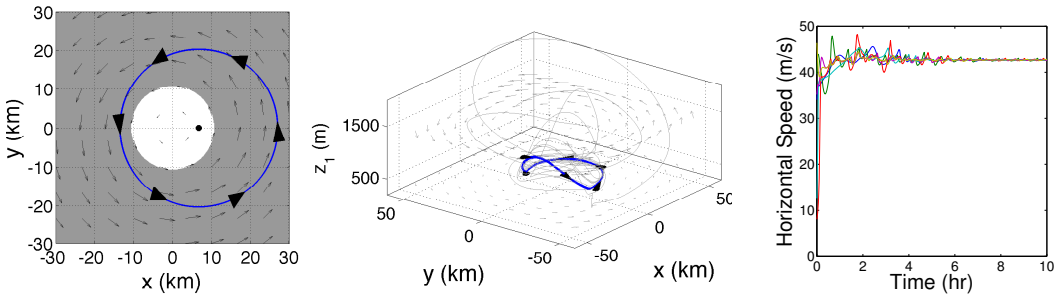


(a) (b) (c)

Figure 4.5: (a) Feasibility of circular formations, illustration of equations of motion (4.1), Corollary 4 and Theorem 2 with $n = 6$ vehicles in a Rankine vortex: (b) formation in three-dimensional space and (c) total horizontal speeds versus time.

over the feasibility map in Figure 4.5(a). Figure 4.5(b) shows transient vehicle trajectories in light blue and the final splay formation centered at $c_0$ with the desired radius in dark blue. Vehicle positions and velocity orientations are represented by black cones. The vertical axis in Figure 4.5(b) is given in meters and the horizontal axes are in kilometers to emphasize the vertical variations made by each vehicle. The resulting horizontal speed plotted versus time is shown in Figure 4.5(c).

The final simulation of Chapter 5 relaxes the zero flight path angle and constant flow-relative velocity assumptions. We also assume the flowfield is unknown and simulate use of the aircraft model (4.1) in a Rankine vortex. The flowfield model is parameterized by $\mathbf{\Omega} = (25.7 \text{ m/s}, 12, 20.1 \text{ km}, 0.6)$ with $h_{ref} = 1$ km and contains random flow perturbations with a standard deviation 1 m/s in the vertical direction and 2 m/s in the horizontal directions. A dynamic feedback control algorithm based on Corollary 4 and Proposition 2 is implemented by replacing the known flowfield with a flowfield estimate generated by the recursive Bayesian filter presented in Chapter 2. In this case the probability density function is 4-dimensional and produces flowfield parameter estimates

$\hat{\mathbf{\Omega}} = (\hat{W}_{ref}, \hat{h}_0, \hat{r}_{max}, \hat{\mu})$, which represent the reference windspeed, the shaping parameter of the vertical shear, the radius of maximum wind, and the exponential decay constant of the Rankine vortex, respectively. The probability density function is initialized uniformly, all initial estimates are zero, and measurements are collected in three minute intervals. The flowfield parameters are time-invariant, implying that the integral in (2.22) is simply the prior probability density $p(\mathbf{\Omega}(t-\Delta t)|\mathbf{A}(t-\Delta t))$. Each vehicle collects noisy measurements of the flow $\tilde{\boldsymbol{\beta}}_k = f(r_k, z_k; \mathbf{\Omega}) + \eta_k$ and assimilates measurements with the likelihood function[2]

$$p(\tilde{\alpha}_k(t)|\mathbf{\Omega}) = \frac{1}{\sqrt{2\pi|\Sigma|}} \exp[-\tfrac{1}{2}[f(r_k, z_k; \mathbf{\Omega}) - \tilde{\beta}_k(t)]^* \Sigma^{-1} [f(r_k, z_k; \mathbf{\Omega}) - \tilde{\beta}_k(t)]], \tag{4.32}$$

where $\Sigma = \text{diag}(\sigma_u^2, \sigma_v^2)$ is a matrix of variances of the measurement noise $\eta_k$. Figures 4.6(a) and 4.6(b) show the three-dimensional vehicle trajectories and projections on the horizontal plane, respectively, plotted over the (noise-free) Rankine model. Note that the vehicles converge to the splay formation even with the zero flight path angle and constant flow-relative velocity assumptions relaxed as well as random perturbations in the flow model included. Marginal probability densities[3] of the flowfield parameters $r_{max}$, $\mu$, $W_{ref}$, and $h_0$ are plotted versus time in Figures 4.6(c)–(f). The color scale denotes the probability density where red corresponds to high probability density and blue indicates the opposite. The magenta lines correspond to flowfield parameter estimates over time, whereas the dashed white lines correspond to the true flowfield parameters. Note that the estimated flowfield parameters converge to the true flow parameters.

[2]The notation $a^*$ represents the complex conjugate of $a$.

[3]The marginal probability density is achieved by summing a multi-dimensional probability density over a set of dimensions.

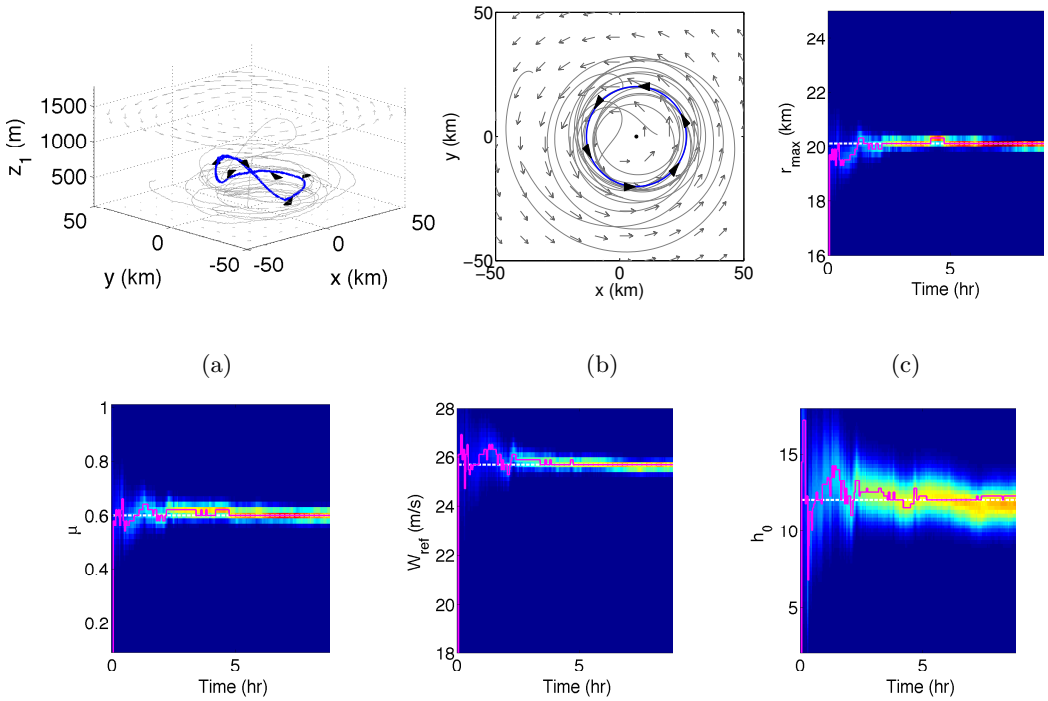


Figure 4.6: Simulation illustrating Corollary 4 with $n = 6$ vehicles in a Rankine vortex with additive noise, dynamic flow-relative speed, and recursive Bayesian estimation of the flowfield: (a,b) three and two-dimensional vehicle trajectories; (c–f) marginal probability densities of estimated flowfield parameters.

# Chapter 5: Application: Hurricane Sampling

Throughout this chapter we consider the challenge of sampling within a tropical cyclone using a group of unmanned aircraft. This problem is motivated by recent results utilizing the Aerosonde platform for low altitude sampling of tropical cyclones [146]. Figure 5.1 shows the sampling trajectory taken by an Aerosonde unmanned aircraft as it collected local flow velocity measurements within tropical storm Ophelia in 2005 [146]. Note as the aircraft enters the stronger winds of the cyclone, the sampling trajectory takes on the shape of a semi-circle or an arc of the spirograph trajectory. This motivates use of the multi-vehicle control algorithms of Chapter 3 that steer a group of sampling vehicles to feasible circular and spirograph formations. Without loss of generality we consider the family of circular formations throughout this chapter. We use measures of flowfield observability to optimize the parameters that characterize the sampling formation.

## 5.1 Control Objective and Background

The general control problem we address here is the optimization of an observer-based feedback controller using observability measures as a design metric. We use measures of flowfield observability to optimize the parameters characterizing the position and shape of the multi-vehicle sampling trajectory. Recall in Chapter 3 that in a Rankine vortex a circular formation is parameterized by the radial position of the circle center $|c_0|$ and the radius of the circle $|\omega_0^{-1}|$, forming the circular formation parameter set $\boldsymbol{\chi} \triangleq (|c_0|, |\omega_0^{-1}|)$, as

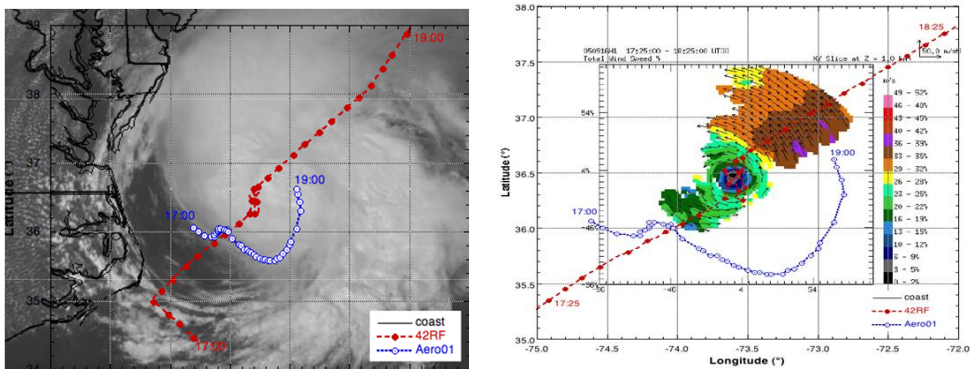


(a) (b)

Figure 5.1: (a) The blue trajectory denotes the flight path of the Aerosonde platform. (b) Aerosonde flight trajectory superimposed over radar measurements. Photo source: [146].

shown in Figure 5.2(a). Figure 5.2(b) illustrates simulation of the control (3.77) steering a single vehicle to three candidate sampling trajectories characterized by $\boldsymbol{\chi}_1 = (2, 10)$, $\boldsymbol{\chi}_2 = (24, 13)$, and $\boldsymbol{\chi}_3 = (35, 20)$, respectively, in a moderate Rankine vortex. The objective of this chapter is to steer a multi-vehicle system to the formation $\boldsymbol{\chi}^*$ that maximizes (minimizes) measures of flowfield observability (unobservability).

Figure 5.3 shows a block diagram of the sampling mission objective. Vehicles gather noisy measurements of the flowfield parameterized by $\boldsymbol{\Omega}$. A recursive Bayesian filter assimilates the measurements, producing an estimate of the flow. The resulting estimate is incorporated into an optimization routine that chooses the parameters $\boldsymbol{\chi}^*$ steering vehicles to a formation that best observes the flowfield.

For simplicity, we assume a fleet of $n$ planer sampling vehicles with dynamics governed by (3.12). Each vehicle collects local measurements of an unknown, time-invariant flowfield characterized by $G$ parameters $\boldsymbol{\Omega} \in \mathbb{R}^G$ and is steered by a decentralized feedback controller parameterized by $Q$ control parameters $\boldsymbol{\chi} \in \mathbb{R}^Q$. ($Q = 2$ for the circular family

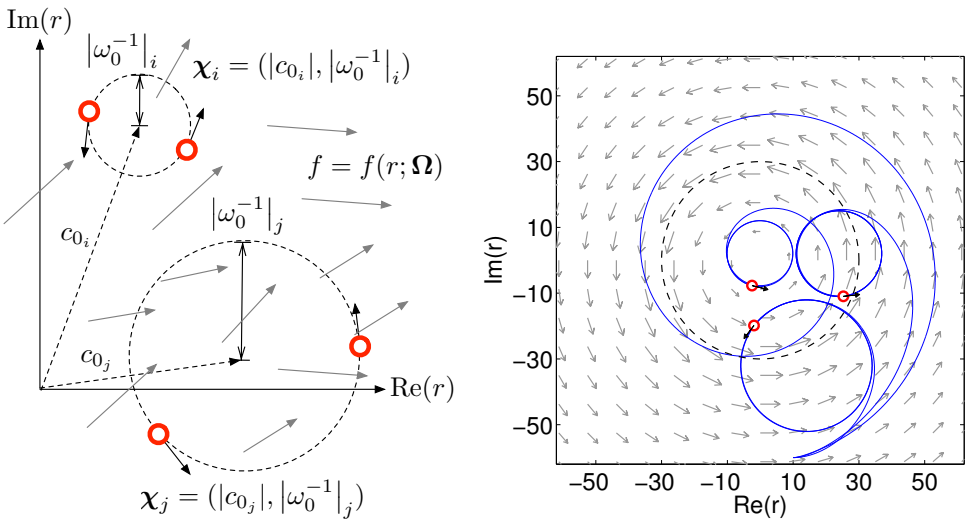


(a) (b)

Figure 5.2: The goal of the sampling mission is to steer the vehicles to the parameterized sampling formation that optimizes flowfield observability. (a) Parameterized family of circular formations; (b) simulation of one vehicle steered to three different parameterized circular formations in a moderate Rankine vortex.

of formations.) In the notation of Chapter 2, the overall nonlinear system is[1]

$$\dot{\mathbf{x}} = \boldsymbol{h}(\mathbf{x}; \boldsymbol{\Omega}) + \sum_{k=1}^{P} \boldsymbol{g}_k \left( \mathbf{x}, u_k(\mathbf{x}, \hat{\boldsymbol{\Omega}}; \boldsymbol{\chi}) \right) \tag{5.1}$$

$$\boldsymbol{\beta} = \boldsymbol{q}(\mathbf{x}; \boldsymbol{\Omega}), \tag{5.2}$$

where $\mathbf{x} = [\mathbf{r}, \boldsymbol{\theta}]^T \in \mathbb{C}^{2n}$ is a state vector containing the positions $\mathbf{r}$ and velocity orientations $\boldsymbol{\theta}$ of all $n$ vehicles. The drift and control vector fields are correspond to the vehicle kinematics in (3.12). The dynamic output feedback control $u_k(\mathbf{x}, \hat{\boldsymbol{\Omega}}; \boldsymbol{\chi})$ is a function of the vehicle states $\mathbf{x}$ augmented by the estimated flowfield parameters $\hat{\boldsymbol{\Omega}} \in \mathbb{R}^G$ and parameterized by $\boldsymbol{\chi} \in \mathbb{R}^Q$. The drift vector field $\boldsymbol{h}(\cdot)$ represents the uncontrolled vehicle dynamics,

[1] We introduce the notation $\mathbf{g}(a, b; \alpha, \beta)$ to represent a function $\mathbf{g}(\cdot)$ that depends on the state variables $a, b$ and the parameters $\alpha$ and $\beta$. We use bold fonts to represent either a column matrix, e.g., state variables $\mathbf{z} = [z_1 \ z_2 \ \ldots \ z_N]^T$, or a set of parameters, e.g., $\boldsymbol{\Omega} = (\Omega_1, \Omega_2, \ldots, \Omega_G)$.

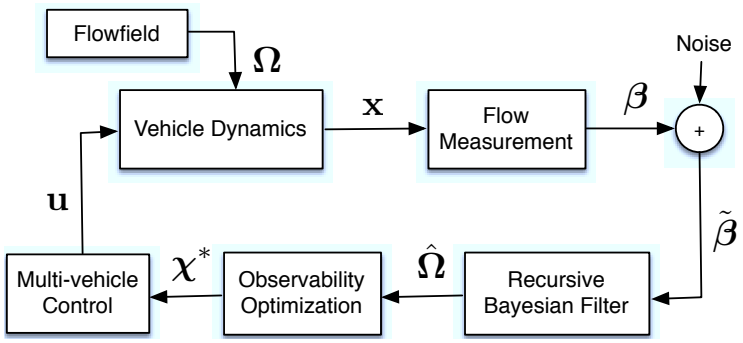


Figure 5.3: Vehicles collect noisy, local measurements of the flow, which are used to generate a flowfield estimate. The estimated flow is used to optimize the multi-vehicle sampling formation.

which are affected by the flow and therefore depend on the true flowfield parameters $\boldsymbol{\Omega}$. The output vector $\boldsymbol{\beta}$ is composed of flowfield measurements such that

$$\boldsymbol{\beta} = \boldsymbol{f}(\mathbf{r}; \boldsymbol{\Omega}) \in \mathbb{C}^n, \tag{5.3}$$

where $\boldsymbol{f}(\mathbf{r}) \in \mathbb{R}^n$ is a vector of flowfield measurements collected at vehicle positions $\mathbf{r}$.

An observer is implemented to provide estimates of the flowfield parameters $\hat{\boldsymbol{\Omega}}$ from noisy measurements. The observer dynamics are

$$\dot{\hat{\boldsymbol{\Omega}}} \;=\; \boldsymbol{\Phi}(\mathbf{x}, \hat{\boldsymbol{\Omega}}, \tilde{\boldsymbol{\beta}}), \tag{5.4}$$

where $\tilde{\boldsymbol{\beta}} = \boldsymbol{\beta} + \boldsymbol{\eta}$ are measurements corrupted by noise $\boldsymbol{\eta}$. The function $\boldsymbol{\Phi}(\cdot)$ represents the observer dynamics which, for example, may represent the update equations to the recursive Bayesian filter (2.22) or the particle filter (2.27). Here we implement (5.4) in discrete time using the recursive Bayesian filter formulation of Section 2.4 with likelihood function (4.32). The goal is to optimize the control parameters $\boldsymbol{\chi}$ using the flowfield estimates $\hat{\boldsymbol{\Omega}}$ such that the resulting measurements improve observability of $\hat{\boldsymbol{\Omega}}$.

Throughout this chapter we consider the idealized, time-invariant hurricane model

(3.34) known as the Rankine vortex. Recall from (3.34), the Rankine vortex is characterized by radially symmetric flow whose flowspeed increases linearly to the maximum flowspeed $v_{max}$ at the radius of maximum wind $r_{max}$, and decays exponentially outside $r_{max}$ with radial decay constant $\mu$. Thus, the flowfield is parameterized by $\mathbf{\Omega} = (r_{max}, v_{max}, \mu) \in \mathbb{R}^3$.

## 5.2 Observability Analysis of Sampling Formation Parameterizations

This section analyzes the observability of the time-invariant flowfield parameters $\mathbf{\Omega}$ given local measurements of the flow gathered by a single vehicle whose sampling formation is characterized by the formation parameters $\boldsymbol{\chi}$. For brevity and simplicity of presentation, we consider the circular sampling formation parameterized by the distance of the circle center from the vortex center $|c_0|$ (since the flowfield is radially symmetric) and the radius of the circular formation $|\omega_0|^{-1}$, i.e. $\boldsymbol{\chi} = (|c_0|, |\omega_0|^{-1}) \in \mathbb{R}^2$. However, the analysis is extensible to any of the parameterized sampling formations of Chapter 3.

For simplicity we consider a time-invariant flowfield, however, the empirical observability Gramian (2.15) is capable of assessing the observability of time-varying flowfield parameters, which enriches the problem by introducing a *spatiotemporal* sampling component in which formations must target measurements in both space and time. Targeting temporal measurements is the subject of ongoing work.

As outlined in Chapter 2, the empirical observability Gramian maps the input-to-state and state-to-output behavior of a nonlinear system more accurately than the observability Gramian found by linearization [127] and is defined by (2.15). In this application we assess the observability of the Rankine flowfield parameters $\mathbf{\Omega}$. To perform this analysis, we augment the vehicle dynamics (5.1) with the (time-invariant) flowfield

parameter states $\mathbf{\Omega}$ and perform perturbations only on the flowfield parameter states. Following (2.15), the empirical observability Gramian $W_O \in \mathbb{R}^{3\times 3}$ is a Hermitian matrix that captures the sensitivity of measurements to perturbations in the flow, where the measurements are dictated by the formation parameters $\boldsymbol{\chi}$.

Calculating the empirical observability Gramian via integration of (5.1) with particle dynamics (3.2) reveals the input-output observability of the flowfield parameters $\mathbf{\Omega} = (r_{max}, v_{max}, \mu)$ over a given particle trajectory. The steering control input $\nu_k(\mathbf{x}; \boldsymbol{\chi})$ given by (3.77) dictates the sampling trajectory and is designed to stabilize candidate sampling formations. The perturbation size is chosen to be a fixed percentage of the nominal state size. For example, a 20% perturbation for $r_{max} = 30$ is $\epsilon_1 = 6$.

In a known flowfield, a set of sampling parameters $\boldsymbol{\chi}$ produces a corresponding unobservability index $\xi(\boldsymbol{\chi})$ calculated from (2.20), and the empirical observability Gramian (2.15). The optimal trajectory is found by optimizing over the space of sampling parameters

$$\boldsymbol{\chi}^* = \text{argmin } \xi(\boldsymbol{\chi}). \tag{5.5}$$

Since this optimization technique iterates over the low-dimensional sampling parameter space, rather than the space of all possible sampling trajectories, it can be computed rapidly even by an exhaustive search.

Figure 5.4 shows analysis of circular trajectory optimization in the Rankine vortex (3.34). Here, the sampling parameter space $\boldsymbol{\chi} = (|c_0|, 10)$ is the set of circular formation center distances $|c_0|$ from the origin, assuming circular formations of radius $|\omega_0|^{-1} = 10$. Figure 5.4(a) shows the log of the unobservability index as a function of the sampling parameter $|c_0|$. Figure 5.4(b) shows four sampling trajectories corresponding to the red data points of Figure 5.4(a). In each case, the initial position of the vehicle is located

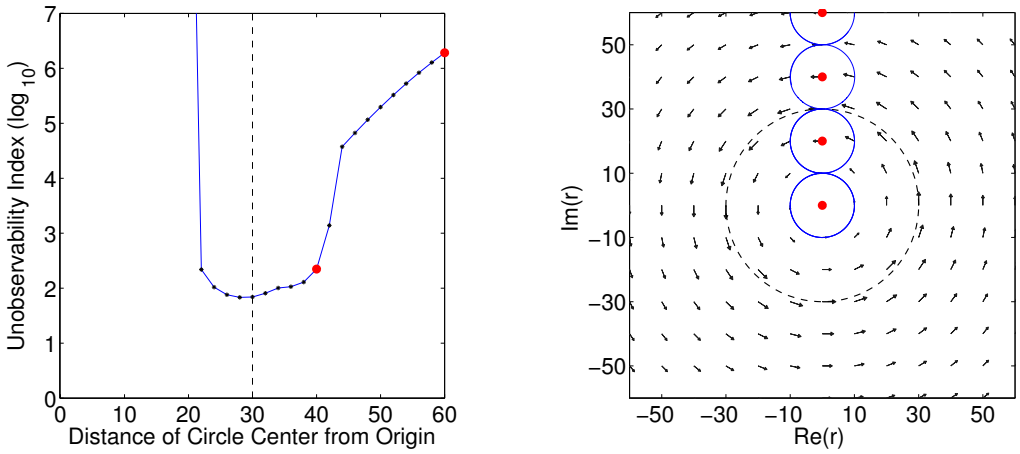


(a) (b)

Figure 5.4: (a) Unobservability index versus distance of circular sampling formation from vortex origin. (b) An illustration of candidate sampling formations. The red circle centers at $y = 40$ and $y = 60$ correspond to the red data points of (a).

on the desired circle to eliminate the effect of transient behavior on the unobservability analysis. The flowfield parameters are $\mathbf{\Omega} = (30, 0.6, 0.8)$. $r_{max}$ is shown by the dashed line in both figures. Notice that the unobservability is minimized by traveling in a circle with $|c_0|^* = 28$. For $|c_0| < 20 = r_{max} - |\omega_0|^{-1}$ the unobservability index is infinite because the flowfield parameter $\mu$, corresponding to the decay in flowspeed outside of $r_{max}$, is unobservable, i.e. $\sigma_{min} = 0$. For $|c_0| > 40$ the parameters are less observable because the flow strength decreases exponentially outside the radius of maximum wind.

The analysis illustrated in Figure 5.4 reveals that the unobservability is significantly decreased by crossing $r_{max}$, which is intuitive since this spatial region contains contributions from all flow parameters in the observations. Measurements obtained by sampling only inside $r_{max}$ fail to capture perturbations in the decay constant $\mu$ and measurements obtained by sampling only outside $r_{max}$ have more difficulty identifying the correct combination of $r_{max}$ and $v_{max}$. Extending this analysis to circular formations of varying

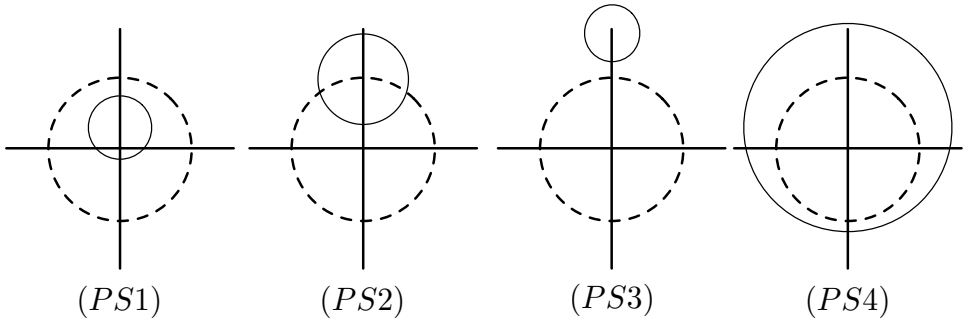


Figure 5.5: Pattern subsets associated with a circular sampling formation in a Rankine vortex. The dashed line represents $r_{max}$. Only pattern subset 2 (PS2) crosses the radius of maximum wind.

position and radius ($\boldsymbol{\chi} = (|c_0|), |\omega_0|^{-1}$), one expects pattern subsets to emerge within the parameter space, dictated by crossing of $r_{max}$.

Figure 5.5 shows four pattern subsets of the sampling parameter space we expect to provide significantly different observability. Pattern subset #1 ($PS1$) contains circular trajectories that lie entirely inside $r_{max}$, whereas $PS2$ trajectories cross $r_{max}$. $PS3$ lies entirely outside $r_{max}$ and $PS4$ contains $r_{max}$. Since the Rankine vortex model is radially symmetric, the circle centers are depicted as being constrained to the $y$-axis, without loss of generality.

Figure 5.6 shows the results of unobservability analysis over $\boldsymbol{\chi} = (|c_0|, |\omega_0|^{-1})$, in which the parameter-space boundaries of the pattern subsets are evident. The flowfield is parameterized by $\boldsymbol{\Omega} = (30, 0.6, 0.8)$. Figure 5.6(a) depicts example trajectories from within each subset as well as the subset boundaries, which we calculate analytically by considering the geometry of Figure 5.5. Figure 5.6(b) shows the unobservability index over the parameter space. In both figures $|c_0|$ and $|\omega_0|^{-1}$ are normalized by $r_{max}$.

Note that, as predicted, areas of low unobservability correspond to trajectories crossing $r_{max}$ ($PS2$), whereas highly unobservable trajectories remain entirely inside ($PS1$) or

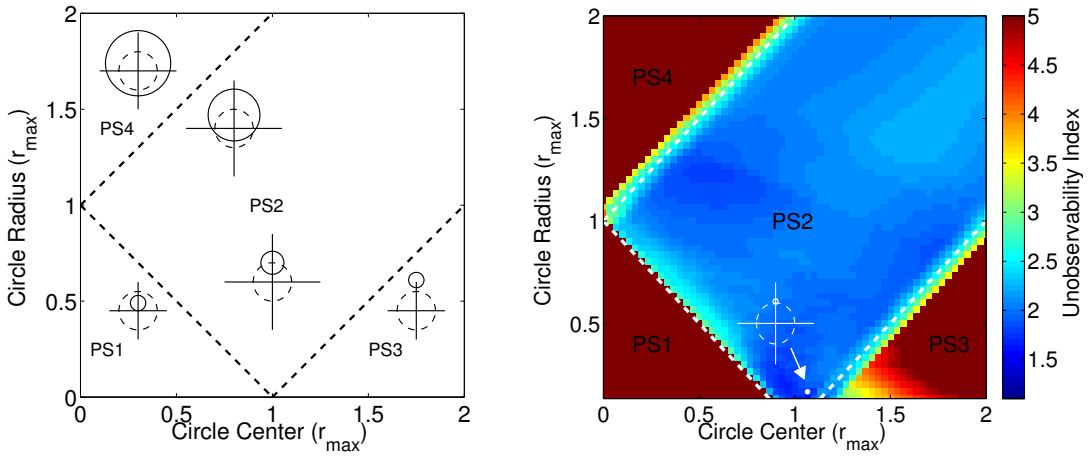


(a) (b)

Figure 5.6: Observability of a Rankine vortex characterized by $\mathbf{\Omega} = (30, 0.6, 0.8)$ using a circular sampling pattern. (a) Pattern subsets over the parameter space $\boldsymbol{\chi} = (|c_0|, |\omega_0|^{-1})$ normalized by $r_{max}$; (b) the unobservability index $\xi(\boldsymbol{\chi})$ with minimum denoted by the white dot.

outside $(PS4)$ $r_{max}$. Trajectories in pattern subset $(PS3)$ are less observable than $(PS2)$, but more observable than $(PS1)$ and $(PS4)$. The minimum of the unobservability index is denoted by the white dot in Figure 5.6(b), along with a scaled image of the optimal trajectory, which is a small circular formation centered near $r_{max}$. Note that Figure 5.6 corresponds to the flowfield parameters $\mathbf{\Omega} = (30, 0.6, 0.8)$. In general, varying $v_{max}$ and $\mu$ produces slight changes in the minimum of the unobservability index but has little effect on the pattern subset structure. $r_{max}$ defines the pattern subsets and is therefore the dominant parameter driving the pattern subset structure.

## 5.3 Observability-based Adaptive Sampling Framework in an Estimated Flowfield

In this section we combine the results of Sections 5.1 and 5.2 in an optimal sampling algorithm and provide numerical simulations of vehicles traveling in both moderate and

strong Rankine vortices. We use the recursive Bayesian filter to estimate the flowfield parameters, which are utilized to calculate vehicle steering controls and determine optimal sampling parameters over time interval $T_{opt}$. The multi-vehicle control algorithm (3.77) is implemented using the flowfield estimate and the optimal sampling parameters, such that vehicles are steered to trajectories with optimal observability.

The sampling algorithm proceeds as follows. First, the probability density function for the flowfield parameters $\mathbf{\Omega}$ is initialized either uniformly within known bounds or from a known prior distribution. The maximum of the probability density function corresponds to the initial flowfield parameters $\hat{\mathbf{\Omega}}(0)$ upon which the initial flowfield estimate $\hat{f}_k = f(r_k; \hat{\mathbf{\Omega}}(0))$ is based. The initial flowfield parameter estimate is utilized to calculate $W_O(\boldsymbol{\chi})$ using (2.15) over a time horizon $T_{opt}$ and sampling parameters $\boldsymbol{\chi}$. (Note that in this step the transient behavior of the vehicles as they converge to the formation $\boldsymbol{\chi}$ is taken into account and can significantly affect the unobservability index; the initial positions of each particle are used to calculate (2.15).) The choice of $T_{opt}$ depends on the expected accuracy of the flowfield estimate. For instance, one may choose $T_{opt}$ to be relatively short initially since the vehicles have yet to collect measurements. In this work, we assume a constant horizon time.

The optimal sampling parameters $\boldsymbol{\chi}^*$ over $T_{opt}$ found using (5.5) are implemented in the control algorithm (3.6), with $\nu_k = \nu_k(\mathbf{r}, \hat{f}_k; \boldsymbol{\chi}^*)$, where $\nu_k$ is given by (3.77). The control steers vehicles to a circular formation parameterized by $\boldsymbol{\chi}^*$. Each particle travels with closed-loop feedback control collecting noisy measurements $\tilde{\boldsymbol{\beta}}_k(t)$ and using the flowfield estimate $\hat{f}_k = f(r_k; \hat{\mathbf{\Omega}}(t))$ in its decentralized control. After time $T_{opt}$ has elapsed, the process is repeated on $T_{opt}$ intervals to update the set of optimal sampling parameters $\boldsymbol{\chi}^*$ from the new flowfield parameter estimate $\hat{\mathbf{\Omega}}(t)$ until the mission completes. An

**Table 1 Observability-based Sampling Algorithm**.

**Inputs:** Probability density $p(\hat{\boldsymbol{\Omega}}(t)|\tilde{\boldsymbol{\beta}}(0))$ and initial flowfield estimate $\hat{\boldsymbol{\Omega}}(0)$; initial control parameters $\boldsymbol{\chi}(0)^*$ and initial vehicle positions; time interval $T_{opt}$ and $T_{final}$.

**for** $t \leq T_{final}$ **do**

1: Generate flowfield using estimated parameters, $\hat{f}_k(t) = \vec{f}(r_k(t); \hat{\boldsymbol{\Omega}}(t))$ for $k = 1, \ldots, n$ vehicles.

2: Use the estimated flowfield and the current optimal sampling parameters to calculate the steering control $\nu_k(t) = \nu(\mathbf{r}, \hat{f}_k(t); \boldsymbol{\chi}^*)$.

3: Update the flowfield parameter estimate by assimilating measurements, so that $\hat{\boldsymbol{\Omega}}(t) = \sup p(\hat{\boldsymbol{\Omega}}(t)|\mathbf{A}(t))$.

**if** $t \bmod T_{opt} = 0$ **then**

4: Find the optimal sampling parameters over the observability iteration time using the current particle positions and current flowfield parameter estimate,

$\boldsymbol{\chi}^* = \operatorname{argmin} \xi(\boldsymbol{\chi}; \hat{\boldsymbol{\Omega}}(t), T_{opt})$.

**end if**

5: Set $t = t + \Delta t$

**end for**

overview of the sampling algorithm is shown in Table 1. Figure 5.7 shows the general block diagram in Figure 5.3, including the observability optimization block as well as added feedback connections where state and estimate information is shared. In Figure 5.7 the flow measurement and vehicle dynamics blocks from Figure 5.3 are merged.

Though the adaptive algorithm of Table 1 steers vehicles to formations improving observability, stability of the algorithm is inherently dependent on both convergence of the flowfield estimates to the true values and the choice of the optimization horizon time. Poor flowfield estimates may cause the vehicles to diverge from the desired formation or cause the observability optimization to steer the vehicles to optimal formations with respect to

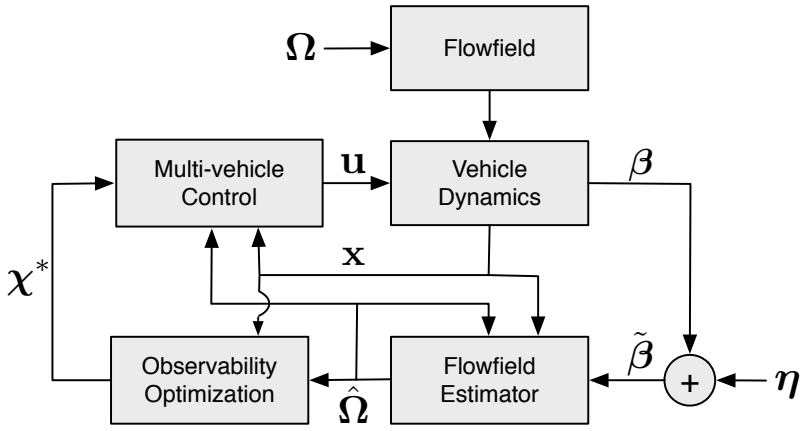


Figure 5.7: A schematic diagram of the observability-based sampling algorithm. A recursive Bayesian filter provides flowfield parameter estimates $\hat{\mathbf{\Omega}}$. The estimated flowfield parameters are used to calculate optimal control parameters $\boldsymbol{\chi}^*$ that characterize the multi-vehicle sampling formation.

an incorrectly estimated flowfield.

Proving stability of the recursive filter is dependent both on the magnitude of noise present in the measurements as well as the trajectories traversed by the vehicles, which is a difficult problem worthy of future research. In addition to stability of the filtering algorithm, one must choose the horizon time $T_{opt}$ such that the vehicles have sufficient time to achieve the formation or run the risk of never overcoming transient behavior.

If one assumes the flowfield is known, several works have addressed the stability of formations with time-varying centers and radial parameters. Peterson [42] and Paley [23], [147] established asymptotic stability of circular formations with time-varying circle center positions in a uniform flowfield. Similarly, Arranz et al. [148], [21], [17] established stability conditions that, when met, prove convergence of multi-vehicle motion to circular formations with time-varying circle center position and radius in a flow-free setting. The adaptive algorithm is similar to previous work in that the circle center position and radius

vary in time; however, the algorithm differs in that step inputs to the formation parameters are applied rather than the continuously differentiable formation inputs of the previous work. We leave it to future work to establish stability of the algorithm in terms of the optimization horizon time.

## 5.4 Simulation Results and Analysis

This section illustrates simulations of the adaptive sampling algorithm in a Rankine vortex. Without loss of generality, we consider a collection of $n = 5$ vehicles sampling in a Rankine vortex parameterized by $r_{max} = 30$ and $\mu = 0.8$ for all simulations. Sections 5.4.1 and 5.4.2 consider a moderate flowfield with $v_{max} = 0.6$ to evaluate the adaptive sampling algorithm in flows where all formation parameters are feasible, whereas Section 5.4.3 considers a strong flow characterized by $v_{max} = 1.2$. The duration of each sampling mission was 1350 time units with observability iteration occurring every $T_{opt} = 150$ time units, resulting in nine iterations of the observability-optimization routine.

### 5.4.1 Optimization of Formation Position

We begin by optimizing over the parameter $|c_0|$ dictating the distance of the circle center from the origin of the vortex, assuming $|\omega_0|^{-1} = 10$ is the fixed circle radius such that $\boldsymbol{\chi} = (|c_0|, 10)$. Figure 5.8 illustrates simulation of the observability-based sampling algorithm estimating the unknown flowfield parameters $\boldsymbol{\Omega} = (r_{max}, v_{max}, \mu)$ of the Rankine vortex model (3.34). The probability density function was initialized uniformly over the parameter space $r_{max} \in [0, 100]$, $v_{max} \in [0, 1]$, and $\mu \in [0, 1]$, and the initial flowfield parameter estimate was selected randomly from the parameter space.

Figure 5.8(a) shows the vehicle trajectories over the course of the simulation. Fig-

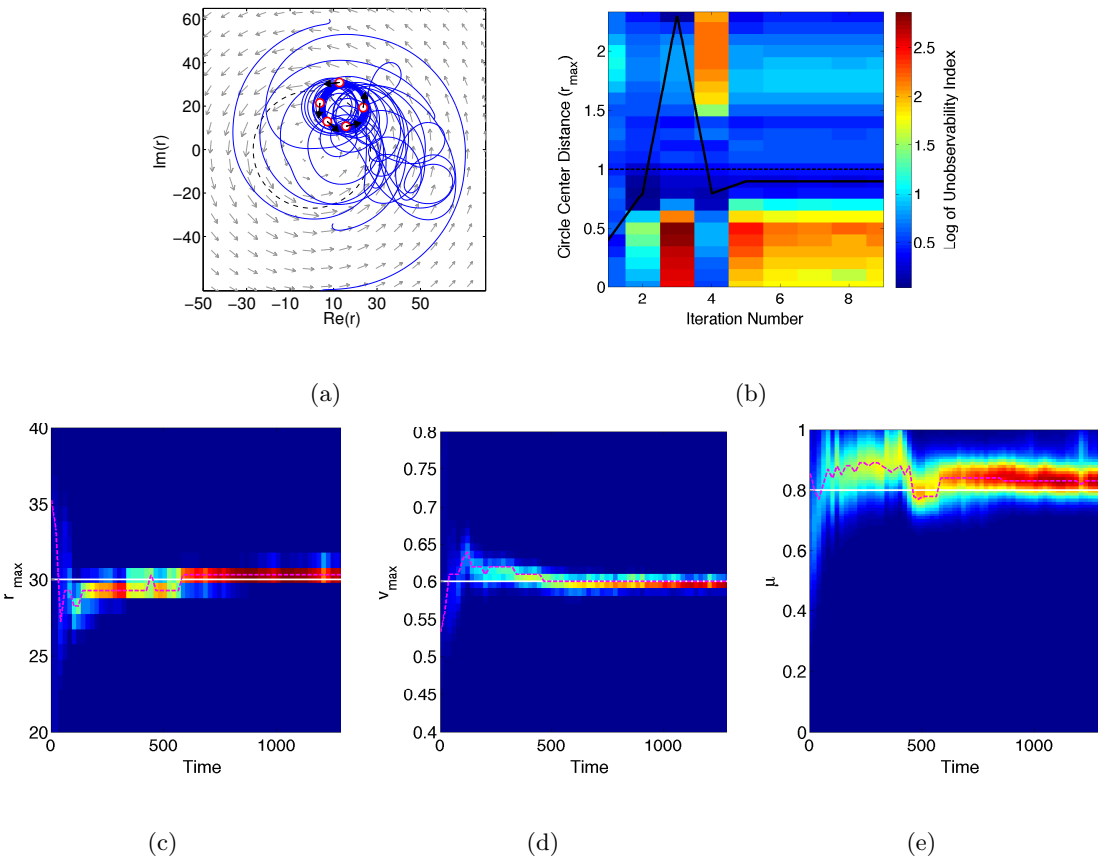


Figure 5.8: Simulation results of the adaptive sampling algorithm optimizing the circle center distance $|c_0|$ for fixed circle radius $|\omega_0|^{-1} = 10$ using estimates of the flowfield. (a) Vehicle trajectories; (b) circle center position and observability analysis; (c)-(e) marginal probability densities of the recursive Bayesian filter.

ure 5.8(b) shows the optimal formation parameter $|c_0|$ plotted for each iteration of the observability optimization procedure, normalized by the radius of maximum wind $r_{max}$. The solid black line shows the optimal circle center distance after each iteration, whereas the dashed black line corresponds to a formation centered at $r_{max}$. The underlying color plot illustrates log of the unobservability index for all circle center positions after each iteration. Note that the circle center distance reaches a steady-state value of $|c_0| = 0.9r_{max}$ after four iterations of the unobservability optimization.

Figures 5.8(c), 5.8(d), and 5.8(e) show marginal probability densities[2] of the flowfield parameters $r_{max}$, $v_{max}$, and $\mu$ versus time. In each figure the solid white line corresponds to the ground truth parameters, whereas the dashed magenta line corresponds to the estimate. Note that the estimate from the recursive Bayesian filter converges around the true flowfield parameters.

Note in Figure 5.8 that after a few iterations the circle center is attracted toward formations that cross radius of maximum wind, consistent with the analysis of Figure 5.4. To further investigate the attractive properties of the $r_{max}$ in the adaptive sampling algorithm, Figure 5.9 illustrates the result of four hundred simulations optimizing the circle center position $|c_0|$ with fixed circle radius $|\omega_0^{-1}| = 10$, normalized by $r_{max} = 30$. In each simulation, we initialize the vehicle positions randomly within the domain. The blue line denotes the average circle center position over all simulations for each iteration of the optimization procedure. The shaded gray area denotes one standard deviation of all simulations at each iteration, whereas the dashed black line indicates $|c_0| = r_{max}$. Note that the average observability-optimal circle center position is attracted toward $r_{max}$ as predicted by the analysis of Section 5.2 and the standard deviation decreases with successive iterations of the optimization routine.

### 5.4.2 Optimization of Formation Position and Radius in a Moderate Flowfield

In this example we optimize over the full parameter space defining the circular sampling family $\boldsymbol{\chi} = (|c_0|, |\omega_0|^{-1})$ using the adaptive sampling algorithm in Table 1 and $n = 5$ vehicles. Figure 5.10 illustrates results of the observability-based adaptive sampling algorithm. Figure 5.10(a) shows the sampling trajectories taken by each vehicle over

[2]The marginal probability density is achieved by summing a multi-dimensional probability density over a set of dimensions.

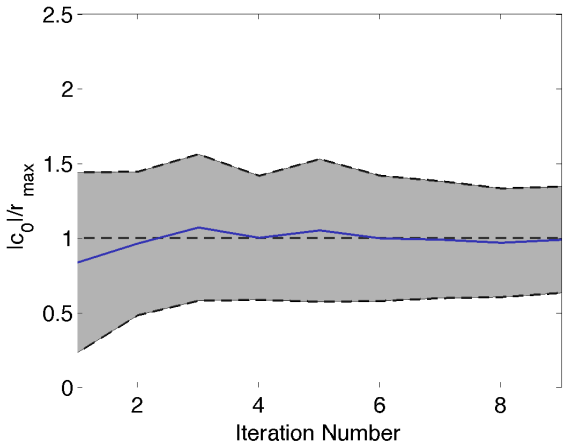


Figure 5.9: The average optimal circle center position (blue) plotted versus the iteration number of the adaptive algorithm over four hundred simulations. Note the circle center is attracted toward $r_{max}$. The gray area denotes one standard deviation of circle center positions over all simulations.

the course of the sampling mission. Figure 5.10(b) shows marginal probability densities of $r_{max}$, $v_{max}$, and $\mu$, respectively. In each figure the solid white line denotes the true parameter values, whereas the dashed magenta line denotes the parameter estimates over time.

Figures 5.10(c) and 5.10(d) illustrate the result of nine iterations of the observability optimization routine. In Figure 5.10(c), each surface illustrates the unobservability index over the space of circle center positions and circle radii, normalized by the radius of maximum wind $r_{max} = 30$. The solid black line shows the optimal parameter values over the course of the simulation. The dashed black line denotes $r_{max}$ projected on the $|\omega_0|^{-1} = 0$ plane. Figure 5.10(d) shows the circle center distance $|c_0|$, and circle radius $|\omega_0|^{-1}$ over each iteration. In each figure the solid black line denotes the observability-optimal parameters normalized by $r_{max}$, whereas the dashed black line denotes $r_{max}$. Note the algorithm is attracted toward parameters that produce formations crossing $r_{max}$, which

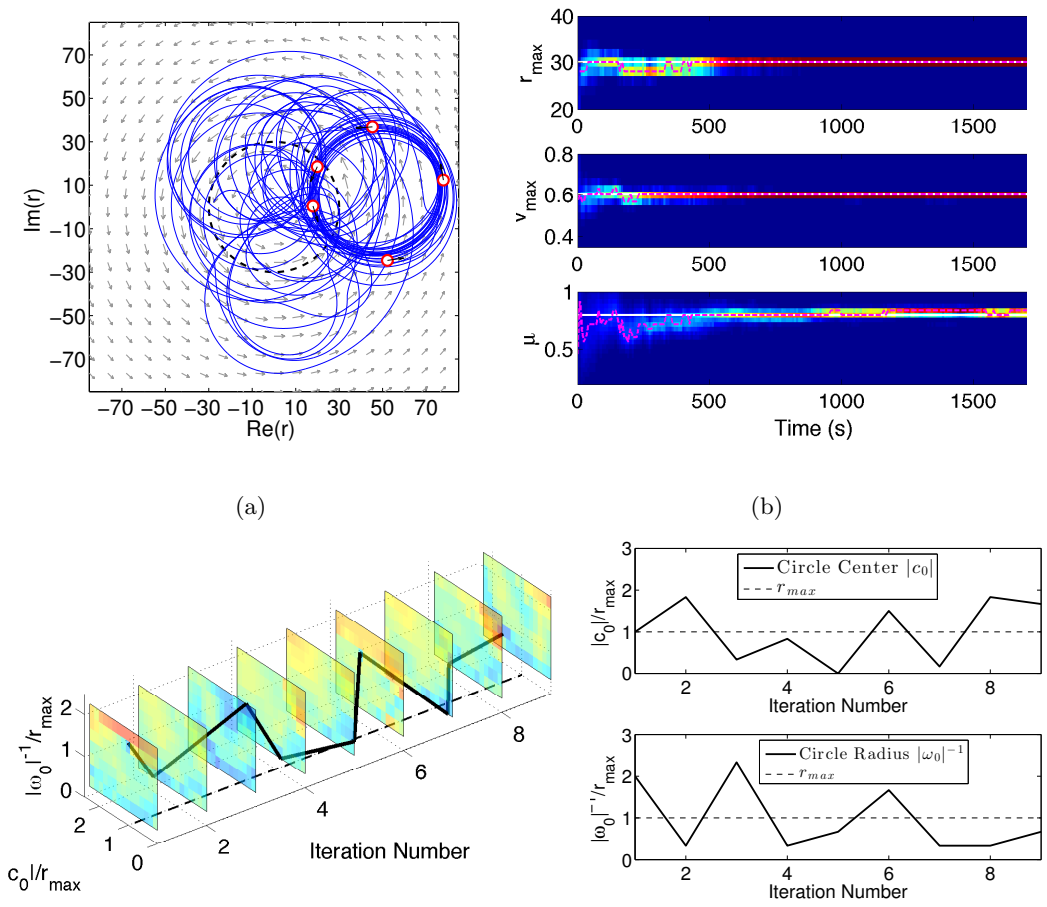


Figure 5.10: Simulation results of the adaptive sampling algorithm optimizing the circle center distance $|c_0|$ and circle radius $|\omega_0|^{-1}$ using estimates of the flowfield. The algorithm is attracted toward formations that cross $r_{max}$.

is in agreement with the analysis of Section 5.2.

Performing four hundred simulations of the algorithm, we see a trend similar to Section 5.4.1 that the circle center distance $|c_0|$ is attracted toward $|c_0| = r_{max}$. Interestingly, the radius of the circular formation also tends toward $r_{max}$. Figure 5.11(a) illustrates the optimal circle center distance and radius averaged over four hundred simulations of the adaptive sampling algorithm (blue line). The gray tube represents one standard deviation of all simulations, whereas the dashed black line illustrates the radius of maximum wind.

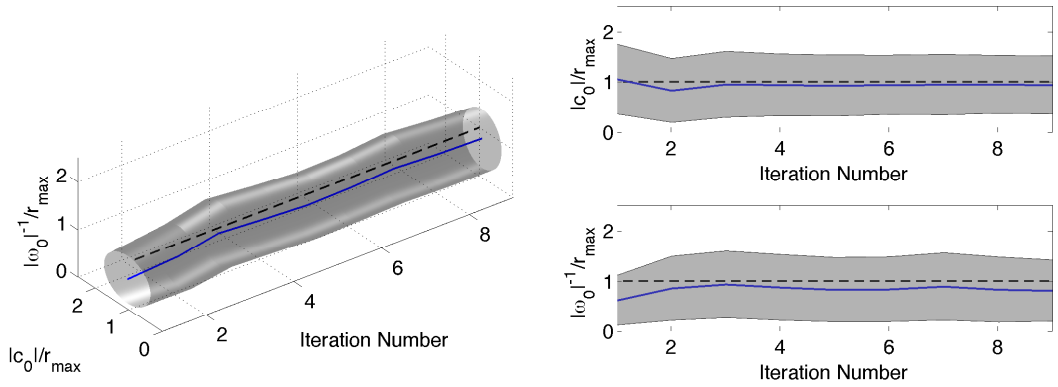


(a) (b)

Figure 5.11: The optimal circle center position $|c_0|$ and radius $|\omega_0|^{-1}$ normalized by $r_{max} = 30$ and plotted versus the iteration number of the adaptive algorithm over four hundred simulations. Note the circle center and radius tend toward $r_{max}$. The shaded regions denote one standard deviation of all simulations.

Each quantity is normalized by the radius of maximum wind $r_{max} = 30$. Figure 5.11(b) shows circle center position and circle radius plotted individually versus the iteration number. Note the circle center distance and formation radius tend toward $r_{max}$. Moreover, the circle radius is biased toward $|\omega_0|^{-1} < r_{max}$ since the standard deviation tends toward circular formations with radius less than $r_{max}$ rather than those with larger radii.

### 5.4.3 Optimization of Formation Position and Radius in a Strong Flowfield

As a final example we simulate the adaptive sampling algorithm of Table 1 in a Rankine vortex whose maximum flowspeed exceeds that of the vehicle. In this case, a subset of the sampling parameter space $\boldsymbol{\chi}$ becomes infeasible since vehicles cannot maintain forward progress at all areas in the flow. Therefore, we perform observability analysis over the space of *feasible* sampling parameters with respect to the flowfield estimate $\hat{\boldsymbol{\Omega}}$ in the optimization routine.

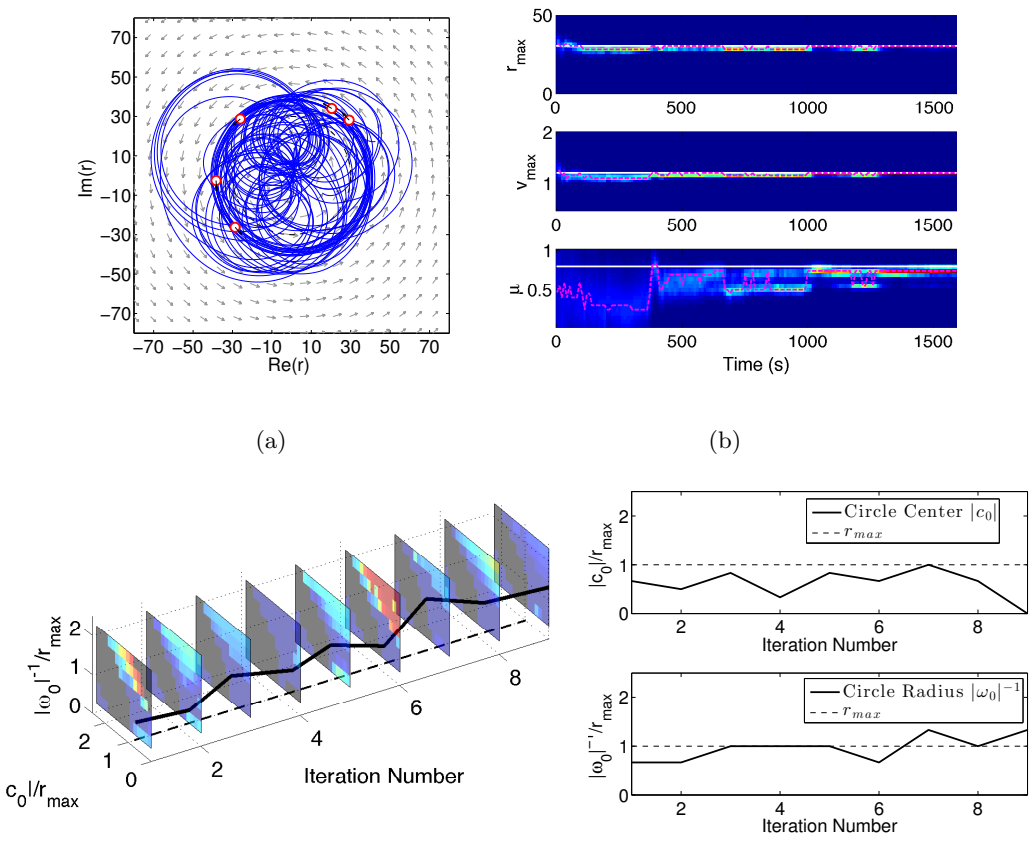


Figure 5.12: Simulation results of the adaptive sampling algorithm optimizing the circle center distance $|c_0|$ and circle radius $|\omega_0|^{-1}$ in a strong Rankine vortex. In a strong flowfield a subset of the sampling parameter space is infeasible, shown by the black regions in the observability analysis of (c).

Figure 5.12 illustrates simulation results of the observability-based sampling algorithm in a strong Rankine vortex parameterized by $\mathbf{\Omega} = (30, 1.2, 0.8)$. Figure 5.12(a) shows the vehicle trajectories over the duration of the sampling algorithm. Figure 5.12(b) illustrates marginal probability densities of the recursive Bayesian filter. The solid white line illustrates the true flowfield parameters, whereas the dashed magenta line denotes the parameter estimates.

Figure 5.12(c) shows the unobservability index plotted over the sampling parameter

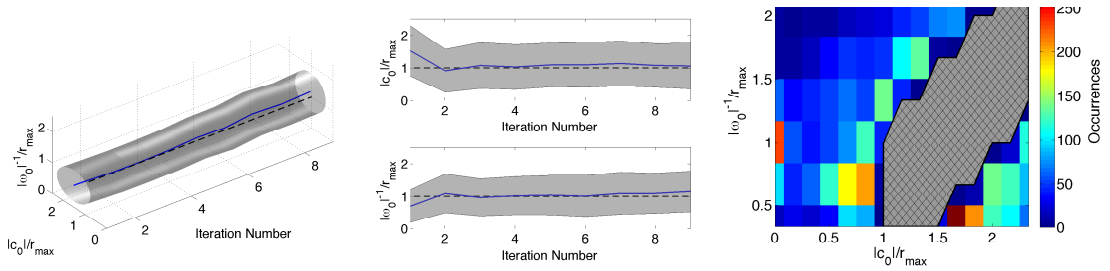


(a) (b) (c)

Figure 5.13: The optimal circle center position $|c_0|$ and radius $|\omega_0|^{-1}$ normalized by $r_{max} = 30$ and plotted versus the iteration number of the adaptive algorithm over four hundred simulations. The shaded regions in (a)-(b) denote one standard deviation of all simulations. (c) A histogram of the optimal sampling parameters $\boldsymbol{\chi}^*$ over all simulations.

set $\boldsymbol{\chi} = (|c_0|, |\omega_0|^{-1})$ for each iteration of the sampling mission. Each surface corresponds to the unobservability index of the parameter set $\boldsymbol{\chi}$ at each iteration. The parameter combinations shown in black were deemed infeasible based on the estimated flowfield parameters. Figure 5.12(d) shows the desired circle center offset $|c_0|$ and circle radius $|\omega_0|^{-1}$ plotted over the sampling mission, normalized by $r_{max} = 30$. Note, unlike simulations in the moderate flow regime, the circle center distance $|c_0|$ remains inside $r_{max}$ in this simulation.

Figure 5.13 illustrates results of a Monte Carlo simulation over four hundred iterations of the adaptive sampling algorithm in the strong Rankine vortex. Analogous to Figure 5.11, Figures 5.13(a) and 5.13(b) illustrate the mean circle center position and circle radius with the gray shaded area representing one standard deviation over all simulations. Note that in the strong flow the average circle center tends toward $r_{max}$. Compared to the moderate flow case, the radius tends to be larger to accommodate feasibility constraints in the strong flow. Figure 5.13(c) shows a histogram of all iterations of the sampling algorithm, over all four hundred simulations. The cross-hatched region corresponds to

infeasible circle center and radius combinations. Since the feasibility analysis is based on the estimated flowfield parameters, it is possible for the algorithm to select infeasible elements of the parameter space. Over all simulations, less than five percent of iterations were infeasible with respect to the true flowfield. Note that the observability analysis is attracted toward circle centers slightly less than or larger than those that are infeasible. Many iterations are also attracted toward a circle centered at the vortex origin with radius equal to $r_{max}$, illustrated by the red entry at the parameter space coordinate $\boldsymbol{\chi} = (0, r_{max})$. Interestingly, very few iterations correspond to large circle centered at the origin

# Chapter 6: Application: Wake Tracking in Close Formation Flight

As airspaces of the world grow congested with manned and unmanned aircraft, closely coordinated multi-aircraft formations may provide a method of organizing the sky. Before such benefits can be realized for autonomous systems, individual vehicles must have reliable methods to sense other aircraft in the formation. This chapter proposes a method of sensing using the aerodynamic effects caused by aircraft flying in close proximity. We consider a two-aircraft leader-follower formation and use nonlinear observability, estimation, and control techniques of Chapter 2 to enable the follower to estimate the lead aircraft's wake and to position itself at a desired location relative to the leader. The control and estimation designs are applied to instances of close formation flight including aerial refueling and positioning for increased aerodynamic efficiency.

## 6.1 Aerodynamic Model of Two-Aircraft in Close Formation

This section develops an aerodynamic model of a follower aircraft flying in a lead aircraft's wake, similar to that of Hemati et al. [68] and Pachter et al. [60] Consider two aircraft in steady level flight through an inviscid, incompressible, irrotational fluid. Let the reference frame $\mathcal{B} = (O, \boldsymbol{b}_1, \boldsymbol{b}_2, \boldsymbol{b}_3)$ with origin $O$ be centered at the leading edge of the follower aircraft's wing with basis vectors $\boldsymbol{b}_1, \boldsymbol{b}_2$, and $\boldsymbol{b}_3$ as shown in Figure 6.1(a). Assume the follower aircraft maintains kinematic control of its vertical and horizontal velocities such that the velocity of frame $\mathcal{B}$ with respect to the lead aircraft in steady level flight

is $\mathbf{V}_f = V_y\mathbf{b}_2 + V_z\mathbf{b}_3$ (the $\mathbf{b}_1$ component is assumed to be zero). The lead aircraft has wingspan $b$ and the position of its center of mass is $\boldsymbol{r}_L = x_L\boldsymbol{b}_1 + y_L\boldsymbol{b}_2 + z_L\boldsymbol{b}_3$ relative to $O$. Assume $|x_L|$ is sufficiently large (greater than two wingspans [60]) such that the wake of the lead aircraft is adequately represented using potential flow theory as the sum of two infinite line vortices. The vortices extend horizontally behind the wingtips of the lead aircraft along the $\boldsymbol{b}_1$ direction with circulation strength $\Gamma_L$. The Biot-Savart law gives the following vertical component of the wake [57], [60], [68] at a point $(x, y, z)$ along the $\boldsymbol{b}_2$ axis ($x = z = 0$) as a function of the lead aircraft position[1]:

$$w_L(y; \Gamma_L, y_L, z_L, b) = \frac{\Gamma_L(y-y_L-b/2)}{2\pi(z_L^2+(y-y_L-b/2)^2)} - \frac{\Gamma_L(y-y_L+b/2)}{2\pi(z_L^2+(y-y_L+b/2)^2)}. \tag{6.1}$$

Note that equation (6.1) is symmetric about $z_L$. This occurrence necessitates use of a second sensing modality to break the vertical symmetry, which is discussed later. The aerodynamic signature on the follower aircraft created by the upwash field of the lead aircraft is used to estimate the position $\mathbf{r} = (y_L, z_L)$ of the leader relative to the follower and the circulation strength $\Gamma_L$ of the lead aircraft wake. The position estimate $\hat{\mathbf{r}}$ is used in an optimal controller to steer the follower aircraft to a desired relative position.

To model the flow around the follower aircraft in response to the upwash field of the lead aircraft, we employ the lifting-line solution, following that of Katz and Plotkin [63, pp. 331–340]. The follower aircraft is represented by a thin, flat, rectangular wing with large aspect ratio ($\mathcal{AR} > 4$) and chord length $c$ as shown in Figure 6.1(b). (Note this method is capable of modeling more sophisticated wing geometries, including wing sweep and dihedral [63].) Since the fluid is inviscid, incompressible, and irrotational its motion can be represented by the gradient of a potential function $\Phi$ that satisfies Laplace's equation

[1]For simplicity we ignore the sidewash field, assuming sensors mounted flush on the wing surface are unable to detect sidewash.

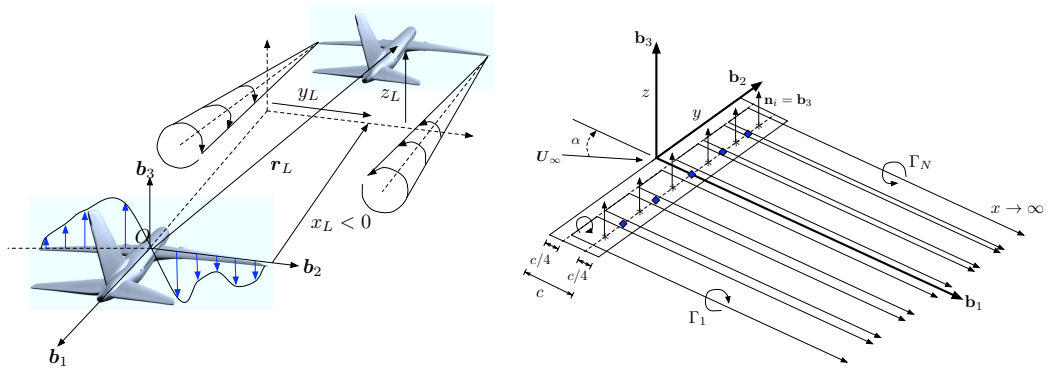


(a) (b)

Figure 6.1: Leader and follower aircraft representations. (a) The wake of the lead aircraft produces an aerodynamic signature on the follower aircraft through its upwash field (blue). (b) Horseshoe vortices are used to model the flow around a finite, slender wing with large aspect ratio, $\mathcal{AR} > 4$.

[63]

$$\nabla^2 \Phi = 0. \tag{6.2}$$

In addition, at every point on the wing the potential function must satisfy the boundary-value constraint, which ensures that there is no flow normal to the wing surface. Assuming the wing is thin, its normal vector $\mathbf{n}_i$ at any point $(x_i, y_i, z_i)$ on the wing surface is approximately $\mathbf{n}_i \approx \mathbf{b}_3$, which implies

$$\nabla \Phi \cdot \mathbf{b}_3 = 0, \tag{6.3}$$

as shown in Figure 6.1(b). To satisfy these constraints, lifting-line theory uses a collection of line vortices to represent a suitable potential function. $D$ equally spaced horseshoe vortices are bound to the quarter chord of the wing such that $2D$ trailing vortices extending infinitely downstream. The $k$th bound horseshoe vortex has circulation strength $\Gamma_k$ as shown in Figure 6.1(b). The number $D$ of horseshoe vortices must be chosen large enough for adequate model fidelity, yet small enough to remain computationally tractable. The

freestream fluid velocity $\mathbf{U}_\infty$ has magnitude $U_\infty$ and angle of attack $\alpha$ relative to the wing. (Assume the freestream velocity has zero sideslip and $\alpha$ is small.)

The line vortex is a solution to Laplace's equation [63] (6.2), implying that the flow due to the freestream velocity, lead aircraft upwash, and horseshoe vortices must satisfy the normal flow constraint (6.3). Therefore, (6.3) evaluated at any given point on the wing must satisfy

$$w_{hs} + w_L + V_z + U_\infty \sin\alpha = 0, \tag{6.4}$$

where $w_{hs}$ is the $\mathbf{b}_3$ component of the flow due to the collection of horseshoe vortices, $w_L$ is given by (6.1), $V_z$ is the $\mathbf{b}_3$ component of the inertial velocity of the follower aircraft expressed in frame $\mathcal{B}$, and the fourth term on the left-hand side is the normal component of the freestream velocity. Note that this model neglects aerodynamic influences due to aircraft pitching, rolling, and sideslip maneuvers, under the assumption that in close proximity these motions are negligible in comparison to the aerodynamic effect of vertical motion. (The inclusion of higher fidelity aircraft dynamics in the aerodynamic model is a worthy topic for ongoing research.)

The collocation method [63], [64] is used to solve for the horseshoe vortex strengths $\Gamma_k$ that satisfy (6.4). Following Katz and Plotkin [63, pp. 331-334], impose the constraint (6.4) at $D$ collocation points centered at each horseshoe vortex along the 3/4-chord line, as shown in Figure 6.1(b). Since the flow at any collocation point is linearly dependent on the circulation strength $\Gamma_k$ of the $k$th horseshoe vortex, (6.4) applied at the $D$ collocation points forms a set of $D$ linear algebraic equations with $D$ unknown circulation strengths

[63] $\Gamma_k$, $k = 1 \ldots, D$

$$\begin{bmatrix} a_{11} & \cdots & a_{1D} \\ \vdots & \ddots & \vdots \\ a_{D1} & \cdots & a_{DD} \end{bmatrix} \begin{bmatrix} \Gamma_1 \\ \vdots \\ \Gamma_D \end{bmatrix} = -(Q_\infty \sin\alpha + V_z) \begin{bmatrix} 1 \\ \vdots \\ 1 \end{bmatrix} - \mathbf{w}_L, \tag{6.5}$$

where $a_{ij} = \mathbf{v}_{ij} \cdot \mathbf{b}_3$ is the normal component of the flow $\mathbf{v}_{ij}$ at the $i$th collocation point due to the $j$th horseshoe vortex, $V_z$ is a control variable, and $\mathbf{w}_L$ is an $D \times 1$ column matrix formed by evaluating (6.1) at the $\mathbf{b}_2$ component of the $D$ collocation points. Since the horseshoe vortex nearest each collocation point has the largest influence, the solution is stable [63], which implies that the coefficient matrix is invertible and equation (6.5) can be solved for the circulation strength distribution $\Gamma_1, \ldots, \Gamma_D$.

Let $\Gamma_k = \Gamma(y_k)$ and $\Delta y = y_{k+1} - y_k$, for any $k \in \{1, \ldots, D-1\}$. The circulation strength distribution $\Gamma(y) = \lim_{\Delta y \to 0} \Gamma_k$ is used to calculate measurable quantities that can be used in the nonlinear wake estimation process. For example, Hemati, Eldredge, and Speyer [68], [69], [149] assume measurements of the differential pressure coefficient:

$$\Delta C_p(x, y) = \tfrac{-4\Gamma(y)}{\pi U_\infty c} \left(\tfrac{c}{x} - 1\right)^{1/2}. \tag{6.6}$$

For consistency, this chapter assumes measurements of differential pressure at the 3/4-chord line $x = 3c/4$ at five equally spaced positions along the span of the wing

$$\boldsymbol{\Delta C}_p = [\Delta C_{p_1}, \ldots, \Delta C_{p_5}]^T, \tag{6.7}$$

as shown by the blue squares in Figure 6.1(b). To break the $\pm z_L$ symmetry in (6.1), assume the follower aircraft is outfitted with a simple camera system or range finder that

provides a (noise-free) reading of the sign of $z_L$, i.e.,

$$\zeta(t) = \text{sgn}(z_L(t)) = \begin{cases} 1, & z_L(t) > 0 \\ 0, & z_L(t) = 0 \\ -1 & z_L(t) < 0. \end{cases} \tag{6.8}$$

Let $\mathbf{q}(\mathbf{\Omega}) = [\Delta C_{p1} \dots \Delta C_{p5}, \zeta(t)]^T$ be a $6 \times 1$ column matrix of five differential pressure measurements calculated using (6.6) at the collocation points in Figure 6.1(b) and one relative altitude measurement given by (6.8). The output equation $\boldsymbol{q}(\mathbf{\Omega})$ is combined with the lead aircraft dynamics in frame $\mathcal{B}$ to write the state-space form of the input-output relationship between the wake parameter states and the measurements. In the notation of Chapter 2, the state vector $\mathbf{x} = \mathbf{\Omega} = [y_L, z_L, \Gamma_L]^T \in \mathbb{R}^3$ has time derivative with zero drift term $\boldsymbol{h}(\mathbf{x}) = 0$ and control vector fields $\boldsymbol{g}_1(\mathbf{x}, u_1) = [-u_1, 0, 0]^T$, $\boldsymbol{g}_2(\mathbf{x}, u_2) = [0, -u_2, 0]^T$, where $u_1 = V_y$ and $u_2 = V_z$. This gives

$$\begin{aligned} \dot{\mathbf{x}} = \dot{\mathbf{\Omega}} &= \begin{bmatrix} -u_1 \\ -u_2 \\ 0 \end{bmatrix} \\ \boldsymbol{\beta} &= \mathbf{q}(\mathbf{\Omega}). \end{aligned} \tag{6.9}$$

The model (6.9) is used in subsequent sections to evaluate the observability of the state $\mathbf{\Omega}$ given the output equation $\boldsymbol{q}(\mathbf{\Omega})$, to design an observer to estimate $\mathbf{\Omega}$ from noisy output measurements, and to design an optimal controller for the follower aircraft.

## 6.2 Observability of Lead Aircraft Wake Parameters

This section assesses the observability of the wake parameters in the aerodynamic model of Section 6.1. This application seeks to observe the wake parameter states $\mathbf{\Omega} = [y_L, z_L, \Gamma_L]^T$ given the output equation $\boldsymbol{q}(\mathbf{\Omega})$. Equation (6.6) is dependent on $\mathbf{\Omega}$ indirectly

through the circulation strength distribution $\Gamma(y)$ of the horseshoe vortices, which motivates the need to quantitatively assess the observability of the desired parameters as part of the implementation of an observer-based controller.

Since the flow model in Section 6.1 is solved numerically, it is justified to pursue empirical techniques for calculating the observability Gramian of the nonlinear system [100], [150]. Moreover, by using numerical observability techniques, the analysis can be extended to higher fidelity state-space realizations of the aerodynamic model that more accurately capture the aerodynamic effects of the leader aircraft wake.

When applied to the two aircraft aerodynamic model (6.9), the $(i,j)$th component of the $3 \times 3$ empirical observability Gramian $\boldsymbol{W}_O$ is given by (2.15) [99] where the three dimensional state $\boldsymbol{\Omega}^{\pm i} = \boldsymbol{\Omega} \pm \epsilon_i \mathbf{e}_i$ produces the six dimensional output $\boldsymbol{\beta}^{\pm i} = \boldsymbol{q}(\boldsymbol{\Omega}^{\pm i})$. Measures of the observability of a nonlinear system are obtained by applying the unobservability index (2.20) and estimation condition (2.21) to $\boldsymbol{W}_O$.

In the context of the formation flight application, observability analysis provides a method of mapping "blind spots" (for $\mathbf{u}(t) = 0$) or "blind trajectories" (for $\mathbf{u}(t) \neq 0$) in which the follower aircraft may not be able to estimate the lead aircraft wake parameters because they are highly unobservable. To analyze the dependence of the unobservability index and estimation condition on the lead aircraft position, we evaluate the empirical observability Gramian (2.15) as a function of the stationary lead aircraft position in the ($\mathbf{b}_2$,$\mathbf{b}_3$) plane rather than along a predefined leader aircraft trajectory.

For simulation purposes, assume $D = 40$ horseshoe vortices are used to define the aircraft wing model. The wing dimensions and flight conditions are modeled after a C-17 aircraft ($b = 51.75$ meters, $\mathcal{AR} = 7.586$) at cruise $Q_\infty = 230.556$ m/s. All quantities are non-dimensionalized using wingspan and cruise speed, though, so they can be generalized

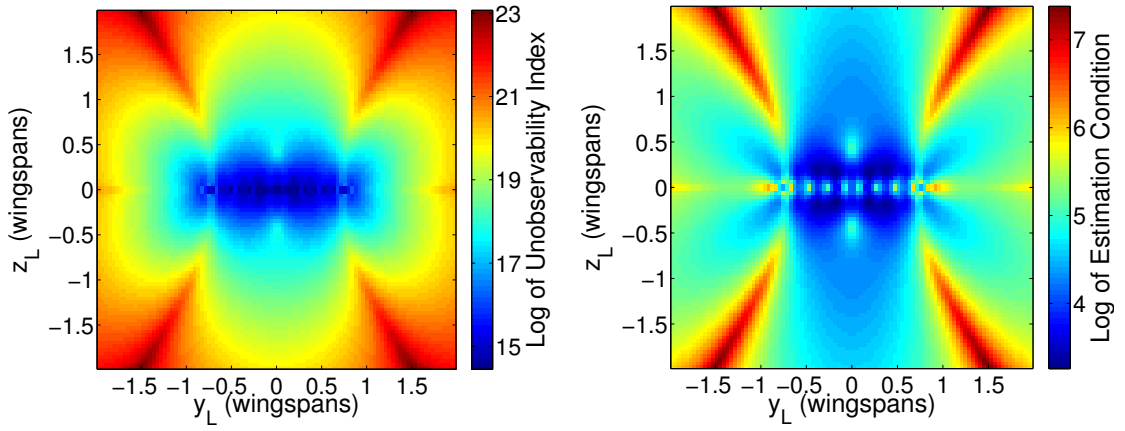


(a) (b)

Figure 6.2: The log of the (a) unobservability index and (b) estimation condition plotted versus the lead aircraft wake position.

to other aircraft, including unmanned ones.

At each relative position value $\mathbf{r} = [y_L \; z_L]^T$, the log of the observability measures (2.20) and (2.21) are shown in Figure 6.2. Note that the unobservability index in Figure 6.2(a) generally increases with increasing $||\mathbf{r}||$ and is symmetric in the ($\mathbf{b}_2$,$\mathbf{b}_3$) plane, which is expected due to the symmetries of the upwash model (6.1). Interestingly, pockets of high unobservability (poor observability) extend diagonally outward from the wing tips of the follower. A large degree of variability in observability is observed between one and two wingspans from the origin of the ($\mathbf{b}_2$,$\mathbf{b}_3$) plane. The unobservability index is nearly seven orders of magnitude larger two wingspans away than at the origin, implying that one can expect dramatically worse estimation performance as $\|\mathbf{r}\|$ increases, though this pattern is not radially symmetric.

It is also interesting to note that the singular value associated with the circulation strength parameter $\Gamma_L$ is the smallest singular value throughout the majority of the mapping in Figure 6.2(a). This implies that $\Gamma_L$ is the least observable state in $\mathbf{\Omega}$ and will be

the most difficult to estimate. Also note that the estimation condition in Figure 6.2(b) is large along diagonals outward from the wingtips, similar to the unobservability index. This indicates that in these areas the estimation problem is poorly conditioned and the smallest singular value is the dominant term in the estimation condition metric.

The following section describes the recursive Bayesian filter implementation used to estimate the lead aircraft parameters. By coupling the recursive estimation scheme with an observability-based optimal control algorithm, the follower aircraft maintains adequate observability over its trajectory. This guarantees performance of the filtering scheme because the estimated states will never become unobservable.

## 6.3 Bayesian Estimation of Lead Aircraft Wake Parameters

In previous work Hemati, Eldredge, and Speyer [68], [69] compared the performance of an extended Kalman filter and a particle filter in estimating the lead aircraft wake parameters [68]. Both nonlinear estimation methods suffered from filter divergence at specific initial conditions. Due to the fact that there are only a few states and each have a known, linear time dependence, the grid-based recursive Bayesian estimation scheme of Chapter 2 is selected for this application for its ease of implementation. The filter estimates the state vectors $\mathbf{\Omega} = [y_L \ z_L \ \Gamma_L]^T$, from which the differential pressure distribution (6.6) is reconstructed. The lead aircraft wake model (6.1) has kinematics that are modeled in nonlinear state-space form in (6.9). The recursive Bayesian filter update equation is given by (2.22), where in this application the motion model $p(\mathbf{\Omega}(t)|\mathbf{\Omega}(t{-}\Delta t))$ represents an operator that updates the probability density function from $t{-}\Delta t$ to $t$, [130, pp. 372-375] assuming known control inputs $\mathbf{u} = [V_y, V_z]^T$. The motion matrix is $\Psi = \Delta t \text{diag}([-V_y \ -V_z \ 0]^T)$ and $p(\mathbf{\Omega}(t)|\mathbf{\Omega}(t{-}\Delta t)) = \mathcal{N}(\Psi\mathbf{\Omega}(t{-}\Delta t); \Sigma_p)$, where $\mathcal{N}(\Psi\mathbf{\Omega}(t{-}\Delta t); \Sigma_p)$ is normally distributed

white noise with mean $\Psi\boldsymbol{\Omega}(t-\Delta t)$ and variance $\Sigma_p$. At $t=0$ the prior probability is assumed to be uniformly distributed in the absence of information other than the parameter lower and upper bounds.

The likelihood function $p(\boldsymbol{\beta}|\boldsymbol{\Omega})$ assigns a probability density to a measurement $\boldsymbol{\beta}$, given a state $\boldsymbol{\Omega}$. Suppose the differential pressure measurements are corrupted by additive noise:

$$\boldsymbol{\Delta\tilde{C}}_p(t) = \boldsymbol{\Delta C}_p(t) + \boldsymbol{\eta}_p(t),$$

where the noise $\boldsymbol{\eta}_p(t) \sim \boldsymbol{\mathcal{N}}(0, \boldsymbol{\Sigma}_p^2)$ is a $5\times1$ column matrix in which each element has zero mean and variance $\boldsymbol{\Sigma}_p^2$; $\boldsymbol{\Delta C}_p$ is given by (6.7). Assume the relative altitude measurement is also corrupted by zero-mean noise such that $\tilde{\zeta}(t) = \zeta(t) + \eta_\zeta(t)$, where $\eta_\zeta(t) \sim \mathcal{N}(0, \sigma_\zeta^2)$ has variance $\sigma_\zeta^2$. Multivariate Gaussian likelihood functions are chosen for each point $\boldsymbol{\Omega}(t)$ in the three dimensional state space to fuse contributions from both sensing types, i.e.,

$$p(\tilde{\boldsymbol{\beta}}(t)|\boldsymbol{\Omega}(t)) = p(\boldsymbol{\Delta\tilde{C}}_p(t)|\boldsymbol{\Omega}(t))p(\tilde{\zeta}(t)|\boldsymbol{\Omega}(t)). \tag{6.10}$$

The likelihood functions for the differential pressure and relative altitude measurements are

$$p(\boldsymbol{\Delta\tilde{C}}_p(t)|\boldsymbol{\Omega}(t)) = \tfrac{1}{\sqrt{2\pi|\boldsymbol{\Sigma}_p|}} \exp\Big[-\tfrac{1}{2}[\boldsymbol{\Delta C}_p(\boldsymbol{\Omega}(t)) - \boldsymbol{\Delta\tilde{C}}_p(t)]^T \boldsymbol{\Sigma}_p^{-1} [\boldsymbol{\Delta C}_p(\boldsymbol{\Omega}(t)) - \boldsymbol{\Delta\tilde{C}}_p(t)]\Big], \tag{6.11}$$

and

$$p(\tilde{\zeta}(t)|\boldsymbol{\Omega}(t)) = \tfrac{1}{\sqrt{2\pi}\sigma_\zeta} \exp[-\tfrac{1}{2\sigma_\zeta^2}(\mathrm{sgn}(z_L(\boldsymbol{\Omega}(t))) - \tilde{\zeta}(t))^2], \tag{6.12}$$

respectively. The term $z_L(\boldsymbol{\Omega}(t))$ in (6.12) represents the $z_L$ value associated with the state $\boldsymbol{\Omega}(t)$ and $\sigma_\zeta^2$ represents the variance in the relative altitude measurement. The maximum likelihood estimate $\hat{\boldsymbol{\Omega}}$ is used in the optimal controllers presented in the following section.

## 6.4 Observability-based Optimal Control

Section 6.2 showed that the unobservability index $\xi = \xi(\mathbf{r})$ and estimation condition $\lambda = \lambda(\mathbf{r})$ quantify the observability over the space of relative aircraft positions $\mathbf{r}$. The observability map can be viewed as a cost metric for an optimal control strategy that steers the follower aircraft to a desired relative position while maintaining observability along the trajectory. By maintaining observability along a trajectory, the performance of the estimation scheme is guaranteed, which increases the control algorithm performance when estimates are used in feedback control. This section presents the control derivation as an optimal control problem following the optimal control formulations in Chapter 2.

The optimal control problem is posed as follows. Suppose that for aerodynamic efficiency or aerial refueling purposes the follower aircraft must maintain a desired position relative to the leader aircraft $\mathbf{r}_{des} = [y_{des}, z_{des}]^T$, assuming the longitudinal separation between the aircraft $x_L$ is held fixed through a separate control strategy not described here. The kinematics of the lead aircraft position with respect to the follower are given by (6.9). For simplicity of presentation, we neglect the time-invariant quantity $\Gamma_L$ in (6.9) and consider only the relative position terms $\mathbf{r} \subset \mathbf{\Omega}$. Thus, the simplified leader aircraft equations of motion are

$$\dot{\mathbf{r}} = \sum_{k=1}^{2} \boldsymbol{g}_k(\mathbf{u}) = \begin{bmatrix} -u_1 \\ \\ -u_2 \end{bmatrix}, \tag{6.13}$$

where $\mathbf{r} = [y_L \; z_L]^T$, $\boldsymbol{g}_1(\mathbf{u}) = [-u_1, 0]^T$, and $\boldsymbol{g}_2(\mathbf{u}) = [0, -u_2]^T$. Equation (6.13) is in the standard form of the optimal control formulations in Chapter 2, from which the following sections derive two optimal control algorithms steering the follower aircraft to a desired relative position.

### 6.4.1 Receding-Horizon Optimal Control

The goal is to design a control $\mathbf{u}(t)$ that produces a trajectory optimizing observability from the initial condition $\mathbf{r}(t_0) = [y_L(t_0), z_L(t_0)]^T$ at time $t_0$ to the desired position $\mathbf{r}_{des}$ at time $t_0 + T_f$. Following Section 2.1.2 of Chapter 2, consider the metric (2.6) with cost function

$$l(\mathbf{r}(t)) = \kappa\, \xi(\mathbf{r}(t)), \tag{6.14}$$

where $\xi(\mathbf{r})$ is given by (2.20), $\mathbf{R} \in \mathbb{R}^{2\times 2}$, and $\kappa > 0$. The terms $\boldsymbol{R}$ and $\kappa$ are positive (definite) and constant. The cost function (6.14) is positive semi-definite since $\xi(\mathbf{r}) \geq 0$ by definition. Minimizing (2.6) with cost function (6.14) is a constrained nonlinear optimization problem whose solution gives the control sequence $\mathbf{u}(t)$ that produces the optimal observability trajectory. An additional constraint $||\mathbf{u}(t)|| \leq u_{max}$ ensures a bounded control signal, where $u_{max} = \sqrt{V_{y_{max}}^2 + V_{z_{max}}^2}$. The optimization problem is solved numerically using the GPOPS [117], [118] optimization software in MATLAB and produces the optimal controls $V_y^*$ and $V_z^*$.

Figure 6.3 shows optimal trajectories of the lead aircraft for $\kappa = 0$, 0.1, 0.3, and 0.8, $\boldsymbol{R} = I_{2\times 2}$, and arbitrarily chosen initial and desired conditions $\mathbf{r}_0 = [1.7 \;\; -1.7]^T$ wingspans and $\mathbf{r}_{des} = [-1.7 \;\; -1.7]^T$ wingspans, respectively. (In this particular application $\xi(\mathbf{r}) \gg 0$ so $\log \xi(\mathbf{r})$ is used instead of $\xi(\mathbf{r})$ in the cost function.) Figure 6.3(a) shows the optimal trajectories for the various values of $\kappa$ and Figure 6.3(b) shows the $V_z$ component of the control signal $\mathbf{u}(t)$ versus time. The $V_y$ component maintains its maximum value $V_{y_{max}} = 0.7$ wingspans/s for all solutions. Note in Figure 6.3(a) that as $\kappa$ increases the trajectory approaches areas of the domain where observability improves, as depicted by the underlying plot of the unobservability index. Decreasing $\kappa$ causes the

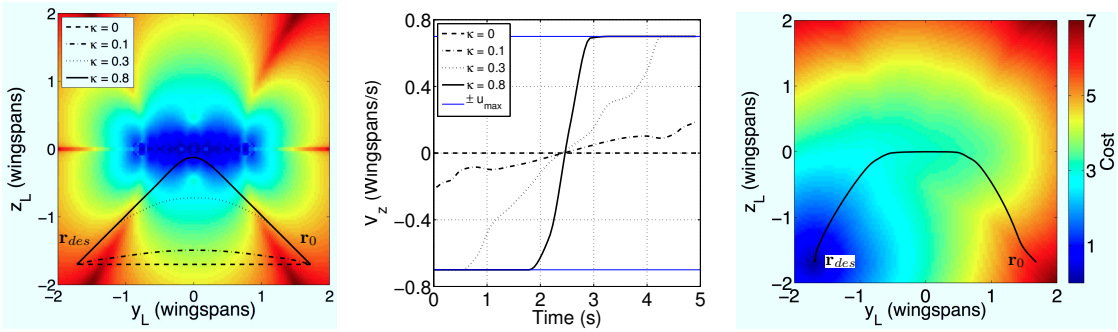


Figure 6.3: (a) Optimal trajectory solutions of the cost metric (2.6) with cost function (6.14) and (b) corresponding $V_z$ component of the control $\mathbf{u}(t)$. (c) Optimal trajectory using level set method (6.15).

trajectory to approach the desired location more directly, but via a route that achieves larger unobservability.

The control $\mathbf{u}(t)$ that minimizes the metric (2.6) with cost function (6.14) produces the optimal observability trajectory for a given horizon time $T_f$ and initial condition $\mathbf{r}_0$. To incorporate state estimates from the recursive Bayesian filter, this method uses the estimated lead aircraft states $\hat{\mathbf{r}}_0$ as the initial condition in the control calculation and recalculate the control iteratively in the following sense. At the start of each planning cycle of duration $T_e$ the optimal trajectory to $\mathbf{r}_{des}$ is computed using the estimated initial condition $\hat{\mathbf{r}}_0$ and the follower executes the optimal control $V_y^*(t)$, $V_z^*(t)$ for $t \in [t_0, t_0 + T_e]$; then the cycle repeats. Incorporating observability into the optimal control calculation ensures the performance of the recursive filter. As the estimates converge, the follower aircraft approaches the optimal trajectory.

### 6.4.2 Optimal Control Using Level Set Methods

The receding-horizon optimal control strategy presented above requires iterative calculation of the optimal control, which is computationally expensive. It also requires specification of horizon times that may be too large or infeasible depending on the leader aircraft's relative position. An alternative approach incorporates a weighted wavefront expansion, known as the fast marching method [119], to generate an optimal "cost-to-go" potential map relative to the desired position. The fast marching method belongs to the general class of optimal path planning solution algorithms known as level set methods [119] that produce a cost potential function whose gradient provides the optimal control with respect to a given cost function. This method does not require iterative calculation of the control since the potential is calculated over the entire relative position space, making the control computationally inexpensive compared to the receding-horizon control.

Following the optimal control formulation of Section 2.1.3, the path planning problem is to find the path $\mathcal{L}(\upsilon) : [0, \infty) \rightarrow \mathbb{R}^2$ from $\mathbf{r}_{des}$ to any point $\mathbf{r}_0$ that minimizes the observability-based cost metric (2.7) [119], where the cost function $l(\mathbf{r}) = \xi(\mathbf{r})$ uses the unobservability index (2.20) to penalize large values of unobservability along the trajectory.

The fast marching method [119] efficiently computes $J_{WF}(\mathbf{r})$ for the domain around the leader aircraft [119, pg. 86–99]. Figure 6.3(c) shows the cost potential (2.7) with $\mathbf{r}_{des} = (-1.7, -1.7)$ wingspans. Note that each contour of the potential function indicates the locus of points that can reach $\mathbf{r}_{des}$ with equal unobservability along the optimal path. The optimal path from $\mathbf{r}_0 = (1.7, -1.7)$ wingspans is denoted by the black line and follows the gradient of the potential function. Note this path planning approach does not incorporate

time, nor utilize the magnitude of the control in its cost function, and therefore differs from the paths generated in Figure 6.3(a).

Since the optimal path descends the gradient of $J_{WF}(\mathbf{r})$, an observer-based feedback control incorporates estimates of the relative position $\hat{\mathbf{r}}$ according to

$$\mathbf{u} = -K_{WF}\nabla J_{WF}(\hat{\mathbf{r}}), \tag{6.15}$$

where the gain $K_{WF} > 0$. The constraint $|\mathbf{u}| \leq u_{max}$ limits the control authority. Assuming the desired final location is fixed, the cost potential $J_{WF}(\mathbf{r})$ need be calculated only once to produce all possible optimal paths.

## 6.5 Wake Sensing and Control Examples

This section provides numerical simulations of the observability-based optimal control algorithms from the previous section. The control strategies are applied to two examples of close formation flight; the first considers a two-aircraft formation in which the follower aircraft steers itself to a position that, according to Pachter et al., [60] will increase aerodynamic efficiency, whereas the second example simulates the follower aircraft positioning itself for aerial refueling. Both simulations assume noise $\Sigma = 10^{-5}$ units in the differential pressure coefficient measurements, optimization constant $\kappa = 2$, and horizon time $T_f = 5$ seconds. The control optimization calculation is iterated every second, i.e., $T_e = 1$ second, assuming the recursive Bayesian filter assimilates measurements at 5 Hz.

### 6.5.1 Formation Flight for Aerodynamic Efficiency

This section incorporates estimates of the leader aircraft position into the control algorithms of Section 6.4 to steer the two-aircraft model (6.9) into a formation that increases aerodynamic efficiency for the follower aircraft. The desired final orientation

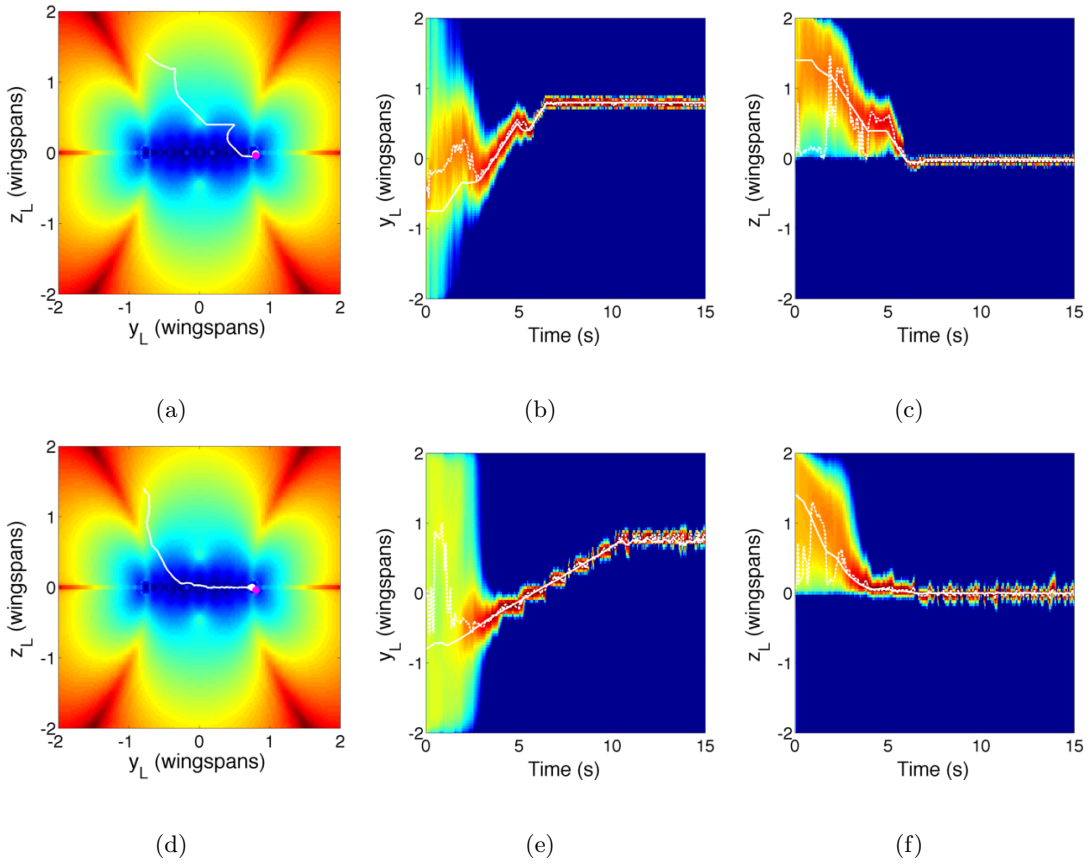


Figure 6.4: Simulation illustrating formation flight with optimal control algorithms of Section 6.4. Figures (a)-(c) illustrate the receding horizon optimal control algorithm, whereas Figures (d)-(f) illustrate the level set method.

$\mathbf{r}_{des} = [\pi b/4\ 0]^T$ wingspans reduces the induced drag on the follower aircraft, increasing its fuel efficiency [60]. The initial condition is $\mathbf{r}_0 = [-0.8\ 1.4]^T$ wingspans and the simulation time is $T = 3T_f = 15$ seconds.

Figures 6.4(a)–(c) illustrate the result of simulating the receding-horizon control algorithm. Figure 6.4(a) shows the leader aircraft trajectory (white) and the unobservability index. The white circle represents the final position of the leader aircraft and the magenta circle represents the final position estimate. Figures 6.4(b,c) show the marginal probability density of the estimated relative position over time. A solid white line represents the

trajectory of the leader aircraft and a dashed white line shows the trajectory of the state estimate. Note in Figure 6.4(a) that the leader aircraft is generally steered toward $\mathbf{r}_{des}$ with deviations from a direct path created by estimation errors in the observability-based control optimization. Figures 6.4(b,c) show the marginal probability densities converging to the true aircraft states. Figures 6.4(d)–(f) illustrate the results of simulating the wavefront-propagation control algorithm. Note in Figures 6.4(a) and 6.4(d), the wavefront-propagation algorithm steers the vehicle along a route to the desired position with fewer deviations due to estimation error when compared to the receding-horizon algorithm.

### 6.5.2 Autonomous Aerial Refueling

In aerial refueling the follower aircraft positions itself to intercept a filling nozzle that extends outward from the tail of the leader [65]. Therefore, the follower must maintain a desired relative position $\mathbf{r}_{des} = [0\ 0]^T$ wingspans, where $z_{des} = 0$ wingspans is chosen without loss of generality. The total simulation time is $T = 3T_f = 15$ seconds and the horizon time $T_f = 5$ seconds is chosen to be consistent with the previous example. Note that this implementation assumes the aerodynamic effects of the filling nozzle on the follower aircraft are minimal at the sensor positions. Figure 6.5 illustrates simulation results with the same initial and operating conditions of Section 6.5.1.

Figure 6.5(a) shows the trajectories of the lead aircraft (white) plotted over the unobservability index for the receding horizon control algorithm. Figures 6.5(b) and 6.5(c) show the marginal probability densities for the receding horizon control simulation plotted versus time. Note that in general the control algorithm steers the follower aircraft such that the leader maintains the desired position $\mathbf{r}_{des}$. Prior to $t = 5$ seconds the error in the $y_L$ estimate causes the control algorithm to steer the vehicle with less control authority

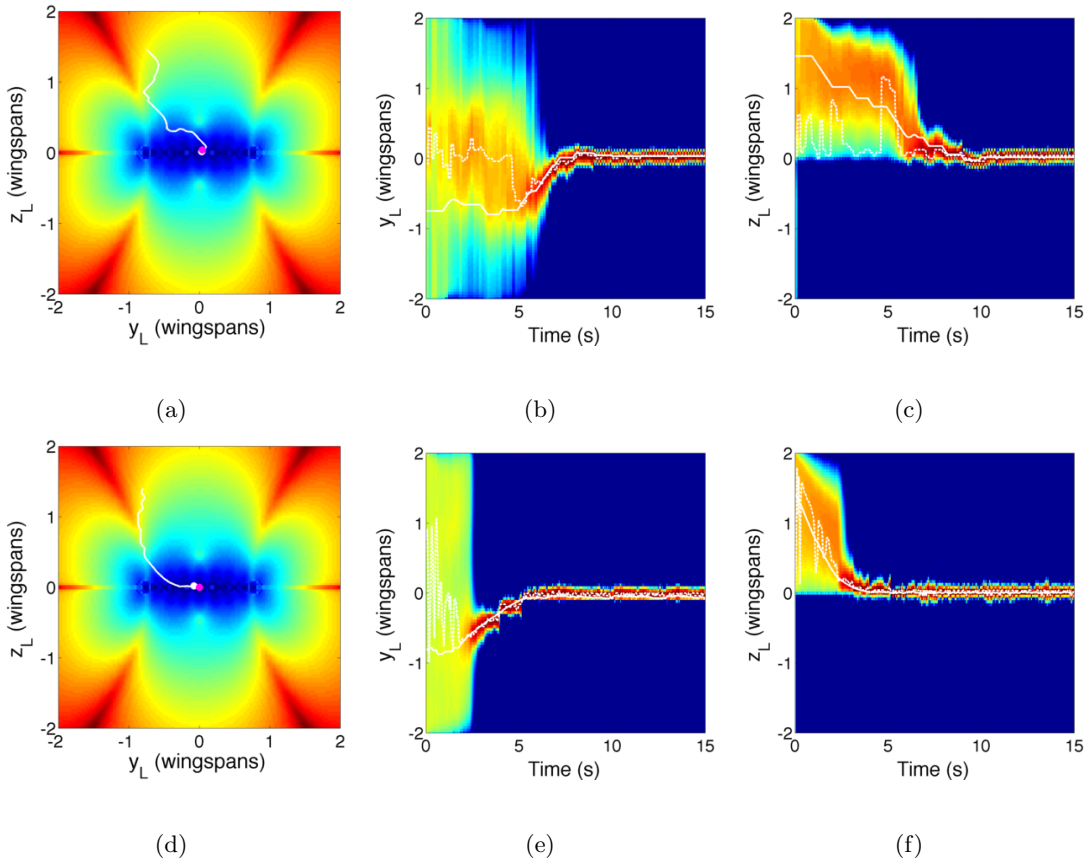


Figure 6.5: Simulation illustrating aerial refuel positioning with observability-based optimal control. (a)–(c) Leader aircraft position trajectory and marginal probability densities using receding-horizon method. (d)–(f) Trajectory and marginal probability densities using level set method.

in the $y_L$ direction as shown in Figures 6.5(a) and 6.5(b). After $t = 5$ seconds the estimates improve and the controller steers the follower to $\mathbf{r}_{des}$ along a path that increases observability.

Figures 6.5(d) illustrates the trajectory of the leader aircraft plotted over the unobservability index for the wavefront-propagation control algorithm, whereas Figures 6.5(e) and 6.5(f) show the marginal probability densities of the relative position estimates plotted versus time. Comparing Figures 6.5(a) and 6.5(d), note the receding-horizon method has less control authority in the $y_L$ direction due to the estimation error. Initial errors in

the position cause the wavefront-propagation control to steer the follower aircraft to the desired position with slight deviations toward unobservable regions. In these simulations the wavefront propagation technique produced a trajectory causing the recursive Bayesian filter to converge twice as fast as the receding horizon method, which was common in most simulations. Over many simulations, we also found that the performance of estimating $y_L$ and $z_L$ may be decoupled from estimation of $\Gamma_L$ in the fact that even when the estimate of $\Gamma_L$ converged slowly, the estimate of $(y_L, z_L)$ appeared to remain unaffected.

# Chapter 7: Application: Bio-inspired Flow Sensing and Feedback Control

This chapter applies tools from observability, estimation, and control toward distributed flow sensing and autonomous control of a bio-inspired underwater vehicle. The goal of the application is to steer an underwater vehicle to rheotactic and station-holding behavior in an unknown flowfield. Rheotaxis is the tendency of fish to orient upstream in an oncoming flow, whereas station-holding is the tendency of fish to hold position behind an upstream obstacle. Tools from observability are used to (1) derive a sensor placement strategy that increases observability of a uniform flowfield and (2) analyze a sensor configuration's ability to observe vortices in its vicinity. Grid-based recursive Bayesian and particle filtering techniques are used to estimate important properties of the flow used in feedback control. Control of the vehicle position and orientation is accomplished using Lyapunov-based techniques.

## 7.1 Fluid and Vehicle Modeling

This section describes a two-dimensional model of fluid flow past a streamlined body or foil. Using elementary potential functions, this section models the flow around a disk in the complex plane, which is mapped to flow around a foil using conformal mapping [151]. The flow models developed in this section are used in Sections 7.2 and 7.6 to design and implement estimation and control strategies for bio-inspired behavior. Section 7.1.1 describes a model of a foil in the presence of a uniform flowfield without obstacles. Section

7.1.2 augments the uniform flow model by including a bluff body upstream at moderate to high Reynolds numbers and Section 7.1.3 models the characteristic wake at low Reynolds numbers. At moderate to high Reynolds numbers ($\text{Re} \gtrsim 10^4$) the obstacle produces a turbulent wake [152], [4], whereas at lower Reynolds numbers ($40 < \text{Re} \lesssim 10^3$) the wake is modeled by a collection of vortices with alternating circulation, known as a Karman vortex street [152], [153], [76].

### 7.1.1 Obstacle-free Flow Model

Consider a point $\xi \in \mathbb{C}$ in the complex plane. The coordinate transformation [151]

$$z = \xi + \frac{c_0^2}{\xi} \in \mathbb{C}, \tag{7.1}$$

maps shapes according to the transformation variable $c_0 \in \mathbb{R}$. In particular $\xi = Re^{i\theta} + \xi_0$, where $\theta \in [0, 2\pi)$ rad, defines a disk with radius $R$ offset along the real axis by $\xi_0 \in \mathbb{R}$ [151]. Choosing $c_0 = R - |\xi_0|$ maps the disk to a symmetric, streamlined foil as shown in Figure 7.1. Note, the foil shape is defined by the transformation (7.1) and the parameters $(R, \xi_0)$. (When $\xi_0 \in \mathbb{C}$, the mapping produces a non-symmetric, cambered foil.)

Using (7.1), one can model the flow around a disk in the complex plane and map the result to the corresponding flow around a foil. Assuming an inviscid, incompressible, and irrotational fluid, which is justified at low flowspeeds where flow separation and viscous effects are minimal [151], the flow around a disk is represented by a sum of elementary potential functions corresponding to a uniform flow, a doublet, and a vortex located at the center of the disk [151], [152]. Let $U > 0$ be the freestream speed of the uniform flow, $\alpha \in [0, 2\pi)$ rad denote the angle of attack of the body relative to the free stream flow, and $\Gamma_{disk} \in \mathbb{R}$ denote the circulation of the vortex. (Note the potential flow approximation is valid only for small angles of attack, so assume $\alpha \in [-15°, 15°]$ to be consistent with

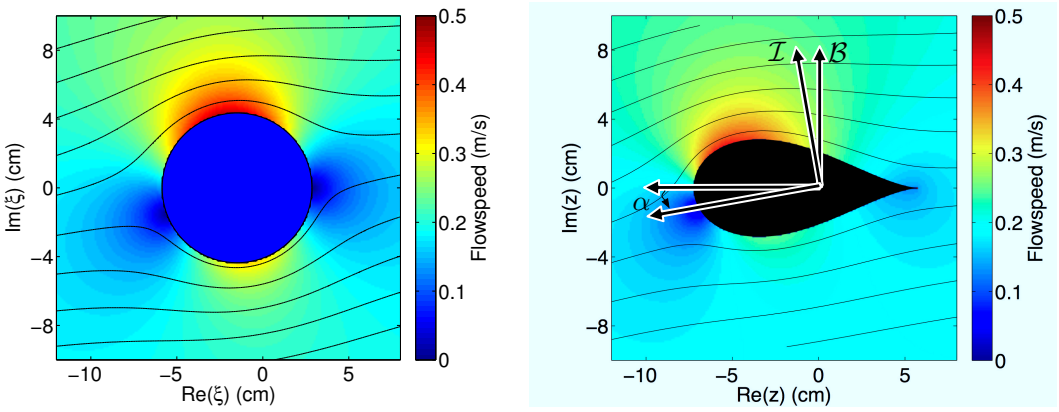


(a) (b)

Figure 7.1: Simulated flowfield around (a) a disk and (b) a foil with $(R, \xi_0) = (4.35, -1.5)$ cm at angle of attack $\alpha = 10^\circ$ and free stream flowspeed $U = 0.2$ m/s.

symmetric foils at low Reynolds numbers [154].) The velocity potential is [151], [152]

$$W_{uni}(\xi) = U(\xi - \xi_0)e^{-i\alpha} + \frac{R^2}{\xi - \xi_0}Ue^{i\alpha} - \frac{i\Gamma_{disk}}{2\pi}\ln(\xi - \xi_0). \tag{7.2}$$

The final term on the right-hand side of (7.2) represents the potential due to a vortex centered at $\xi_0$ that enforces flow stagnation at the trailing edge of the foil [151].

For any velocity potential function $W$ the conjugate flow $f^* = u - iv$ at $\xi$ is the gradient of (7.2), i.e., [151]

$$f^*(\xi) = \frac{\partial W}{\partial \xi}, \tag{7.3}$$

and the conjugate flow around the foil is [151]

$$f^*(z) = \frac{\partial W}{\partial \xi}\left(\frac{\partial z}{\partial \xi}\right)^{-1}. \tag{7.4}$$

For any velocity potential corresponding to flow around the foil, the Kutta condition [151], [152] stipulates that the flow must be continuous around the foil, which implies that the flow must stagnate at the foil's trailing edge. This condition determines the vortex circulation $\Gamma_{\text{disk}}$ in (7.2) by enforcing $f^*(z) = 0$ in (7.4) at $\xi = Re^{i0} + \xi_0$; solving for $\Gamma_{\text{disk}}$

yields $\Gamma_{\text{disk}} = -4\pi RU \sin\alpha$ [151], [152]. For a known body shape $(R, \xi_0)$, the uniform flowfield (7.4) is parameterized by $\mathbf{\Omega}_{uni} = (U, \alpha)$. Equation (7.3) with velocity potential (7.2) generates the streamlines and flowspeed illustrated in Figure 7.1(a).

Note that (7.4) provides the flow around the foil in $\xi$-plane coordinates rather than in $z$ coordinates. The inverse Joukowski mapping [76]

$$\xi = \xi_x + i\xi_y = \tfrac{1}{2}(z \pm \sqrt{z^2 - 4c_0^2}), \tag{7.5}$$

yields $z$ coordinates. This work considers only the root corresponding to points outside the disk to calculate the conjugate flow $f^*$ in $z$ coordinates, as shown in Figure 7.1(b). The figure also shows how the angle of attack $\alpha$ of the body reference frame $\mathcal{B}$ attached to the foil is measured relative to the lab-fixed reference frame $\mathcal{I}$ aligned with the upstream direction.

### 7.1.2 Flow Model in the Presence of an Obstacle at Moderate and High Reynolds Number

This section augments the uniform flow model by including the wake behind an obstacle. At relatively high flowspeeds (equivalently Reynolds numbers) the wake becomes turbulent and is characterized by an envelope of turbulent water downstream of the obstacle [4]. The flow field is a solution to the two dimensional Navier-Stokes equation, which can not be solved in real time but often admits simplified approximations [155]. Many authors have used potential theory to approximate the obstacle wake structure by including a combination of elementary potential functions such as sources and sinks [156], [157]. To address this issue while maintaining simplicity in the model, approximate the flow by modeling the obstacle and its associated wake as a point source located at the center of the true obstacle position.

Let $z_{obs} = x_{obs} + iy_{obs}$ denote the position of the obstacle in the $z$-plane, where $x_{obs}$ is the upstream component and $y_{obs}$ denotes the cross-stream component relative to the foil (at $\alpha = 0$) [4]. This method generates an obstacle commonly referred to as a Rankine half body [4], [152]. The inverse Joukowski mapping (7.5) gives the obstacle position relative to the cylinder in $\xi$ coordinates, denoted by $\xi_{obs}$. Following the Milne-Thomson Circle Theorem [158], we ensure there is no normal flow through the surface of the disk by including a mirror source term found by evaluating the conjugate of the elementary source potential at $R^2/\xi^*$, where $\xi^*$ represents the complex conjugate of $\xi$. Let $d$ be the obstacle diameter. Augmenting the uniform flow potential (7.2) with the point source and mirror term gives the obstacle potential function

$$W_{obs}(\xi) \;\; = \;\; W_{uni} + \tfrac{d}{2}\ln(\xi - \xi_{obs}) + \tfrac{d}{2}\ln(\tfrac{R^2}{\xi} - \xi^*_{obs}). \tag{7.6}$$

Equation (7.4) with velocity potential (7.6) provides the conjugate flow relative to the foil in $\xi$ coordinates, which is converted to $z$ coordinates using (7.5). Note that the wake model is characterized by four parameters, i.e., $\mathbf{\Omega}_{obs} = (U, \alpha, z_{obs}, d)$. Figure 7.2(a) illustrates the flowfield model (7.6) for a cylindrical obstacle with diameter $d = 5$ cm. The obstacle is superimposed over the source strength location and its position $z_{obs} = x_{obs} + iy_{obs}$ relative to the foil is shown. Note the streamlines curving outward around the obstacle surface.

### 7.1.3 Flow Model in the Presence of an Obstacle at Low Reynolds Number

At low flowspeeds the wake behind the obstacle is characterized by a series of vortices shed with opposite circulation strength, known as a Karman vortex street. This section models the vortex street by injecting a series of vortices with alternating circulation strength behind a virtual obstacle [76]. Let $z_{v_k}$ denote the position of the center of a vortex with circulation strength $\Gamma_k$ in the $z$-plane, corresponding to the position $\xi_{v_k}$

outside the disk in the $\xi$-plane. We model the presence of a vortex near the streamlined body using the sum of three vortex potential functions [76], [159]; one at $\xi_{v_k}$ represents the external vortex, and two mirror vortices inside the disk ensure there is no normal flow through the body surface (while also enforcing the Kutta condition). The first mirror vortex is centered at $\xi_0 + R^2/(\xi^*_{v_k} - \xi_0)$ and has circulation $-\Gamma_k$. The second vortex is located at $\xi_0$ with circulation $\Gamma_k$ to satisfy the Kutta condition. Thus, the potential flow contribution due to $n_v$ vortices near a disk is [159], [160]

$$W_{vort} = \sum_{k=1}^{n_v} \frac{i\Gamma_k}{2\pi} \left[ \log(\xi - \xi_0) + \log(\xi - \xi_{v_k}) - \log(\xi - \xi_0 - \frac{R^2}{\xi^*_{v_k} - \xi_0}) \right]. \tag{7.7}$$

The flow potential (7.7) augments the uniform flow potential (7.2) to produce the Karman vortex potential function

$$W_{Kar}(\xi) \quad = \quad W_{uni} + W_{vort}, \tag{7.8}$$

whose flow velocity at any point outside the streamlined body in $z$ coordinates is found using (7.4) and (7.5). The Karman vortex street flowfield is thus characterized by the $(2 + 2n_v)$-dimensional set of parameters

$$\mathbf{\Omega}_{Kar} = (U, \alpha, z_{v_1}, \ldots, z_{v_{n_v}}, \Gamma_{v_1}, \ldots, \Gamma_{v_{n_v}}),$$

corresponding to the free stream flow parameters and the vortex position and circulation strengths $(z_{v_k}, \Gamma_k)$, where $k = 1, \ldots, n_v$.

Let St $\approx 0.22$ be the Strouhal number and $U$ denote the free stream flowspeed. Assuming a cylindrical obstacle of diameter $d$ at position $z_{obs} = x_{obs} + iy_{obs}$ relative to the foil, vortices are shed from the cross-stream edges of the obstacle at a constant frequency $\omega = \text{St}(U/d)$ sec$^{-1}$ [155]. Once shed from the obstacle, each vortex convects through the fluid according to Routh's rule [100], [161], which provides the velocity of each vortex

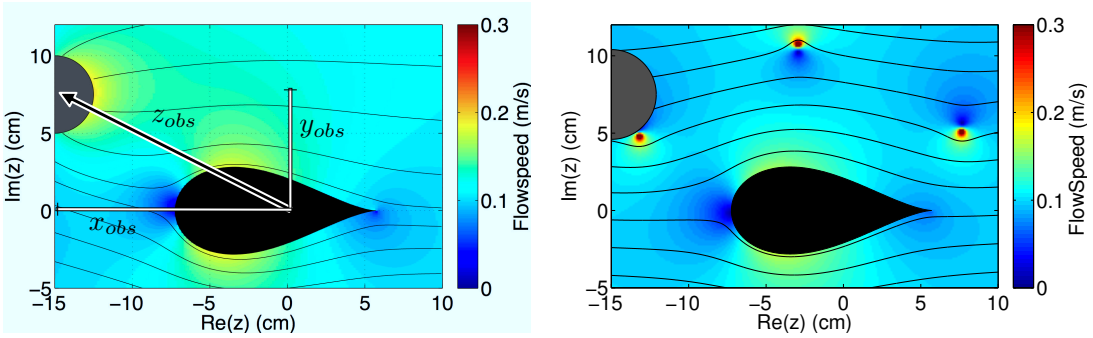


(a) (b)

Figure 7.2: Simulated flow field around a foil with an upstream obstacle at (a) moderate and (b) low Reynolds number.

resulting from all other flow entities. Let $W_{k,Kar}$ be the complex potential due to to all elements *except* the $k$th vortex in the $\xi$-domain. According to Routh's rule, the conjugate velocity at the $k$th vortex position is[1] [161]

$$g^*(z_{v_k}; \boldsymbol{z}_v) = \left( \frac{\partial W_{k,kar}}{\partial \xi} \Big|_{\xi_{v_k}} + \frac{c_0^2}{\xi_{v_k}(\xi_{v_k}^2 - c_0^2)} \right) \left( \frac{\partial z}{\partial \xi}^{-1} \right) |_{\xi_{v,k}} , \tag{7.9}$$

where $\boldsymbol{z}_v = [z_{v_1}, \ldots, z_{v_{n_v}}]^T$ is an $n_v \times 1$ vector of vortex positions and (7.5) transforms the equation into $z$-coordinates. The velocity of the $k$th vortex is [161]

$$\dot{z}_{v_k} = g(z_{v_k}; \boldsymbol{z}_v). \tag{7.10}$$

Figure 7.2(b) shows a simulated Karman vortex street created using the velocity potential function (7.8) by shedding vortices from the cross-stream edges of the obstacle. The vortices are convected according to (7.10). A representation of the obstacle generating the vortices is shown in gray. The position of the $k$th vortex at the instant it is shed is $z_{v_k}(t_{k,shed}) = z_{obs} \pm id/2$, where $d$ is the diameter of the obstacle. The cross-stream position $y_{obs}$ of the obstacle is estimated in Section 7.6 using noisy local flow measurements taken around the fish body to accomplish station-holding in low Reynolds number flows.

[1]The notation $g(a; \boldsymbol{\Omega})$ represents a function $g(\cdot)$ evaluated at $a$ that depends on the variables $\boldsymbol{\Omega}$.

## 7.2 State-Space Model

This section uses the flow models of the previous section to derive state-space representations of the foil motion and corresponding sensor measurements in an underwater environment, consistent with the notation of Chapter 2. Assume the foil is connected to a robotic gantry system capable of kinematic control of its cross-stream position $y$ and orientation $\alpha$ relative to the oncoming flow. Let $y \in \mathbb{R}$ be the cross-stream position of the streamlined body relative to a lab-fixed reference frame $\mathcal{I}$ aligned with the flow and $\alpha \in \mathbb{R}$ describe the orientation of the body frame $\mathcal{B}$ with respect to $\mathcal{I}$, as shown in Figure 7.1(b). Let $\mathbf{x} = [y, \alpha]^T \in \mathbb{R}^2$. The kinematic-control assumption results in the equations of motion

$$\dot{\mathbf{x}} = \begin{bmatrix} \dot{y} \\ \\ \dot{\alpha} \end{bmatrix} = \begin{bmatrix} u_1 \\ \\ u_2 \end{bmatrix}, \tag{7.11}$$

where $u_1$ and $u_2$ are the cross-stream velocity and angular velocity control inputs, respectively.

Assume the foil is outfitted with $N_f$ flow sensors located at $z_{f_i} \in \mathbb{C}$, $i = 1, \ldots, N_f$ with sensor length $l \in \mathbb{R}$ and $N_p$ pressure sensors located at $z_{p_j}$, $j = 1, \ldots, N_p$. The flow velocity at each sensor position is given by the conjugate of the flow models (7.4), (7.6), or (7.8) evaluated at the sensor location. Assume that the $i$th flow sensor measures the square of the component of the flow normal to the sensor at its tip $|f_n(z_{f_i})|^2$, i.e.

$$f_n(z_i) = \langle f(z_i; \mathbf{\Omega}), e_n \rangle, \tag{7.12}$$

where $e_n$ represents the complex unit vector normal to the body surface at $z_i$. (Section 7.3 assumes each sensor measures the total flow $f(z_i)$ rather than the component normal to the sensor orientation in order to simplify the analytical derivation of the observability

Gramian.)

Each pressure sensor measures the local pressure given by Bernoulli's equation [152]

$$P(z_{p_j};\mathbf{\Omega}) = C - \tfrac{1}{2}\rho|f(z_{p_j};\mathbf{\Omega})|^2, \tag{7.13}$$

where $\rho$ is the density of water and $C$ is a constant. To eliminate dependence on the constant $C$, the measurement model uses the difference in pressure between two measurement locations $\Delta P_{i,j} = P(z_{p_i};\mathbf{\Omega}) - P(z_{p_j};\mathbf{\Omega})$, analogously to the canal neuromast architecture in fish. The measurement equations are

$$\begin{aligned}
\beta_1 &= |f_n(z_{f_1};\mathbf{\Omega})|^2 \\
&\vdots \\
\beta_{N_f} &= |f_n(z_{f_{N_f}};\mathbf{\Omega})|^2 \\
\beta_{N_f+1} &= \Delta P_{1,2} \\
&\vdots \\
\beta_{N_f+N_m} &= \Delta P_{N_p-1,N_p},
\end{aligned} \tag{7.14}$$

where $N_m = \frac{N_p!}{2!(N_p-2)!}$ is the number of unique pressure-sensor pairs. Let $\boldsymbol{z} = \begin{bmatrix} z_1 \dots z_{N_f+N_p} \end{bmatrix}^T$ and $\boldsymbol{\beta} = \begin{bmatrix} \beta_1 \dots \beta_{N_f+N_m} \end{bmatrix}^T$ be $N_i \times 1$ vectors of the measurement positions and square of flow velocity components, respectively. Combining the motion model (7.11) with the measurement model (7.14) under the assumption that the vehicle moves quasi-statically in a uniform flow (7.4) gives the nonlinear state-space model

$$\begin{aligned}
\dot{y} &= u_1 \\
\dot{\alpha} &= u_2 \\
\boldsymbol{\beta} &= \boldsymbol{q}(\boldsymbol{z};\mathbf{\Omega}_{uni}),
\end{aligned} \tag{7.15}$$

where $\boldsymbol{q}(\cdot) \in \mathbb{C}^{(N_f+N_m)\times 1}$ represents the total measurement function in (7.14). For a known body shape $(R, \xi_0)$, the (uniform) flowfield (7.4) is parameterized by the two-dimensional parameter space $\mathbf{\Omega}_{uni} = (U, \alpha)$.

Section 7.3 uses measures of observability to derive an optimal placement strategy for an array of flow velocity censors. This method is easily applied to pressure sensor placement as well and is addressed in [78]. By assimilating measurements collected at the sensor locations $\boldsymbol{z}$, one can reconstruct the flowfield by estimating $\boldsymbol{\Omega}_{uni}$.

In the presence of an upstream obstacle, the flow is modeled by (7.6) when the free stream flow corresponds to a high Reynolds number and (7.8) for flow with a low Reynolds number. At higher Reynolds number the wake is approximated by a source with position $z_{obs}$ relative to the foil. The kinematics of the obstacle relative to the body frame $\mathcal{B}$, assuming $\alpha(t) = 0 \ \forall t$ for simplicity, are given by the state-space model

$$\begin{aligned} \dot{y}_{obs} &= -u_1 \\ \boldsymbol{\beta} &= \boldsymbol{q}(\boldsymbol{z}; \boldsymbol{\Omega}_{obs}). \end{aligned} \tag{7.16}$$

For flow at low Reynolds number, the Karman vortex street model (7.8) is parameterized by the free stream flowspeed $U$, the angle of attack $\alpha$, and the positions and circulation strengths $(z_{v_k}, \Gamma_i)$ of the vortices relative to the streamlined body, such that $\boldsymbol{\Omega}_{Kar} = (U, \alpha, z_{v_1}, \ldots, z_{v_{n_v}}, \Gamma_1, \ldots, \Gamma_{n_v})$ has dimension $2+2n_v$. Augmenting the state-space model (7.11) with a vector of vortex positions $\boldsymbol{z}_v = [z_{v_1}, \ldots, z_{v_{n_v}}]^T$ and assuming $\alpha(t) = 0$ similar to (7.16) gives

$$\begin{aligned} \dot{y}_{obs} &= -u_1 \\ \dot{\boldsymbol{z}}_v &= g(\boldsymbol{z}_v) \\ \boldsymbol{\beta} &= q(\boldsymbol{z}; \boldsymbol{\Omega}_{Kar}). \end{aligned} \tag{7.17}$$

The following section presents a strategy to optimize the positions of flow velocity sensors $\mathbf{z}$ in order to maximize flowfield observability [78], [111]. Section 7.4.2 assesses the observability of vortices given a sensor configuration.

## 7.3 Sensor Placement Optimization

This section presents a sensor placement strategy that optimizes measures of uniform flowfield observability. To optimize the array configuration with respect to flowfield parameter observability, this section assumes the vehicle's nominal operating environment is in a uniform stream free of obstacles, corresponding to (7.4) with potential function (7.2). Section 7.3.1 calculates the optimal placement of a single sensor based on the unobservability index (2.20) measure of the empirical observability Gramian (2.15). Section 7.3.2 suggests a sensor-placement strategy for an $N_f$-sensor configuration based on the observation that the multi-sensor empirical observability Gramian is the sum of the observability Gramians produced by each sensor. Placement of pressure sensors for optimal flowfield observability is addressed in [78].

### 7.3.1 Placement Optimization for a Single Sensor

A first step in solving the sensor placement problem for a uniform and steady flowfield parameterized by $\mathbf{\Omega}_{uni} = (U, \alpha) \in \mathbb{R}^2$ is to consider a single flow sensor placed at $z_i$ extending a fixed distance from the body that measures the flow[2] $f(z_i)$. Optimization of the placement of a single sensor is motivated by noting that the inner product used to calculate $W_O(i,j)$ in (2.15) is a linear operator, implying that in this application the empirical observability Gramian for an $N_f$-sensor configuration is the sum of the empirical observability Gramians produced by each sensor, i.e.,

$$W_O(i,j;\mathbf{z}) = \sum_{k=1}^{N_f} W_O(i,j;z_k), \tag{7.18}$$

[2]The analysis presented here is easily extensible to the measurement model (7.14); however, for simplicity of the analytical derivation, assume measurement of the total flow.

where $W_O$ is found from (2.15). Consequently, the results of single sensor optimization are directly applicable to the design of a multi-sensor configuration in Section 7.3.2.

Envisioning hair sensors that protrude outside the boundary layer, the empirical observability Gramian from a single measurement at $z_1$ is calculated using (2.15), where $\boldsymbol{\beta} = f_{uni}(z_1)$ assumes the sensor measures the total flow at position $z_i$. The flow $f_{uni}(z_1)$ is given by (7.4) with potential function (7.2). The elements of the $2 \times 2$ empirical observability Gramian are

$$\begin{aligned} W_O(1,1) &= (a_1 \cos\alpha + a_2 \sin\alpha)^2 + (b_1 \cos\alpha + b_2 \sin\alpha)^2 \\ W_O(1,2) &= W_O(2,1) = \tfrac{U \sin\epsilon_\alpha}{\epsilon_\alpha} \left[(a_1 \cos\alpha + a_2 \sin\alpha)(a_2 \cos\alpha - a_1 \sin\alpha)\right. \\ &\quad \left. +(b_1 \cos\alpha + b_2 \sin\alpha)(b_2 \cos\alpha - b_1 \sin\alpha)\right] \\ W_O(2,2) &= \tfrac{U^2 \sin^2\epsilon_\alpha}{\epsilon_\alpha^2} \left[(a_2 \cos\alpha - a_1 \sin\alpha)^2 + (b_2 \cos\alpha - b_1 \sin\alpha)^2\right] \end{aligned} \tag{7.19}$$

where

$$\begin{aligned} a_1 &= m_1 - m_1 m_2 + m_5 m_3 \\ a_2 &= m_1 m_4 - m_1 m_3 - m_5 m_2 + m_5 - m_5 m_6 \\ b_1 &= m_5 - m_5 m_2 + m_1 m_3 \\ b_2 &= m_5 m_4 - m_5 m_3 - m_1 m_2 + m_1 m_6 - m_1 \end{aligned} \tag{7.20}$$

are coefficients dependent on sensor placement and $\epsilon_U, \epsilon_\alpha$ are perturbations to the nominal parameter state $\boldsymbol{\Omega}$. The coefficients $m_1, \ldots, m_6$ are a function of the sensor position $z_1$ mapped to $\xi$-coordinates using (7.5) and the Joukowski mapping parameters $(R, \xi_0, c_0)$

$$\begin{aligned} m_1 &= \tfrac{(\xi_x^2+\xi_y^2)^2 - c_0^2(\xi_x^2-\xi_y^2)}{(\xi_x^2-\xi_y^2-c_0^2)^2+4\xi_x^2\xi_y^2} \\ m_2 &= \tfrac{(R+|\xi_0|)^2(\xi_x^2-\xi_y^2+2\xi_x|\xi_0|+|\xi_0|^2)}{(\xi_x^2-\xi_y^2+2\xi_x|\xi_0|+|\xi_0|^2)^2+(2\xi_x\xi_y+2\xi_y|\xi_0|)^2} \\ m_3 &= \tfrac{2(R+|\xi_0|)^2(\xi_x\xi_y+\xi_y|\xi_0|)}{(\xi_x^2-\xi_y^2+2\xi_x|\xi_0|+|\xi_0|^2)^2+(2\xi_x\xi_y+2\xi_y|\xi_0|)^2} \\ m_4 &= \tfrac{2(R+|\xi_0|)\xi_y}{(\xi_x+|\xi_0|)^2+\xi_y^2} \\ m_5 &= \tfrac{-2c_0^2\xi_x\xi_y}{(\xi_x^2-\xi_y^2-c_0^2)^2+4\xi_x^2\xi_y^2} \\ m_6 &= \tfrac{2(R+|\xi_0|)(\xi_x+|\xi_0|)}{(\xi_x+|\xi_0|)^2+\xi_y^2}. \end{aligned} \tag{7.21}$$

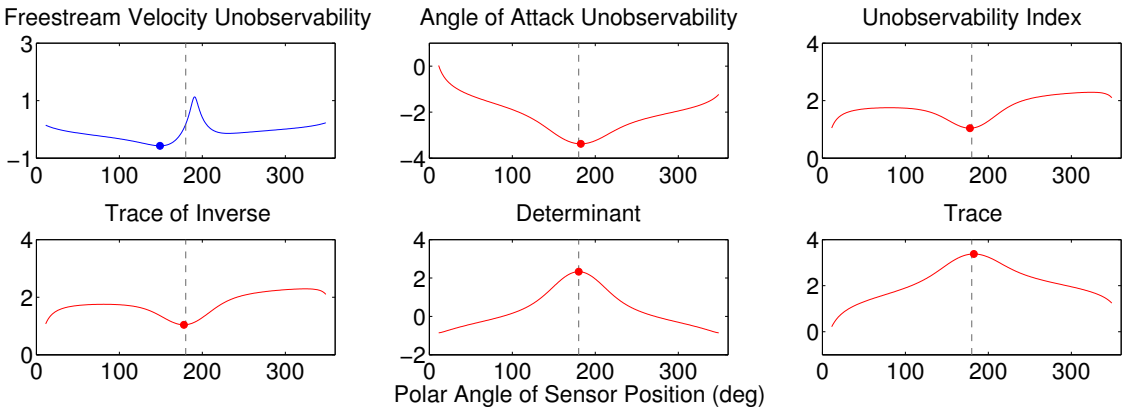


Figure 7.3: Optimality metrics of the empirical observability Gramian plotted versus the polar angle of the sensor position near the fish body for $\mathbf{\Omega} = (0.15 \text{ m/s}, 10 \text{ deg})$. Of all the metrics, the leading edge and the point of maximum flowspeed provide the most observability.

Due to the linear dependence of the flowfield model (7.4) on the parameter $U$ and the definition of the empirical observability Gramian (2.15), the perturbation value $\epsilon_U$ does not appear in (7.19). The first element $W_O(1,1)$ corresponds to the square of the flow magnitude divided by the square of $U$. This element corresponds to a perturbation in the free stream velocity parameter $U$ and is therefore maximum at the point of maximum flowspeed around the foil. Likewise, $W_O(2,2)$ corresponds to perturbations in the angle of attack. Maximizing these elements individually corresponds to maximizing the observability of the free stream velocity parameter $U$ or the angle of attack $\alpha$, respectively.

We calculate the empirical observability Gramian (7.19) as a function of the sensor location and evaluate the observability metrics described in Section 2.3.2 for the parameters $\mathbf{\Omega}_{uni}$, assuming the sensor protrudes 1 cm from the body. Figure 7.3 shows the log of each dimensionless scoring metric plotted versus the polar angle $\arg(z_1)$ of the sensor placement, assuming $\mathbf{\Omega} = (0.15 \text{ m/s}, 10^\circ)$. Figure 7.4(a) shows streamlines of the flow

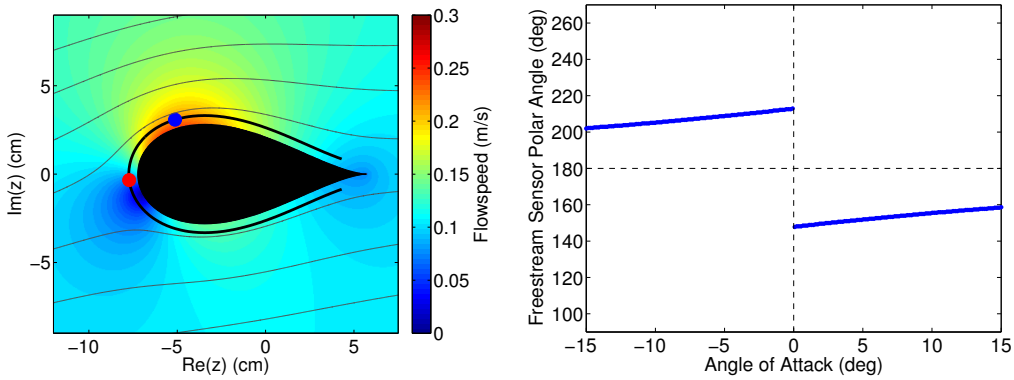


(a) (b)

Figure 7.4: (a) Sensor placement showing the optimal locations of freestream parameter observability $U$ (blue) and remaining optimality metrics (red). (b) Optimal polar angle of Freestream observability sensor $U$ plotted for $-15° \leq \alpha \leq 15°$.

around a foil parameterized by $R = 4.35$ cm and $\xi_0 = -1.5$ cm. The possible sensor placement positions are shown by the black line around the foil, where sensor positions are restricted to polar angles in the range $\left[\frac{\pi}{6}, \frac{11\pi}{6}\right]$ to avoid the cusp near the trailing edge. (In practice, one may assume a propulsive mechanism near the trailing edge will create significant turbulent flow structures in its vicinity that are not captured in the uniform flow model.)

Note in Figures 7.3 and 7.4(a) that there are two primary sensor locations of interest, one at or near the nose of the foil (red metrics) and one in a region of high flowspeed (blue). Optimization of the free stream flow observability corresponding to element $W_O(1,1)$ (shown in blue in Figure 7.3) places the sensor at the location of the maximum flowspeed, illustrated by the blue circle in Figure 7.4(a). The extrema of the remaining optimality metrics including the angle of attack element $W_O(2,2)$, unobservability index, trace, determinant, and the trace of the inverse (red) lie on or near the tip of the body ($\arg(z_k) = 180°$), indicating that sensors placed in this region of the body

maximize the independence between the angle of attack $\alpha$ and flowspeed $U$ and optimally observe the angle of attack parameter [98]. The red circle in Figure 7.4(a) denotes the optimal position for the angle of attack element $W_O(2,2)$.

Performing the observability analysis for nominal flowspeeds $U \in [0.01, .6]$ m/s and angle of attack $\alpha \in [-15°, 15°]$ indicates how sensor placement varies with $\mathbf{\Omega}_{uni}$. Since the flow (7.2) is linearly dependent on $U$, the observability of the freestream parameter $U$ increases with $U$ at any $z_k$ or $\alpha$ but does not change the position of the optimal location. Figure 7.4(b) shows the optimal polar angle of the sensor for varying angles of attack and fixed velocity parameter $U = 0.15$ m/s when optimizing over the freestream velocity element $U$ of the observability Gramian, $W_O(1,1)$. Note the optimal sensor placement varies with $\alpha$ to follow the point of maximum flowspeed a fixed distance from the foil. The optimal placement with respect to the remaining metrics lies within $\pm 5°$ of the tip of the body for all angles of attack and flowspeeds.

### 7.3.2 Optimization of a Multi-Sensor Configuration

Motivated by the single sensor placement results, this section considers the optimization of a multi-sensor configuration. Assume the flowfield parameters $\mathbf{\Omega}_{uni}$ lie within a predefined range and each of the $N_f$ sensors are placed a fixed distance 1 cm from the body. Under these assumptions the empirical observability Gramian from measurements at $\mathbf{z} = [z_1, \ldots, z_{N_f}]^T$ is given by (7.18).

A desirable configuration optimizes observability over a range of the parameter space $\mathbf{\Omega}_{uni}$, assuming the flowfield model is valid for angles of attack $\alpha \in [-15°, 15°]$. At any given $\alpha$ a desirable configuration is one in which at least one sensor is optimally placed. This motivates choosing a configuration (assuming $N_f$ is odd) in which $N_f - 1$ sensors

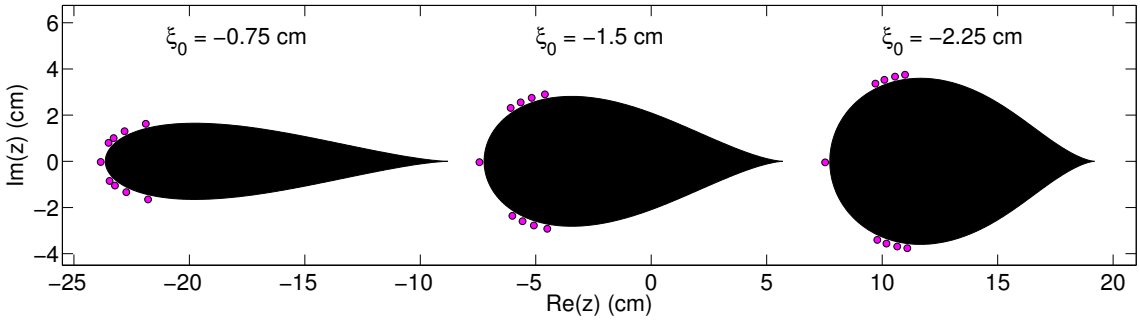


Figure 7.5: Optimized sensor configurations for three fish-like foil shapes parameterized by $R = 4.35$ cm and $\xi_0 = -0.75, -1.5$, and $-2.25$ cm, respectively.

are placed symmetrically about the body with the polar angle of each sensor optimizing at angles of attack in $15^\circ/N_f$ intervals. A single sensor is placed at the tip of the body to optimize the remaining metrics. This sensor configuration therefore satisfies all of the optimality criterion along equal intervals of the flowfield parameter space $\mathbf{\Omega}_{uni}$. Figure 7.5 shows the optimized sensor configuration scheme for $N_f = 9$ sensors and three streamlined bodies parameterized by $R = 4.35$ cm and $\xi_0 = -0.75$, $-1.5$, and $-2.25$ cm, respectively.

The performance of the optimal sensor configuration is analyzed by comparing perfect knowledge of the flow parameters to the likelihood function achieved by assimilating measurements over the array. Consider the likelihood function

$$p(\boldsymbol{\beta}|\mathbf{\Omega}_{uni}) = \frac{1}{\sqrt{2\pi}\sigma_u\sigma_v}\prod_{k=1}^{N_f}\exp\left[-\frac{1}{2}\left(\frac{\mathrm{Re}(f(z_k;\mathbf{\Omega}_{uni})-\beta_k)^2}{\sigma_u^2}+\frac{\mathrm{Im}(f(z_k;\mathbf{\Omega}_{uni})-\beta_k)^2}{\sigma_v^2}\right)\right], \tag{7.22}$$

achieved by assimilating measurements of the flow velocity $f(z_k;\mathbf{\Omega}_{uni})$ at sensor position $z_k$. Equation (7.22) assigns a probability density to element of the parameter space $\mathbf{\Omega}_{uni}$ given measurements over the array, where $\hat{\mathbf{\Omega}}_{uni}$ corresponds to the element in parameter space with the highest probability density (i.e. the mode). Perfect statistical knowledge of the flow parameters corresponds to a Kronecker delta function where $p(\boldsymbol{\beta}|\mathbf{\Omega}_{uni}) = 1$

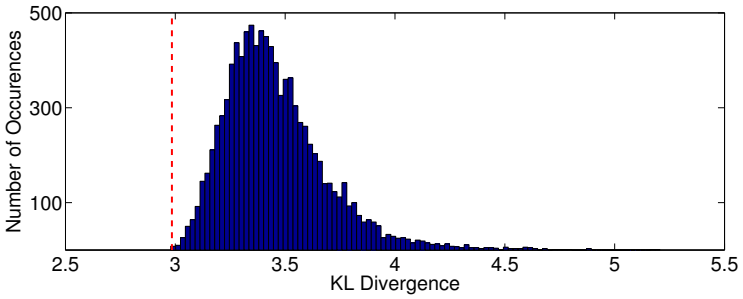


Figure 7.6: Histogram of KL divergence for 10000 random sensor configurations. The KL divergence of the observability-based optimal configuration is denoted by the dashed red line.

when $\hat{\mathbf{\Omega}}_{uni} = \mathbf{\Omega}_{uni}$ and zero elsewhere.

The Kullback-Liebler divergence (KL divergence) is a non-symmetric scaler measure of the information lost when a probability density function $\boldsymbol{\zeta}(\cdot)$ is used to represent a probability density $\boldsymbol{\phi}(\cdot)$ and is defined for discrete distributions by [162]

$$\mathrm{KL}(\boldsymbol{\phi}||\boldsymbol{\zeta}) = \sum_j \ln\left(\frac{\phi_j}{\zeta_j}\right)\phi_j, \tag{7.23}$$

where $\phi_j$ represents the $j$th element of the probability density $\boldsymbol{\phi}$. The KL divergence is commonly denoted as the distance between two probability distributions; however, since the measure is non-symmetric note that it is not a true distance metric by definition.

To compare performance, this setting calculates the KL divergence between the likelihood function achieved by assimilating measurements over the array, and a likelihood function given by the Kronecker delta function centered on the flowfield parameters generating the measurements, which represents perfect knowledge of the flow parameters. Thus, the KL divergence provides a metric to compare the performance of candidate sensor configurations. It measures the distance of the posterior probability density function from perfect statistical knowledge of the flow parameters for a given sensor configuration.

Figure 7.6 shows a histogram illustrating results of a Monte Carlo simulation com-

paring the KL divergence of 10000 candidate sensor array configurations to the observability-based optimal sensor placement strategy. Each candidate array is composed of $N_f = 9$ sensors selected randomly around the foil, assuming each sensor protrudes 1 cm from the body and foil parameters $R = 4.35$ cm and $\xi_0 = -1.5$ cm. The probability density function is calculated by assimilating a noise-free measurement from each sensor, where the measurements are generated using (7.2) with free stream flow parameters $U = 0.3$ m/s and $\alpha = 10°$. Each bin represents the number of random configurations with KL divergence within $\pm 0.03$ of the bin's center; the KL divergence resulting from the observability-based optimal placement strategy is denoted by the dashed red line. Note that although the optimal placement strategy does not place sensor directly at the optimal position for observing the free stream flow parameter $U$, the optimal configuration outperforms 99.97% of the random configurations, indicating that one can expect improved estimation performance with the observability-optimized sensor configuration over a range of angles of attack.

## 7.4 Flow Sensing and Feedback Control for Bio-inspired Behavior

This section designs flow sensing and feedback control algorithms steering a vehicle to bio-inspired motion primitives. We consider two primary behaviors, rheotaxis and station-holding, which are valuable motion primitives for unmanned underwater vehicle operation. For rheotaxis and station-holding at high Reynolds number, we use a recursive Bayesian framework to estimate the flowfield parameters $\mathbf{\Omega}$ needed for feedback control. A particle filter is used for station-holding at low Reynolds number. Assume the vehicle is outfitted with a multi-modal artificial lateral line producing the measurements (7.14). Here, the spatial configuration of the sensor array is modeled after the experimental pro-

totype presented in Section 7.5.

### 7.4.1 Multi-Modal Flow Estimation and Control for Rheotaxis

Rheotaxis occurs when a fish orients itself upstream. This behavior falls within the broader control objective of maintaining a desired angle of attack with respect to a uniform oncoming flow. The vehicle kinematics and measurements follow the state-space model (7.15), where without loss of generality we neglect the arbitrary cross-stream position $y$. Since the uniform flowfield model (7.2) has a low dimensional parameterization $\mathbf{\Omega}_{uni} = (U, \alpha) \in \mathbb{R}^2$ with linear kinematics in the angle of attack parameter, the recursive Bayesian filter is used for its simplicity of implementation.

For recursive Bayesian estimation of the uniform flowfield model (7.2), incorporate the flowfield parameters $\mathbf{\Omega}_{uni}$ into the Bayesian filter formulation (2.22), assuming time step $\Delta t$. Discrete time temporal integration of the probability density function is accomplished in using the motion matrix $\Psi = \Delta t \text{diag}([0,\ u_2]^T)$ such that $p(\mathbf{\Omega}(t)|\mathbf{\Omega}(t-\Delta t)) = \mathcal{N}(\Psi\mathbf{\Omega}(t-\Delta t); \Sigma_p)$, where $\mathcal{N}(\Psi\mathbf{\Omega}(t-\Delta t); \Sigma_p)$ is normally distributed white noise with mean $\Psi\mathbf{\Omega}(t-\Delta t)$ and variance $\Sigma_p$.

For each point $\mathbf{\Omega}$ in the $G$-dimensional state space, we choose a multivariate Gaussian likelihood function for the flow measurements $\tilde{\beta}_k$, $k = 1, \ldots, N_f$,

$$p(\tilde{\beta}_k|\mathbf{\Omega}) = \frac{1}{\sqrt{2\pi}\sigma_{f_k}} \exp\left[-\frac{1}{2\sigma_{f_k}^2}\left(|f_n(z_{f_k}; \mathbf{\Omega})|^2 - \tilde{\beta}_k\right)^2\right], \tag{7.24}$$

and for the pressure difference measurements $\tilde{\beta}_j$, $j{=}N_f{+}1, \ldots, N_f + N_m$,

$$p(\tilde{\beta}_j|\mathbf{\Omega}) = \frac{1}{\sqrt{2\pi}\sigma_{p_j}} \exp\left[-\frac{1}{2\sigma_{p_j}^2}\left(\Delta P_j(\mathbf{\Omega}) - \tilde{\beta}_j\right)^2\right], \tag{7.25}$$

respectively. Assuming that the measurements are taken from $N_f + N_m$ sensors, the posterior probability density of the parameter estimate $\mathbf{\Omega}$ is obtained using the joint

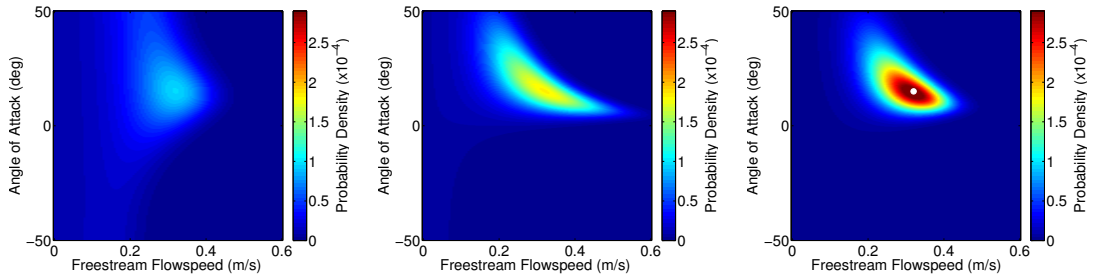


(a) (b) (c)

Figure 7.7: Assimilation of spatially distributed velocity and pressure measurements. (a) Likelihood function from eight flow sensor measurements; (b) likelihood function from six pressure difference measurements; and (c) the resulting posterior probability density. The ground truth parameter values are shown by the white circle.

measurement likelihood combining both flow and pressure difference measurements as follows:

$$p(\mathbf{\Omega}|\mathbf{A}) = \kappa \left( \prod_{k=1}^{N_f+N_m} p(\tilde{\beta}_k|\mathbf{\Omega}) \right) p(\mathbf{\Omega}|\mathbf{A}_0), \tag{7.26}$$

where $p(\tilde{\beta}_k|\mathbf{\Omega})$ is given by (7.24) for $k = 1, \ldots, N_f$ and (7.25) for $k = N_f+1, \ldots, N_f+N_m$. The point $\hat{\mathbf{\Omega}}$ in the parameter space corresponding to the maximum (mode) of the posterior probability $p(\mathbf{\Omega}|\mathbf{A})$ provides the maximum likelihood estimate of the flowfield parameters.

Figure 7.7 illustrates the likelihood and posterior probability density functions corresponding to assimilation of flowspeed and pressure difference measurements at one time instant, assuming the uniform flow parameters $\mathbf{\Omega}_{uni} = (0.3 \text{ m/s}, 10^\circ)$ and a uniform prior distribution. Figure 7.7(a) shows the likelihood function resulting after assimilating eight flow sensor measurements, where $\sigma_{f_k} = 0.01$ m/s for sensors $k = 1, \ldots, 8$. Figure 7.7(b) illustrates the likelihood function resulting from assimilation of six pressure difference measurements (from four pressure sensors), where $\sigma_{p_j} = 0.2$ kPa for all $j = 1, \ldots, 6$ pressure differences.

A key benefit of the Bayesian approach is its ability to fuse data from multiple sensing modalities. Figure 7.7(c) shows the posterior probability density resulting from combined flow and pressure sensing, whose likelihood functions are shown in Figures 7.7(a) and 7.7(b), respectively. The white circle corresponds to the true flowfield parameters. Note in Figures 7.7(a) and 7.7(b) that the flow velocity and pressure difference measurements are complementary in the following sense. At least at this angle of attack, the flow velocity measurements tend to reduce uncertainty in the flowspeed, whereas the pressure difference measurements tend to reduce uncertainty in the angle of attack. Fusing the two modalities results in a tighter probability density around the true flowfield parameters than would be obtained from either one alone.

The KL divergence between the likelihood functions achieved by assimilating flow velocity and pressure difference measurements provides further analysis of the complementarity between each modality for estimation of the uniform flowfield parameters. Since the KL divergence is a non symmetric measure, we use the symmetrized KL divergence

$$\mathrm{KL}_{sym}(p_{flow}, p_{press}) = \tfrac{1}{2}\left(\mathrm{KL}\left(p_{flow}||p_{press}\right) + \mathrm{KL}\left(p_{press}||p_{flow}\right)\right), \tag{7.27}$$

between the likelihood function $p_{flow}$ produced by the flow velocity sensors and the likelihood function $p_{press}$ from the pressure difference measurements, where $\mathrm{KL}\left(p_{flow}||p_{press}\right)$ is calculated using 7.23. Figure 7.8 illustrates the symmetrized KL divergence between the likelihood functions after assimilating measurements at varying free stream flowspeeds $U$ and angles of attack $\alpha$. Note that at flowspeeds below $U < 0.3$ m/s the modalities provide similar information about the flow parameters, whereas at flowspeeds $U > 0.3$ m/s the likelihood functions provide complementary information, implying that at higher flowspeeds and angles of attack the dual-modality system will perform better than either modality alone.

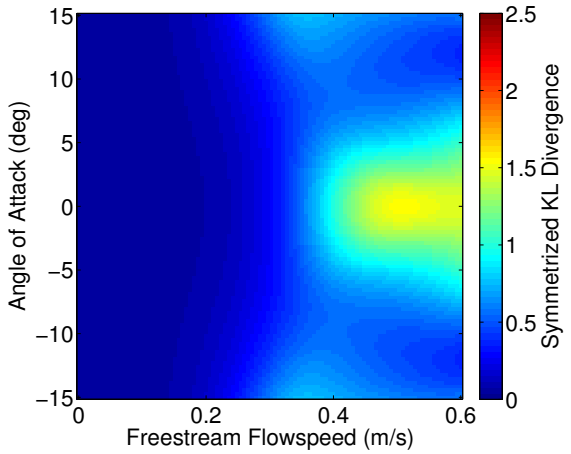


Figure 7.8: The symmetrized KL divergence measures the amount of redundant information provided by the flow velocity and pressure difference likelihood functions. Small values of the symmetrized KL divergence imply the modalities provide redundant information, whereas large values imply each modality contributes unique information.

By employing recursive Bayesian filtering with an optimized sensor placement configuration the flowfield can be estimated even in the presence of measurement noise. We use the estimated angle of attack to stabilize the vehicle about a desired orientation $\alpha_{des}$. Rheotaxis corresponds to $\alpha_{des} = 0$, when the body orients upstream. Assuming the motion of the body is governed by (7.11) and the cross-stream position is held fixed (i.e., $u_1 = 0$), the control $u_2 = u_2(\hat{\mathbf{\Omega}}_{uni})$ is designed using feedback of the parameter estimates $\hat{\mathbf{\Omega}}_{uni} = (\hat{U}, \hat{\alpha})$ [111].

Suppose the estimated angle of attack can be modeled as $\hat{\alpha} = \alpha + \psi$, where the perturbation $|\psi| \leq \zeta$ is bounded [111]. Using a proportional control [111]

$$u_2(t) = K_\alpha(\alpha_{des} - \hat{\alpha}), \quad K > 0, \tag{7.28}$$

gives the closed-loop equation

$$\dot{\alpha} = K_\alpha(\alpha_{des} - (\alpha + \psi)). \tag{7.29}$$

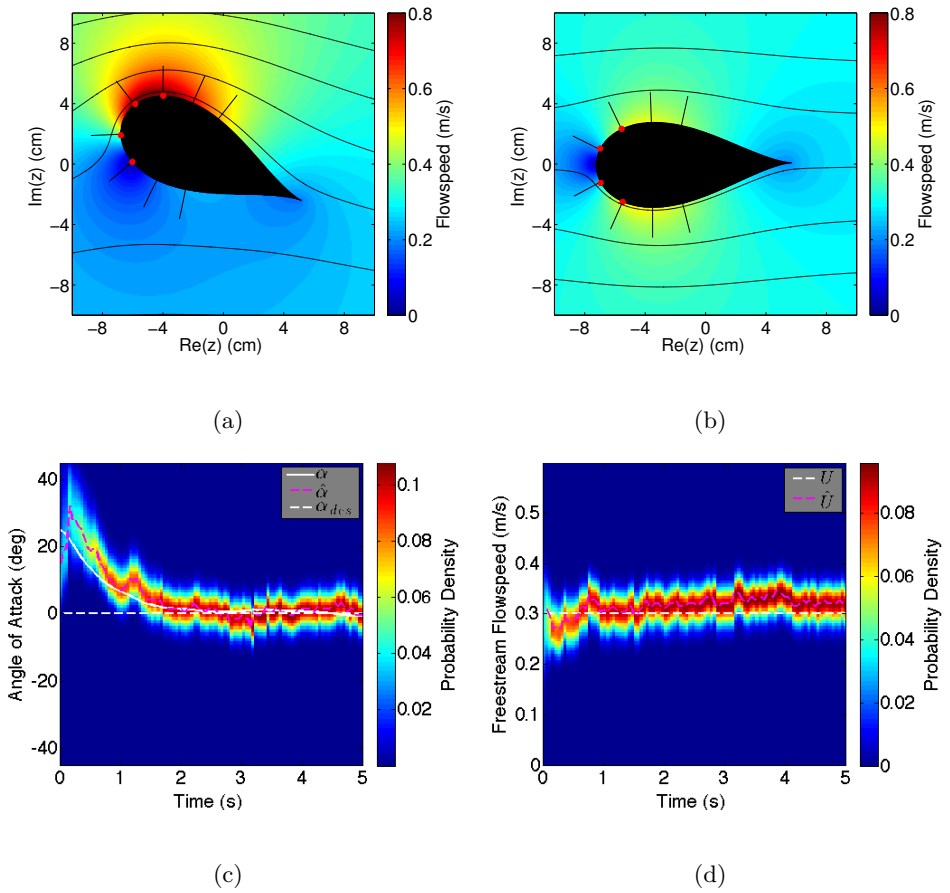


Figure 7.9: Simulation of the dynamic feedback control (7.28). (a,b) The initial and final orientation of the streamlined body; (c,d) marginal probability densities of the recursive Bayesian filter.

The Lyapunov function $V = (\alpha - \alpha_{des})^2/2$ reveals that if $\psi = 0$ and $\dot{\alpha}_{des} = 0$, then the quantity $\alpha - \alpha_{des} = 0$ is exponentially stable (see, e.g. [116, p. 114]). For $\psi \neq 0$, $\alpha(t)$ is uniformly, ultimately bounded for $|\psi| \leq \zeta$ with ultimate bound $|\alpha(t) - \alpha_{des}| \leq \zeta/K_\alpha$ [116, p. 347]. That is, by increasing $K_\alpha$ the steady-state error $\alpha - \alpha_{des}$ decreases.

Figure 7.9 shows a first-order, discrete-time simulation of the closed-loop control (7.29) using time step $\mathrm{d}t = 0.1$ seconds. Eight velocity sensors measure the square of the local flow velocity normal to the sensor and four pressure sensors measure six pairwise pressure differences. The pressure sensors are denoted by red circles and the flow

velocity sensors by protruding black lines, as shown in Figures 7.9(a) and 7.9(b). This sensor configuration corresponds to the experimental sensor positions that are presented in Section 7.5. The estimated angle of attack $\hat{\alpha}$ is provided by the recursive Bayesian filter (2.22) and the control gain is $K_\alpha = 1$. We assume the flow sensors are corrupted by white noise with $\sigma_{f_k} = 0.02$ m/s and the pressure sensors by $\sigma_{p_j} = 0.08$ kPa. The Bayesian filter is implemented with the motion matrix $\Psi = \Delta t \text{diag}([0\ u_2]^T)$ and process noise $\Sigma_p = \text{diag}([0.025\ (\text{m/s})^2, 0.05\ (\text{rad/s})^2])$.

Figures 7.9(a) and 7.9(b) show the initial and final orientation of the foil, respectively; Figures 7.9(c) and 7.9(d) show the marginal probability densities of the angle of attack $\alpha$ and freestream velocity parameter $U$. The actual flowspeed $U = 0.3$ m/s and angle of attack are depicted by the solid white lines; the parameter estimates are represented by a dashed magenta line. The desired angle of attack $\alpha_{des}$ is illustrated by the dashed white line. Note that the control (7.28) orients the body toward $\alpha = 0$ with estimation errors causing small deviations from zero angle of attack, consistent with the boundedness analysis above.

### 7.4.2 Multi-Modal Flow Estimation and Control for Station-Holding

In the presence of an obstacle the flowfield is approximated by (7.16) at high Reynolds number and (7.17) at lower Reynolds number. We approach the obstacle estimation problem separately, using the recursive Bayesian approach for the low-dimensionally parameterized flow model at high Reynolds number and a particle filter for the high-dimensional vortex model at low Reynolds number. The resulting estimate of the obstacle position is used in a proportional controller to enable station-holding. In both scenarios the free stream flowspeed and upstream position of the obstacle are known and the angle

of attack is fixed at $\alpha = 0$. These assumptions are justified in that a typical underwater mission could start in a uniform flow, in which case the results of Section 7.4.1 can be used to estimate the free stream parameters prior to approaching the obstacle.

In a high Reynolds number flow, the model (7.6) is parameterized by $\mathbf{\Omega}_{obs} = (U, \alpha, z_{obs}, d)$. Since the free stream flowspeed, angle of attack, and upstream obstacle position are assumed known, we estimate a subset of the obstacle parameters $\mathbf{\Omega}_{obs} = (y_{obs}, d)$ using the recursive Bayesian filter.

For station-holding control, the angle of attack is fixed (i.e., $\alpha = 0$, $u_2 = 0$) and the control $u_1 = u_1(\hat{\mathbf{\Omega}}_{obs})$ is designed using feedback of the estimated cross-stream obstacle position $\hat{y}_{obs}$. Similar to the rheotactic control, suppose the estimated cross-stream position of the obstacle can be modeled as $\hat{y}_{obs} = y_{obs} + \psi$, where the perturbation $|\psi| \leq \zeta$ is bounded. The proportional control

$$u_1(t) = K_s \hat{y}_{obs}, \quad K_s > 0, \tag{7.30}$$

gives the closed-loop equation for cross-stream obstacle position relative to the streamlined body (7.16), (7.17)

$$\dot{y}_{obs} = -K_s(y_{obs} + \psi). \tag{7.31}$$

Lyapunov analysis reveals that $y_{obs}(t)$ is exponentially stable for $\psi = 0$ and uniformly, ultimately bounded for $|\psi| \leq \zeta$ with bound $|y(t)| \leq \zeta / K_s$ [116, p. 347].

Figure 7.10 shows a first-order, discrete-time simulation of the closed-loop control (7.30) using time step $\mathrm{d}t = 0.1$ seconds. The free stream flowspeed is $U = 0.2$ m/s. We assume the same sensor configuration and noise characteristics as Section 7.4.1 with control gain $K_s = 1$. The Bayesian filter is implemented with the motion matrix $\Psi = \Delta t \mathrm{diag}([0\ u_1]^T)$ and process noise $\Sigma_p = \mathrm{diag}([1, 1])$ $(\mathrm{cm/s})^2$. Figures 7.10(a) and 7.10(b) show the initial and final position of the streamlined body relative to the obstacle, which is

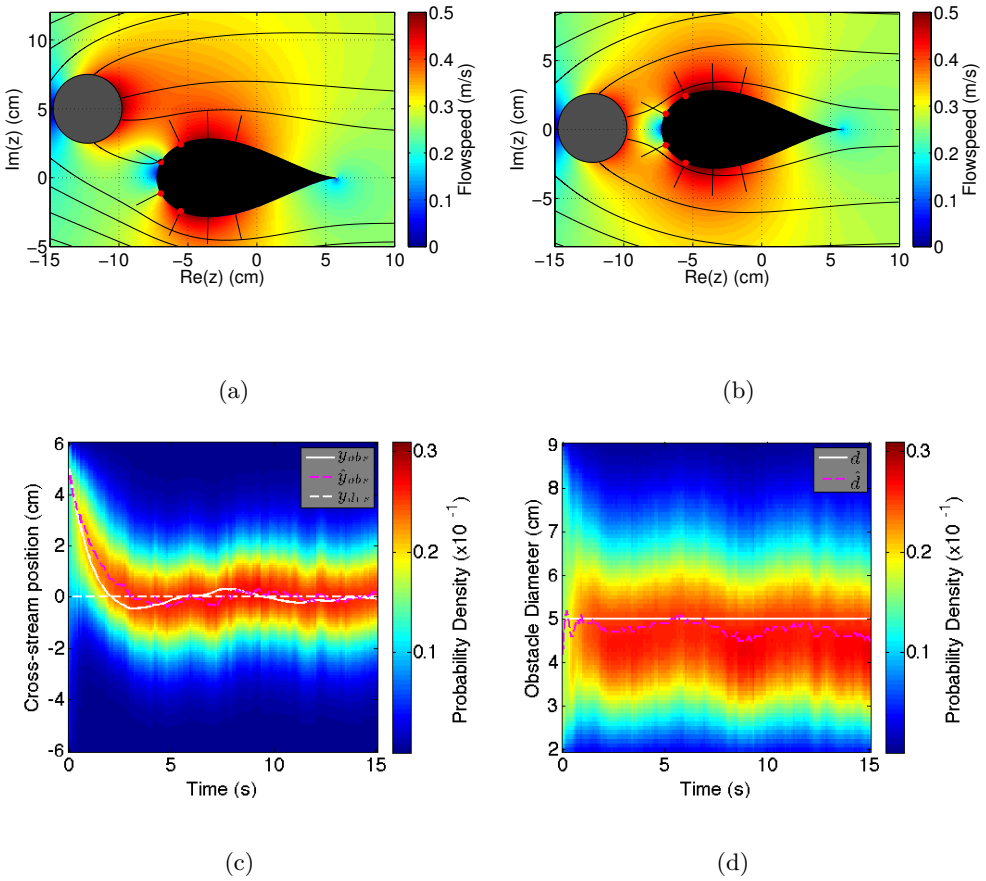


Figure 7.10: Simulation of the dynamic control (7.30). (a,b) The initial and final position of the foil; (c,d) marginal probability densities of the recursive Bayesian filter.

illustrated by the black circle. Figures 7.10(c) and 7.10(d) show the marginal probability densities of the obstacle position $y_{obs}$ and diameter $d$. The actual obstacle position and diameter are depicted by the solid white lines; the parameter estimates are represented by a dashed magenta line. The position corresponding to station-holding $y_{obs} = 0$ is illustrated by the dashed white line. Flow sensor positions are denoted by black lines protruding from the body in Figures 7.10(a) and 7.10(b), whereas pressure sensor positions are denoted by red circles. Note that the control (7.30) steers the foil toward $y_{obs} = 0$ with estimation errors causing small deviations from $y_{obs} = 0$, consistent with the boundedness analysis above. The recursive Bayesian filter also accurately estimates the obstacle diameter, as

shown in Figure 7.10(d).

At low Reynolds number, the parameter space of the flowfield model (7.17) associated with the Karman vortex street is defined by the vortex positions $\boldsymbol{z}_v$, circulation strengths $\boldsymbol{\Gamma}_v$, and free stream flow parameters $(U, \alpha)$. Because of the high dimensionality and nonlinear dynamics of this parameter space, the grid-based recursive Bayesian filter becomes computationally intractable, motivating the need for an alternative nonlinear estimation scheme for estimation of flowfield parameters $\boldsymbol{\Omega}_{Kar}$. Recall from Section 7.1.3, the Karman vortex street model (7.17) convects vortices through the flow; each vortex is injected into the flow from a cross-stream edge of the upstream obstacle. By estimating the vortex positions, one can reconstruct the position and diameter of the obstacle.

The success of this filtering algorithm is predicated on sensing the presence of a vortex from measurements collected by the artificial lateral line. The unobservability index provides a useful tool for quantifying the observability of the vortex near the foil. We calculate the empirical observability Gramian formed by assuming a single stationary vortex in the model (7.17). Under this assumption the empirical observability Gramian $W_O(z_v, \Gamma_v) \in \mathbb{R}^{3\times 3}$ is formed by perturbing the vortex position $z_v$ and circulation strength $\Gamma_v$. Evaluating $W_O$ for $z_v$ in the vicinity of the foil reveals the observability of a vortex for a given sensor configuration.

Figure 7.11 illustrates the unobservability index of the empirical observability Gramian for vortex positions near the foil. The foil is shown in solid black, where the black lines represent the flow velocity sensors and the red circles represent the pressure sensor positions. Note since the vortex circulation decays with distance, the unobservability index increases radially from the foil. Interestingly, symmetric areas of higher unobservability protrude diagonally toward the front and rear shoulders of the foil, indicating decreased vortex

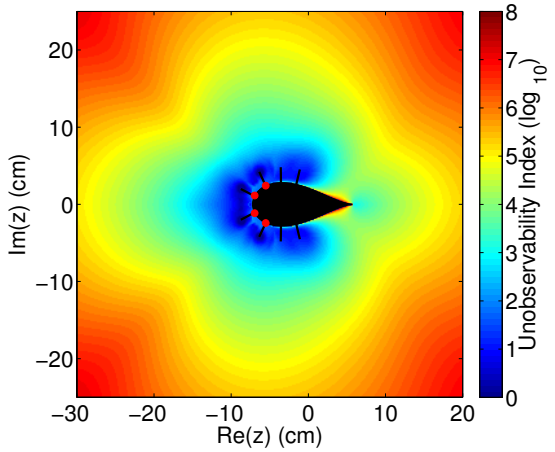


Figure 7.11: The unobservability index of a single vortex plotted around the vicinity of the foil. Areas of large unobservability index indicate "blind spots" where the measurements have difficulty observing the vortex.

observability in these areas. Since the unobservability is smallest near the foil, one can expect better estimation performance as a vortex approaches and decreasing performance after the vortex passes its point of closest approach.

By assuming that vortices move in approximately straight lines when not in the immediate vicinity of the foil, i.e. by ignoring Routh's rule [76], the cross-stream position of the vortex can be approximated as a function of the obstacle position and diameter, which allows one to minimize and transform the number of estimated parameters in $\mathbf{\Omega}_{Kar}$ to those needed for feedback control. Consider the Karman vortex street model (7.17). When the foil has sufficient stream-wise separation from the obstacle, the vortex street is characterized by vortices of opposite circulation strength in an alternating pattern [76]. The cross-stream position of the $j$th vortex is approximately $y_{v_j} \approx y_{obs} + \text{sign}(\Gamma_j)d/2$, giving the position of the $j$th vortex

$$z_{v_j} \approx x_{v_j} + i(y_{obs} + \text{sign}(\Gamma_\text{j})d/2), \tag{7.32}$$

where $x_{v_j}(0) = x_{obs}$. Substituting (7.32) into (7.17) yields a simplified model of vortex motion in terms of the cross-stream position of the obstacle.

We further simplify the model by assuming that the sensor array measures the presence of only a single vortex. This assumption is justified by noting that the flowspeed generated by a single vortex is inversely proportional to the distance from the vortex center, implying that in a Karman vortex street the component of the measurements produced by the closest vortex to the sensor array will dominate the signal. Under this assumption, the equations of motion of the obstacle shedding a single vortex relative to the foil are

$$\begin{aligned} \dot{y}_{obs} &= -u_1 \\ \dot{x}_v &= \mathrm{Re}\left(g(x_v + i(y_{obs} + \mathrm{sign}(\Gamma_v)d/2))\right) \\ \dot{\Gamma}_v &= 0 \\ \dot{d} &= 0 \\ \boldsymbol{\beta} &= q(\boldsymbol{z}; U, x_v, \Gamma_v, y_{obs}, d). \end{aligned} \tag{7.33}$$

The equations of motion in (7.33) represent the simplified kinematics of the Karman vortex street model (7.17) by assuming vortices convect in straight downstream lines and have sufficient stream-wise separation relative to the foil length such that only one vortex is in the foil's immediate vicinity. The particle filtering algorithm uses (7.33) to estimate the parameters $(y_{obs}, d)$ representing the cross-stream position and diameter of the vortex-generating obstacle.

Particle filtering has been used previously for bio-inspired flowfield estimation [83] and is well suited for this estimation problem because of its ability to incorporate nonlinear vortex dynamics, parameter constraints, and (possibly) nonlinear measurement noise models. Figure 7.12 illustrates simulation results of the station-holding control (7.30) using obstacle position estimates generated by the particle filter. The filtering algorithm

uses five hundred particles and assumes flow and pressure difference measurements following (7.14). In the simulation, the particles are integrated in time using equation (7.33), whereas the actual vortex advection and measurements are simulated using (7.17). Vortices are shed from the obstacle at a rate of 0.75 Hz, consistent with a free stream flowspeed of 0.2 m/s according to the Strouhal formula $\omega = \mathrm{St}(U/d)$ [155]. The particle filter assumes process noise with variance 0.05 m/s in the vortex motion, and measurement noise of $\sigma_f = 0.03$ m/s for the flow velocity sensors and $\sigma_p = 0.08$ kPa for the pressure difference measurements.

Figure 7.12(a) illustrates the component of each particle corresponding to the vortex position as a blue circle. The estimated vortex position is a magenta circle and the corresponding obstacle position and diameter estimate are illustrated by the gray half-circle. The actual vortices are represented by small black squares. The black half-circle illustrates the actual cylinder position. Figure 7.12(b) shows the estimated cross-stream position and diameter of the obstacle plotted versus time. Note that although the particle filter assumes there is one vortex in its vicinity, the estimation and control algorithm can perform station-holding when there are multiple simulated vortices near the foil. However, because the width of the foil and the obstacle are similar, vortices are deflected around the foil, breaking the linear motion assumption. This causes the particle filter to slightly over estimate the diameter of the obstacle, as illustrated in Figure 7.12(b).

## 7.5 Experimental Testbed for Flow Sensing and Control

This section describes the experimental hardware and software architecture for demonstrating the bio-inspired sensing, estimation, and control algorithms. Section 7.5.1 presents the IPMC sensor and foil design and fabrication. Section 7.5.2 describes the flow

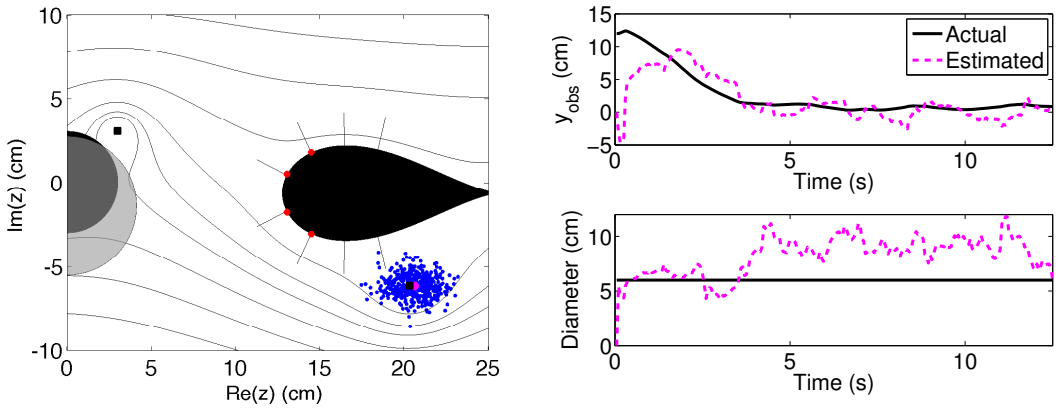


(a) (b)

Figure 7.12: Simulation of closed-loop control for station-holding at low Reynolds number. (a) illustration of the estimation algorithm at $t = 8$ seconds. (b) True and estimated cross stream position and diameter of the obstacle.

tank hardware and gantry system for controlling the streamlined body motion. Section 7.5.3 presents experimental data indicating that the IPMC sensors measure the square of the component of the flow normal to the sensor at its location. Section 7.5.4 presents a novel calibration strategy that employs the pressure sensors to calibrate the IPMC sensors at multiple angles of attack and flowspeeds.

### 7.5.1 IPMC Flow Sensors

Ionic polymer-metal composites (IPMCs) are an important class of electroactive polymers (EAPs) with built-in actuation and sensing capabilities [163], [164]. An IPMC sample typically consists of a thin ion-exchange membrane (e.g., Nafion), chemically plated with a noble metal as electrodes on both surfaces. IPMCs have inherent sensing properties: an applied force or deformation on an IPMC beam yields a detectable electrical signal (typically open-circuit voltage or short-circuit current) across the electrodes [165]. The direct mechanosensory property and inherent polarity of IPMCs are essential to the construction

of an artificial lateral line system and the collection of flow information [87], [166].

The IPMC sensors described here are fabricated with the traditional impregnation-reduction ion-exchange process [167]. Nafion-1110 (254 $\mu$m) films from Dupont are first roughened with fine sandpapers and the resulting residues on the film are removed with an ultrasonic cleaner. After the initial cleaning each film undergoes a two-step boiling procedure, first for thirty minutes in dilute 2 wt% hydrochloric acid to remove ions and impurities, then for thirty minutes in deionized (DI) water to remove the acid and swell the films. Following the boiling procedure, each film is immersed in a platinum complex solution ($[Pt(NH_3)_4]Cl_2$) for more than twelve hours to allow platinum ions to completely diffuse into the Nafion films through the ion-exchange process. Then, each film is rinsed with de-ionized water and immersed in a water bath at 40°C. The water is gradually heated to 60°C while 2 ml of sodium borohydride solution (5 wt% $NaBH_4$ aq) is added to the solution every thirty minutes to act as a reducing agent and complete the platinum deposition process. Finally, we cut each film into beam-shaped samples measuring 20 mm long and 2.5 mm wide, and solder two electric wire connectors to the platinum electrodes.

To prevent corrosion and maintain consistent sensing properties, we encapsulate each IPMC sensor with thick parylene (25 $\mu$m) in a parylene coater (PDS2035, Specialty Coating System, Inc.), where parylene C was deposited conformally on each sensor under a low pressure of 30 mTorr [168]. Although this process extends each sensor's useful life, the low-pressure parylene coating process dries the material, which inhibits operation. To counteract the drying effect, we soak each encapsulated IPMC sensor in a hot water bath of 80°C for sufficient time to reach proper operating levels of ionic hydration. A custom-built circuit box conditions the IPMC sensor signals, providing up to 20 channels of two-tier amplification and noise-reduction. The sensing signals of IPMCs, in the form

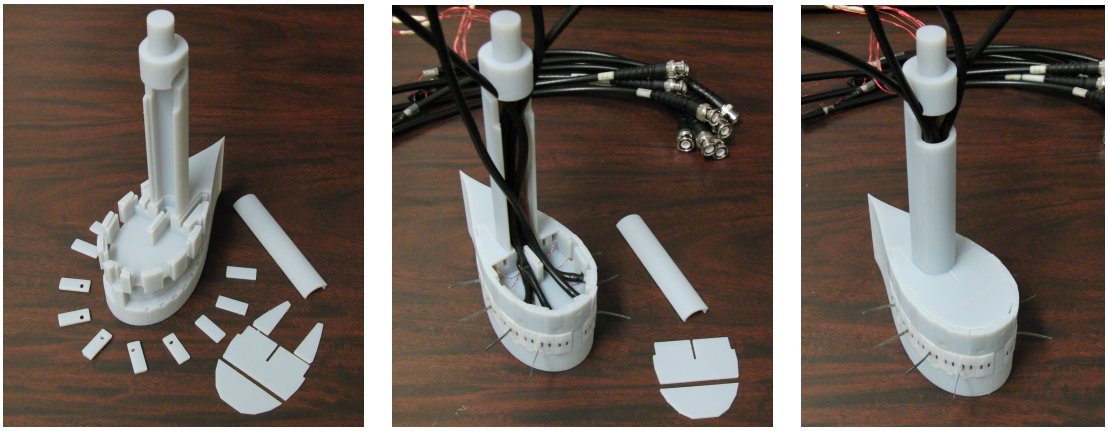

(a) (b) (c)

Figure 7.13: Modular design of robotic foil. An array of eight IPMC sensors are installed below an array of four pressure sensors.

of short-circuit current, are first converted into voltage signals and then amplified.

We designed and constructed a robotic fish prototype outfitted with eight IPMC sensors and four embedded pressure sensors [169], [165]. The robot prototype is a 3D-printed 2D-airfoil shape characterized by Joukowski mapping parameters $(R, \xi_0, c_0) = (4.35, -1.5, 2.85)$ cm and extruded in the vertical direction, as shown in Figure 7.13. The streamlined body is designed using a modular approach to (1) enable convenient installation and replacement of both IPMC and pressure sensors, (2) maintain flexibility in the number and placement of sensors around the body, and (3) ensure a compact structure appropriate for its operating environment. The body has ten clamping blocks on each side, providing twenty sensor mounting slots for IPMC sensors, as shown in Figure 7.13(b). Each IPMC sensor clamps into a block with its wires routed inside the body. Above the IPMC sensor blocks, the body has nine slots for mounting the pressure sensors, as shown in Figure 7.13(a).

The pressure sensors are mounted above the IPMC sensor block to minimize fluid

effects created by the longer IPMC sensors, which protrude into the flow. There are four pairs of symmetric slots and an additional slot at the nose of the body. We use four Millar Instruments (SPR-524) Mikro-Tip Catheter Pressure Transducers encased in an open ended delrin sheath using Teflon tape. The sensors are mounted in the forward-most symmetric slots, as shown in Figure 7.13(b) [78]. When mounted in this fashion the pressure sensors measure the static pressure, which enables analysis using the potential flow model in Section 7.1. The extra slots allow flexibility in the sensor configuration and provide the opportunity to expand the sensor array for future experiments. This compact design maintains the smooth surface of the body while providing enough clamping force to hold all the sensors, as shown in Figure 7.13(c).

### 7.5.2 Instrumentation, Control Hardware, and Flowfield Generation

Eight IPMC sensors are placed around the front of the prototype to measure the flowfield subject to manufacturing design constraints. The polar angles of the sensors are $\pm 84.9^\circ$, $\pm 105.6^\circ$, $\pm 130.7^\circ$, and $\pm 161.0^\circ$ measured with respect to the origin defined in Section 7.1.1. The sensor length direction is normal to the body surface and each sensor is mounted such that it responds to the two-dimensional flow ($z$-plane) tangential to the body surface at the mount point. Similarly, the polar angles of the four pressure sensors are $\pm 156.3^\circ$ and $\pm 170.7^\circ$, respectively. IPMC sensor signals are passed through the custom-designed amplifier and pressure signals are amplified via two PCU-2000 Pressure Control Units (Millar Instruments). The amplified signals are measured and processed using a National Instruments NI USB-6225 data acquisition board and LabVIEW software. Sensor measurements are assimilated into the recursive Bayesian filter by incorporating Matlab functionality within the LabVIEW software interface.

We generate a uniform flowfield using a 185 L flow tank manufactured by Loligo Systems (SW10275, modified) with an enclosed test section measuring $25 \times 25 \times 87.5$ cm. The test section of the flow tank is calibrated using a Hack FH950 portable flow meter [78]. The vehicle's orientation and cross-stream position are controlled using an overhead gantry system, elevated using a custom made 80/20 support structure. An LS-100-18-H linear lead screw table (Anaheim Automation, Inc.) coupled with a stepper motor (STM23Q-XAE, Applied Motion Products, Inc.) controls cross-stream motion and a second (STM23Q-XAE) rotary stepper motor attached to the linear screw table controls orientation. Each stepper motor takes commands from LabVIEW via an RS-232 serial connection. The drives contain built-in motion controllers that accept high-level ASCII text commands, most notably feed-to-length and jog commands for control of motor position or angular velocity. The stepper motors contain integrated encoders that can be queried directly from LabVIEW [78].

### 7.5.3 IPMC Flow Sensor Analysis

IPMC sensors produce measurements whose magnitudes are proportional to the amplitude of vibration. The structural and electro-mechanical modeling of an IPMC sensor subjected to pressure distributions created by a moving fluid remains the subject of ongoing work. This motivates the need to better understand basic components of the flow captured by each IPMC sensor measurement. This section presents experimental results suggesting that the standard deviation of the magnitude of each IPMC measurement closely corresponds to the component of the flow normal to the beam, evaluated at the tip of the sensor.

By collecting data at varying angles of attack and flowspeeds, we find a strong

correlation between the amplitude of the AC signal measured by each sensor and the square of the component of flow velocity normal to the sensor evaluated at the sensor tip, as generated using the potential flow model (7.2). Figure 7.14(a) shows the result of fitting the standard deviation $\chi(z_{f_k}; \mathbf{\Omega}_{uni})$ of measurements collected by the sensor with polar angle 130.7° ($k = 3$) for twenty seconds at flowspeeds $U \in [0, 0.6]$ m/s and angles of attack $\alpha \in [-30°, 30°]$ to the potential flow model (green). Calibration data are collected for 20 seconds at 500 Hz for each flowspeed and angle of attack combination. The standard deviation $\chi(z_k; \mathbf{\Omega}_{uni})$ of each 20 second data collection at $M$ different flowspeed and angle of attack combinations was calculated to generate the gray surface shown in Figure 7.14(a). Note that while each sensor's performance varies due to the manufacturing process, the sensors used here can generally detect flowspeeds as low as about 0.07 m/s when compared to measurements in still water.

The flowfield estimation algorithm requires a mapping between the sensor measurements (in $\mu A$) and the potential flow measured at the sensor location (in m/s). To accomplish this mapping we compute optimal fitting coefficients $(a_k, b_k)$ to the potential model by minimizing the fitting metric

$$J_k = \sum_{j=1}^{M} \|(a_k \chi_j(z_k; U_j, \alpha_j) + b_k) - |f_n(z_k; U_j, \alpha_j)|^2\|, \tag{7.34}$$

for sensors $k = 1, \ldots, 8$ and flow condition combinations $j = 1, \ldots, M$. The gray surface in Figure 7.14(a) shows the fitted standard deviation measurements corresponding to the sensor with polar angle 130.7°. The average error in each sensor over all flowspeeds and angles of attack is shown in Figure 7.14(b) (green), where each error bar is plotted at the sensor position. The error resulting from measurements of the square of the normal component of the flow (green) are plotted along with the average error assuming measurements of the square of the total flowspeed (blue) for comparison. Note that the two

measurement assumptions have similar average error for all sensors. Use of the normal component of the flow is justified under the assumption that deflection of an IPMC sensor is primarily due to fluid motion normal to the sensor face, thereby enabling this calibration strategy to accommodate measurement models incorporating higher fidelity sensor deflection dynamics in the future.

Note that Figure 7.14(a) shows one of the poorest model fits, yet the general structure still follows the trend of the potential flow model. Also note that the areas of the flowspace $(U, \alpha)$ corresponding to the largest disagreement between the measured and theoretical data lie at higher angles of attack where unmodeled flow separation and viscous effects are likely. This effect is the primary cause of the larger average error for sensors near the front of the foil as compared to those toward the rear of the foil in Figure 7.14(b).

Computing the calibration coefficients for each sensor as described above requires external references of the angle of attack and flowspeed. Prior work has shown that assimilating pressure difference measurements provides accurate estimation of flowspeed but often incorrectly estimates the angle of attack [78]. However, using simple pressure differencing in the control [78], [79] and selecting non-symmetric sensor pairs, the vehicle can be steered to a fixed angle of attack relative to the free stream flow velocity. Thus, by estimating the flowspeed at fixed, analytically derived angles of attack, the calibration procedure can be completed without a priori knowledge of the flow condition.

### 7.5.4 Pressure Array IPMC Sensor Calibration: Bootstrapping

The IPMC sensor array is a valuable sensing modality for underwater operation. However, since the electromechanical properties of these sensors are not well understood, a calibration procedure is required to associate a sensor measurement with a local flowspeed

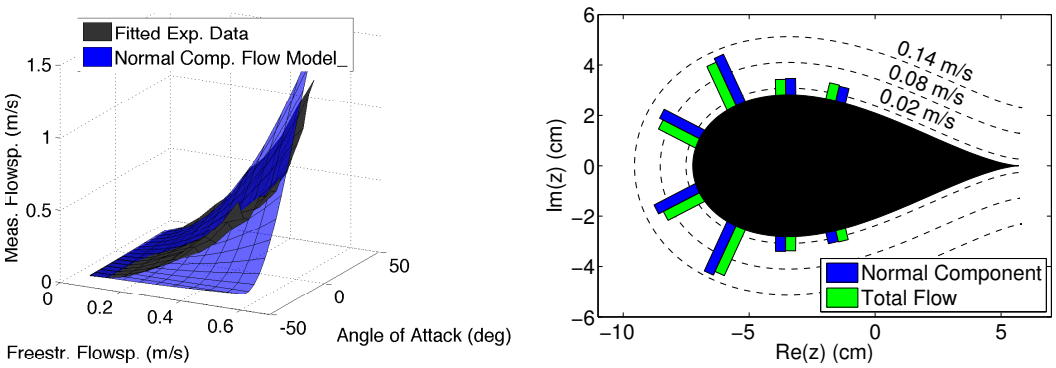


(a) (b)

Figure 7.14: (a) Calibration result fitting the standard deviation of IPMC measurements (gray) to the normal component of the flow (blue) for sensor located at polar angle 130.7°. (b) Average fit error for each sensor over all flow parameter combinations. The green error bars denote average error resulting from measurements of the total flow at the sensor tip, whereas the blue error bars represent the error resulting from measurements of the component of flow normal to the sensor.

measurement. This section presents a novel calibration procedure that utilizes the pressure sensor array to calibrate the IPMC sensor array without external position or orientation references. The procedure leverages the ability of pressure sensors to provide accurate estimation of the free stream flowspeed and utilizes pressure differencing control to steer the vehicle toward an orientation with zero pressure difference based on a chosen pair of sensors, as illustrated in Figure 7.15. We use a proportional feedback controller based on the pressure difference $\Delta P_{ij} = P(z_{p_i}; \mathbf{\Omega}_{uni}) - P(z_{p_j}; \mathbf{\Omega}_{uni})$ such that the steering control $u_2$ is [78]

$$u_2 = -K_p \Delta P_{ij}, \quad K_p > 0, \tag{7.35}$$

where $i$ and $j$ correspond to sensors placed on opposite sides of the body. Figure 7.15(a) shows three sensor pairing combinations used in the calibration process denoted by the

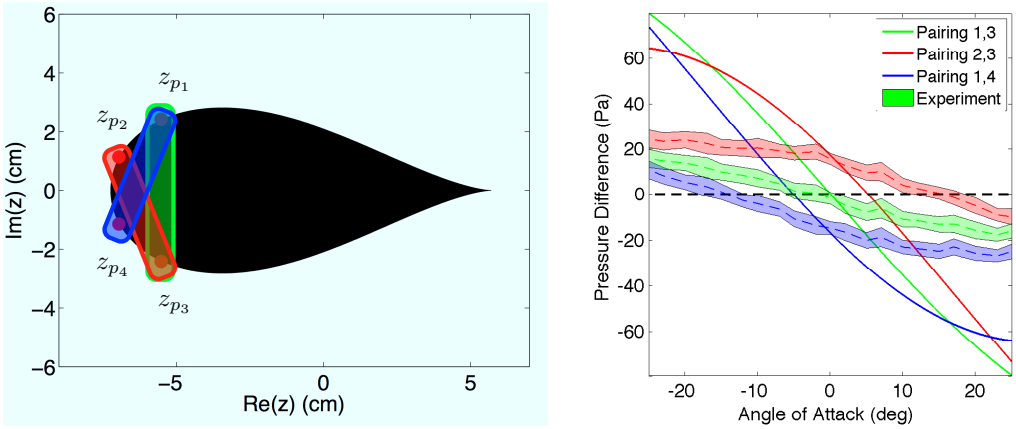


(a) (b)

Figure 7.15: (a) Sensor pair combinations for the bootstrapping calibration procedure. (b) Pressure difference as a function of angle of attack for the pressure sensor pairings.

blue pairing $(z_{p_1}, z_{p_4})$, the green pairing $(z_{p_1}, z_{p_3})$, and the red pairing $(z_{p_2}, z_{p_3})$. The corresponding pressure differences are plotted versus the angle of attack in Figure 7.15(b) for free stream flowspeed $U = 0.17$ m/s. The solid colored lines correspond to pressure differences based on potential flow theory, whereas the dashed lines correspond to experimental pressure differences. The shaded region of the experimental data curves correspond to one standard deviation of the measured differences. Note, due to flow separation, unmodeled viscous effects, and three-dimensional flow effects [78], the experimental pressure differences are less than the theoretically predicted differences at high angles of attack, resulting in larger angles of zero pressure difference for non-symmetric sensor pairs. The estimated flowspeeds and analytically derived angles of zero pressure difference in Figure 7.15(b) provide flow conditions from which the IPMC sensor calibration procedure in equation (7.34) calculates the required calibration coefficients.

The calibration procedure is as follows. The body is placed in an unknown uniform flow condition. The steering control (7.35) calculates the angular rate using pressure dif-

ferences between a symmetric pair of pressure sensors. Choosing a symmetric pair steers the vehicle to zero angle of attack. Meanwhile, the recursive Bayesian filter assimilates distributed pressure difference measurements and produces an estimate of the free stream flowspeed. After sufficient settling time, we collect 500 samples from each IPMC sensor and compute the standard deviation from each sensor's samples. Recording the estimated flowspeed, zero angle of attack, and standard deviation from each of the $N_f = 8$ IPMC sensors comprises sufficient data for all eight IPMC sensors at one flow condition combination in equation (7.34). Next, a pair of pressure sensors is chosen to stabilize a non-zero angle of attack, which we calculate analytically using the uniform potential flow model. Following a similar estimation and data collection process, one generates an additional flow condition for equation (7.34). Repeating the process for all remaining non-symmetric sensor pairs completes data collection for a given flowspeed. We then change the free stream flowspeed and repeat the estimation and data collection procedure to produce a sufficient number of data points to calculate the optimal coefficients $(a_k, b_k)$ in equation (7.34) for all $k = 1, \ldots, N_f$ IPMC sensors. This work considers three pressure sensor pair combinations corresponding to the pressure sensors located on the surface of the foil with polar angles $(156.3°, -156.3°)$, $(170.7°, -156.3°)$, and $(156.3°, -170.7°)$ whose analytical zero pressure differences correspond to $0°$, $5.1°$, and $-5.1°$ angles of attack, respectively.

## 7.6 Experimental Results

This section presents experimental results demonstrating the rheotaxis and station-holding results of Sections 7.4.1 and 7.4.2 using the hardware described in Section 7.5.

### 7.6.1 Experimental Demonstration of Rheotactic Control

This section uses the estimated flowfield parameters from the recursive Bayesian filter in a dynamic feedback controller that stabilizes the vehicle about a desired angle of attack $\alpha_{des}$. The calibration procedure of Section 7.5.4 enables use of each IPMC sensor measurement as a measurement of the square of the normal component of the flow at the sensor location. Assimilating the IPMC flow measurements and pressure difference measurements into the recursive Bayesian filter provides an estimate of the free stream flowspeed and angle of attack of the body over time. The estimated angle of attack is used in the feedback control algorithm (7.28) to steer the vehicle toward a desired angle of attack. We assume pressure and IPMC measurement variances of $\sigma_p^2 = .08$ kPa and $\sigma_{IPMC}^2 = 0.03$ m/s, respectively. The controller gain is $K = 0.2$ and the control and estimation loop runs at ~5 Hz.

Figure 7.16 illustrates experimental results of the flowfield estimation and control for rheotaxis under step inputs to the desired angle of attack. Figure 7.16(a) illustrates the marginal probability density of the angle of attack estimation plotted versus time for a 75 second experiment. The dashed white line corresponds to the desired angle of attack $\alpha_{des}$ versus time, whereas the magenta and solid white lines correspond to the estimated $\hat{\alpha}$ and actual $\alpha$ angles of attack, respectively. Note that the recursive Bayesian filter converges to the actual angle of attack and the control algorithm steers the vehicle to the desired orientation. Figure 7.16(b) shows the marginal probability density of the free stream flowspeed estimation versus time along with the actual (solid white) and estimated (dashed magenta) flowspeed.

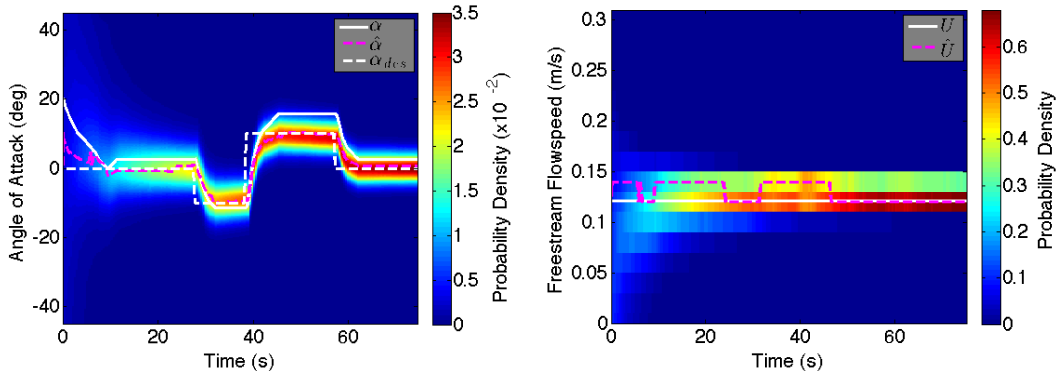


(a) (b)

Figure 7.16: Experimental implementation of estimation and control for rheotaxis. (a) Marginal probability density of angle of attack plotted versus time. (b) Marginal probability density of free stream flowspeed estimation plotted versus time.

### 7.6.2 Experimental Demonstration of Station-holding Control

This section presents experimental results of the station-holding control following Section 7.4.2. Figure 7.17 illustrates experimental results of the flowfield estimation and control algorithms for station-holding using the potential flow model (7.4) with velocity potential (7.6) and cross-stream control (7.30). An obstacle with diameter $d = 5.08$ cm was centered 5.08 cm upstream of the foil. To account for the significant model error, assume measurement noise $\sigma_{f_k} = 0.1$ m/s and $\sigma_{p_j} = 0.2$ kPa for the calibrated IPMC and pressure difference measurements, respectively. The free stream flowspeed is $U = 0.25$ m/s.

Figure 7.17(a) shows the marginal probability density of the estimated cross-stream position $y_{obs}$. The solid white line corresponds to the actual cross-stream position, whereas the dashed white and magenta lines correspond to the desired and estimated cross-stream positions, respectively. The initial cross-stream position was $-5.5$ cm. Note that although the filter shows steady-state estimation error, when coupled with feedback control

the algorithm steers the foil such that it maintains its position within one centimeter position error. The potential flow model (7.6) shows significant deviation from experimental measurements for almost all sensors, which can introduce estimation error or even filter divergence. However, since potential flow theory captures the large scale effects of the wake, the distributed nature of the array and multi-modal functionality of the artificial lateral line overcomes the model error when estimating the cross-stream position of the obstacle.

Figure 7.17(b) shows the marginal probability density of the estimated obstacle diameter. The estimated diameter is illustrated by the dashed magenta line, whereas the actual obstacle diameter is illustrated by the solid white line. Note that due to unmodeled viscous and boundary layer effects, the recursive filter significantly overestimates the diameter of the obstacle. This may be attributed to flow separation occurring further upstream on the obstacle than in the potential flow model, which causes the measurements to emulate a larger obstacle than predicted by the theoretical model.

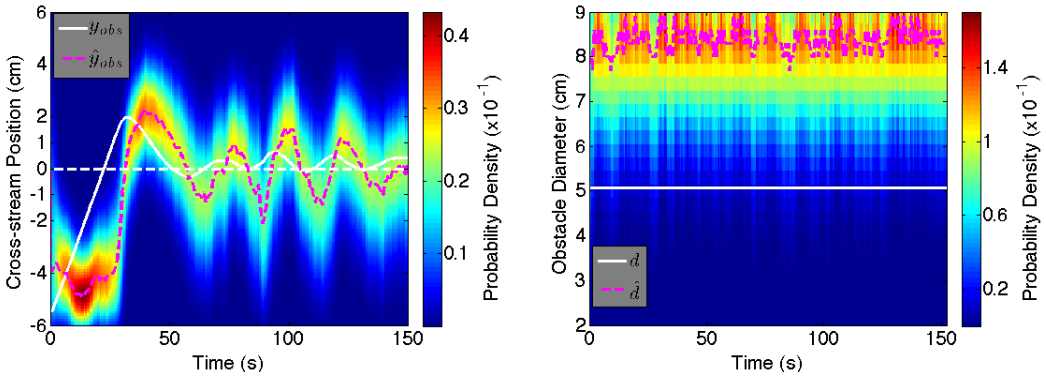


(a) (b)

Figure 7.17: Experimental implementation of station-holding estimation and control. Marginal probability density of (a) cross-stream position and (b) diameter of obstacle plotted versus time with actual (solid white) and estimated (dashed magenta) quantities. The dashed white line shows $y_{obs} = 0$ corresponding to when the foil lies directly behind the obstacle.

# Chapter 8: Conclusions and Suggestions for Future Work

## 8.1 Summary of Contributions

This dissertation describes an observability-based framework for optimizing the control of a multi-agent system tasked with sensing a flowfield. By improving a multi-sensor system's ability to observe a flowfield, the performance of a flowfield estimation scheme increases. Indeed flowfield observability is important for applications such as environmental sampling in hurricanes, wake sensing for formation flight, and bio-inspired sensing, where estimates of flow properties are required in feedback control.

A main advantage of using the observability framework is that it is independent of the specific estimation strategy used and therefore applies to any estimation application. This dissertation derives dynamic, nonlinear output feedback control strategies incorporating both flowfield estimates and measures of flowfield observability to optimize closed-loop control for flowfield sensing. Numerical simulations illustrate the value of the nonlinear control strategies for hurricane sampling with multiple unmanned aircraft, wake sensing to formation flight of two aircraft, and bio-inspired, hydrodynamic sensing for feedback control of a robotic underwater vehicle with a multi-modal artificial lateral line. In each application the observability-based optimization framework serves as a useful tool for experimental design.

Sections 8.1.1–8.1.3 review the contributions of the observability-based control and

sensing framework in the context of the three applications presented in this dissertation. Section 8.2 describes ongoing work and proposes areas for future research.

### 8.1.1 Environmental Sampling with Multi-vehicle Systems

A strong flow presents challenges to controlling multiple autonomous vehicles to a desired formation. The presence of strong flows limits the authority of the vehicle to completely dictate its inertial direction of travel, making path planning and collective formation control algorithms more difficult to design. However, this dissertation uses feasibility analysis and Lyapunov-based control to design decentralized multi-vehicle control algorithms driving particles to desired feasible formations in strong flowfields. We utilize an idealized vehicle model consisting of identical unit-speed Newtonian particles with gyroscopic steering control in a flowfield whose magnitude can exceed unity. We provide feasibility criteria for trajectories in a flowfield, and derive steering control algorithms that stabilize vehicle trajectories to straight lines, circles, a family of non-convex curves called folia, and spirographs. Using the curvature control, decentralized multi-vehicle control algorithms stabilize parallel, circular, folia, or spirograph formations with specified position of the formation in an inertial reference frame.

This dissertation not only expands the applicability of multi-vehicle control to strong flowfields, but also derives control algorithms to steer vehicles to non-convex patterns, namely the quadrifolium and the spirograph. These formations may produce better data in environmental sampling missions than those currently in use. Coupled with kinematic constraints analyzing the feasibility of families of sampling trajectories, the control algorithms derived in this dissertation can be used to provide vital information for multi-vehicle sampling missions by allowing researchers to choose from various families of formations

based on both the goals of the sampling mission and the feasibility of the sampling trajectories.

Chapter 4 addresses how a flowfield with vertical shear can be exploited as a means of controlling vehicle speed via altitude regulation. We present a three-dimensional model of self-propelled particle motion in which each particle moves at constant speed relative to the flow in the horizontal plane and controls its climb rate. Decentralized multi-vehicle control algorithms are derived to stabilize feasible parallel formations with equal horizontal speed and circular formations with equal particle spacing. In addition, a recursive Bayesian filter framework allows estimation of parameters defining and unknown flowfield; the resulting flowfield estimates are utilized in the control algorithms.

Using the multi-vehicle control algorithms of Chapter 3, Chapter 5 presents an adaptive, observability-based, multi-vehicle sampling algorithm that maximizes the observability of an estimated flowfield. The algorithm steers vehicles to optimal sampling trajectories selected from a parameterized family of candidate sampling formations. The observability of the parameters characterizing the flowfield are evaluated along candidate formations using measures of the empirical observability Gramian. Optimal flowfield observability is achieved by minimizing the unobservability index, which is the reciprocal of the smallest singular value of the empirical observability Gramian. A recursive Bayesian filter provides estimates of the flow to the steering control algorithm, enabling operation in an unknown flowfield. Numerical simulations of the adaptive algorithm in a Rankine vortex suggest that for circular sampling formations the algorithm is attracted to formations that cross the radius of maximum wind, specifically formations where the center of the circular formation is near the radius of maximum wind.

### 8.1.2 Wake Sensing for Formation Flight

Aircraft may operate in close proximity to increase flight endurance, particularly for aerial refueling and for reducing induced drag. To perform these tasks autonomously, an unmanned aircraft must estimate its position relative to other aircraft in the formation. This dissertation addresses how measurements of the aerodynamic effects caused by flying in close proximity can be used to estimate the relative positions of two aircraft in formation flight.

Chapter 6 uses lifting-line theory to model a two-aircraft formation and derives observability-based optimal control strategies that steer the follower aircraft to a desired relative position. The follower aircraft collects noisy measurements of the aerodynamic signature created by the leader's wake. We assess the observability of the leader aircraft using measures of the empirical observability Gramian and implement a recursive Bayesian filter to estimate the leader aircraft's wake parameters. Receding-horizon and level set methods of optimal control use the unobservability index as a cost metric and incorporate estimates of the leader's position provided by the Bayesian filter. The resulting trajectories avoid regions prone to degraded estimation performance, thus improving the feedback control. Numerical simulations of formation flight and aerial refueling applications illustrate that the proposed control algorithms successfully steer the vehicle to a desired relative position while simultaneously estimating the wake parameters.

### 8.1.3 Bio-inspired Flow Sensing and Feedback Control

Toward bio-inspired flow sensing and control, this dissertation describes the design and implementation of a multi-modal artificial lateral line for flow sensing and feedback control of an underwater vehicle. Tools from potential flow theory are used to model the

flow around a foil in a uniform flow and in the presence of an upstream obstacle. Using the fluid model, we derive a measurement model consisting of local flow velocity and pressure difference measurements inspired by the superficial and canal neuromasts of the fish lateral line.

The uniform flow model is characterized by the free stream flowspeed and angle of attack of the foil relative to the oncoming flow. This dissertation derives observability-based sensor placement strategies for maximizing observability of the uniform flow parameters. Analysis of multiple measures of the empirical observability Gramian reveal two optimal sensor locations, one at the nose optimally observes the angle of attack and one at the point of maximum flowspeed optimally observes the free stream flowspeed. We incorporate the single sensor results to optimize a multi-sensor configuration by exploiting linearity of the Hermitian empirical observability Gramian. The proposed placement, in which one sensor is located at the nose of the foil and the remaining sensors are distributed around the foil to optimally observe the free stream flowspeed at varying angles of attack, outperforms 99.9% of random sensor configurations at estimating the flow parameters. Performance is assessed using the KL divergence, which measures the distance of the posterior probability density function of the recursive Bayesian filter from perfect statistical knowledge of the flow parameters.

Chapter 7 designs theoretically justified Bayesian filtering strategies based on the flow and measurement models to estimate properties of the flow for use in feedback control. The recursive Bayesian filter highlights the complementary nature of flow velocity and pressure difference measurements for estimating the flowspeed and angle of attack of a foil in a uniform flowfield. In addition, we present a recursive Bayesian filter for estimating the cross-stream position of an obstacle in a moderate to high Reynolds number environment

where the wake of the obstacle is turbulent, as well as a particle filtering algorithm for estimating the cross-stream position by sensing the presence of vortices shed from the obstacle in the low Reynolds number regime. The estimated flow properties motivate the design of feedback control strategies to steer an underwater vehicle for bio-inspired behaviors including (positive) rheotaxis (the tendency to orient upstream) and station-holding (the tendency to hold position behind an upstream obstacle). Lyapunov-based techniques justify the derivation of control algorithms steering the vehicle to a desired angle of attack or cross-stream position behind an obstacle using estimated flow properties in feedback control.

This dissertation also presents experimental results demonstrating bio-inspired hydrodynamic sensing and control algorithms on a robotic prototype outfitted with a multi-modal artificial lateral line. We demonstrate autonomous rheotaxis and station-holding behaviors using a robotic foil outfitted with an array of distributed pressure and ionic-polymer metal composite (IPMC) sensors. Potential flow models show a correlation between the standard deviation of measurements from an IPMC sensor and the square of the component of flow normal to the sensor. Using this result, we derive a novel bootstrapping calibration strategy leveraging the strengths of pressure difference measurements to generate calibration coefficients for the IPMC sensors and demonstrate performance of the multi-modal system. Incorporating bio-inspired sensing and control strategies like those presented in this dissertation may one day allow underwater vehicles to operate in dark, murky, and cluttered environments where traditional sensing modalities are hindered.

## 8.2 Ongoing Work and Suggestions for Future Research

### 8.2.1 Ongoing Work

This dissertation uses tools from observability to optimize sampling in multi-agent systems, specifically for improving estimation of flowfields. Increasing observability results in improved estimation performance, which applies to any estimation strategy (particle filter, grid-based recursive Bayesian filter, Kalman filter, etc.). However, challenges remain in proving a direct correspondence between observability and estimator performance. Though Chapter 2 shows observability has a relation to estimation performance through the Fisher-information matrix, it applies only to time-invariant parameter estimation applications. A time-varying equivalent remains to be shown.

In general, observability is dependent on the state-space realization of the model, implying that observability analysis may reveal different results for alternate state-space realizations of the same model. Moreover, computation of the empirical observability Gramian suffers from the curse of dimensionality; for high-dimensional state-spaces, observability analysis can be computationally expensive, necessitating new, more efficient computational and analysis techniques. Tools from principal component analysis [170] may prove valuable for assessing the observability of more realistic infinite dimensional flowfield models by decomposing the model into a finite number of principal modes that capture the dominant flow dynamics.

Also note that this dissertation considers observability of time-invariant parameters defining a flowfield, rather than dynamic parameters. Considering time-varying states in the observability analysis introduces a temporal component to the coordinated sampling problem, weighting measurements in both *space* and *time*, rather than just space. This

is particularly applicable to environmental sampling where time-varying flows introduce temporal weighting to the sampling trajectories and wake sensing where vehicle velocities significantly affect the structure of the wake and therefore its observability.

The following paragraphs address ongoing work specific to each of the three applications presented in this dissertation. Section 8.2.2 proposes areas for future research.

**Environmental and Hurricane Sampling**

There are a number of directions the adaptive sampling algorithm can be expanded. At the multi-vehicle control level, future research seeks to derive control algorithms stabilizing a wider set of sampling formations in strong flows and continues investigation of general flowfield properties that dictate the feasibility and convergence properties of multi-vehicle formations. Additionally, experimental validation of the strong flow multi-vehicle control algorithms would lend further credence to the applicability of this control framework in real applications.

The adaptive sampling algorithm used observability as a metric to optimize the sampling formation, but many other metrics may prove useful. For example, the algorithm optimizes the sampling formation parameters using the estimated flowfield parameters, not accounting for uncertainty in the estimate. Future algorithms could incorporate uncertainty by scaling the size of the perturbations in the empirical observability Gramian based on the uncertainty of the flowfield states in the estimator. Other possible avenues for optimization could include information criteria [171], [172] or minimizing the uncertainty in a forecast model [52], [173].

**Wake Sensing for Formation Flight**

For close formation flight, observability measures served as a cost metric for deriving optimal control algorithms that steer a follower aircraft to a position relative to the leader.

We use infinite line vortices to represent the wing-tip vortices shed from the lead aircraft and lifting-line theory to represent the wing of the follower aircraft. This approach provides a basic model for assessing the feasibility of wake estimation and control that has been used throughout the literature [68], [60], [149], but realistic aerodynamics of two aircraft in formation are significantly more rich. A higher fidelity model must incorporate time-varying, unsteady fluid dynamics that produce a complex wake structure. In proximities within half a wingspan, the trailing vortices of the lead aircraft can be dispersed by the presence of the follower, which is unmodeled in the analysis of this dissertation. In addition, we ignore effects created by additional structural components (fuselage, elevator, rudder, etc.) in the aerodynamic model as well as the effect of relative velocities on the observability of the wake.

The optimal control algorithms used to derive observability maximizing trajectories use simplified kinematics of the relative motion of the aircraft. We assume the follower aircraft kinematically controls its velocity relative to the leader and neglect longitudinal motion between the vehicles, assuming the leader remains a fixed distance ahead of the follower at all times. A high fidelity six degree-of-freedom motion model including elevator, aileron, and rudder dynamics can facilitate derivation of more realistic optimal control strategies that incorporate observability measures and are robust to model uncertainty and wind disturbances that are likely in the highly unsteady aerodynamic regime associated with close formation flight.

**Bio-inspired Control and Hydrodynamic Sensing**

The bio-inspired flow sensing and control work of Chapter 7 can be expanded in a few areas. Section 7.4.2 presents a particle filtering strategy for estimating the position of an obstacle in flows with Reynolds number corresponding to the existence of a Karman

vortex street. Experimentally, we did not detect the presence of vortices in the range of Reynolds numbers corresponding to the Karman vortex street regime. This may be due to unmodeled hydrodynamic and electromechanical interactions between the vortices and sensors that mask the signature created by a passing vortex or dissipate the oncoming vortices as they approach the sensor array. In ongoing work, we seek to adapt the experimental procedure and sensor configuration in order to detect the presence of vortices shed from an upstream obstacle. Current work employs dye injection techniques to visualize vortex shedding and quantify their sensor signature on the artificial lateral line. In addition, continued refinement of the fabrication and manufacturing process of the IPMC sensors can miniaturize each sensor while maintaining or improving the robustness and signal-to-noise characteristics of the array.

Potential flow models provide a first step toward analytical derivation of sensor placement strategies and model-based flowfield estimation, but represent highly idealized models of real underwater flow environments. Because the empirical observability Gramian requires only the ability to simulate a system, future work could expand the sensor placement problem to high fidelity, three-dimensional flowfield and vehicle models and weigh tradeoffs between different sensing modalities incorporated into the artificial lateral line. By analyzing three-dimensional fluid models with fish-shaped bodies, observability analysis may explain the spatial distributions of superficial and canal neuromast sensory systems on various fish species.

### 8.2.2 Suggestions for Future Research

**Modality-based Optimization for Multi-vehicle Sampling**:

In current surveillance and environmental monitoring applications, autonomous and

remotely piloted vehicles are typically outfitted with a single sensing modality such as a camera [45], [29] or flow velocity sensor [9]. As the cost, size, and power requirements of multi-modal sensing systems enable operation on fleets of autonomous and remotely piloted vehicles, scientists will receive unprecedented data from dynamical processes in our environment. Before such systems can be implemented effectively, there exists a need to coordinate sampling trajectories of vehicles in the fleet to autonomously execute their mission while optimizing trajectories specific to each agent's sensing capability.

Future sampling missions may contain a fleet of heterogenous vehicles, each outfitted with sensing capabilities specialized for a given task. Optimizing the sampling performance of such a fleet of vehicles will require development of new feedback algorithms. Particular attention must be focused on (1) coordination of vehicles with heterogenous dynamics and (2) optimization of spatiotemporal sampling of vehicles with mixed sensing capabilities. For example, while monitoring extreme weather like hurricanes, manned assets must fly at altitudes above 5000 ft and typically collect wind, temperature, and pressure data, as shown in Figure 8.1. Simultaneously, weather satellites pass over the storm collecting data in the electromagnetic spectrum. In the future, high altitude unmanned aircraft may autonomously fly over the storm gathering radar and precipitation data [2], while smaller unmanned aircraft collect windspeed, pressure, and temperature data in the lower altitudes where the thermodynamic interactions of the air-sea interface take place. Additionally, ocean drifters [174] and controlled gliders [8] may operate at and under the ocean surface collecting further data. This fleet has sensing agents with constrained dynamics (satellites and drifters) and controllable agents (UAVs, manned aircraft, and underwater gliders) whose trajectories can be coordinated to complement the spatiotemporal sampling density of the constrained sensors. Coordinated control can exploit specific sensing capabilities

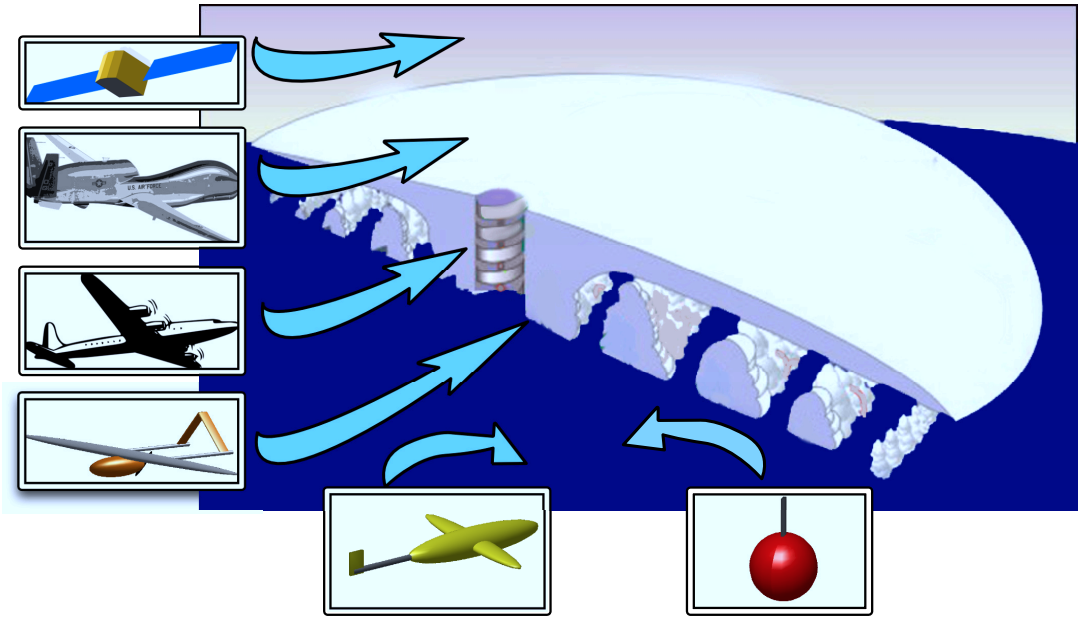

Figure 8.1: A fleet of sampling vehicles can improve hurricane forecasts by coordinating motion to (1) target measurements specific to their sensing capability, and (2) provide continuous coverage of the sampling domain. Photo credit [175].

allowing the fleet to better capture dynamical processes within the storm.

**Sensing and Actuation in Bio-inspired Systems**:

Chapter 7 derives sensing and steering strategies for bio-inspired behavior, assuming quasistatic motion so the foil's movements have minimal effect on the surrounding fluid behavior. This assumption allowed derivation of an optimal placement strategy for observing properties of the flow. However, observation of a flowfield can be improved both by configuring a sensor array *and* steering the vehicle to optimally capture fluid dynamical effects. Figure 8.2(a) illustrates two methods for observing a flowfield with an array of sensors. Figure 8.2 illustrates the problem addressed in Chapter 7, where the goal is to optimize the configuration of the sensing array on the body of the vehicle. Figure 8.2(b) illustrates how one may actuate the vehicle in order to better observe the surrounding

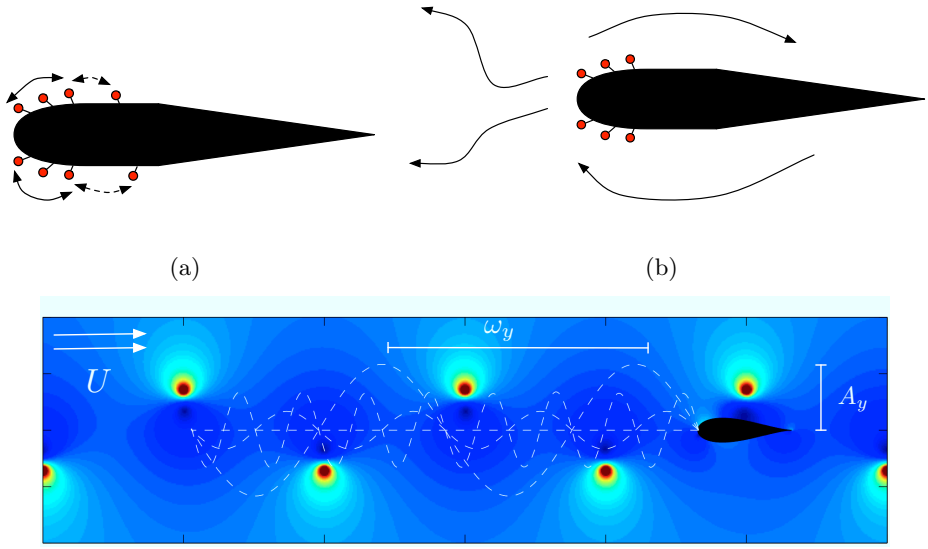


Figure 8.2: An array of sensors can observe a flowfield by (a) optimally placing sensors on the vehicle and (b) optimally actuating the vehicle to capture significant flow characteristics, such as (c) an optimized slalom pattern for observing the Karman vortex street.

flow. An example of how actuation may better observe the flow is shown in Figure 8.2(c), where the underwater vehicle may slalom within the Karman vortex street at optimal spatial amplitudes $A_y$ and frequencies $\omega_y$ in order to better observe the wake model.

In reality, a underwater vehicle's interaction with the flow is never passive. Even minute actuation can induce flow separation, vortex shedding, or similar fluid dynamic effects. Recent studies have separately addressed biomimetic actuation [176], [177], [178], [179] or sensing [180], [79], [149], [181], [182], [183] for robotic underwater platforms, but very few have addressed both. In recent work combining the two research areas, Phelan et al. [184] designed a robotic fin to investigate sensorimotor control in fish. The ribs of the fin were outfitted with strain gauges to detect propulsive forces and pressure sensors were mounted at the flank of the fin to detect flows during actuation [185]. However, this work studied sensory systems for prediction of propulsive forces generating fish motion,

rather than exploring the effect of actuation on sensing externally generated hydrodynamic phenomena.

The effects of self-actuation on bio-inspired sensing are not well understood. The Mexican blind cavefish exhibits repeated kick and glide cycles in its swimming locomotion that is thought to correspond to a propulsion phase (kick) followed by a sensing phase (glide) where the lateral line detects the animal's nearby surroundings [186]. Does this behavior suggest that actuation blinds the fish to external hydrodynamic phenomena during the kick phase, requiring the animal to glide in order to regain lateral line sensing ability, or does the fish induce fluid motion during the kick phase to produce a scannable flowfield for lateral line sensing? Conversely, trout exhibit Karman gaiting, a continuous sinusoidal-like motion in which the fish slaloms between vortices shed by an upstream obstacle [187], [75]. This behavior might suggest that the animal can sense external hydrodynamic structures during continuous actuation, rather than in cyclic fashion like the blind cavefish in still water.

A future research direction might seek to understand the effects of actuation on sensing ability in flexible robotic systems. By modeling the hydrodynamic and body interactions during actuation, one can better understand the effect of self-induced fluid motion on sensing of external hydrodynamic structures with an artificial lateral line. This research will require the use of high fidelity unsteady fluid dynamic models and flexible body dynamics to accurately model flow phenomena that alter response characteristics of the artificial lateral line during propulsive actuation. With a better understanding of the coupling between actuation and sensing, experimental vehicles can be designed to utilize sensorimotor advantages of both biomimetic actuation and sensing. Such work may enhance the performance and autonomy of unmanned underwater vehicles by broadening

the flow regimes in which they can safely operate.

# Bibliography


[1] National Aeronautics and Space Administration. Weather forecasting through the ages.
http://earthobservatory.nasa.gov/Features/WxForecasting/wx2.php, April 2014.

[2] Ruba A. Amarin et al. Estimates of hurricane wind speed measurement accuracy using the airborne hurricane imaging radiometer. In *Proceedings of the 29th Conference on Hurricane and Tropical Meteorology*, Tucson, AZ, May 2010.

[3] S. J. Portugal, T. Y. Hubel, J. Fritz, S. Heese, D. Trobe, B. Voelkl, S. Hailes, A. M. Wilson, and J. R. Usherwood. Upwash exploitation and downwash avoidance by flap phasing in ibis formation flight. *Nature*, 505:399–402, January 2014.

[4] V. I. Fernandez. *Performance Analysis for Lateral-line-inspired Sensor Arrays*. PhD thesis, Massachusetts Institute of Technology, June 2011.

[5] L.L. Whitcomb, M.V. Jakuba, J.C. Kinsey, S.C. Martin, S.E. Webster, J.C. Howland, C.L. Taylor, D. Gomez-Ibanez, and D.R. Yoerger. Navigation and control of the Nereus hybrid underwater vehicle for global ocean science to 10,903 m depth: Preliminary results. In *Robotics and Automation (ICRA), 2010 IEEE International Conference on*, pages 594–600, May 2010.

[6] S. W. Squyres, A. H. Knoll, R. E. Arvidson, J. W. Ashley, J. F. Bell, W. M. Calvin, P. R. Christensen, B. C. Clark, B. A. Cohen, P. A. de Souza, L. Edgar, W. H. Farrand, I. Fleischer, R. Gellert, M. P. Golombek, J. Grant, J. Grotzinger, A. Hayes, K. E. Herkenhoff, J. R. Johnson, B. Jolliff, G. Klingelhöfer, A. Knudson, R. Li, T. J. McCoy, S. M. McLennan, D. W. Ming, D. W. Mittlefehldt, R. V. Morris, J. W. Rice, C. Schröder, R. J. Sullivan, A. Yen, and R. A. Yingst. Exploration of victoria crater by the mars rover opportunity. *Science*, 324(5930):1058–1061, 2009.

[7] J. Elston, B. Argrow, E. Frew, and A. Houston. Evaluation of UAS concepts of operation for severe storm penetration using hardware-in-the-loop simulations. In *AIAA Guidance, Navigation, and Control Conference*, pages 8178–8193, Toronto, Canada, August 2010.

[8] N. Leonard, D. A. Paley, F. Lekien, R. Sepulchre, D. Fratantoni, and R. Davis. Collective motion, sensor networks, and ocean sampling. *Proceedings of the IEEE*, 95(1):48–74, 2007.

[9] P. Lin. Observations: The first successful typhoon eyewall-penetration reconnaissance flight mission conducted by the unmanned aerial vehicle, Aerosonde. *Bulletin of the American Meteorological Society*, 87:1481–1483, 2006.

[10] S. J. Majumdar, et al. Targeted observations for improving numerical weather prediction: An overview. *World Weather rsearch Programme/THORPEX*, 2012.

[11] Patrick Lynch. NASA tops off earl research with historic global hawk flight. http://www.nasa.gov/mission_pages/hurricanes/missions/grip/news/GRIPHistoricFlight.html, September 2010.

[12] L. Jenner and B. Dunbar. NASA science aircraft monitor Hurricane Earl on Sept. 2. http://www.nasa.gov/centers/dryden/status_reports/GRIP_status_09_03_10.html#.U15Q361dWY0, September 2010.

[13] Jack Elston. *Semi-Autonomous Small Unmanned Aircraft Systems for Sampling Tornadic Supercell Thunderstorms*. PhD thesis, University of Colorado, 2011.

[14] R. Sepulchre, D. A. Paley, and N. E. Leonard. Stabilization of planar collective motion: All-to-all communication. *IEEE Transactions on Automatic Control*, 52:811–824, May 2007.

[15] D. A. Paley and C. Peterson. Stabilization of collective motion in a time-invariant flowfield. *AIAA Journal of Guidance, Control, and Dynamics*, 32:771–779, June 2009.

[16] L. Techy, D. A. Paley, and C.A. Woolsey. UAV coordination on closed convex paths in wind. *AIAA Journal of Guidance, Control, and Dynamics*, 33:1946–1951, 2010.

[17] L. Brinon Arranz, A. Seuret, and C. Canudas de Wit. Contraction control of a fleet circular formation of AUVs under limited communication range. In *In Proc. of the 2010 American Control Conference*, pages 5991–5996, Baltimore, MD, June 2010.

[18] E. W. Justh and P. S. Krishnaprasad. Equilibria and steering laws for planar formations. *Systems and Control Letters*, 52:25–38, 2004.

[19] F. Zhang. Coordinated patterns on smooth curves. *Proc. of IEEE International Conference on Networking, Sensing and Control*, 2006.

[20] F. Zhang and N. E. Leonard. Coordinated patterns of unit speed particles on a closed curve. *Systems and Control Letters*, 56:397–407, 2007.

[21] L. Brinon Arranz, A. Seuret, and C. Canudas de Wit. Translation control of a fleet circular formation of AUVs under finite communication range. In *Proc. of the 48th IEEE Conference on Decision and Control*, pages 8345–8350, Shanghai, China, December 2009.

[22] E. Frew, D. Lawrence, and S. Morris. Coordinated standoff tracking of moving targets using Lyapunov guidance vector fields. *AIAA Journal of Guidance, Control, and Dynamics*, 31:290–306, March 2008.

[23] C. Peterson and D. A. Paley. Multi-vehicle coordination in an estimated time-varying flowfield. *AIAA Journal of Guidance, Control, and Dynamics*, 34:177–191, 2011.

[24] E. Bakolas and P. Tsiotras. Minimum-time paths for a light aircraft in the presence of regionally-varying strong winds. In *In AIAA Infotech at Aerospace*, Atlanta, GA, April 2010. AIAA Paper 2010-3380.

[25] E. W. Justh and P. S. Krishnaprasad. Natural frames and interacting particles in three dimensions. In *In Proc. of the IEEE Conference on Decision and Control*, pages 2841–2846, December 2005.

[26] L. Scardovi, N. Leonard, and R. Sepulchre. Stabilization of three-dimensional collective motion. *Communication in Information and Systems*, page 15, June 2008.

[27] S. Hernandez and D. A. Paley. Three-dimensional motion coordination in a time-invariant flowfield. In *In Proc. of the IEEE Conference on Decision and Control*, pages 7043–7048, 2009.

[28] W. Ren and R. W. Beard. Trajectory tracking for unmanned air vehicles with velocity and heading rate constraints. *IEEE Transactions on Control Systems Technology*, 12(5):706–716, September 2004.

[29] R. W. Beard and T. W. McLain. *Small Unmanned Aircraft: Theory and Practice*. Princeton University Press, February 2012.

[30] C. Peterson and D. A. Paley. Distributed estimation for motion coordination in an unknown spatiotemporal flowfield. In *In Proc. of AIAA Guidance, Navigation, and Control Conference*, 2011.

[31] R. Bencatel, J. Sousa, M. Faied, and A. Girard. Shear wind estimation. In *In Proc. of the AIAA Guidance, Navigation, and Control Conference*, Portland Oregon, August 2011.

[32] K. M. Lynch, I. B Schwartz, P. Yang, and R. A. Freeman. Decentralized environmental modeling by mobile sensor networks. *IEEE Transactions on Robotics*, 24(3):710–724, 2008.

[33] C. K. Peterson and D. A. Paley. Distributed estimation for motion coordination in an unknown spatially varying flowfield. *To appear in AIAA Journal of Guidance, Control, and Dynamics*, 2013.

[34] H. Chao and Y. Chen. Surface wind profile measurement using multiple small unmanned aerial vehicles. In *In Proc. of the 2010 American Control Conference*, pages 4133–4138, June-July 2010.

[35] S. Mulgund and R. F. Stengel. Optimal nonlinear estimation for aircraft flight control in wind shear. *Automatica*, 32(1):3–13, 1996.

[36] N. R. J. Lawrance and S. Sukkarieh. Autonomous exploration of a wind field with a gliding aircraft. *AIAA Journal of Guidance, Control, and Dynamics*, 34(3):719–733, May-June 2011.

[37] J. W. Langelaan, N. Alley, and J. Neidhoefer. Wind field estimation for small unmanned aerial vehicles. *AIAA Journal of Guidance, Control, and Dynamics*, 34(4):1016–1030, July-August 2011.

[38] D. R. Thompson, S. Chien, Y. Chao, P. Li, B. Cahill, J. Levin, O. Schofield, A. Balasuriya, S. Petillo, M. Arrott, and M. Meisinger. Spatiotemporal path planning in strong, dynamic, uncertain currents. In *IEEE International Conference on Robotics and Automation*, pages 4778–4783, Anchorage, AK, 2010.

[39] V. R. Desaraju and J. P. How. Decentralized path planning for multi-agent teams with complex constraints. *Autonomous Robots*, 32(4):385–403, 2012.

[40] A. Bolger, M. Faulkner, D. Stein, L. White, S. Yun, and D. Rus. Experiments in decentralized robot construction with tool delivery and assembly robots. In *Proc. IEEE/RSJ Int. Conf. on Intelligent Robots and Systems*, 2010.

[41] L. Chaimowicz, B. Grocholsky, J. F. Keller, V. Kumar, and C. J. Taylor. Experiments in multirobot air-ground coordination. In *Proc. IEEE/RSJ Int. Conf. on Robotics and Automation*, 2004.

[42] C. K. Peterson. *Motion coordination of multiple autonomous vehicles in a spatiotemporal flowfield*. PhD thesis, University of Maryland, 2012.

[43] L. Techy, C. A. Woolsey, and D. G. Schmale III. Path planning for efficient UAV coordination in aerobiological sampling missions. In *Proc. IEEE Conf. on Decision and Control*, Cancun, Mexico, December 2008.

[44] M. Pivtoraiko, D. Mellinger, and V. Kumar. Quadrotor maneuver generation using motion primitives. In *Proc. IEEE Int. Conf. on Robotics and Automation*, 2013.

[45] R. C. Leishman, T. W. McLain, and R. W. Beard. Relative navigation approach for vision-based aerial GPS-denied navigation. *J. of Intelligent and Robotic Systems*, 74(1-2):97–111, 2014.

[46] S. Napora and D. A. Paley. Observer-based feedback control for stabilization of collective motion. *IEEE Trans. on Control Systems Technology*, 21(5):1846–1857, 2013.

[47] R. Smith, Yi Chao, Peggy P. Li, D. A. Caron, B. H. Jones, and G. S. Sukhatme. Planning and implementing trajectories for autonomous underwater vehicles to track evolving ocean processes based on predictions from a regional ocean model. *The International Journal of Robotics Research*, 29(12):1475–1497, 2010.

[48] S. O. Napora. Observer-based feedback control for stabilization of collective motion. Master's thesis, University of Maryland, College Park, MD, 2011.

[49] NOAA. Hurricane basics. http://hurricanes.noaa.gov/pdf/hurricanebook.pdf, National Oceanographic and Atmospheric Administration (NOAA), May 1999.

[50] S. R. Ramp, P.F.J. Lermusiaux, I. Shulman, Y. Chao, R. E. Wolf, and F. L. Bahr. Oceanographic and atmospheric conditions on the continental shelf north of the monterey bay during august 2006. *Dynamics of Atmospheres and Oceans*, 52:192–223, 2011.

[51] J. Cortes, S. Martinez, T. Karatas, and F. Bullo. Coverage control for mobile sensing networks. *IEEE Transactions on Robotics and Automation*, 20(2):243–255, April 2004.

[52] H. Choi and J. P. How. Continuous trajectory planning of mobile sensors for informative forecasting. *Automatica*, 46:1266–1275, April 2010.

[53] N. Sydney and D. A. Paley. Multivehicle coverage control for a nonstationary spatiotemporal field. *Automatica*, In press, 2014.

[54] B. Maskew. Formation flying benefits based on vortex lattice calculations. Technical report, NASA CR-151974, 1974.

[55] D. Hummel. Aerodynamic aspects of formation flight in birds. *J. of Theoretical Biology*, 104(3):321–347, 1983.

[56] S. A. Ning. *Aircraft Drag Reduction Through Extended Formation Flight.* PhD thesis, Stanford University, August 2011.

[57] W. Blake and D. Multhopp. Design, performance, and modeling considerations for close formation flight. In *Proc. of the AIAA Guidance, Navigation, and Control Conf.*, August 1998.

[58] D. F. Chichka, J. D. Wolfe, and J. L. Speyer. Aerodynamically coupled formation flight of aircraft. In *In Proc. of the 10th Med. Conf. on Control and Automation*, Lisbon, Portugal, July 2002.

[59] H. P. Thien, M. A. Moelyadi, and H. Muhammad. Effects of leader's position and shape on aerodynamic performances of v flight formation. *CoRR*, abs/0804.3879, 2008.

[60] M. Pachter, J. J. D'Azzo, and A. W. Proud. Tight formation flight control. *AIAA J. of Guidance, Control, and Dynamics*, 24(2):246–254, March-April 2001.

[61] J. Ding and Q Fan. A multi-uav tight formation flight controller. In *2012 IEEE Int. Conf. on Comp. Science and Automation Eng. (CSAE)*, volume 1, pages 60–64, May 2012.

[62] Z. A. Bangash, R. P. Sanchez, and A. Ahmed. Aerodynamics of formation flight. In *In Proc. of the AIAA Aerospace Sciences Meeting*, Reno, NV, January 2004. AIAA 2004-725.

[63] J. Katz and A. Plotkin. *Low-Speed Aerodynamics.* Cambridge University Press, second edition, 2001.

[64] J. Moran. *An Introduction to Theoretical and Computational Aerodynamics.* John Wiley and Sons, 1984.

[65] A. Dogan, S Sato, and W. Blake. Flight control and simulation for aerial refueling. In *In Proc. of AIAA Guidance, Navigation, and Control Conf.*, San Francisco, CA, August 2005.

[66] A. Dogan, T. A. Lewis, and W. Blake. Flight data analysis and simulation of wind effects during aerial refueling. *J. of Aircraft*, 45(6):2036–2048, Nov.-Dec. 2008.

[67] C. E. Hanson, J. Ryan, M. J. Allen, and S. R. Jacobsen. An overview of flight test results for a formation flight autopilot. In *Proc. AIAA Conf. Guidance, Navigation, and Control*, Monterey, California, 2002.

[68] M. S. Hemati, J. D. Eldredge, and J. L. Speyer. Wake sensing for aircraft formation flight. In *In Proc. of AIAA Guidance, Navigation, and Control Conf.*, Minneapolis, MN, August 2012.

[69] M. S. Hemati, J. D. Eldredge, and J. L. Speyer. Wake sensing for aircraft formation flight. *AIAA Journal of Guidance, Control, and Dynamics*, 37(2):513–524, 2014.

[70] C. F. Baker and J. C. Montgomery. The sensory basis of rheotaxis in the blind Mexican cavefish, *Astyanax fasciatus*. *Journal of Comparative Physiology*, 184(5):519–527, 1999.

[71] S. Coombs. Smart skins: Information processing by lateral line flow sensors. *Autonomous Robots*, 11(3):255–261, 2001.

[72] B. L. Partridge and T. J. Pitcher. The sensory basis of fish schools: Relative roles of lateral line and vision. *Journal of Comparative Physiology*, 135(4):315–325, 1980.

[73] M.J. McHenry, K.E. Feitl, J.A. Strother, and W.J. Van Trump. Larval zebrafish rapidly sense the water flow of a predator's strike. *Biology Letters*, 5(4):477–479, 2009.

[74] H. Bleckmann. Reaction time and stimulus frequency in prey localization in the surface-feeding fish *Aplocheilus lineatus*. *Journal of Comparative Physiology*, 140(2):163–172, 1980.

[75] A. M. Sutterlin and S. Waddy. Possible role of the posterior lateral line in obstacle entrainment by brook trout (*Salvelinus fontinalis*). *J. of the Fisheries Research Board of Canada*, 32(12):2441–2446, 1975.

[76] Z. Ren and K. Mohseni. A model of the lateral line of fish for vortex sensing. *Bioinspiration & Biomimetics*, 7(3), May 2012.

[77] S. Coombs and S. VanNetten. The biomechanics and hydrodynamics of octavolateris sensory systems with special emphasis on the lateral line. In *Biomechanics (G. Lauder and R. Shadwick, eds). Fish Physiology*. Academic Press, 2006.

[78] F. D. Lagor, L. DeVries, K. Waychoff, and D. A. Paley. Bio-inspired flow sensing and control: Autonomous rheotaxis using distributed pressure measurements. *J. of Unmanned Systems Technologies*, 1(3):78–88, 2013.

[79] R. Venturelli, O. Akanyeti, F. Visentin, J. Jezov, Chambers L. D., G. Toming, J. Brown, M. Kruusmaa, W. M. Megill, and P. Fiorini. Hydrodynamic pressure sensing with an artificial lateral line in steady and unsteady flows. *Bioinspiration & Biomimetics*, 7(3), Apr. 2012.

[80] A. B. Kroese and N. A. Schellart. Velocity and acceleration sensitive units in the trunk lateral line of the trout. *Journal of Neurophysiology*, 68:2212–2221, 1992.

[81] Y. Yang, J. Chen, J. Engel, S. Pandya, N. Chen, C. Tucker, S. Coombs, D. L. Jones, and C. Liu. Distant touch hydrodynamic imaging with an artificial lateral line. *Proceedings of the National Academy of Sciences*, 103(50):18891–18895, 2006.

[82] J. Tao and B. Yu. Hair flow sensors: from bio-inspiration to bio-mimicking—a review. *Smart Materials and Structures*, 21(11), 2012.

[83] V. I. Fernandez, A. Maertens, F. M. Yaul, J. Dahl, J. H. Lang, and M. S. Triantafyllou. Lateral-line-inspired sensor arrays for navigation and object identification. *Marine Technology Society J.*, 45(4):130–146, 2011.

[84] Y. Yang, N. Nguyen, N. Chen, M. Lockwood, C. Tucker, H. Hu, H. Bleckmann, C. Liu, and D. L. Jones. Artificial lateral line with biomimetic neuromasts to emulate fish sensing. *Bioinspiration & Biomimetics*, 5(1), 2010.

[85] A. Klein and H. Bleckmann. Determination of object position, vortex shedding frequency and flow velocity using artificial lateral line canals. *Beilstein J. Nanotechnology*, 2:276–283, June 2011.

[86] A. M. K. Dagamseh, T. S. J. Lammerink, M. L. Kolster, C. M. Bruinink, R. J. Wiegerink, and G. J. M. Krijnen. Dipole-source localization using biomimetic flow-sensor arrays positioned as lateral-line system. *Sensors and Actuators*, 162(2):355–360, August 2010.

[87] A. T. Abdulsadda and X. Tan. Underwater tracking of a moving dipole source using an artificial lateral line: Algorithm and experimental validation with IPMC flow sensors. *Smart Materials and Structures*, 22:045010, 2013.

[88] A. Qualtieri, F. Rizzi, G. Epifani, A. Ernits, M. Kruusmaa, and M. De Vittorio. Parylene-coated bioinspired artificial hair cell for liquid flow sensing. *Microelectronic Engineering*, 98(0):516–519, 2012.

[89] S. Peleshanko, M. D. Julian, M. Ornatska, M. E. McConney, M. C. LeMieux, N. Chen, C. Tucker, Y. Yang, C. Liu, A. C. Humphrey, and V. V. Tsukruk. Hydrogel-encapsulated microfabricated haircells mimicking fish cupula neuromast. *Advanced Materials*, 19(19):2903–2909, 2007.

[90] A. Gao and M. Triantafyllou. Bio-inspired pressure sensing for active yaw control of underwater vehicles. In *Oceans 2012*, pages 1–7, Oct 2012.

[91] T. Salumae and M. Kruusmaa. Against the flow: A Braitenberg controller for a fish robot. In *Proc. of the IEEE International Conference on Robotics and Automation*, pages 4210–4215, 2012.

[92] T. Salumae and M. Kruusmaa. Flow-relative control of an underwater robot. *Proc. of the Royal Soc. A*, 469(2153), March 2013.

[93] S. Skogestad and I. Postlethwaite. *Multivariable Feedback Control: Analysis and Design*. Wiley and Sons, West Sussex, England, 1996.

[94] H. Nijmeijer and A. J. van der Schaft. *Nonlinear Dynamical Control Systems*. Springer, 1990.

[95] R. Hermann and A. J. Krener. Nonlinear controllability and observability. *IEEE Trans. Auto. Control*, 22(5):728–740, 1977.

[96] S. Lall, J.E. Marsden, and S.A. Glavaski. A subspace approach to balanced truncation for model reduction of nonlinear control systems. *Int. J. of Robust and Nonlinear Cont.*, 12(6):519–535, 2002.

[97] A. Krener and K. Ide. Measures of unobservability. In *Proc. 48th IEEE Conf. Decision and Cont.*, pages 6401–6406, Shanghai, China, Dec. 2009.

[98] A. V. Wouwer, N. Point, S. Porteman, and M. Remy. An approach to the selection of optimal sensor locations in distributed parameter systems. *J. of Proc. Cont.*, 10(4):291–300, Aug. 2000.

[99] A. K. Singh and J. Hahn. Determining optimal sensor locations for state and parameter estimation for stable nonlinear systems. *Industrial and Eng. Chem. Research*, 44(15):5645–5659, June 2005.

[100] B. T. Hinson and K. A. Morgansen. Flowfield estimation in the wake of a pitching and heaving airfoil. In *In Proc. of the American Cont. Conf.*, June 2012.

[101] B. T. Hinson, M. K. Binder, and K. A. Morgansen. Path planning to optimize observability in a planar uniform flow field. In *Proc. American Control Conf. (ACC)*, pages 1394–1401, 2013.

[102] H. Salman, L. Kuznetsov, C. Jones, and K. Ide. A method of assimilating Lagrangian data into a shallow-water-equation ocean model. *Monthly Weather Review*, 134:1081–1101, Apr. 2006.

[103] A. J. Krener. Eulerian and lagrangian observability of point vortex flows. *Tellus*, 60:1089–1102, 2008.

[104] Q. Li, F. Guo, Y. Zhou, and W. Jang. Observability of satellite to satellite passive tracking from angles measurements. In *Proc. IEEE Conf. on Control and Automation*, Guangzhou, China, June 2007.

[105] S. Chakrabarti and E. Kyriakides. Optimal placement of phasor measurement units for power system observability. *IEEE Transactions on Power Systems*, 23(3):1433–1440, August 2008.

[106] L. DeVries and D. A. Paley. Multi-vehicle control in a strong flowfield with application to hurricane sampling. *AIAA Journal of Guidance, Control, and Dynamics*, 35(3):794–806, 2012.

[107] L. DeVries, S. J. Majumdar, and D. A. Paley. Observability-based optimization of coordinated sampling trajectories for recursive estimation of a strong, spatially varying flowfield. *J. of Intelligent and Robotic Systems*, 70(1-4):527–544, April 2013.

[108] L. DeVries and D. A. Paley. Dynamic altitude control for motion coordination in an estimated shear flow. *(Submitted)*, 2013.

[109] L. DeVries and D. A. Paley. Wake estimation and optimal control for autonomous aircraft in formation flight. In *Proc. of AIAA Guidance, Navigation, and Control Conf.*, Boston, MA, August 2013.

[110] L. DeVries and D. A. Paley. Multi-vehicle control in a strong flowfield with application to hurricane sampling. In *Proc. AIAA Conf. Guidance, Navigation, and Control*, Portland, Oregon, August 2011.

[111] L. DeVries and D. A. Paley. Observability-based optimization for flow sensing and control of an underwater vehicle in a uniform flowfield. In *Proc. of the 2013 Amer. Cont. Conf.*, Washington, DC, June 2013.

[112] L. DeVries and D. A. Paley. Dynamic altitude control for motion coordination in an estimated shear flow. In *In Proc. AIAA Conf. Giuidance, Navigation, and Control*, 2012.

[113] L. DeVries, S. Majumdar, and D. A. Paley. Observability-based optimization of coordinated sampling trajectories for flowfield estimation. In *In Proc. Int. Conf. Unmanned Aircraft Systems*, Philadelphia, PA, June 2012.

[114] F. D. Lagor, L. DeVries, K. Waychoff, and D. A. Paley. Bio-inspired flow sensing and control for autonomous underwater navigation using distributed pressure measurements. In *In Proc. 18th Int. Symp. Unmanned Untethered Submersible Tech.*, Portsmouth, NH, August 2013.

[115] N. Sydney and D. A. Paley. Multi-vehicle control and optimization for spatiotemporal sampling. In *In Proc. of the IEEE Conf. on Decision and Control*, pages 5607–5612, December 2011.

[116] H. K. Khalil. *Nonlinear Systems*. Prentice Hall, 3rd edition, 2002.

[117] D. A. Benson. *A Gauss Pseudospectral Transcription for Optimal Control*. PhD thesis, Massachusetts Institute of Technology, November 2004.

[118] G. T. Huntington. *Advancement and Analysis of a Gauss Pseudospectral Transcription for Optimal Control*. PhD thesis, Massachusetts Institute of Technology, May 2007.

[119] J. A. Sethian. *Level set methods and fast marching methods: evolving interfaces in computational geometry, fluid mechanics, computer vision, and materials science*. Cambridge University Press, 1999.

[120] J. A. Bondy and U. S. R. Murty. *Graph Theory with Applications*. Elsevier Science Ltd/North Holland, June 1976.

[121] R. Sepulchre, D. A. Paley, and N. E. Leonard. Graph laplacian and lyapunov design of collective planar motions. In *Proc. of the Int. Symposium on Nonlinear Theory and Its Application*, 2005.

[122] M. N. S. Swamy and K. Thulasiraman. *Graphs, Networks, and Algorithms*. John Wiley and Sons, 1981.

[123] J. A Fax and R. M Murray. Graph laplacians and stabilization of vehicle formations. In *Proc. IFAC World Congress*, Barcelona, Spain, 2002.

[124] R. Sepulchre, D. A. Paley, and N. E. Leonard. Stabilization of planar collective motion with limited communication. *IEEE Transactions on Automatic Control*, 53:706–719, April 2008.

[125] A. D. Sontag. A concept of local observability. *Systems and Control Letters*, 5:41–47, October 1984.

[126] A. K. Singh and J. Hahn. Optimal sensor location for nonlinear dynamic systems via empirical gramians. In *Proceedings DYCOPS 7*, Boston, MA, 2004.

[127] J. Hahn and T. F. Edgar. A gramian based approach to nonlinear quantification and model classification. *Industrial and Engineering Chemistry Research*, 40:5724–5731, 2001.

[128] D. Ucinski. *Optimal Measurement Methods for Distributed Parameter System Identification*. CRC Press, 1st edition, Aug. 2004.

[129] N. Bergman. *Recursive Bayesian Estimation Navigation and Tracking Applications*. PhD thesis, Department of Electrical Engineering, Linkoping University, Sweden, 1999.

[130] Y. Bar-Shalom, X. Rong Li, and T. Kirubarajan. *Estimation with Applications to Tracking and Navigation: Theory Algorithms and Software*. Wiley-Interscience, 1st edition, June 2001.

[131] M. S. Arulampalam, S. Maskell, N. Gordon, and T. Clapp. A tutorial on particle filters for online nonline/non-Gaussian Bayesian tracking. *IEEE Transactions on Signal Processing*, 50(2):174–188, 2 200.

[132] D. A. Paley, N. Leonard, and R. Sepulchre. Stabilization of symmetric formations to motion around convex loops. *Systems and Control Letters*, 57:209–215, December 2008.

[133] A. Kwok and S. Martinez. A coverage algorithm for drifters in a river environment. In *Proc. of the 2010 American Cont. Conf.*, June-July 2010.

[134] N. Kasdin and D. A. Paley. *Engineering Dynamics: A Comprehensive Introduction*. Princeton University Press, 2011.

[135] E. C. Weisstein. Quadrifolium. http://mathworld.wolfram.com/Quadrifolium.html, 25 April 2014.

[136] D. A. Paley, N. Leonard, and R. Sepulchre. Collective motion of self-propelled particles: Stabilizing symmetric formations on closed curves. In *Proc. 45th IEEE Conf. Decision and Control*, pages 5067–5072, San Diego, CA, December 2006.

[137] J. A. Fax and R. M. Murray. Information flow and cooperative control of vehicle formations. *IEEE Transactions on Automatic Control*, 49(9):1465–1476, September 2004.

[138] A. Miele and T. Wang. Optimization and acceleration guidance of flight trajectories in a windshear. *AIAA Journal of Guidance, Control, and Dynamics*, 10(4):368–377, 1987.

[139] W. Ren. Trajectory tracking control for a miniature fixed-wing unmanned air vehicle. *Int. J. of Systems Science*, 38(4):361–368, April 2007.

[140] J. L. Frankline, M. L. Black, and K. Valde. Eyewall wind profiles in hurricanes determined by GPS dropwindsondes. http://www.nhc.noaa.gov/aboutwindprofile.shtml, 25 April 2014.

[141] K. Wark, C. F. Warner, and W. T. Davis. *Air Pollution: Its Origin and Control*. Addison Wesley, third edition, 1998.

[142] G. J. Holland and et al. The Aerosonde robotic aircraft: A new paradigm for environmental observations. *Bull. Amer. Meteor. Soc.*, pages 889–901, 2001.

[143] M. Dunbabin and L. Marques. Robotics for environmental monitoring. *IEEE Robotics and Automation Magazine*, pages 24–39, February 2012.

[144] R. Olfati-Saber, J. A. Fax, and R. M. Murray. Consensus and cooperation in networked multi-agent systems. *Proceedings of the IEEE*, 95(1):215–233, January 2007.

[145] W. Ren. Multi-vehicle consensus with a time-varying reference state. *Systems and Control Letters*, 56:474–483, 2007.

[146] NOAA Earth Systems Research Laboratory. Final report: First-ever successful UAS mission into a tropical storm (ophelia - 2005). http://uas.noaa.gov/projects/demos/aerosonde/Ophelia_final.html, 2014.

[147] C. Peterson and D. A. Paley. Multi-vehicle coordination in an unknown flowfield. In *In Proc. AIAA Conf. Giuidance, Navigation, and Control*, Toronto, Canada, 2010.

[148] L. Brinon Arranz. *Cooperative control design for a fleet of AUVs under communication constraints*. PhD thesis, Université de Grenoble, 2011.

[149] M. S. Hemati. *Vortex-Based Aero- and Hydrodynamic Estimation*. PhD thesis, University of California Los Angeles, 2013.

[150] P. Batista, C. Silvestre, and P. Oliveira. Single range aided navigation and source localization: Observability and filter design. *Systems and Control Letters*, 60(8):665 – 673, 2011.

[151] R. L. Panton. *Incompressible Flow*. John Wiley and Sons, 1984.

[152] John D. Anderson. *Fundamentals of Aerodynamics*. McGraw-Hill, 5 edition, Feb. 2011.

[153] P. G. Saffman. *Vortex Dynamics*. Cambridge University Press, 1992.

[154] L. Zhen, H. Beom-soo, K. Moo-rong, and J. Ji-yuan. Experimental and numerical study for hydrodynamic characteristics of an oscillating hydrofoil. *J. of Hydrodynamics*, 20(3):280–287, 2008.

[155] G. Birkhoff and E. H. Zarantonello. *Jets, Wakes and Cavities*. Academic Press, 1957.

[156] G. V. Parkinson and T. Jandali. A wake source model for bluff body potential flow. *J. Fluid Mechanics*, 40(3):577–594, 1970.

[157] M. Kiya and M. Arie. A free-streamline theory for bluff bodies attached to a plane wall. *J. Fluid Mechanics*, 56(2):201–219, 1972.

[158] L. M. Milne-Thomson. *Theoretical Aerodynamics*. Dover Publications, 1966.

[159] T. Sarpkaya. An inviscid model of two-dimensional vortex shedding for transient and asymptotically steady separated flow over an inclined plate. *J. Fluid Mechanics*, 68(1):109–128, 1975.

[160] P. Y. Li and S. Saimek. Modeling and estimation of hydrodynamic potentials. In *Proc. 38th IEEE Conf. Decision and Cont.*, pages 3253–3258, 1999.

[161] P. K. Newton. *The N-Vortex Problem: Analytical Techniques*. Springer-Verlag, New York, NY, 2001.

[162] K. P. Burnham and D. R. Anderson. *Model Selection and Multimodal Inference: A Practical Information-Theoretic Approach*. Springer, second edition, 2002.

[163] Y. Bar-Cohen. *Electroactive Polymer Actuators as Artificial Muscles: Reality, Potential and Challenges*. SPIE, Bellingham, WA, 2001.

[164] M. Shahinpoor and K. J. Kim. Ionic polymer-metal composites: I. Fundamentals. *Smart Materials and Structures*, 10(4):819–833, 2001.

[165] H. Lei, C. Lim, and X. Tan. Modelling and inverse compensation of dynamics of base-excited ionic polymer-metal composite sensors. *J. of Intelligent Material Systems and Structures*, 24(13):1557–1571, 2013.

[166] A. Abdulsadda and X. Tan. Nonlinear estimation-based dipole source localization for artificial lateral line systems. *Bioinspiration & Biomimetics*, 8(2):026005 (15pg), Mar 2013.

[167] K. J. Kim and M. Shahinpoor. Ionic polymer-metal composites: II. Manufacturing techniques. *Smart Materials and Structures*, 12(1):65–79, 2003.

[168] H. Lei, W. Li, G. Zhu, and X. Tan. Evaluation of encapsulated IPMC sensor based on thick parylene coating. In *Proc. of ASME 2012 Conf. on Smart Materials, Adaptive Structures and Intelligent Systems*, pages SMASIS2012–7975, Stone Mountain, GA, 2012. ASME.

[169] X. Chen, G. Zhu, X. Yang, D. L.S. Hung, and X. Tan. Model-based estimation of flow characteristics using an ionic polymer-metal composite beam. *IEEE/ASME Trans. on Mechatronics*, 18(3):932–943, June 2013.

[170] W. Hardle and Hlavka Z. *Multivariate Statistics: Exercises and Solutions*. Springer, 2007.

[171] R. Graham and J. Cortes. Adaptive information collection by robotic sensor networks for spatial estimation. *IEEE Transactions on Automatic Control*, 57(6):1404–1419, June 2012.

[172] H. Choi and J. P. How. Analysis of mutual information for informative forecasting using mobile sensors. In *Proc. Int. Conf. on Control, Automation, Robotics and Vision (ICARCV)*, Singapore, December 2010.

[173] H. Choi. *Adaptive Sampling and Forecasting with Mobile Sensor Networks*. PhD thesis, Massachusetts Institute of Technology, 2009.

[174] R. Lumpkin and M. Pazos. *Lagrangian Analysis and Prediction of Coastal and Ocean Dynamics (LAPCOD)*, chapter Chapter 2. Cambridge University Press, 2006.

[175] National Weather Service. Online Weather Tool. http://www.srh.weather.gov/jetstream/tropics/tc_structure.htm, May 9 2014.

[176] X. Tan, D. Kim, N. Usher, D. Laboy, J. Jackson, A. Kapetanovic, J. Rapai, B. Sabadus, and X. Zhou. An autonomous robotic fish for mobile sensing. In *Proc. IEEE/RSJ Int. Conf. on Intelligent Robots and Systems*, Beijing, China, 2006.

[177] J. Wang, S. Chen, and X. Tan. Control-oriented averaging of tail-actuated robotic fish dynamics. In *Proc. American Control Conf. (ACC)*, 2013.

[178] O. M. Curet, Patankarm N. A., G. V. Lauder, and M. A. MacIver. Mechanical properties of a bio-inspired robotic knifefish with an undulatory propulsor. *Bioinspiration & Biomimetics*, 6(2), 2011.

[179] L. Wen, T. Wang, G. Wu, and J. Li. A novel method based on a force-feedback technique for the hydrodynamic investigation of kinematic effects on robotic fish. In *Proc. IEEE Int. Conf. on Robotics and Automation*, Shanghai, China, 2011.

[180] Y. Yang, A. Klein, H. Bleckmann, and C. Liu. Artificial lateral line canal for hydrodynamic detection. *Appl. Phys. Lett.*, 99, 2011.

[181] A. G. P. Kottapalli, M. Asadnia, J. M. Miao, G. Barbastathis, and M. S. Triantafyllou. A flexible liquid crystal polymer MEMS pressure sensor array for fish-like underwater sensing. *Smart Materials and Structures*, 21(11), 2012.

[182] S. P. Windsor, S. E. Norris, S. M. Cameron, G. D. Mallinson, and J. C. Montgomery. The flowfields involved in hydrodynamic imaging by blind Mexican cave fish (Astyanax fasciatus). Part I: open water and heading towards wall. *The Journal of Experimental Biology*, 213:3819–3831, 2010.

[183] S. P. Windsor, S. E. Norris, S. M. Cameron, G. D. Mallinson, and J. C. Montgomery. The flowfields involved in hydrodynamic imaging by blind Mexican cave fish (Astyanax fasciatus). Part II: gliding parallel to a wall. *The Journal of Experimental Biology*, 213:3832–3842, 2010.

[184] C. Phelan, J. Tangorra, G. Lauder, and M. Hale. A biorobotic model of the sunfish pectoral fin for investigations of fin sensorimotor control. *Bioinspiration and Biomimetics*, 5, 2010.

[185] R. Mittal, H. Dong, M. Bozkurttas, G. V. Lauder, and P. Madden. Locomotion with flexible propulsors: II. Computational modeling of pectoral fin swimming in sunfish. *Bioinspiration & Biomimetics*, 2006.

[186] S. P. Windsor, D. Tan, and J. C. Montgomery. Swimming kinematics and hydrodynamic imaging in the blind Mexican cae fish (Astyanax fasciatus). *The Journal of Experimental Biology*, 211:2950–2959, 2008.

[187] J. C. Liao. Neuromuscular control of trout swimming in a vortex street: implications for energy economy during the karman gait. *J. of Exp. Biology*, 207(20):3495–3506, 2004.

Index